

**Thermal Conductivity Enhancement by Optical Phonon  
Sub-Band Engineering of Nanostructures Based on C and BN**

**DARPA CONTRACT MDA972-02-C-0044**

**SCIENTIFIC AND TECHNICAL REPORT**

***FINAL REPORT***

Submitted by

**NANOTECH INSTITUTE  
UNIVERSITY OF TEXAS AT DALLAS (UTD)**

**DISTRIBUTION STATEMENT A**  
Approved for Public Release  
Distribution Unlimited

Submitted To:  
Dr. Leonard J. Buckley  
DARPA/DSO Program Manager  
[Lbuckley@darpa.mil](mailto:Lbuckley@darpa.mil)

Jim Troutman  
Contracting officer  
[jtroutman@darpa.mil](mailto:jtroutman@darpa.mil)

NanoTech Institute, UTD, MS:BE26, 2601 N. Floyd Rd., Richardson, TX 75083

# FINAL REPORT

## TABLE OF CONTENTS

<u>Section</u>	<u>Page</u>
<b>1. THEORY, MODELING AND DESIGN .....</b>	<b>5</b>
<b>1.1. Thermal Conductivity in CNT Bundles</b>	
1.1.1. Introduction .....	5
1.1.2. Scattering problems .....	5
1.1.3. Thermal conductivity .....	7
1.1.4. Conclusions .....	8
1.1.5. References .....	9
<b>1.2. Theory of Thermal Conductivity by Polaritons.....</b>	<b>10</b>
<b>1.3. Modeling of Phonons and Heat Transfer in Carbon Nanostructures .....</b>	<b>11</b>
1.3.1. Phonon dynamics and thermal properties of zigzag and armchair carbon nanotubes .....	11
a. Phonon dynamics and thermal properties of zigzag carbon nanotubes.....	11
b. Phonon dynamics and thermal properties of free armchair carbon nanotubes.....	30
1.3.2. Carbon heat radiators in polymer surroundings .....	52
a. Dynamics of carbon tubes laterally in contact with external medium .....	53
b. Phonon dynamics of carbon tubes embraced by polymer molecule .....	57
1.3.3. Sound propagation in molecular nets .....	59



a. Phonons and Hypersound in Low-dimensional Molecular Nets .....	60
b. Sound Boundary Conditions .....	64
c. The Hypersound Frequency Bands in Periodic Molecular Nets .....	68
d. Summary .....	73
1.3.4. Conclusions .....	73
1.3.5. References .....	75
2. SYNTHESIS OF NANOSTRUCTURE.....	76
2.1. Synthesis of Zeolite Encapsulated Nanotubes .....	76
2.2. Synthesis of Conjugated Polymer-CNT Complexes .....	84
3. CHARACTERIZATION AND OPTIMIZATION OF PHONON THERMAL SPECTRA, CONDUCTIVITY AND SUPERCONDUCTIVITY.....	91
3.1. Thermal Conductivity Measurements on Nanocomposites with CNTs.....	91
3.1.1. Comparative method in PPMS.....	91
3.1.2. Tunable thermal conductivity in carbon nanotube paper.....	93
a. Experiment.....	93
3.1.3. References.....	98
3.2. Thermal Conductivity of Carbon Inverse Opals.....	99
3.2.1. Experiment.....	100
3.2.2. Results and Discussion.....	100
3.2.3. Conclusion.....	106
3.2.4. References.....	107
4. SUMMARY AND CONCLUSIONS.....	108
4.1. Summary on Carbon Nanotubes.....	108
4.2. Conclusions on Thermal Conductivity Enhancement.....	108

## **5. APPENDICES**

- 5.1. Theory of Thermal Conductivity by Polaritons**
- 5.2. "Vibrations of single-wall carbon nanotube: lattice models and low-frequency dispersion"**
- 5.3. "Simple empirical model for vibrational spectra of single-wall carbon nanotubes"**
- 5.4. "Phonon-Polariton Physics: Thermal Conductivity, Phonon-Polariton Lasers and Phonon Transistors in Nanostructures"**
- 5.5. "Phonons and Thermal Transport in Carbon Nanotube Systems"**



## **Chapter 1: THEORY, MODELING AND DESIGN**

### **1.1 Thermal Conductivity in CNT Bundles**

#### **1.1.1. Introduction**

It is expected that a single-wall carbon nanotube (SWCN) is a very promising object for creation of metamaterials with a high thermal conductivity (TC) [1,2]. The first reason for this expectation is that carbon-based materials, like diamond, have the largest known TC and, the second reason is a molecular perfection of the SWCNs [1]. However, to the best of my knowledge, the highest TC ever observed in SWCN bundles at room temperature is about 220 W/mK and it is ten times smaller than the TC of the natural diamond [3]. This highest result has been reported by Hone et al. [4] for a bulk sample of magnetically aligned nanotubes. The aligned SWCNs form a bundle in which all tubes have a preferable orientation in some direction. Hone et al. showed that the TC of the aligned SWCNs is strongly anisotropic with the largest value in the direction of the alignment.

The enhancement of the TC due to the alignment has been observed also by Zhou et al. [5] and by Choi et al. [6], but the absolute values of the reported TC have been significantly smaller than in [4].

There are many theoretical works on TC of the SWCNs. Some computational ones [7-10] are made by molecular dynamics simulations. The results of these simulations have different values and different T-dependences. They predict mostly very high values of the room temperature TC (for example 6000 in [7].)

Evidently, the main problem of all these works is the small size of the array that can be simulated. There are also some different analytical approaches to the problem [11,12] and wonderful reviews [13-15].

The purpose of this research is to estimate the maximum TC value of aligned nanotubes taking into account that they do necessarily consist of segments with a finite length. It is well known, that tubes in ropes are not infinitely long, but have brakes, because each method of synthesis is able to create separated tubes of only a certain length. It is believed that this length is of the order of a few microns (see [16] and references therein). Then, due to Van der Waals forces, the tubes stick together and create bundles wherein the end of a tube has no chance to make a strong chemical bond to the end of a neighboring tube.

There are many experiments that show that tubes inside bundles have free ends. The idea here is to argue that this effect may be responsible for the relatively low TC as compared to crystalline carbon materials.

#### **1.1.2. Scattering problems**

Consider a bundle of nanotubes perfectly aligned; each segment has a finite length with an average value  $L$ . The nanotubes are organized in an ideal triangular lattice with six nearest neighbors [17]. The cross section in a plane perpendicular to the nanotubes is shown in Fig.1.1(a). The cuts in each line of the nanotubes have random positions. Thus, on the



length of each segment there are in average six cuts of its nearest neighbors. A homogeneous interaction between infinite tubes does not cause the loss of the phonon momentum. However, a phonon flux has to overcome the openings between the segments at the termination points of each nanotube segment. Assume that these openings are so large that a jump of flux occurs with an assistance of all six neighboring rows of the tubes as shown in Fig.1.1(b). A slightly different mechanism of momentum scattering appears in a given nanotube ("0") if one of the neighboring nanotubes has a termination point as shown in Fig.1.1(c).

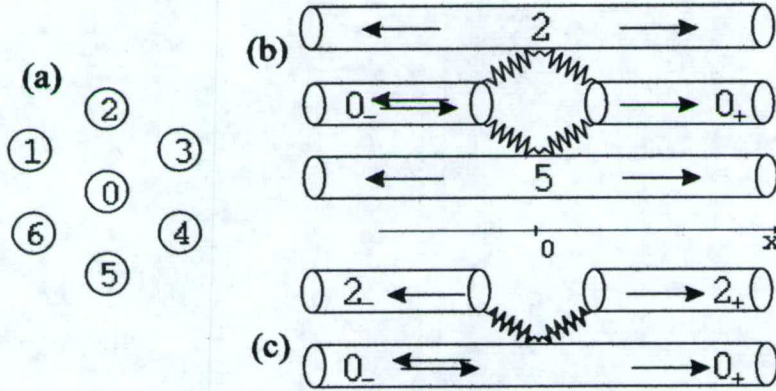


Fig. 1.1: (a) The cross-section of the bundle that shown a nanotube "0" and its nearest neighbors.  
 (b) The first scattering problem - cross-section by the plane of nanotubes 2-0-5. The wave incident from 0. reflects backward and transmits through the opening into 0<sub>+</sub> with simultaneous excitation of the waves in all six neighboring tubes.  
 (c) The second scattering problem. The wave incident from 0. is scattered by the cut in tube 2. It reflects backward, transmits into 0<sub>+</sub> and excites waves in tube 2<sub>+</sub>.

The propagation of heat flux  $Q$  between the scattering points was assumed to be ballistic because the goal is to get a maximum estimate of the TC. Quick phonon exchange at the scattering points leads to a thermalisation of symmetrical parts of the distribution functions of phonons with temperatures that are determined by values of effective thermal resistances between scattering points. It should be noted that calculations could not be applied directly to multiwall carbon nanotubes.

Thus, there are two different scattering problems. Since the bottle neck of problem 1 is a jump through the opening, let us assume strong interaction between tubes as compared to the phonon energy. In this way, we can achieve the upper estimate of TC. In all cases, the scattering is determined by three coefficients: reflection  $D$ , transmission  $C$  and penetration to a neighboring nanotube  $A$ . In this case, the results for transmission and reflection are independent of the spectrum of the phonon mode and determined by the geometry of the problem only.

For the first scattering problem  $|D|^2 = 36/49$ ,  $|C|^2 = |A|^2 = 1/49$  and for the second problem  $|D_1|^2 = |C_1|^2 = |A_1|^2 = 1/4$ .



### 1.1.3. Thermal Conductivity

In the approximation of elastic scattering, the heat flux  $Q$  along each row of the aligned nanotube is conserved because the waves generated in neighboring nanotubes due to scattering have zero total momentum. This leads to a conservation of  $Q$  along the row because in the theory of phonon thermal conductivity any relaxation of  $Q$  is the result of momentum loss. It is important, however, that at the points of scattering of both types considered above, the numbers of phonons in each mode changes. Therefore the symmetric parts of the distribution functions in these points can be considered as in equilibrium with different temperatures for each point. Assume that the propagation is ballistic between the scattering points of both types.

In average every section of a nanotube can be divided into seven ballistic regions such that each boundary of the region corresponds to a cut in one of the six neighboring rows of the nanotubes. The part of one row is shown in Fig. 1.2. The energy flux is the same along the row. Since the scattering is different, the temperature intervals between neighboring boundaries are also different. To calculate the TC, the total temperature difference through all the nanotube at a given flux  $Q$  was found.



Fig. 1.2: Part of the row of nanotubes with two cuts. Dotted lines in the nanotubes correspond to cuts of the neighboring nanotubes. The regions between them are considered to be ballistic.

Consider one region  $i$  of a nanotube and assume that each end of the region perfectly matches a thermal bath. The temperature difference of the left and right boundaries of the region is  $t_i$ . Thermal flux produced in this region is  $Q=G(T)t_i$ , where the function  $G(T)$  is called thermal conductance. It can be written in the form [18]:

$$G(T) = \frac{k_b^2 T}{h} \sum_a \int_{z_1}^{z_2} \frac{x^2 e^x}{(e^x - 1)^2} dx \quad (1.1)$$

where  $z = hw/k_B T$  and the sum is over all monotonously increasing segments of spectrum  $w_s(k)$ ,  $z_1$  and  $z_2$  are the lower and upper boundaries of such segments. Here  $k_B$  and  $h$  are the Boltzmann and the Plank constants respectively. To calculate the above integrals one should know the vibration spectra of nanotubes. They have been calculated previously within different frameworks such as an empirical force constant model [17,19]. The function  $G(T)$  calculated by Yu. Gartstein [20] is used in this experiment. Finally, an equation for TC was obtained,



$$k = NLG(T)/B \quad (1.2)$$

where  $N$  is the number of tubes in the bundle per square meter (assuming triangular lattice, it is easy to get  $N=4 \times 10^{17} \text{ m}^{-2}$  for (10,10) nanotubes),  $L$  is the length of a nanotube,

$$B = \frac{6}{1 - |D_1|^2} + \frac{1}{1 - |D|^2} - 6|C_1|^2 - |C|^2 = 1/0.0976.$$

Since the interaction is assumed to be strong, coefficients in  $B$  are independent of the frequency. As a result the TC can be expressed in terms of  $G(T)$ . Thus, the final result is

$$k = 0.0976G(T)LN \quad (1.3)$$

Fig. 1.3 shows the results at  $L=1, 0.87, 0.7\mu\text{m}$  together with the results by Hone et al. [4]. One can see that the theory reflects well enough both the magnitude and the temperature behavior. In fact, the only parameter here is the average length of a nanotube. The deviation at high temperatures is probably related to the Umklapp processes.

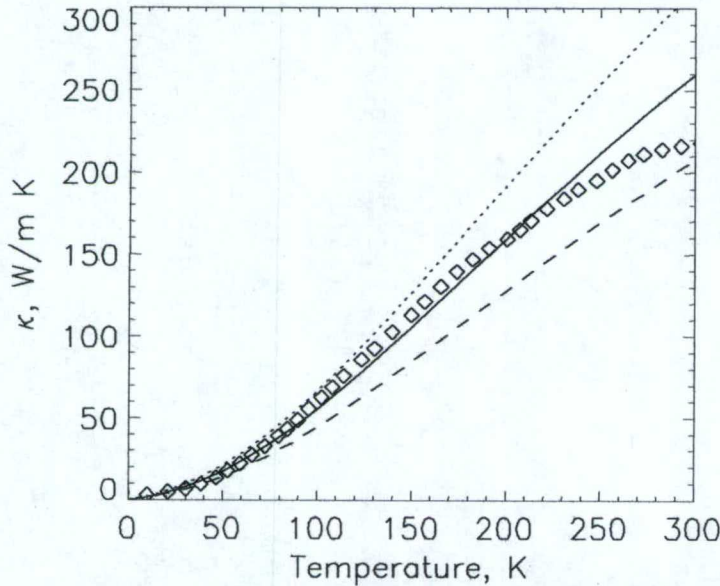


Fig. 1.3: Thermal conductivity as calculated theoretically for the (10,10) tube with  $L=0.7\mu\text{m}$  (dashed line),  $0.87\mu\text{m}$  (solid) and  $1.0\mu\text{m}$  (dotted). The experimental data of [4] are shown by diamonds.

#### 1.1.4. Conclusions

In this paper, the maximum estimate of the TC of perfectly aligned nanotubes, taking into account the scattering of phonons by the terminal points of the nanotubes, was presented. This estimate gives a quantitatively correct description of the thermal conductivity of aligned nanotubes as obtained experimentally by Hone et al. [4] assuming that the length of segments is of the order of  $1\mu\text{m}$ . It follows from these results that the way to make the thermal conductivity of the aligned nanotubes at room temperature larger than  $300 \text{ W/m K}$  is to increase their lengths. Of course, the TC will not increase indefinitely with



length ( $L$ ), as it follows from (1.3), because, sooner or later, the mean free path, due to other scattering processes, will be smaller than  $L/7$ . However, some additional gain may be achieved with increasing  $L$ .

The paper is published in cond-mat/0405499 and sent to Phys. Rev. B

### 1.1.5. References

- [1] Guo-Dong, J. D. Kuntz, J. Wan, and A. K. Mukherjee, *Nature Materials* 2, 38 (2002).
- [2] R. S. Ruoff and D. C. Lorents, *Carbon* 33, 925 (1995).
- [3] T. R. Anthony, W. Banholzer, J. F. Fleisher, L. Wei, P. K. Kuo, R. L. Thomas, and R. W. Pryor, *Phys. Rev. B* 42, 1104 (1990).
- [4] J. Hone, M. Llaguno, N. Nemes, A. Johnson, J. Fischer, D. Walters, M. Casavant, J. Schmidt, and R. Smalley, *Appl. Phys. Letters* 77, 666 (2000).
- [5] W. Zhou, J. Vavro, C. Guthy, K. I. Winey, J. E. Fisher, L. M. Ericson, S. Ramesh, R. Saini, V. Davis, C. Kittrell, et al., *Journal of Appl. Physics* 95, 649 (2004).
- [6] E. S. Choi, J. S. Brooks, D. L. Eaton, M. S. Al-Haik, M. Y. Hussaini, H. Garmestani, D. Li, and K. Dahmen, *Journal of Appl. Physics* 94, 6034 (2003).
- [7] S. Berber, Y.-K. Kwon, and D. Tamaneck, *Phys. Rev. Lett.* 84, 4613 (2000).
- [8] S. Maruyama, *Physica B* 323, 193 (2002).
- [9] M. Osman and D. Srivastava, *Nanotechnology* 12, 21 (2001).
- [10] J. Che, T. Cagin, and W. Goddard, *Nanotechnology* 11, 65 (2000).
- [11] Q. Zheng, G. Su, J. Wong, and H. Guo, *Eur. Phys. J. B* 25, 233 (2002).
- [12] J. X. Cao, X. H. Yan, Y. Xiao, Y. Tang, and J. W. Ding, *Phys. Rev. B* 67, 045413 (2003).
- [13] M. Dresselhaus, G. Dresselhaus, and P. Avouris, eds., *Carbon Nanotubes: Synthesis, Structure, Properties and Applications* (Springer, Berlin, 2000).
- [14] D. Cahill, W. Ford, K. Goodson, G. Mahan, A. Majumdar, H. Maris, R. Merlin, and S. Phillpot, *J. Appl. Phys.* 93, 793 (2003).
- [15] R. Baughman, A. A. Zakhidov, and W. A. de Heer, *Science* 297, 787 (2002).
- [16] Y. Yosida, *Journal of Appl. Physics* 87, 3338 (2000).
- [17] M. Dresselhaus and P. Eklund, *Adv. Phys.* 49, 705 (2000).
- [18] K. Schwab, E. Henriksen, J. Worlock, and M. Roukes, *Nature* 404, 974 (2000).
- [19] R. Saito, G. Dresselhaus, and M. Dresselhaus, *Physical Properties of Carbon Nanotubes* (Imperial College Press, London, 1998).
- [20] Yu. N. Gartstein, unpublished, I am grateful to Dr. Gartstein for calculation of the function  $G(T)$ .

## **1.2    Theory of Thermal Conductivity by Polaritons**

See APPENDIX 5.1 and 5.4

## **1.3    Modeling of Phonons and Heat Transfer in Carbon Nanostructures**

### **1.3.1. Phonon dynamics and thermal properties of zigzag and armchair carbon nanotubes**

**Report-2b:    "Strategies to Increase Thermal Conductivity. Enhancement by Optical  
Phonon Sub-Bands Engineering in 3-D Nanostructures Based on C and  
BN Nanotubes"**

#### **1.3.1a. Phonon dynamics and thermal properties of zigzag carbon nanotubes**

##### **Content**

- I.     Introduction**
- II.    Phonon dynamics in a zigzag carbon nanotube**
- III.   Generalized equation of thermal conductivity in a single nanotube**
- IV.   Thermodynamics and statistics for a carbon nanotube**
- V.     Summary**
- VI.    References**
- VII.   Attachment - Short investigation plan**



## I. Introduction

This report presents the second stage of investigation of phonon fluxes in carbon and BN nanostructures in the framework of the tasks for *"Strategies to Increase Thermal Conductivity. Enhancement by Optical Phonon Sub-Bands Engineering in 3-D Nanostructures Based on C and BN Nanotubes"*.

Here, the dynamics of the heat transfer problem for closed carbon nets (planned point 1c), zigzag tubes (point 2c) and macroscopic manifestations (point 3c) are presented. Phonon eigenstates, density of states and vibration amplitude distribution for each phonon along the molecular fragment are considered for two main tubulene geometries: zigzag and armchair.

The idea of the PQDM approach proposed in the previous report is to use a discrete microscopic model for phonon dynamics of relatively small molecular fragments approximately of phonon mean free path sizes. The dynamics of such a cluster may be described classically in Born approach [1, 2] and all the important data may be obtained: eigenfrequencies, density of states and phonon amplitude distribution inside the molecular fragment during its lifetime. Neighboring fragments of a molecular net are in an uninterrupted process of exchange by phonons. Due to the weak fragment-surrounding medium interaction, the process may be described by Fermi's "golden rule" which determines the value of the transfer rate. This quantum characteristic is a transport process consideration that enables the introduction of a microscopic thermal conductivity coefficient that depends on the temperature difference between opposite sides of the fragment in contact with the baths.

An averaged classical picture of phonon energy (heat) transport and temperature distribution in the big 2D carbon nets, both open (graphene) and closed (tubulenes), and other kinetic and statistical phenomena may be obtained in rough space scale. **The transition to rough scale leads to the generalized phonon kinetics equation describing heat propagation in 2D molecular nets.** Results obtained in the previous report for flat nets have important meaning for comparison with that for closed nets. Considering here phonon dynamics and statistics in tubes with zero-chirality and of zigzag geometry, comparison with data for flat nets will be made.

The general picture of connected subjects for the problem of phonon propagation in molecular nets is shown in Fig.1.



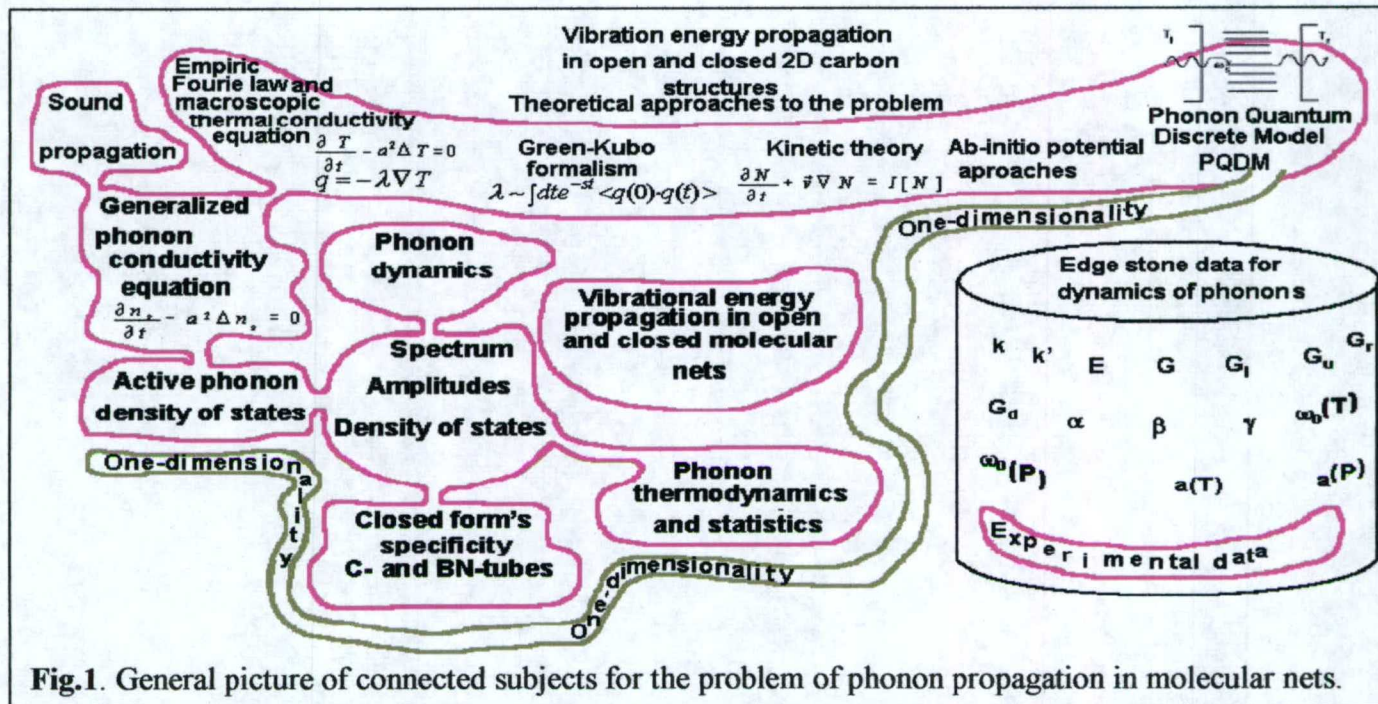


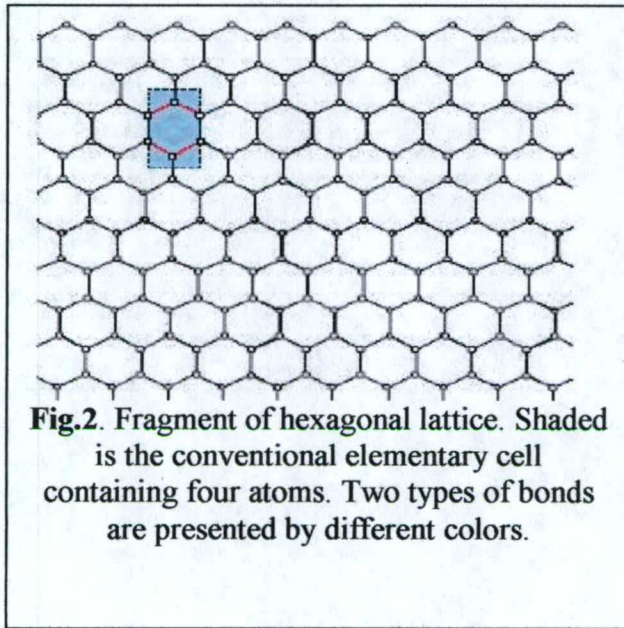
Fig.1. General picture of connected subjects for the problem of phonon propagation in molecular nets.

In Fig.1, fundamental data such as elastic modulus  $E$ ,  $G$  and elastic coefficients  $k$ ,  $k'$  describing forces when shifts are directed along the main axes of the bond potential ellipsoid are presented.  $U(r)$  is the site potential energy of an atom which has to be determined in other approaches; the same for thermal expansion coefficient  $\beta$ , pressure coefficient  $\gamma(T)$ , characteristic frequency (or phonon band width) temperature dependence  $\omega_b(T)$ .

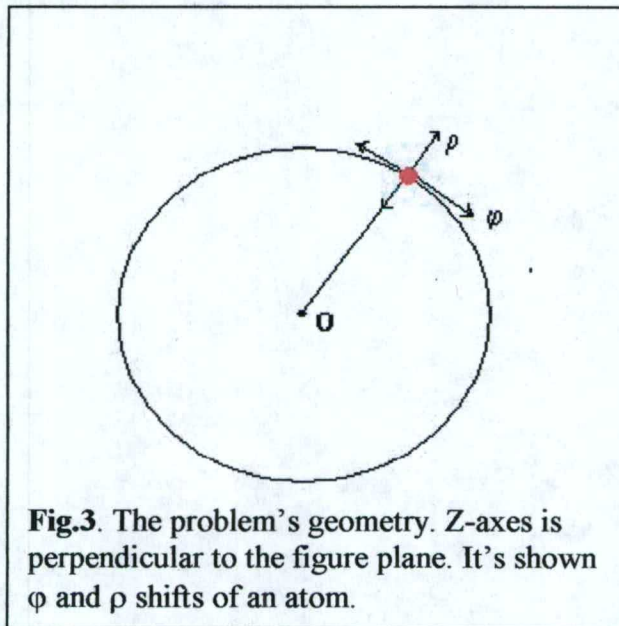
## II. Phonon dynamics in a zigzag carbon nanotube

Linear approximation in phonon dynamics is based on the supposition that small atomic vibrations have harmonic character at least in the case of not too high temperatures. It means that a potential equienergetical surface in the vicinity of atomic equilibrium positions has an ellipsoidal form. Classical motion of atoms near their equilibrium points is described by elastic constants  $k$  that characterizes atom-atom bonds in Born approach [1]. For atomic shifts perpendicular to bond we will use nonzero elastic constant  $k' \ll k$  coming out the framework of linear approximation.





The symmetry of carbon structures dictates three main vibration types (radial  $\rho$ -mode, tangential  $\varphi$ -mode and axial  $z$ -mode) shown in Fig.3. It should be marked that principal difference between vibration branches originates from bonds direction relative the direction of symmetry axes connected with given freedom's degree. This difference manifests itself in phonon band structure for tangential and axial branches in pure zero-chirality case. In presence of helicity the difference vanishes.





In Fig.4, the case when  $\phi$ -mode and axial z-mode have approximately equal orientation shifts relative to both red and blue bonds inside a chosen elementary cell is

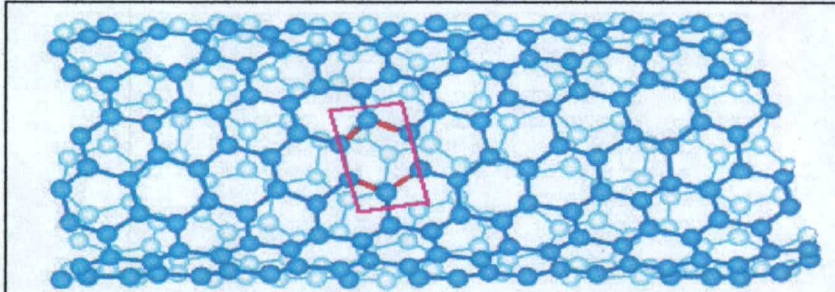


**Fig.4.** Fragment of armchair tubulene (10,5) with non-zero chirality created from a graphene sheet {14,10} by rolling up around the armchair direction. Picked out is the conventional elementary cell containing four atoms. Two types of bonds are marked by different colors.

presented.

Systems of dynamical equations for all three branches of vibrations are calculated taking into account that the motion of each atom is three-dimensional. The zero-approximation approach supposes that radial  $\rho$ -mode, tangential  $\phi$ -mode and axial z-mode should be considered independently.

Consider a zigzag tube (n,0) produced from the fragment shown in Fig.2 by rolling around vertical direction without any shift. In this case, each of the tube fragments is connected with the same fragment. Therefore, contrary to the case of flat fragments connecting external media (Report-1b) all atomic positions and their bonds are described similarly by the same dynamical equations. The difference exists with different vibration types or branches only.

For shifts directed normal to the tube surface, the equation is the following

$$\{m \ddot{\rho}_i = -k'(3\rho_i - \rho_{i1} - \rho_{i2} - \rho_{i3}), \quad (1)$$

where  $i_1, i_2, i_3$  are indexes for atom  $i$  neighbors. Atomic coordinates are not important here. The united atomic number  $i$  is defined using its position in the row and column of initial flat fragment creating the tube. For tangential atomic shifts having in view that atom space coordinates on the tube surface  $x = \varphi R$ , where  $R$  is the tube radius and  $\varphi$  is the azimuth angle. The zigzag case with the absence of chirality is described by the system:

$$\{m \ddot{x}_i = -0.75k(2x_i - x_{i1} - x_{i2}) - k'(x_i - x_{i3}) \quad (2)$$

where coefficient 0.25 characterizes two weak bonds for this vibration. For axial atomic shifts we have



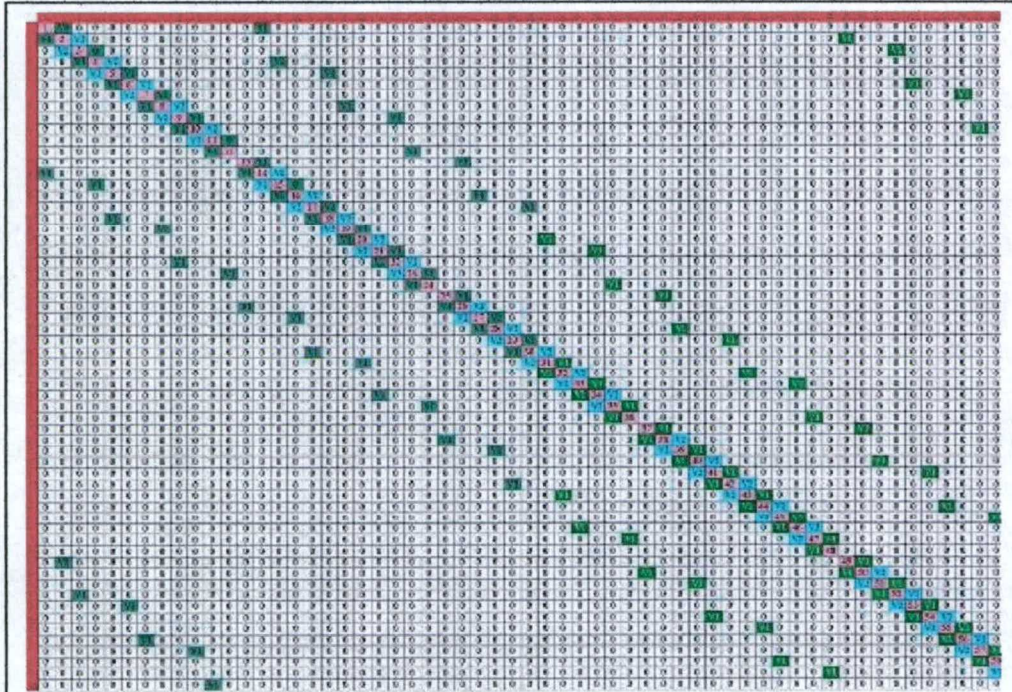


**Fig.5.** Sketch of the dynamical matrix for zigzag tubulene created from a graphene sheet {5,5} containing 60 atoms by its rolling up. Rose-colored spots are diagonal elements, green and blue show two types of bonds, rest elements equal to zero, left and upper red bands contain atomic numbers.

$$\{m \ddot{z}_i = -k(z_i - z_{i1}) - 0.25k(2z_i - z_{i2} - z_{i3}) \quad (3)$$

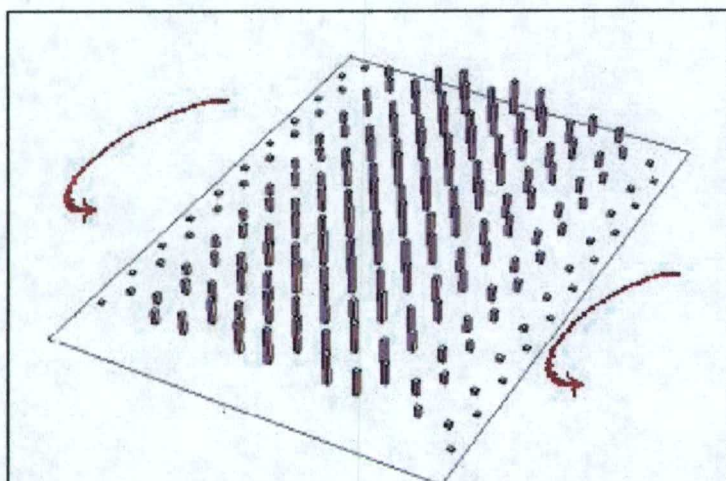
Matrix structure of all equations (1-3) corresponding zigzag (n,0) case is shown in Fig.5.

Fig. 5 shows a zigzag tubulene matrix and vibration amplitudes. Atomic coordinates become important when mode amplitude distribution is presented in the space.

The square of vibration mode  $s=1$  of any type is shown in Fig.6. There are considerable differences in amplitude distribution over the tube surface relative open carbon net. The differences are caused by a change in the topology of the system. The difference between mode frequencies and density of states at the same number of state exists but it is not essential.

The calculations given are for eigenvectors  $|C_{si}|^2$  which is a well known standing wave picture with corresponding number of knot's lines depending on the number of state  $s$ . Increasing the number of states leads to lateral (parallel to z-axes) divided by transversal (circular) knot's lines the tube's surface.





**Fig.6a.** Calculated  $\rho$ -branch amplitude distribution along zigzag tubulene created from a graphene sheet  $\{8,10\}$  by rolling up around marked direction. Ground state.

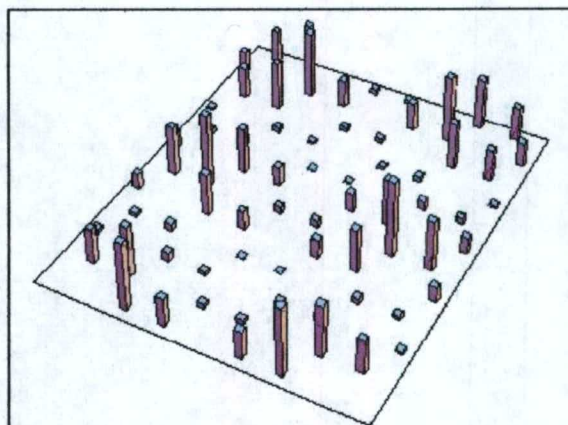


**Fig.6b.**  $\rho$ -branch amplitude distribution along zigzag tubulene created from a graphene sheet  $\{5,5\}$  by rolling up around marked direction. 5th state. Transversal knot's line is degenerated.



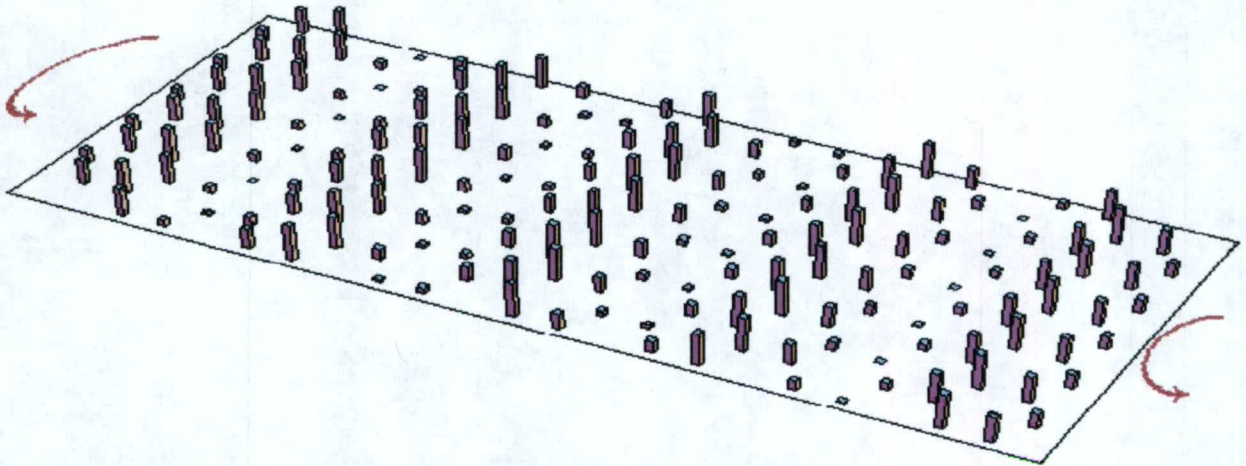


**Fig.6c.**  $\rho$ -branch square amplitude distribution along zigzag tubulene created from a graphene sheet  $\{14,5\}$  by rolling up around marked direction. Four transversal knot's lines correspond to 5th-state.

The Low frequency ground state is shown in Fig.6a. The picture is typical for mean amplitudes distribution: maximal amplitudes situates near the tube's middle. The Fig.6b illustrates amplitude distribution for 5<sup>th</sup> (or  $r$ -4<sup>th</sup>) state where twice degenerated line of knots crossing two non-degenerated lateral lines of knots.

Increasing the tube's length leads to a considerable change in the picture of vibrations. The same 5<sup>th</sup> (or  $r$ -4<sup>th</sup>) state presented in Fig.6c has another combination of knot's lines. The transversal line vanishes and two additional lateral lines of knots arise.

The mean vibration amplitudes  $A_j$  averaged on the state populations  $n_j$  decrease from the lateral ends to the middle axes of the nanobridge.

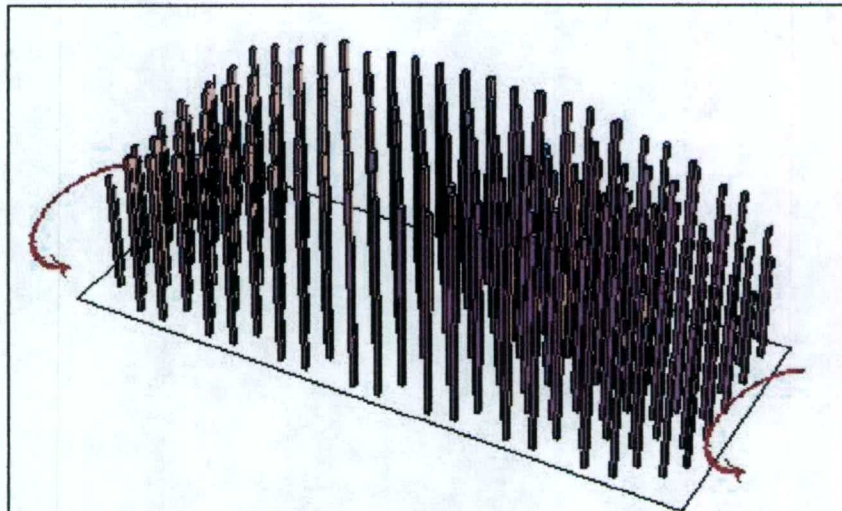


**Fig.6d.** Calculated mean square amplitude distribution along zigzag tubulene created from a graphene sheet  $\{15,5\}$  by rolling up around marked direction.  $T=0.03$  eV. Circular arrows show rolling up of the structure.

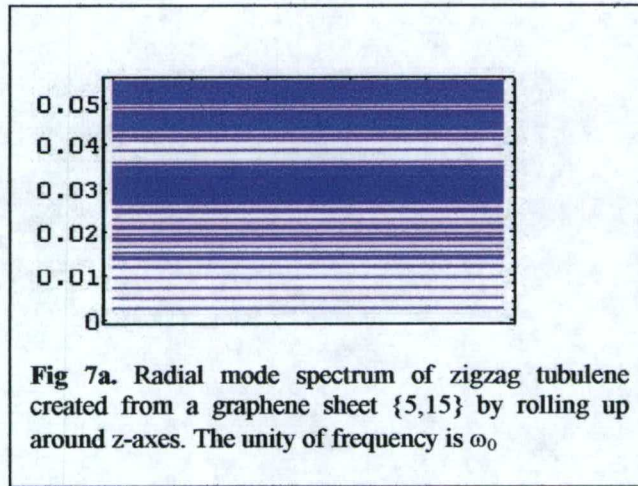


More free lateral atoms have bigger vibration amplitudes.

$$A_j = \sum_{s, \sigma} |C_{sj}|^2 n_{s\sigma}, \quad (4)$$

where  $n_{s\sigma}$  is the population of  $s, \sigma$  state,  $j$  numbers atoms situated on the tube surface and  $C_{sj}$  is the  $s$ -state probability amplitude at  $j$ -position of the net. Mean square amplitudes calculated for temperature  $T=0.03\text{eV}$  by expression (4) are shown in Fig.6d. The averaging was made here on all phonon branches  $\sigma$ . One can see that in contrary with flat carbon terminated nets with free edge atoms the closed structure is harder near the edges and greatest amplitudes of vibrations take place in the middle of the tube. The greater are temperatures the lesser is this effect of hard tube ends. Tube ends are frozen at low temperatures.

The density of states (DOS) for a zigzag tubulene spectrum is shown in Fig 7a.



The density of states may be approximately defined by the expression :

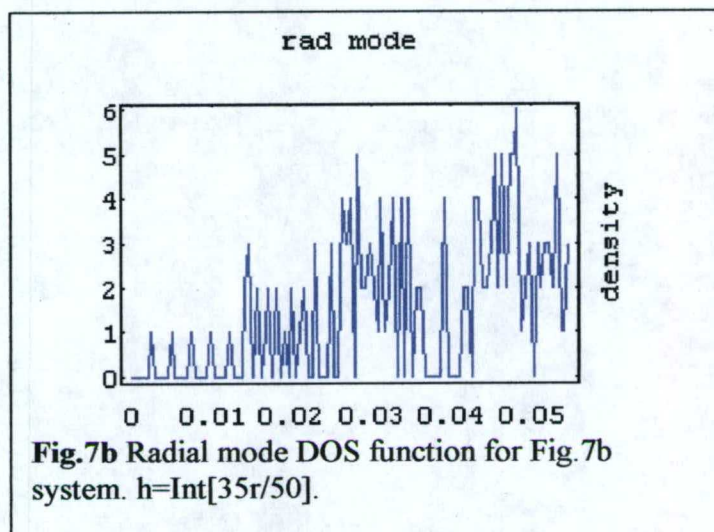
$$g(\omega_{s\sigma}) \approx \frac{1}{\omega_{s\sigma} - \omega_{s-1, \sigma}} \quad (5)$$

that transfers to an exact one if the number of degrees of freedom becomes big enough.

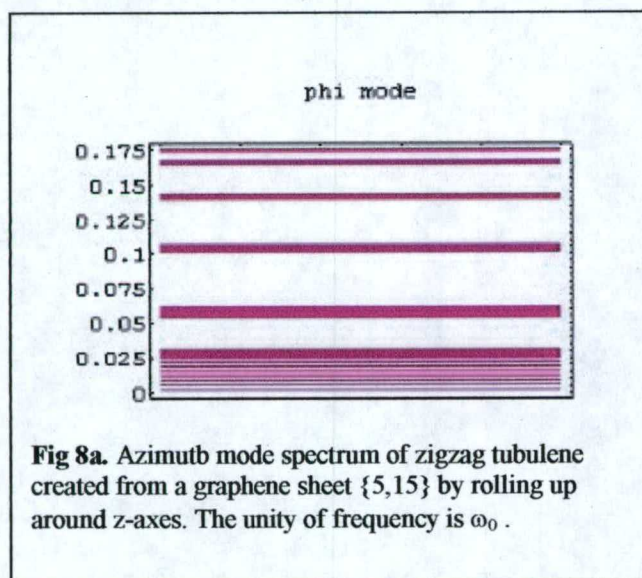
More correctly, the density of states function may be calculated providing preliminary state grouping and density determination inside the each group. DOS calculation were made with preliminary state grouping using dividing the whole frequency band interval into  $h = \text{Int}[35r/50]$  sub-intervals (or near this value) where the number of eigenmodes was counted. The integer numbers are present on vertical axes in figures 7b, 8b and 9b.

Frequency spectrum and DOS function in case of zero chirality are presented in Fig 7-9. The figures 7a, 7b were obtained by numerical calculation in system (1) described by the matrix of eigenvalues problem shown in Fig.5a

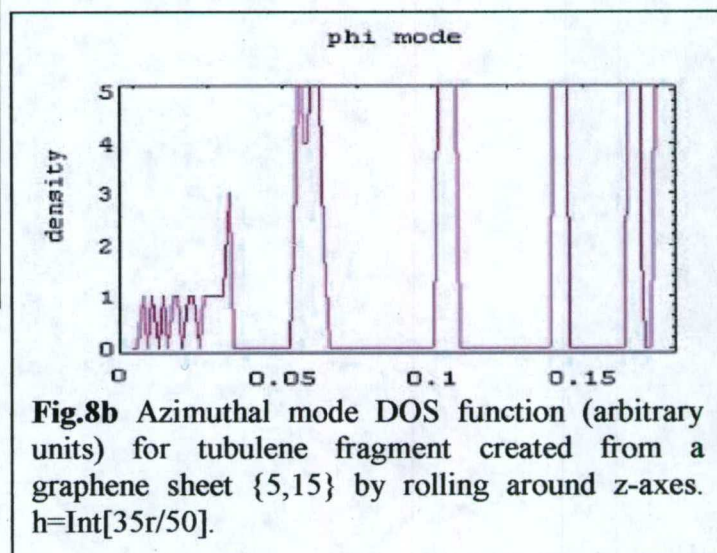




The comparison of these results obtained for the tube radial mode spectrum and DOS function for a graphene fragment of the same number of atoms and zigzag orientation shows the absence of any significant differences. Thus, the process of sheet rolling up into a tube has no influence on spectrum and density of states in this type of vibration case. But vibration amplitudes distribution (Fig.6) differs from that for graphene (see Report-1b, Fig.3, Fig.9a, Fig.9b) where the mean vibration amplitudes of the sheet free edges were bigger than that in the middle (Fig.9a). One can see that the tube has hard edges and soft middle part (Fig. 6a, 6d)



Calculated by system (2), the frequency spectrum and DOS function for azimuth mode are shown in Fig. 8a, 8b. Fig 8c presents the result of numerical calculation for azimuth mode existing in graphene sheet {15,5}, consisting 190 atoms.





The comparison of results in Fig.8b obtained for tube with azimuthal mode spectrum and DOS function for graphene fragment of the same number of atoms Fig.8c shows some differences. The tube's number of bands is twice less than that of a plane sheet. The reason lies in the double degeneration of azimuthal motion around the tube axes. For this type of vibrations, the process of rolling a sheet into a tube has an influence on the spectrum and density of states. The tube creating process is accompanied by subbands uniting due to the fact that rotational symmetry arises.

Vibration amplitudes distribution or space density distribution are similar for all types of phonons as shown in Fig 6.

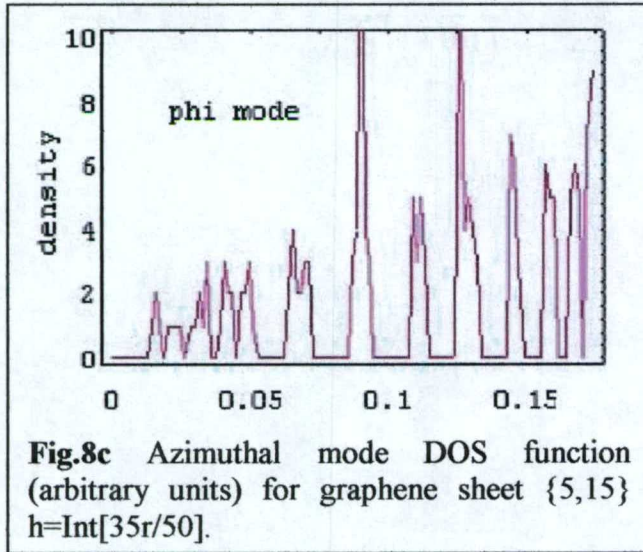


**Fig.8c** Azimuthal mode DOS function (arbitrary units) for graphene sheet {5,15}  $h=\text{Int}[35r/50]$ .

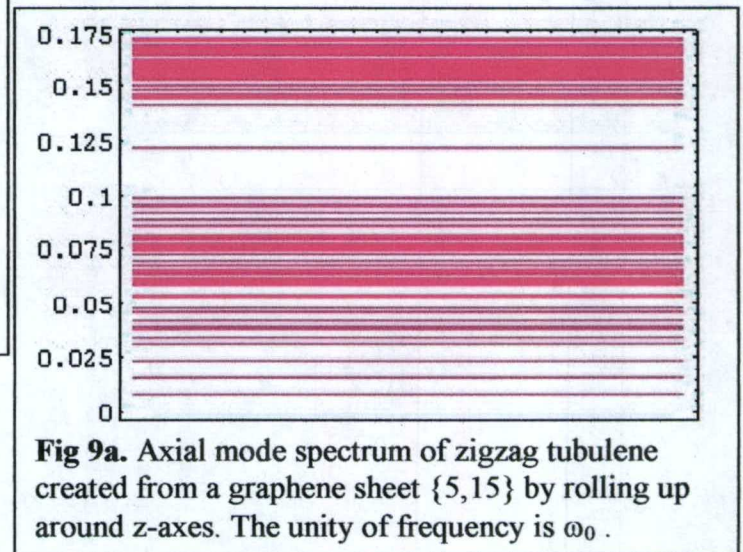
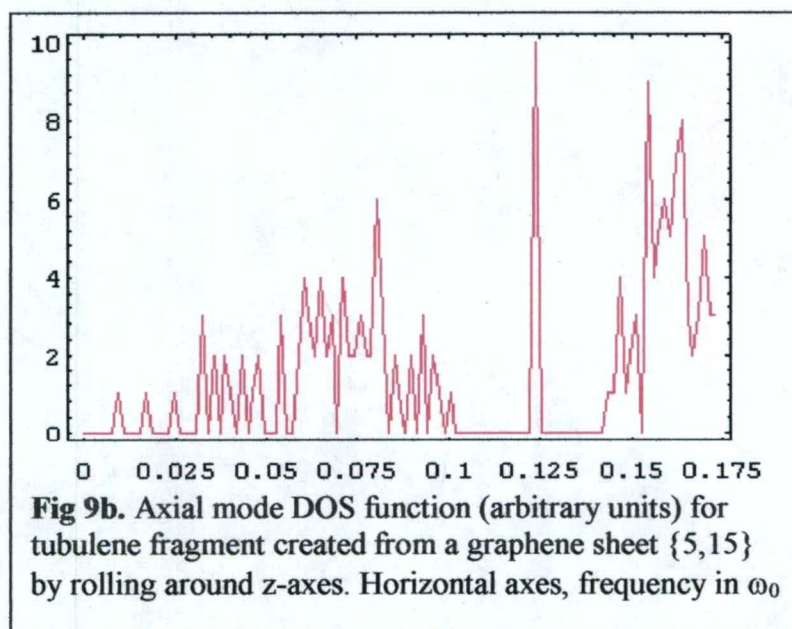


**Fig 9a.** Axial mode spectrum of zigzag tubulene created from a graphene sheet {5,15} by rolling up around z-axes. The unity of frequency is  $\omega_0$ .

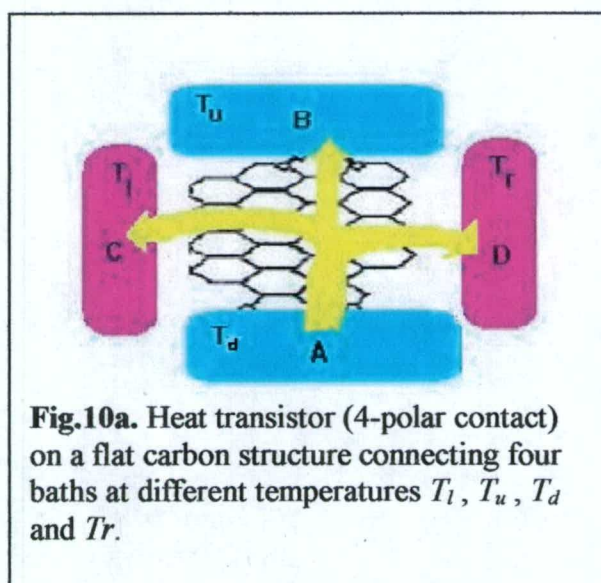
Calculated from the system of equations (3), the frequency spectrum for z-branch modes is shown in Fig. 9a. The arising of a narrow subband near  $0.125\omega_0$  that plays the role of a characteristic "mark" for the changed topology of the system is of great interest. The density of states function for  $h=\text{Int}[35r/50]$  is shown in figure 9b. Superposition of two DOS functions presented in Fig. 9c gives an opportunity to immediately compare the spectra of open and closed graphene structures. In the case of z-type vibrations for zigzag tubulene, one can say that the only consequence is the arising of a narrow subband containing  $2 \cdot n$  levels in the middle of the gap. This is because the new topology permits circular standing waves for z-type vibrations that were forbidden before in the plane structure.





There exist different opinions as to the spectrum transformation when a graphite sheet is rolled up into a tube [3, 4]. These results show that only some of the graphene spectrum characteristics change significantly (case  $\phi$ -mode and z-mode). As to the low-frequency  $\rho$ -branch, one can talk about spectra similarity.

### III. Generalized equation of thermal conductivity in a single nanotube





The PQDM analysis, proposed in Report-1b, considered heat processes from “first principles” using microscopic characteristic on a quantum level including phonon jump probability, phonon-phonon interaction, calculated spectrum and amplitudes distribution along the structure and macroscopic kinetic approach operating by length of phonon decoherence  $l_{ph}$  or phonon mean free path. The time of the phonon state establishing in area  $l_{ph} \times l_{ph}$  is much less than the phonon lifetime. The latter is determined by phonon-phonon scattering and may lay in interval  $(10^{-8}-10^{-7})s$  [???]. This supposition allows one to consider propagation of phonons as a sequence of jumps from one fragment to another with relatively long life on each one. Figures 10a, 10b illustrate 2D phonon propagation by jumps between mean free path-sized areas. Neighboring areas play a role of leads having some fixed temperatures. Taking into account that phonon scattering processes are weak ones we have obtained generalized equation of phonon dynamics.(Report-1b, paperzd-a.doc).

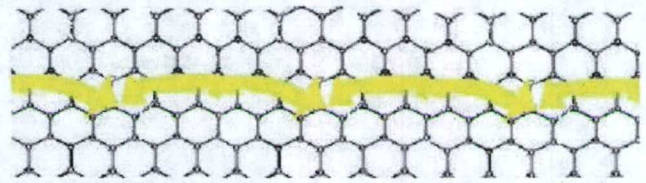


**Fig.10b.** Phonon jumps over a carbon armchair structure (arrows). One-dimensional phonon dynamics in tubulenes.

#### Temperature distribution along the tube

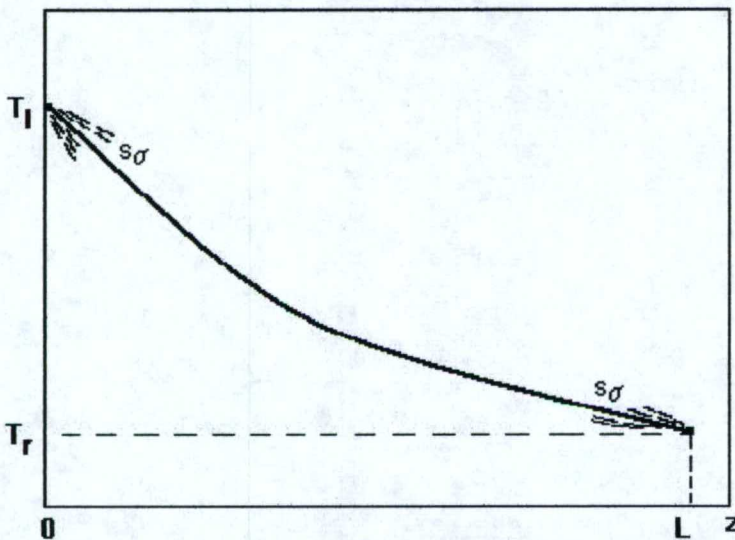


**Fig.11.** One dimensional phonon dynamics. Exact temperature distribution along the tube given by (7).  $T_l$ ,  $T_r$  are end temperatures,  $L$  is the tube length. End points come together all modal (partial) temperatures for each  $s\sigma$ .

The phonon mean free path  $l_{ph}$  decreases with increasing of temperature. Evaluations made in different sources give interval from hundred Angstroms to several micrometers at room temperatures. In any case azimuthal phonon motion may be considered as ballistic one and



jumps or diffusion in tubes may occur only in axial direction. In relation to phonon propagation nanotubes embody an ideal one-dimensional system. In stationary case it is easy to write the exact solution of the 1D variant of equation (6).

$$T(z) = \frac{\omega_{s\sigma}}{\ln\left(1 + \frac{L}{Ln_l(\omega_{s\sigma}) + (n_r(\omega_{s\sigma}) - n_l(\omega_{s\sigma}))z}\right)} \quad (7)$$

Here  $L$  is tube's length,  $z$  is axial coordinate along the tube,  $n_l$ ,  $n_r$  are population numbers  $n_{s\sigma}$  taken at left and right temperatures of both tube ends  $T_l$ ,  $T_r$ . Indeed on the macroscopic level local populations  $n_l$ ,  $n_r$  obeys equilibrium Planck law. The approximate behavior of temperature distribution is shown in Fig.11. The bundle of partial modal temperatures comes together in end points. With increasing temperature, all modal dependences become equal. The difference may be essential at low temperatures.

#### Thermal conductivity and phonon mean free path

Thermal conductivity was calculated here in PQDM approach for tubes of zigzag geometry by expression

$$\lambda'(l_{ph}) = \frac{2\pi l_{ph}}{T^2} \sum_{s,\sigma} |G_{ls}|^2 |G_{rs}|^2 \omega_{s\sigma}^2 g(\omega_{s\sigma}) \frac{N(\omega_{s\sigma})(N(\omega_{s\sigma})+1)}{|G_{ls}|^2 + |G_{rs}|^2}, \quad (8)$$

where  $l_{ph}$  is phonon mean free path, square modulus reflect connections of end atoms of the tube fragment with the rest part of the tube.

$$G_{ls} = \sum_{i_l} G_{i_l} C_{i_l s} \quad (9)$$

Left and right end atoms numbered  $i_l$  and  $i_r$  were taken into account with its bonds orientations. Formula (8) is a partial case of obtained in Report-1b expression (16) for thermal conductivity when left and right DOS functions coincides with own density of states  $g_r = g_l$ .

The  $l_{ph}$  is playing here in some sense the double role. From one side it dictates the length of tube fragment where phonon states occur in ballistic regime. For a zigzag tube made from a graphene sheet  $\{n,m\}$  we have  $l_{ph} = 2ma$ , where  $a$  is the bond length. In accordance with PQDM approach  $l_{ph}$  coincides with the length of calculated fragment with phonon standing waves inside. In contrary, DOS function  $g(\omega_{s\sigma})$  describes the left (=right)



medium. From the other side  $l_{ph}$  depends on phonon-phonon collisions that in own turn depend on the temperature.

It is worth to evaluate temperature dependence of  $l_{ph}$ . General expression for phonon mean free path is given by the surface density of phonons  $S/N$ .

$$l_{ph} \approx \sqrt{\frac{S}{N}} = \sqrt{\frac{l_d \cdot l_{ph}}{N}} \quad l_{ph} \approx \frac{l_d}{\langle N \rangle} \quad (10)$$

$$\langle N \rangle = \frac{1}{\Delta} \int n(\omega) g(\omega) d\omega \quad (11)$$

where  $S$  is the tube surface where phonons propagate,  $l_d$  is the tube circle length,  $\Delta$  is the phonon band width and  $\langle N \rangle$  is mean number of phonons. Taking into account that  $\langle N \rangle \propto T$  we have

$$l_{ph} \sim \frac{1}{T} \quad (12)$$

Implicitly  $l_{ph}$  is contained in upper limit of summation in (8), in  $|G_{ls}|^2$  and in  $g(\omega_{so})$ . The size dependence for zigzag tubes of given diameter and at given temperature was calculated by (8). The Fig.12 presents typical picture of linear  $\lambda$  increasing vs phonon mean free path.

$$\lambda \sim l_{ph} \quad (13)$$

Relations (13), (14) contain an explanation for the well-known experimental fact of thermal

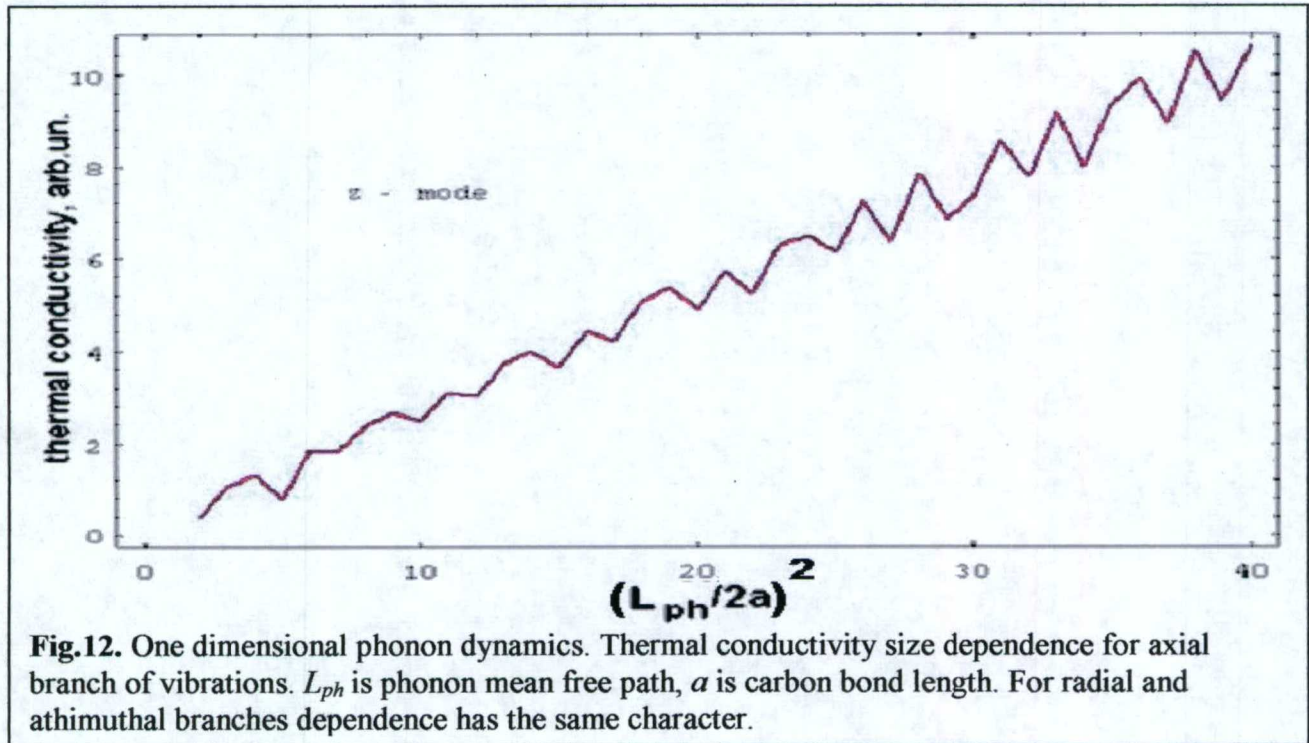


**Fig.12.** One dimensional phonon dynamics. Thermal conductivity size dependence for axial branch of vibrations.  $L_{ph}$  is phonon mean free path,  $a$  is carbon bond length. For radial and athimuthal branches dependence has the same character.



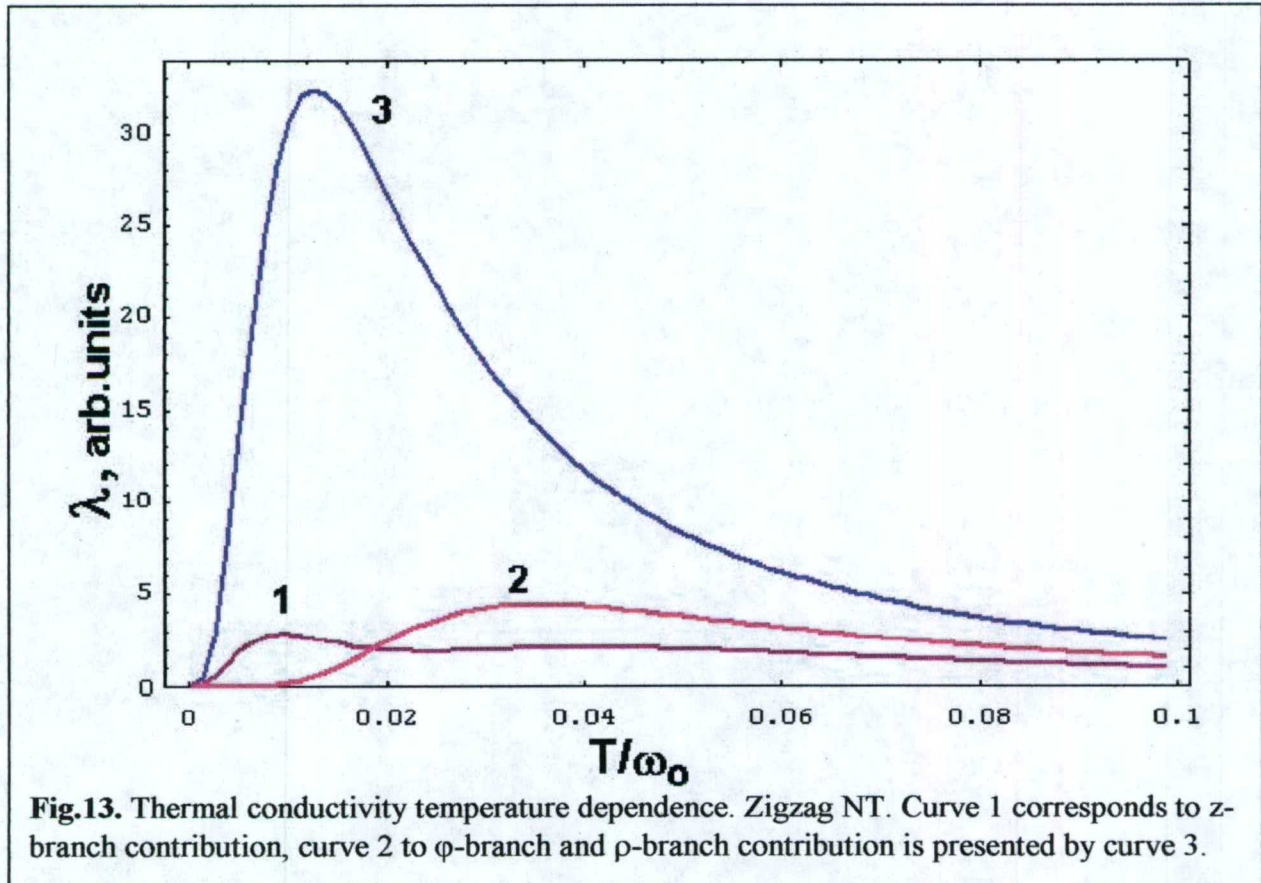
conductivity temperature damping at high temperatures by  $1/T$  law. It is of interest also that the PQDM gives a simple opportunity to connect heat propagation with the definition of phonon mean free path.

The result of thermal conductivity numerical calculations for radial, azimuthal and axial phonon branches ( $\sigma=1,2,3$ ) is presented in Fig.13. It is easy to see that the sum on all  $\sigma$  will be very close to curve 3 connecting with radial  $\rho$ -band. Unity  $\lambda_0$  determined from (8) and (16) from Report-1b is measured in  $W \cdot m/K$

$$\lambda_0 = \frac{2\pi a G_0^2 k}{\hbar \omega_0} \quad (13)$$

where  $a=1.2$  Angstrom is unity of length,  $k$  is Boltzmann constant,  $\omega_0$  is accepted here phonon energy unity and  $G_0$  is the constant of phonon-phonon interaction. Evaluations [4-8] give for characteristic phonon energy interval  $\omega_0 \in [0.8-1.2] \text{eV}$ .

It should be marked that weak temperature dependence has also the structure constant (bond length  $a$ ) of the system. Thermal expansion of single walled nanotubes was investigated in [9-12] but the result obtained there for radial expansion is not a reliable one. Elastic constants and the constant of phonon-phonon interaction  $G_0$  depend on the temperature too.





The conclusion that radial mode contribution into heat transfer is dominating in temperature interval under consideration is based on the supposition that phonon-phonon interaction constant  $G_\theta$  (see (8), (9), (13)) participating in end atoms constants  $G_{II}$  does not depend on the phonon type ( $\rho$ ,  $\varphi$  or  $z$ ). Then due to big density of states in narrow low-frequency  $\rho$ -band comparatively with that for  $\varphi$ - and  $z$ -vibrations essential prevail of  $\rho$ -vibrations arises. So at actual temperatures  $\rho$ -branch of phonons determines heat propagation through single-walled nanotube. One should wait the same effect and for armchair geometry too. The problem of phonon-phonon constants for different vibration types is open now and should be investigated in detail in following study.

#### IV. Thermodynamics and statistics of zigzag nanotubes

Static thermodynamic characteristics of non-helical zigzag nanotubes of different sizes have been calculated. If the system exists in equilibrium state, the atomic heat capacitance  $C(T)$  and entropy  $S(T)$  are as follows,

$$C(T) = \frac{1}{r} \sum_{s,\sigma} \omega_{s\sigma} \frac{\partial N(\omega_{s\sigma})}{\partial T} = \frac{1}{rT^2} \sum_{s,\sigma} \omega_{s\sigma}^2 N(\omega_{s\sigma})(N(\omega_{s\sigma})+1), \quad (14)$$

where  $r=2n(m+1)$  is the number of atoms in a zigzag tube of length  $2ma$  and radius  $a/(2\sin(\pi/n))$ .

$$S(T) = \int \frac{C(T)dT}{T} = \frac{1}{r} \int \frac{dT}{T^3} \sum_{s,\sigma} \omega_{s\sigma}^2 N(\omega_{s\sigma})(N(\omega_{s\sigma})+1), \quad (15)$$



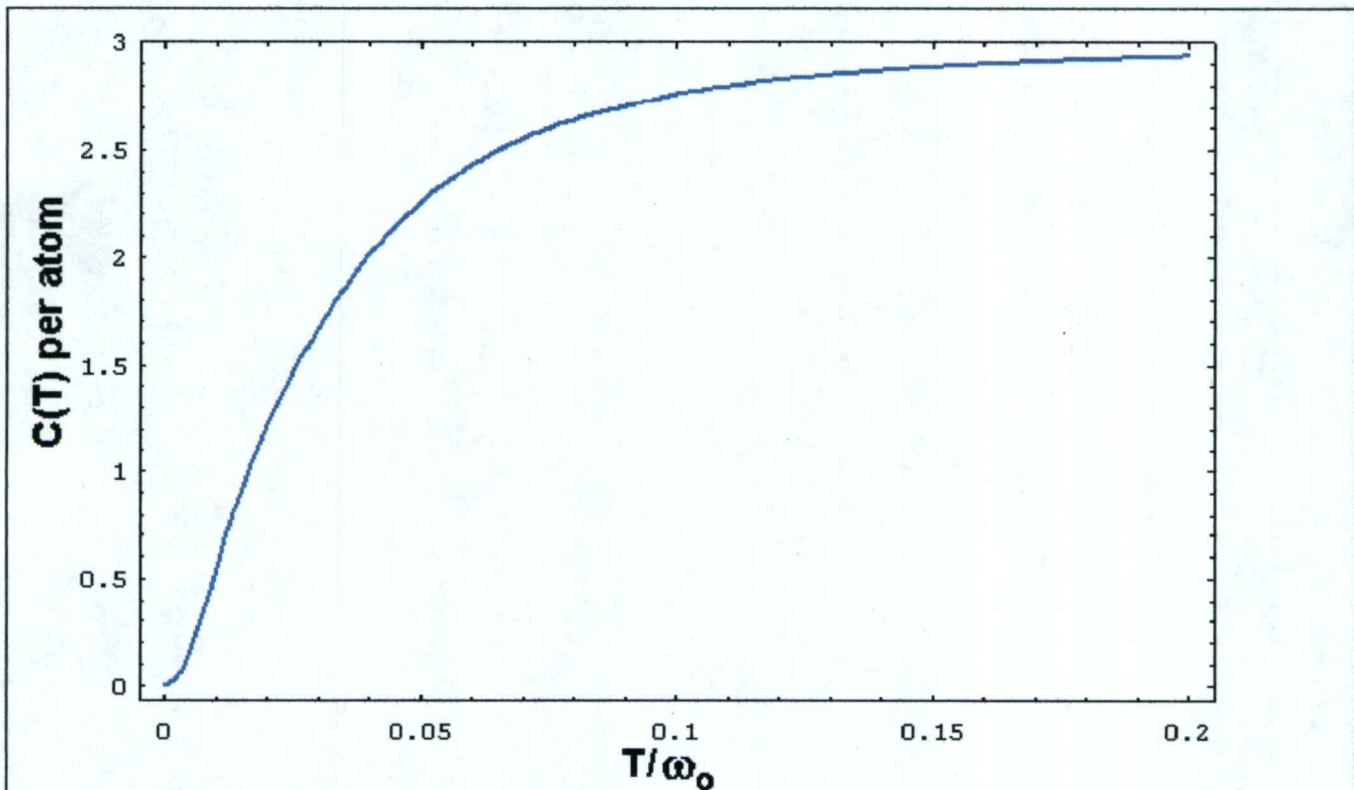


**Fig.14.** Heat capacitance vs temperature dependence for zigzag nanotube. Dulong-Petit law and W.Nernst theorem.  $\omega_0 \in (0.8, 1.2)\text{eV}$ .

The calculated temperature dependence for heat capacitance is shown in Fig.14. The curve illustrates the third thermodynamical law (W.Nernst theorem) at low temperatures and Dulong-Petit law at high temperatures ( $T > 0.1\omega_0$ ). The entropy behavior has similar character at low temperatures and shows logarithmic growth at high temperatures.

## V. Summary

A complex approach PQDM was applied to describe dynamics, kinetics and statistics of phonons in carbon nanotubes with zero-chirality.

Atom vibration dynamics was considered for carbon nanotubes of zigzag geometry in comparison with the results obtained for graphene sheets. Vibrational eigenmodes, density of states and amplitude distribution for tube fragments of the length up to 40 hexagons were calculated in linear approximation for three types of vibration: athimuthal or tangential  $\phi$ -mode, radial  $\rho$ -mode and longitudinal  $z$ -mode.

Thermal fluxes and thermal conductivity were considered in PQDM. Temperature dependences were obtained. The mechanism of heat conductivity temperature damping was analyzed.



The exact solution of generalized thermal conductivity equation was obtained for nanotubes. Temperature distribution along the tube was derived analytically.

Size dependences were considered for thermal conductivity. It was shown the linear increasing of heat conductivity with the growth of the phonon mean free path.

Statistical properties were investigated. Heat capacitance and the entropy of carbon linear tubes were calculated as the function of temperature.

## VI. References

- 1 M.Born, K.Xuang Dynamical Theory of Crystal Lattice. London: Oxford Univ.Press, 1954.
- 2 J.Tersoff. New empirical approach for the structure and energy of covalent systems. Phys.Rev. **B37**, 6991 (1988).
- 3 N.G.Chopra, A.Zettl. Measurement of the elastic modulus of a multi-wall BN nanotube. Sol.St.Comm. **105**, 297 (1998).
- 4 L.X.benedict, S.G.Louie, M.L.Cohen. Sol.St.Comm. **100**, 177 (1996).
- 5 J.Yu, R.K.Kalia, P.Vashishta. Phonons in graphitic tubules: a tight binding molecular dynamics study. J.Chem.Phys. **103**, 6697 (1995).
- 6 J.Hone, M.Whitney, C.Piskoti, A.Zettl. Thermal conductivity of single-walled carbon nanotubes. Phys.Rev. **B59**, R2514 (2000).
- 7 J.W.Kang, H.J.Hwang. Thermal properties of ultra-thin copper nanobridges. Nanotechnology **13**, 503 (2002).
- 8 D.Tomanek. "Thermal and electrical conductance of carbon nanostructures" in Nanostructured Carbon for Advanced Applications, ed. G.Benedek et al. , NATO Science Series, **24**,263 (2000). S.Berber, Y.-K. Kwon, D.Tomanek. Unusually high thermal conductivity of carbon nanotubes. E-archive: cond-mat/0002414.
- 9 Yu.Maniwa et.al Thermal expansion of single-walled carbon nanotube bundles: X-ray diffraction study. Phys.Rev. **B64**, 241402 (2002).
- 10 C.G.Ho, R.W.Powell, P.E.Lilley Thermal conductivity of simples chemical compaunds, J.Che.Ref.Data, **1** , 279-425, (1972).
- 11 R.Berman, Thermal conductivity in solids, Clarendon Press, Oxford, 1976.



## VII. Attachment: Short investigation plan

### 1. Phonon(vibron) bands. Direct calculation in elastic approximation.

- a) Graphene molecules of various kinds, free and contacting with two leads. Influence of the number of bounding atoms on phonon structure.
- b) Phonon structure of 3-polar and 4-polar molecular bridges.
- c) Carbon tubes of various radii. Short fragments. Free and contacting with leads.
- d) BN- flat structures. Free and contacting.
- e) BN-tubes of various radii. Short fragments. Free and contacting with leads.
- f) More complicate geometry. Torus. Two wall C-tube as a heat conductor.

### 2 Heat transport investigation in PQDM.

- b) Linear carbon chains connecting electrodes (analytical approach)
- c) Graphene molecules of various kinds contacting with leads. Calculation.
- d) Carbon tubes of various radii. Short fragments. Free and contacting with leads.
- e) BN- flat structures. Free and contacting.
- f) BN-tubes of various radii. Short fragments. Free and contacting with leads

### 3 Macroscopic manifestations of phonon propagation in carbon nets.

- a) Generalized 2D and 3D equation of thermal conductivity in carbon nets.
- b) Boundary problem and temperature distribution in macroscopic carbon nets.
- c) Boundary problem for heat conductivity in carbon and BN tubulenes and temperature distribution along tubulene bridge..
- g) Carbon tubes of various radii. Short fragments. Free and contacting with leads.

### 4 Phonon-phonon effects in charge and heat transport.

- a. Spectrum modification due to phonon-phonon processes;
- b. Non-linear transport through flat carbon structures;
- c. Non-linear transport along carbon tubulenes;

### 5 Thermodynamics and statistics of closed and open carbon nets

- a. Statistical sum and entropy of carbon nets (graphene and tubulene).
- b. Heat capacitance of graphene and tubulene structures

### 6 Heat-transistor effects.

- a. Three pole systems;
- b. Four pole systems;

### 7 Electron-phonon effects in charge and heat transport.

- a. Transport through linear carbon chains connecting electrodes (analytical approach). Dragging in linear bridges.
- b. United transport in graphene molecules of various kinds, free and contacting with leads. Calculation.
- c. Electron-vibron interaction in carbon tubes of various radii. Short fragments. Free and contacting with leads.



### **1.3.1b. Phonon dynamics and thermal properties of free armchair carbon nanotubes**

**Report-3a: "Strategies to Increase Thermal Conductivity. Enhancement by Optical Phonon Sub-Bands Engineering in 3-D Nanostructures Based on C and BN Nanotubes"**

#### **Content**

**VIII. Introduction**

**IX. Phonon dynamics in an armchair carbon nanotube**

**X. Generalized equation of thermal conductivity in armchair single-walled nanotube**

**XI. Thermodynamics and statistics for a carbon nanotube**

**XII. Summary and discussion**

**XIII. References**

**XIV. Attachment - Short investigation plan**



## I. Introduction

The content of Report-3a presents the third stage of the investigation of phonon fluxes in carbon and BN nanostructures in the framework of the tasks for "*Strategies to Increase Thermal Conductivity. Enhancement by Optical Phonon Sub-Bands Engineering in 3-D Nanostructures Based on C and BN Nanotubes*".

Here, dynamics (planned point 1c, see attachment), heat transfer problem for closed carbon nets – armchair tubes (point 2c) and macroscopic manifestations (point 3c) are presented. Two main tubulene geometries: zigzag and armchair are compared with respect to phonon eigenstates, density of states, vibration amplitude distribution and thermal conductivity.

The idea of the PQDM approach proposed before is to use a discrete microscopic model for phonon dynamics of relatively small molecular fragments approximately of phonon mean free path (MFP) sizes.

The dynamics of such a cluster may be described classically in Born approach [1, 2] and all the important data may be obtained: eigenfrequencies, density of states and phonon amplitude distribution inside the molecular fragment during its lifetime. Neighboring parts of the nanotube are in an uninterrupted process of exchange by phonons. Due to the weak fragment-surrounding medium interaction, the process may be described by Fermi's "golden

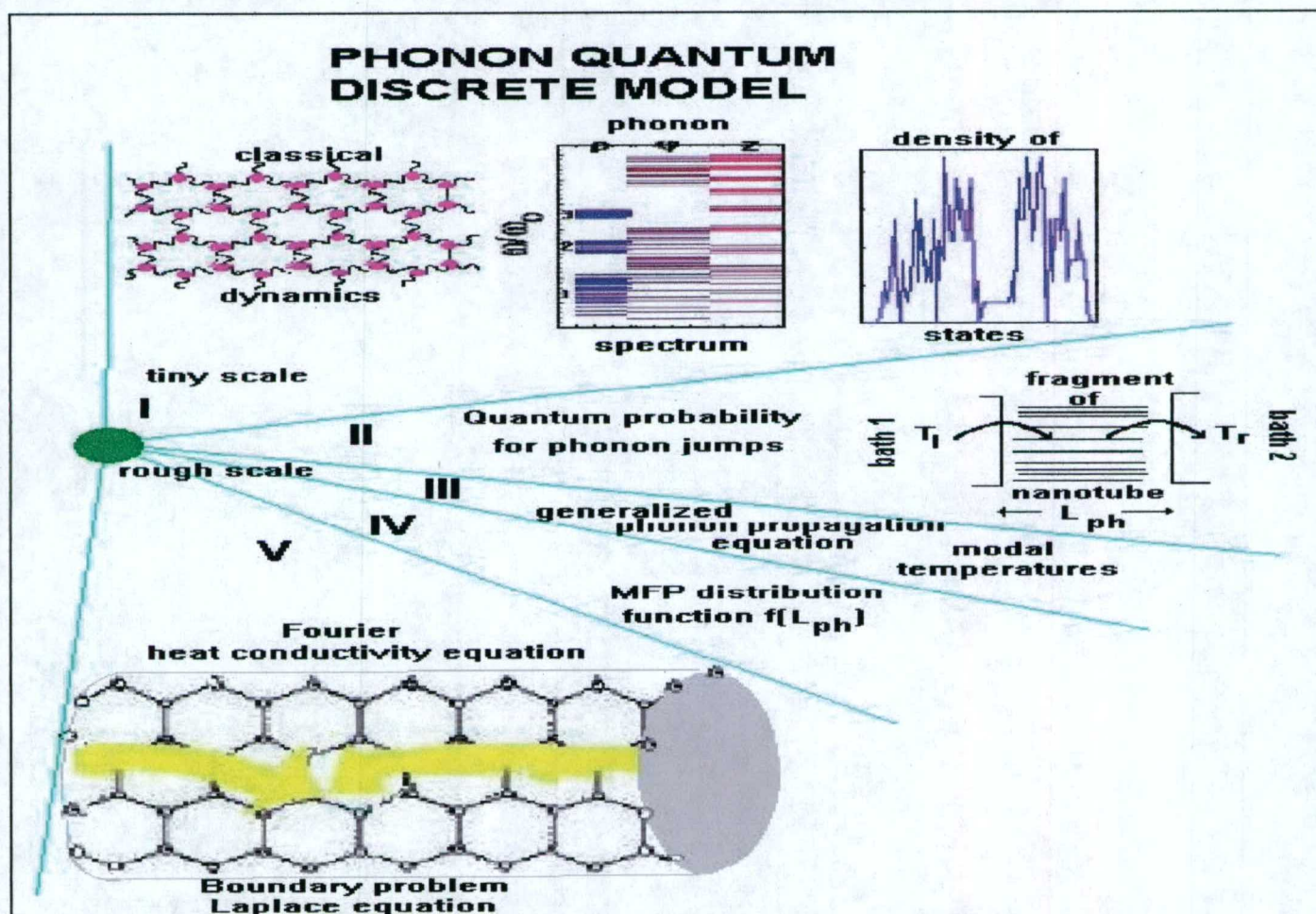


**Fig.2.1.** Structure of PQDM approach. I-II small scale processes, III-V rough scale processes.  $L_{ph}$  is phonon mean free path. I stage, classical dynamics, atomic scale; II stage, phonon jumps between nanotube areas. III stage, transition to averaging, The notion of statistical temperature erases at IV stage. V stage . macroscopic thermodynamics and kinetics.



rule" which determines the value of the transfer rate. This quantum characteristic is a transport processes consideration that enables the introduction of a microscopic thermal conductivity coefficient that depends on the temperature difference between opposite sides of the fragment in contact with the baths. An averaged classical picture of phonon energy (heat) transport and temperature distribution along pulled carbon nanotubes and other kinetic and statistical phenomena may be obtained in rough space scale. **The rough scale leads to the generalized phonon kinetics equation describing heat propagation in 2D molecular nets.**

The general scheme of the developed PQDM approach is shown in Fig.1.1. The tiny scale stages (I-II) involve classical dynamics on the atomic level and weak phonon-phonon transformations and jumps. The parameters of this model are the elastic constants determined from atom-atom quantum-mechanical potentials, the geometry and symmetry of the system, the lattice constants, and the phonon-phonon interaction constant. At this level processes are ballistic. The discrete system of contacting separate atoms vibrates and the complicate motion is represented as the superposition of modes that group into three branches. Each mode (=degree of freedom=standing wave) is described by the eigenfrequency and distribution of atomic amplitudes inside the corresponding standing wave. On the second stage, phonon standing waves jump between neighboring areas along the nanotube. Due to the actual "compactification" of circular degrees of freedom ( $\phi$ ) the phonon motion is a purely one-dimensional process (Report-2a). The rough scale processes occur on distances of the order of (or slightly greater than) phonon mean free path lengths ( $L_{ph}$ ) (stages III-V). The transition to averaging (stage III) gives a picture for phonon population along the molecular system. If the phonon-phonon interaction is elastic, there arise local or modal temperatures describing thermodynamic equilibrium between phonons of a given mode. The notion of statistical temperature is erased at stage IV when the averaging of different phonon mean free path lengths is performed. After the transition to a macroscopic description (stage V), the ballistic processes vanish and macroscopic thermodynamics and kinetics can be used.

Taking the phonon band structure and dividing by different phonon branches has significant meaning in describing thermal conductivity. This investigation shows a dominating contribution from the radial branch of vibration in heat propagation in zigzag NT and graphene sheets. The radial breathing mode (RBM) was investigated experimentally and theoretically in [3-5]. The mean frequency of RBM vibrations was estimated there within the interval  $(100-300)\text{cm}^{-1}$  that corresponds to estimations made here for the radial phonon band width  $(0.004-0.007)\text{eV}$  for graphene and single walled zigzag nanotubes.

Phonon engineering of low-dimensional structures and heat conductivity properties of nanotubes are actively discussed in physical literature [6-8]. Establishing a concrete law for the temperature dependence of thermal conductivity at high temperatures as well as a law for the increasing at low temperatures is among the most common current problems. Different sources give the data for maximal thermal conductivity for a solitary carbon tube in a wide interval from 200 W/mK to 3000 W/mK. The temperature of maximal thermal conductivity for many carbon tubes also varies within a wide interval from 150 K to 300 K from different authors. Another point of interest is the differences in thermal conductivity for solitary carbon tubes depending on type (armchair or zigzag), chirality and size.

Phonon dynamics and kinetics in tubes with armchair geometry and zero-chirality are considered below and compared with data for zigzag nanotubes.



## I. Phonon dynamics in an armchair carbon nanotube

Linear approximation in phonon dynamics is based on the supposition that small atomic vibrations have harmonic character at least in the case of not too high temperatures. It means that the potential iso-energy  $l$  surface in the vicinity of atomic equilibrium positions has an ellipsoidal form. Classical motion of atoms near their equilibrium points is described by elastic constant  $k$  that characterizes atom-atom bonds in the Born approximation. In this investigation, nonzero elastic constant  $k' \ll k$ , from the framework of linear approximation, is used for atomic shifts perpendicular to the bond. The symmetry of carbon structures dictates three main types of vibration (radial  $\rho$ -mode, tangential  $\varphi$ -mode and axial  $z$ -mode)

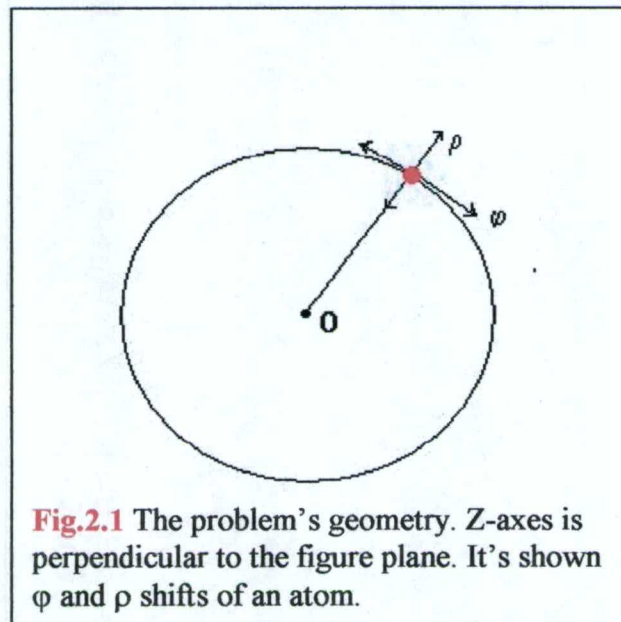
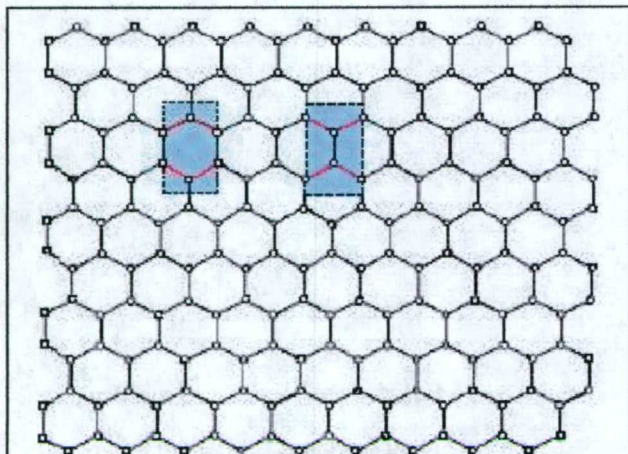


Fig.2.1.





**Fig.2.2.** A fragment  $\{9,9\}$  of hexagonal lattice. Shaded are two equivalent conventional elementary cells containing four atoms. Two types of bonds are presented by different colors. Rolling around horizontal axes could be implemented only for even number horizontal rows  $\{8,9\}$

It should be noted that the principal difference between the vibration branches originates from the direction of bonds relative to the direction of the axes of symmetry associated with the given degree of freedom (Fig.2.2). This difference manifests itself in the phonon band structure for the tangential and axial branches in the case of pure zero-chirality. In the presence of helicity the difference vanishes. In Fig.2.3 (the case with non-zero chirality), the situation when the tangential  $\phi$ -mode and axial  $z$ -mode have approximately equal orientation shifts relative to both red and blue bonds inside a chosen elementary cell is presented.

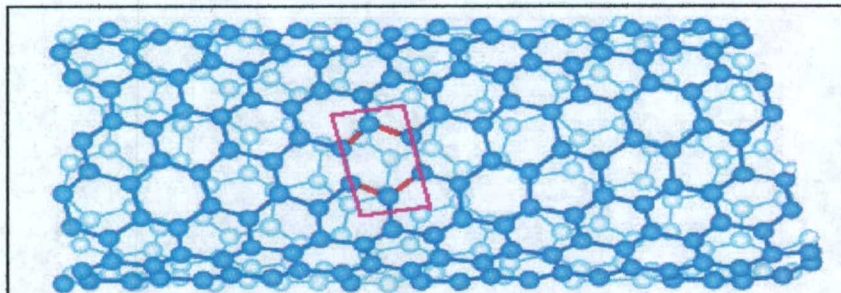


**Fig.2.3.** Fragment of armchair tubulene  $(10,5)$  with non-zero chirality created from a graphene sheet  $\{14,10\}$  by rolling up around the armchair direction. Picked out is the conventional elementary cell containing four atoms. Two types of bonds are marked by different colors.

Dynamical equations for all three branches of vibrations can be calculated taking into account that the motion of each atom is three-dimensional. The zero-approximation



approach supposes that the radial  $\rho$ -mode, tangential  $\varphi$ -mode and axial  $z$ -mode should be considered independently.

Consider an armchair tube  $(n,0)$  produced from the fragment shown in Fig.2.2 by rolling around horizontal direction without any shift. In this case each of the tube fragments is connected with the same fragments. Therefore, contrary to the case of flat fragments connected to the external media, all atomic positions along with their bonds are described by the same dynamical equations. The difference exists between different vibration types or branches only.

For shifts directed normal to the tube surface the equation is the following:

$$\{ m \ddot{\rho}_i = -k (3 \rho_i - \rho_{i1} - \rho_{i2} - \rho_{i3}) , \quad (2.1)$$

where  $i_1, i_2, i_3$  are indexes for atom  $i$  neighbors. Atomic coordinates are not important here. The universal atomic number  $i$  is defined using its position in the row and column of the initial flat fragment creating the tube. This type of vibration is called the radial breathing mode (RBM) in literature [3-5].

For tangential atomic shifts, taking into account the atom space coordinates on the tube surface  $x=R\varphi$ , where  $R$  is the tube radius and  $\varphi$  is the azimuth angle, the armchair case with the absence of chirality is described by the system:

$$\{ m \ddot{x}_i = -k (x_i - x_{i1}) - 0.25k (2x_i - x_{i2} - x_{i3}) \quad (2.2)$$

where coefficient 0.25 characterizes two weak bonds for this vibration.

For axial atomic shifts we have

$$\{ m \ddot{z}_i = -0.75k (2z_i - z_{i1} - z_{i2}) - k (z_i - z_{i3}) \quad (2.3)$$



The matrix structure of all equations (1-3) corresponding to the armchair (n,0) case is shown in Fig.4.

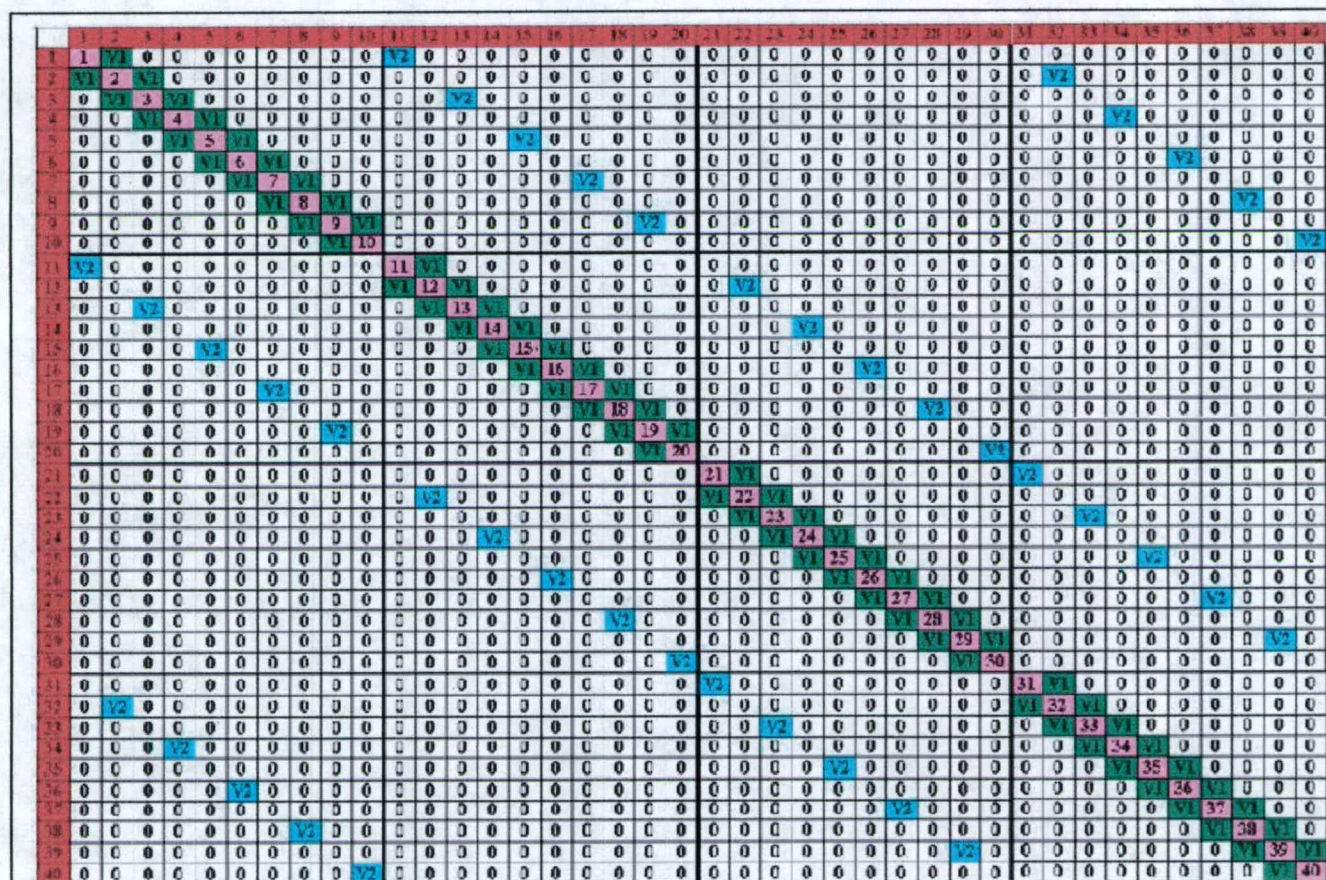


**Fig.2.4.** Sketch of the dynamical matrix for armchair tubulene created from a graphene sheet {5,5} containing 60 atoms by its rolling up. Rose-colored spots are diagonal elements, green and blue show two types of bonds, rest elements equal to zero, left and upper red bands contain atomic numbers.

### Armchair tubulene matrix and vibration amplitudes

Atomic coordinates become important when the mode amplitude distribution is presented in the space. The vibration amplitudes for mode  $s=5$  of any type are shown in Fig.2.5. As in the case of zigzag NT, there are considerable differences in amplitude distribution over the armchair tube surface compared to the open carbon net. The differences are caused by the changed topology of the system. A difference exists between the frequency of modes and density of states at the same state but it is not essential.



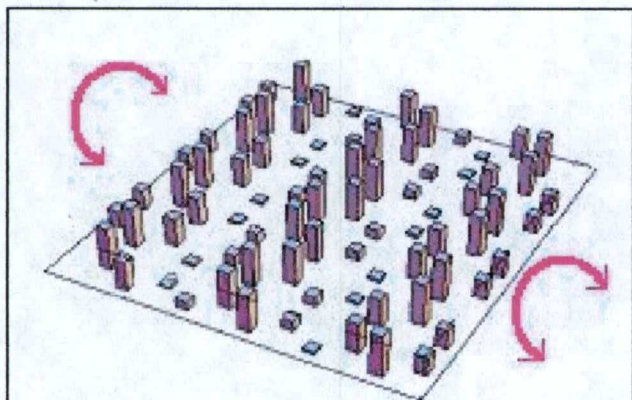


**Fig.2.5.** Calculated  $\rho$ -branch amplitude distribution  $s=5$  along armchair tubulene created from a graphene sheet  $\{6,5\}$  by rolling up around marked direction. Transversal knot's lines are degenerated.

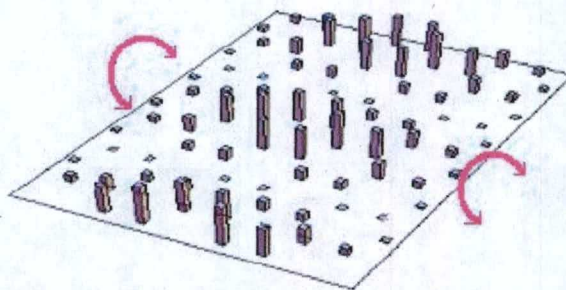


**Fig.2.6.**  $\rho$ -branch amplitude distribution along zigzag tubulene created from a graphene sheet  $\{6,5\}$  by rolling up around marked direction. 5th state. Longitudinal knot's lines are degenerated.

The calculations performed with the system of equations (1-3) give  $|C_{si}|^2$  for eigenvectors which is a well known standing wave picture with the corresponding number of knot's lines depending on the state number  $s$ . Increasing the number of states leads to the formation of lateral (parallel to  $z$ -axes) and transverse (circular) knot's lines dividing the tube's surface. Fig.2.5 illustrates the well known knot's theorem for the 5<sup>th</sup> (or  $r-4^{\text{th}}$ ) state where two twice degenerated knot's lines cross circularly to the tube's surface. Increasing the



**Fig.2.7.** Calculated mean square amplitude distribution along armchair tubulene created from a graphene sheet  $\{15,5\}$  by rolling up around marked direction.  $T=0.03$  eV. Circular arrows show rolling up of the structure.

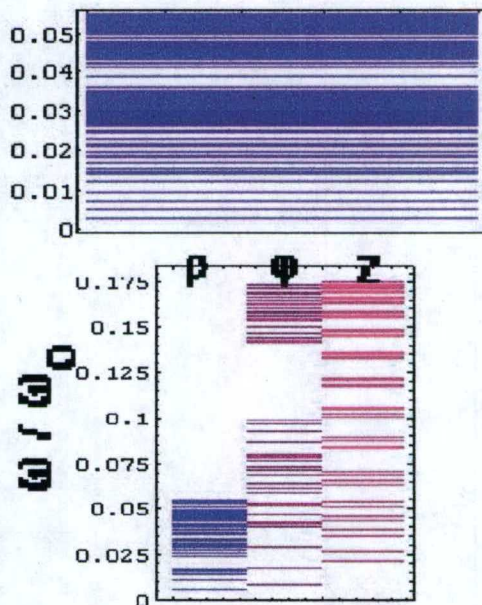


**Fig.2.8.** Lower part. Three branches of phonon spectrum for armchair tubulene created from a graphene sheet  $\{8,15\}$  by rolling up around  $z$ -axes. Upper part. Radial phonon band for zigzag  $\{8,15\}$  NT.



tube's length leads to a considerable change in the picture of vibrations. The same 5<sup>th</sup> (or 4<sup>th</sup>) state in the zigzag case, presented in Fig.2.6, has knot's lines perpendicular to those of the armchair case.

The mean vibration amplitudes  $A_j$ , averaged for the state populations  $n_s$ , are almost constant and do not deviate sufficiently along the tube surface. There is a difference in zigzag nanotubes where  $|C_{sj}|^2$  decreases from the lateral ends to the middle axes of the nanobridge.

$$A_j = \sum_{s, \sigma} |C_{sj}|^2 n_{s\sigma}, \quad (2.4)$$

where  $n_{s\sigma}$  is the population of  $s, \sigma$  state,  $j$  numbers atoms situated on the tube surface and  $C_{sj}$  is the  $s$ -state probability amplitude at  $j$ -position of the net. Coefficients  $C_{sj}$  are the components of eigenvectors arising as the solution of systems (1-3). Mean square amplitudes calculated for temperature  $T=0.03\text{eV}$  by expression (4) are shown in Fig.2.7. The averaging was made here over all phonon  $\sigma$ -branches. One can see that in contrast with flat carbon terminated nets with free edge atoms (Report-1b) and to some extent zigzag carbon tubes (report-2b), the closed armchair structure has almost constant amplitudes along all directions over the surface of the tube.

Phonon mode frequencies are obtained from expressions (1-3) as eigenvalues. In Fig.2.8, three branches of the phonon spectrum for an armchair tubulene having 8 honeycombs in the circumference are presented.

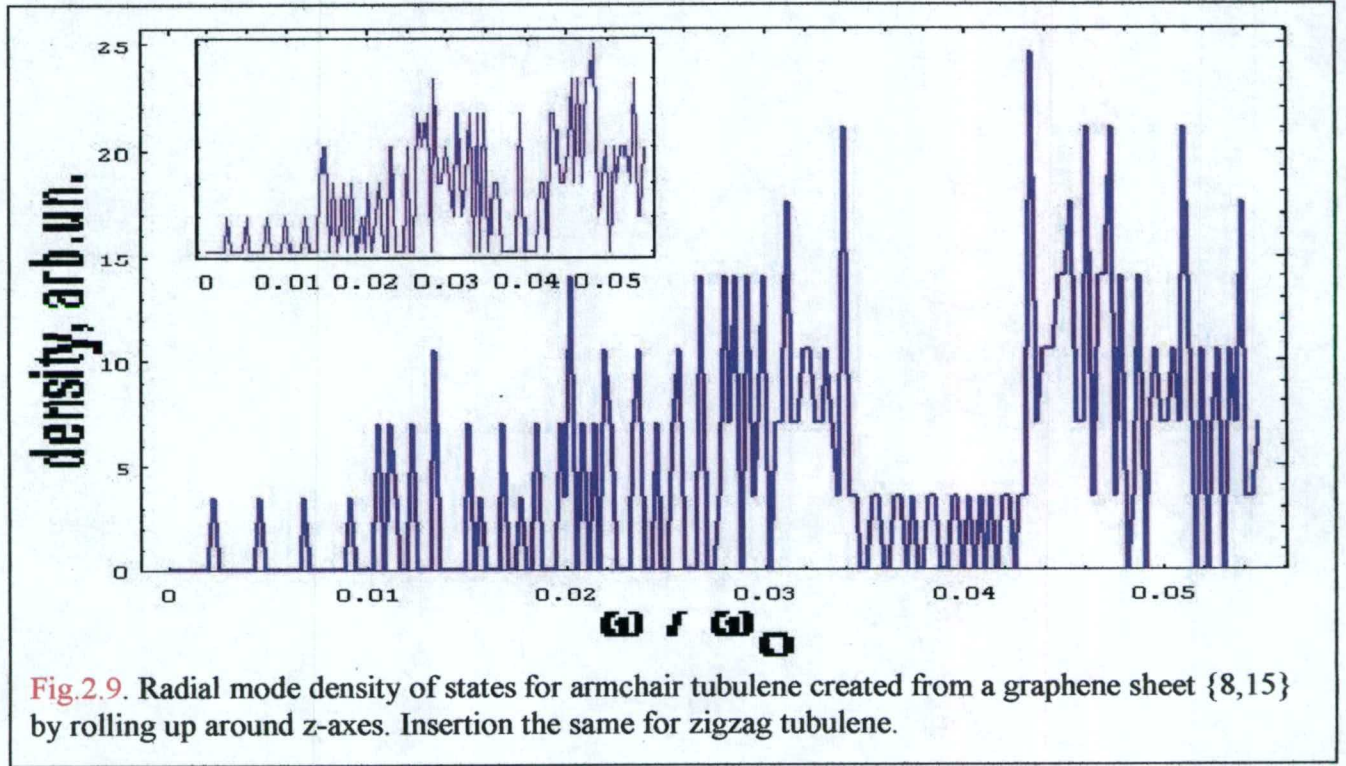
#### Armchair tubulene spectrum and DOS

The density of states may be approximately defined by the following expression.

$$g(\omega_{s\sigma}) = \frac{\partial N_{s\sigma}}{\partial \omega_{s\sigma}} \quad (2.5)$$



This transforms into an exact equation if the number of degrees of freedom becomes large enough. Here,  $N_{s\sigma}$  numbers phonon states with frequency  $\omega_{s\sigma}$ . More correctly, the density of states function may be calculated providing preliminary state grouping and density determination inside each group.



DOS with preliminary state grouping have been calculated by dividing the whole frequency band interval into  $h = \text{Int}[4r/5]$  sub-intervals (or near this value) within which the number of eigenmodes were counted. The frequency spectrum and DOS function in the zero chirality armchair nanotube case are presented in Figs. 9-11. Fig. 9 was obtained by numerical calculation of system (1) described by the matrix of eigenvalues problem shown in Fig. 2.4.



The comparison between results obtained for armchair tube radial mode spectrum and DOS functions for a zigzag tube and a graphene fragment with the same number of atoms shows the absence of any significant differences.

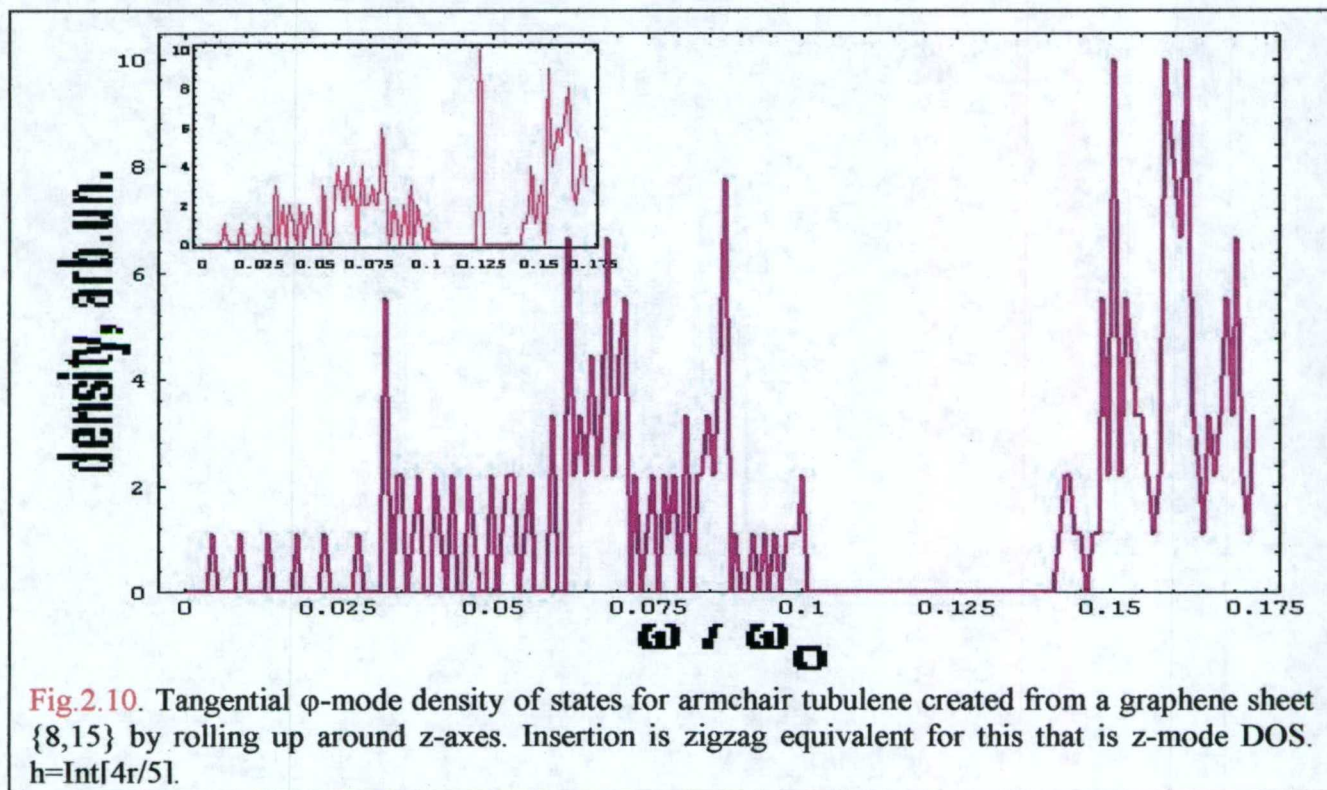


**Fig.2.10.** Tangential  $\phi$ -mode density of states for armchair tubulene created from a graphene sheet {8,15} by rolling up around z-axes. Insertion is zigzag equivalent for this that is z-mode DOS.  $h = \text{Int}[4r/5]$ .

Thus, the process of rolling a sheet up into a tube does not influence the spectrum and density of states in this type of vibration case. But the distribution of vibration amplitudes (Fig.7) differs from that for graphene (see Report-1b, Fig.3, Fig.9a, Fig.9b) where the mean vibration amplitudes of the sheet's free edges were bigger than that in the middle.

The density of states frequency function for the tangential branch of vibrations calculated with equation (2) is shown in Fig. 2.10. The insertion shows the result of numerical calculations performed before for the  $\phi$ -branch in an armchair geometry equivalent to the z-branch in a zigzag NT. Note the narrow subband near  $0.125\omega_0$  (see insertion) that plays the role of a characteristic "mark" for the changed topology of the system. This subband contains  $2*n$  levels in the middle of the gap that occur because the new topology now permits circular standing waves z-type vibrations that were forbidden before in the plane structure. In the armchair geometry, circular atomic chains are absent (for  $\phi$ -type vibrations) and the middle-gap subband vanishes again.

Comparing results obtained for zigzag and armchair tubes for the DOS function shows some differences. The subband inside the gap (see insertion) originates from circular chains of equivalent atoms in zigzag geometry while for armchair geometry the circles are absent. On the other hand, graphene z-branch DOS is very similar to tangential armchair due to the absence of circular symmetry.



The frequency spectrum for z-branch modes calculated from the system of equations (3) is shown in Fig.2.11.

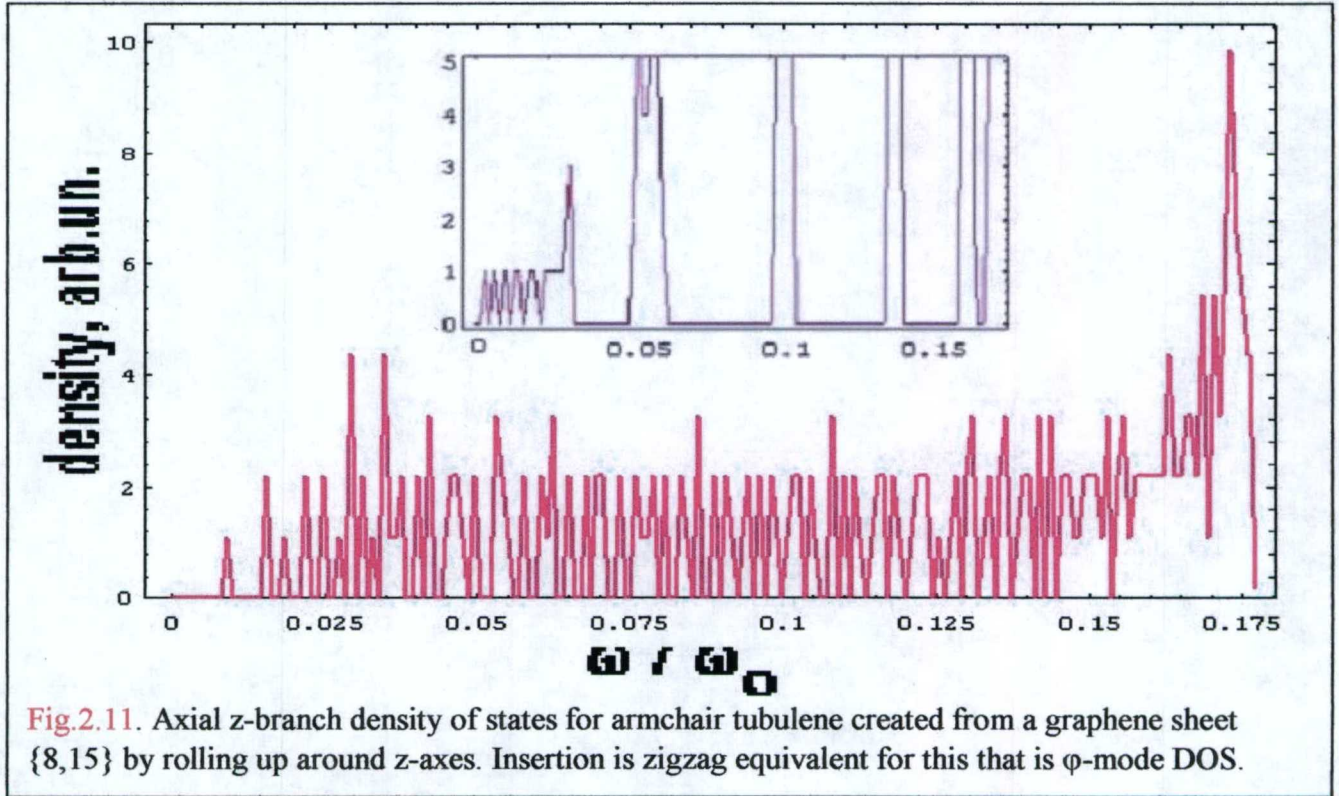


**Fig.2.11.** Axial z-branch density of states for armchair tubulene created from a graphene sheet {8,15} by rolling up around z-axes. Insertion is zigzag equivalent for this that is  $\phi$ -mode DOS.

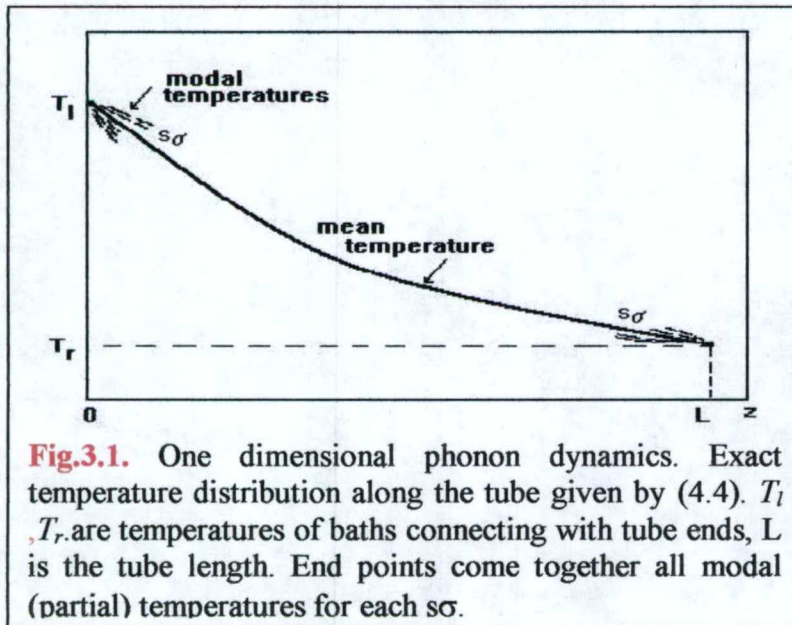


**Fig.3.1.** One dimensional phonon dynamics. Exact temperature distribution along the tube given by (4.4).  $T_l$ ,  $T_r$  are temperatures of baths connecting with tube ends,  $L$  is the tube length. End points come together all modal (partial) temperatures for each  $s\sigma$ .

## II. Generalized equation of thermal conductivity in a single nanotube

The PQDM analysis proposed in Report-1b consider heat processes from “first principles” both using microscopic characteristic on quantum level including phonon jump probability, phonon-phonon interaction, calculated spectrum and amplitudes distribution along the structure and macroscopic



kinetic approach operating by length of phonon decoherence  $l_{ph}$  or phonon mean free path. The time of the phonon state establishing in area  $l_{ph} \times 2\pi R$  is much less than the phonon lifetime. The latter is determined by phonon-phonon scattering and may lay in interval  $(10^{-8}-10^{-7})$ s [2]. This supposition allows one to consider propagation of phonons as a sequence of jumps from one fragment to another with relatively long life on each one. In a tube of not too big radius  $R$  the phonons propagate by jumps between mean free path-sized areas. Neighboring areas play a role of leads having some fixed temperatures. Taking into account that phonon scattering processes are weak ones we have obtained generalized equation of phonon dynamics (Report-1b, paperzd-a.doc). In 1D case it has the form

$$\frac{\partial n_{s\sigma}}{\partial t} = D_{s\sigma}^z \frac{\partial^2 n_{s\sigma}}{\partial z^2} \quad (3.1)$$

#### Temperature distribution along the tube

The phonon mean free path  $l_{ph}$  decreases with increasing of temperature. Evaluations made in different sources give interval from hundred Angstroms to several micrometers at room temperatures. In any case azimuthal phonon motion may be considered as ballistic one and jumps or diffusion in tubes may occur only in axial direction. In relation to phonon propagation nanotubes embody an ideal one-dimensional system. In stationary case it is ease to write the exact solution of the one-dimensional equation (1) if to start from generalized equation written for populations  $n_{s\sigma}$  (Report-2b).

$$T(z) = \omega_{s\sigma} / Ln \left( 1 + \frac{L}{n_l(\omega_{s\sigma}) + [n_r(\omega_{s\sigma}) - n_l(\omega_{s\sigma})]z} \right) \quad (3.2)$$

Here  $L$  is tube's length,  $z$  is axial coordinate along the tube,  $n_l$   $n_r$  are population numbers  $n_{s\sigma}$  taken at left and right temperatures of both tube ends  $T_l$  ,  $T_r$ . Indeed on the macroscopic level local populations  $n_l$   $n_r$  obeys equilibrium Planck law. The approximate behavior of temperature distribution is shown in Fig.3.1. The bundle of partial modal temperatures comes together in end points. With increasing of temperature all modal dependences become equal. The difference may be essential at low temperatures.

#### Thermal conductivity and phonon mean free path

Thermal conductivity was calculated here in PQDM approach for tubes of armchair geometry by expression obtained in previous reports 1b and 2b.



$$\lambda'(l_{ph}) = \frac{2\pi l_{ph}}{T^2} \sum_{s,\sigma} |G_{ls}|^2 |G_{rs}|^2 \omega_{s\sigma}^2 g(\omega_{s\sigma}) \frac{N(\omega_{s\sigma})(N(\omega_{s\sigma})+1)}{|G_{ls}|^2 + |G_{rs}|^2}, \quad (3.3)$$

where  $l_{ph}$  is phonon mean free path, square modulus reflect connections of end atoms of the tube fragment with the rest part of the tube.

$$G_{ls} = \sum_{i_l} G_{i_l} C_{i_ls} \quad (3.4)$$

Left and right end atoms numbered  $i_l$  and  $i_r$  were taken into account with its bonds orientations. Formula (3) is a partial case of obtained in Report-1b expression (16) for thermal conductivity when left and right DOS functions coincides with own density of states  $g_r = g_l$ .

The  $l_{ph}$  is playing here in some sense the double role. From the one side it dictates the length of tube fragment where phonon states occur in ballistic regime. For an armchair tube made from a graphene sheet  $\{n,m\}$  we have  $l_{ph}^2 = 3m^2 a^2 / 4$ , where  $a$  is the bond length. In accordance with PQDM approach  $l_{ph}$  coincides with the length of calculated fragment with phonon standing waves inside. In contrary, DOS function  $g(\omega_{s\sigma})$  describes the left (=right) medium. From the other side  $l_{ph}$  depends on phonon-phonon collisions that in own turn depend on the temperature.

It is worth to evaluate temperature dependence of  $l_{ph}$ . General expression for phonon mean free path is given by the surface density of phonons  $S/N$ .

$$l_{ph} \approx \sqrt{\frac{S}{N}} = \sqrt{\frac{l_d \cdot l_{ph}}{N}} \quad , \quad l_{ph} \approx \frac{l_d}{\langle N \rangle} \quad (3.5)$$

$$\langle N \rangle = \frac{1}{\Delta} \int n(\omega) g(\omega) d\omega \quad (3.6)$$

where  $S$  is the tube surface where phonons propagate,  $l_d$  is the tube circle length,  $\Delta$  is the phonon band width and  $\langle N \rangle$  is mean number of phonons. Taking into account that  $\langle N \rangle \propto T$  we have

$$l_{ph} \sim \frac{1}{T} \quad (3.7)$$

Implicitly  $l_{ph}$  is contained in upper limit of summation in (3), in  $|G_{ls}|^2$  and in  $g(\omega_{s\sigma})$ . The size dependence for armchair tubes of given diameter and at given temperature was calculated by (3). The Fig.3.2 presents typical picture of quadratic increasing for  $\lambda$  vs phonon mean free path.



$$\lambda \sim l_{ph}^2$$

(3.8)

Relations (7), (8) contain an explanation for the well-known experimental fact of thermal conductivity temperature damping at high temperatures by  $1/T^2$  law. This phenomenon is observed both in 3D and low-dimensional systems. Proposed here PQDM approach gives a simple opportunity to connect heat propagation with the definition of phonon mean free

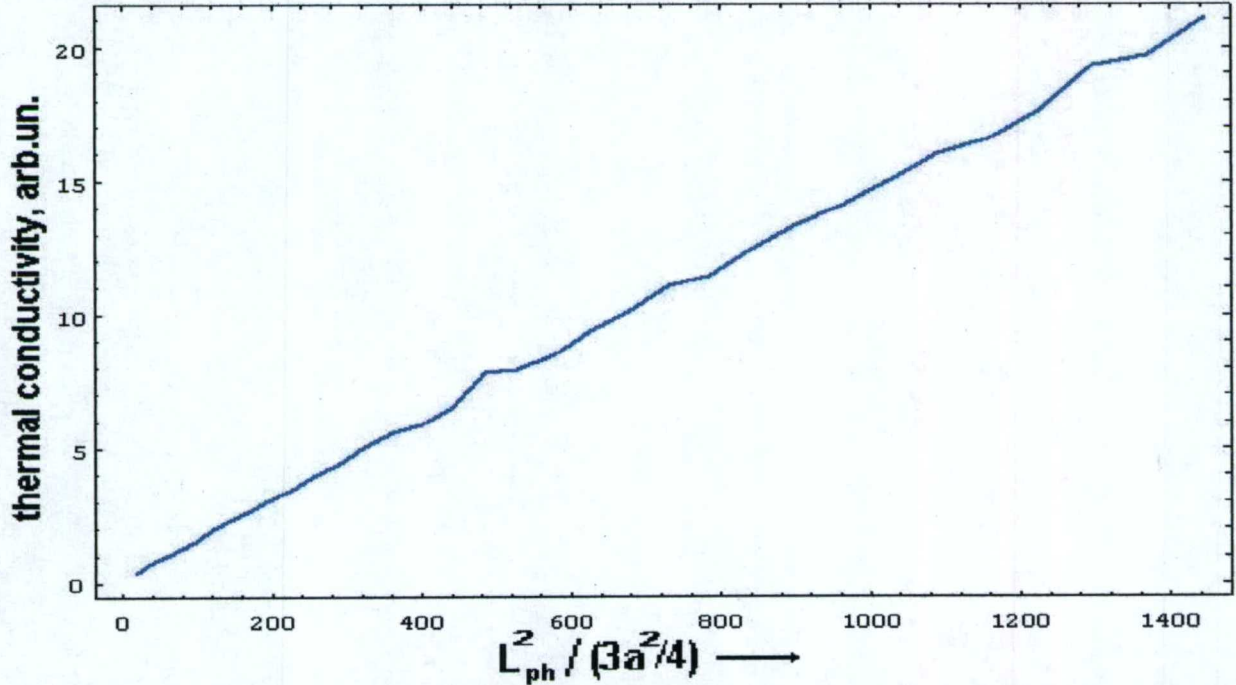


**Fig.3.2.** One dimensional phonon dynamics. Calculated total thermal conductivity length dependence that includes all vibration branches of armchair NT.  $L_{ph}$  is phonon mean free path,  $a$  is carbon bond length.

path.

The thermal conductivity dependence on the radius of SWNT is also approximately quadratic (Fig.3.2, insertion).

The result of thermal conductivity numerical calculations for radial, azimuthal and axial phonon branches ( $\sigma=1,2,3$ ) is presented in Fig.3.3. It is easy to see that the sum on all  $\sigma$  will be very close to curve 1 connecting with radial  $\rho$ -band (Fig.3.4). The unity  $\lambda_0$  determined from (3) and formula (16) from Report-1b is measured in  $Wm/K$

$$\lambda_0 = \frac{2\pi a G_0^2 k}{\hbar \omega_0} \quad (3.9)$$

where  $a=1.2$  Angstrom is unity of length,  $k$  is the Boltzmann constant,  $\omega_0$  is accepted here phonon energy unity and  $G_0$  is the constant of phonon-phonon interaction. Evaluations using data of [8] and [9] give for characteristic phonon energy very wide interval  $\omega_0 \in [0.8-1.6]eV$ .



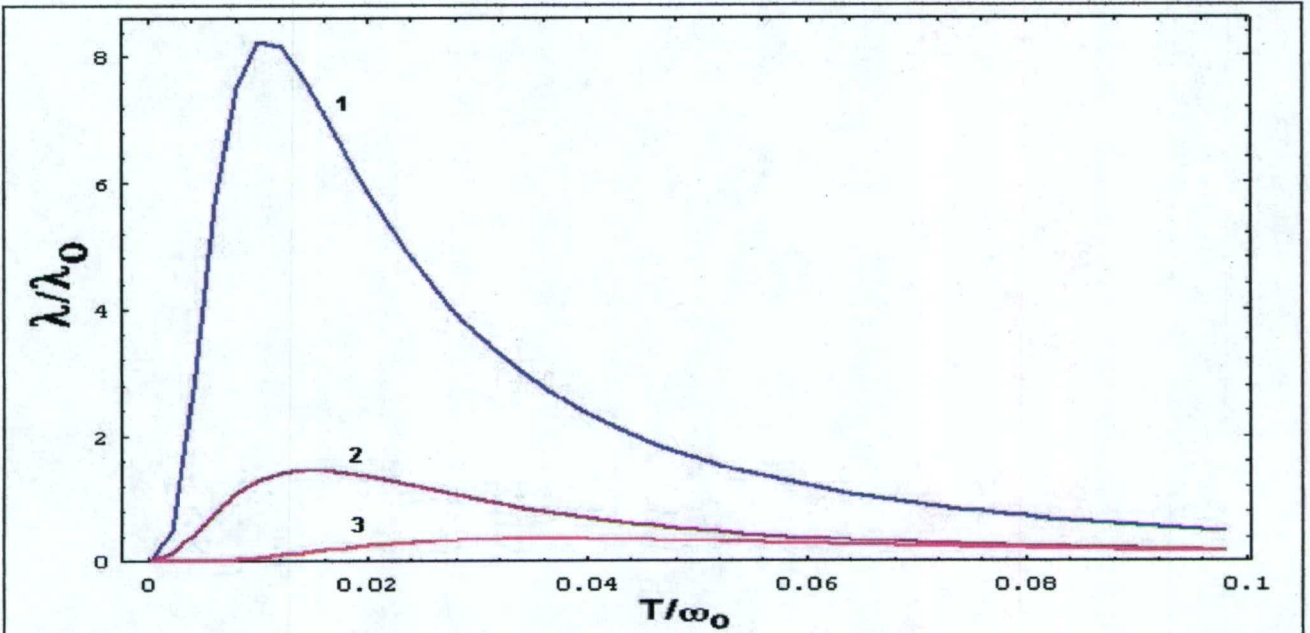


**Fig.6.** Thermal conductivity temperature dependence. Armchair NT. Curve 1 corresponds to z-branch contribution, curve 2 to  $\varphi$ -branch and  $\rho$ -branch contribution is presented by curve 3.

It should be noted that the weak temperature dependence also has the structure constant (bond length  $a$ ) of the system. Thermal expansion of single walled nanotubes was investigated in [10] but the result obtained there for radial expansion is not a reliable one and deviates from negative to positive values. Elastic constants and the constant of phonon-phonon interaction  $G_\theta$  depend on the temperature too.

The maximum is situated near  $1.5\omega_\theta$  both in armchair (Fig.3.4) and zigzag case (Report-2b, Fig.13). It means that the difference between two geometries exists only on the dynamical level of tiny scale processes and vanishes after the transition to rough scale processes. The insertion to Fig.3.4 presents the law of initial temperature rising of thermal conductivity at low temperatures. Our conclusion  $\lambda \sim T^2$  for an isolated SWNT coincides with experimental data obtained in direct measurement for MWNT by [11] and is in contradiction

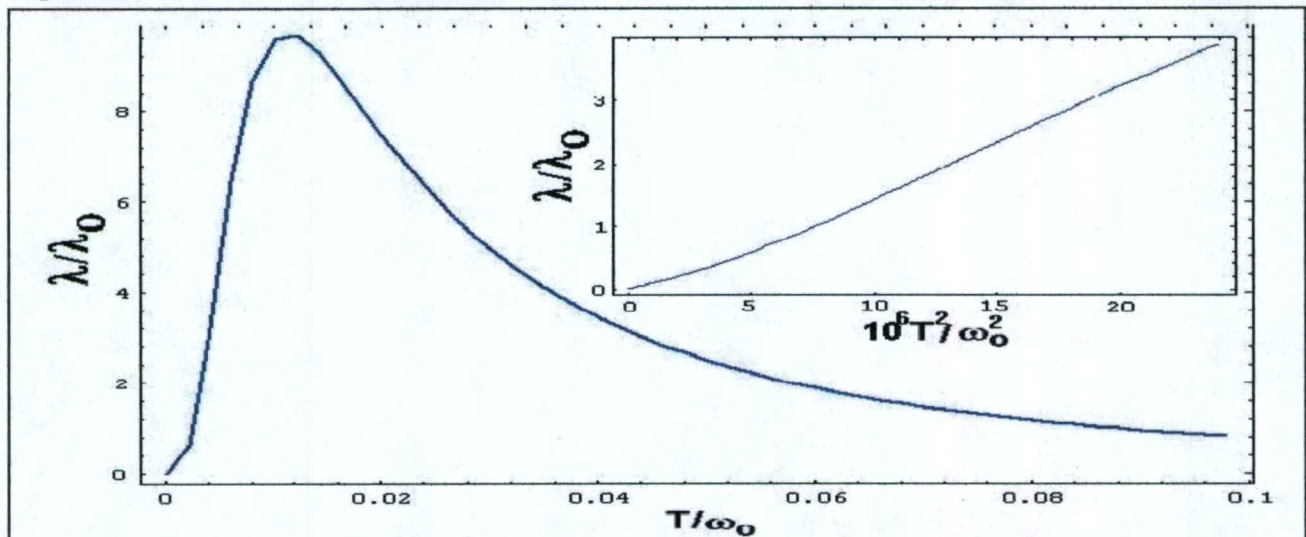


**Fig.3.4.** Total thermal conductivity temperature dependence. Armchair NT. Eight honeycombs along the circumference. Insertion: the law of increasing at low temperatures:  $\lambda \sim T^2$ ,  $T \in (0, 0.005)\omega_\theta$ .



with linear temperature law obtained in [12] for SWNT bundles.

The conclusion that the radial mode contribution to heat transfer is dominating in the temperature interval under consideration is based on the supposition that the phonon-phonon interaction constant  $G_\theta$  (see (3), (4), (9)) participating in end atoms constants  $G_{ii}$  does not depend on the phonon type ( $\rho$ ,  $\varphi$  or  $z$ ). Then due to the large density of states in narrow low-frequency  $\rho$ -band comparatively with that for  $\varphi$ - and  $z$ -vibrations essential prevail of  $\rho$ -vibrations arises. So at actual temperatures  $\rho$ -branch of phonons determines heat propagation through single-walled armchair nanotube. The same effect was obtained before and for zigzag geometry too. Of course, the problem of phonon-phonon constants  $G_\theta$  for different vibration types exists now and should be investigated in detail in following study. It should be mentioned also very important in PQDM starting constant  $\omega_0$  that have to be found from comparison with experimental data for isolated SWNT. As well the problem of mean free path distribution function is open and should be investigated more detail.

#### IV Thermodynamics and statistics of armchair nanotubes

Static thermodynamic characteristics of non-helical armchair nanotubes of different sizes have been calculated. If the system exists in equilibrium state, the atomic heat capacitance  $C(T)$  and entropy  $S(T)$  are given by the following expressions,

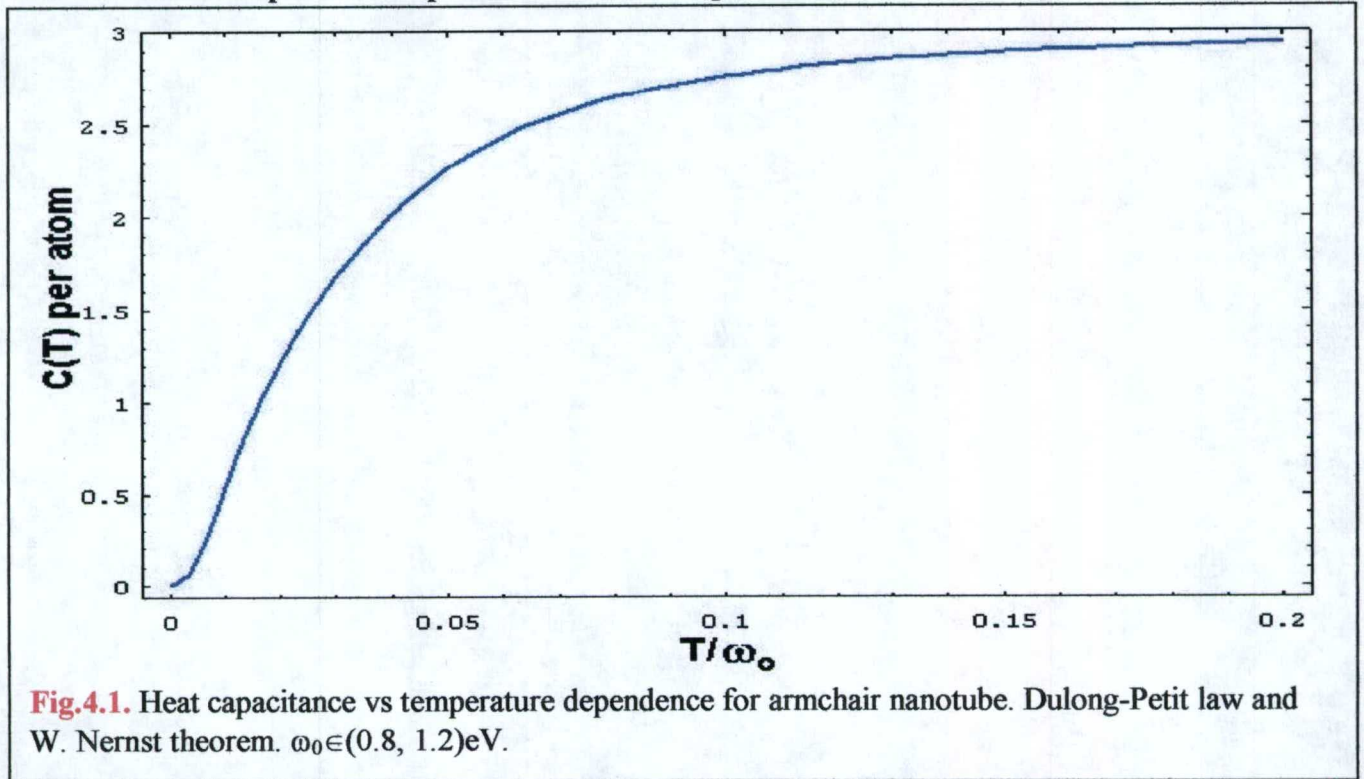
$$C(T) = \frac{1}{r} \sum_{s,\sigma} \omega_{s\sigma} \frac{\partial N(\omega_{s\sigma})}{\partial T} = \frac{1}{rT^2} \sum_{s,\sigma} \omega_{s\sigma}^2 N(\omega_{s\sigma})(N(\omega_{s\sigma}) + 1), \quad (4.1)$$

where  $r=2n(m+1)$  is the number of atoms in a armchair tube of length  $1.7ma$  and radius  $a/\sin(\pi/n)$ .

$$S(T) = \int \frac{C(T)dT}{T} = \frac{1}{r} \int \frac{dT}{T^3} \sum_{s,\sigma} \omega_{s\sigma}^2 N(\omega_{s\sigma})(N(\omega_{s\sigma}) + 1), \quad (4.2)$$



The calculated temperature dependence for heat capacitance is shown in Fig.4.1.



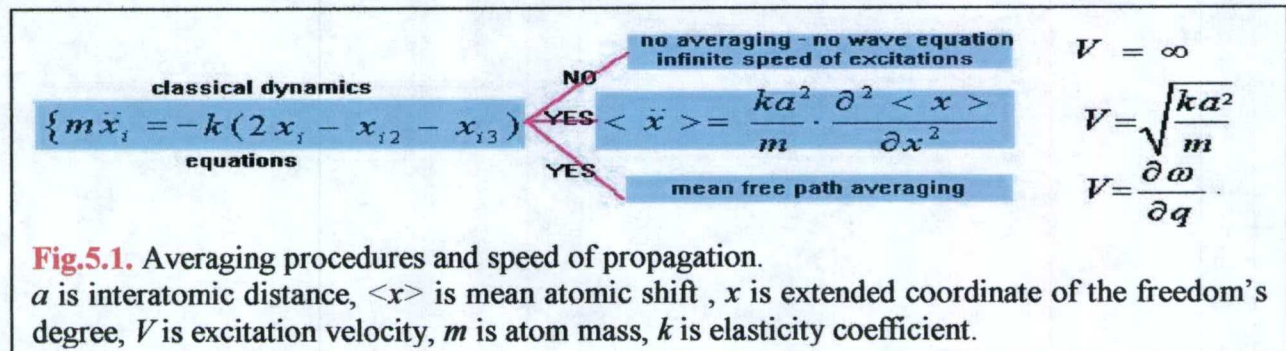
The curve illustrates the third thermodynamical law (W.Nernst theorem) at low temperatures and Dulong-Petit law at high temperatures ( $T > 0.1\omega_0$ ). An absolutely equivalent curve was obtained before for zigzag NT (Report-2b). This means that from a thermodynamical point of view both NT symmetries, armchair and zigzag, are equivalent at all temperatures.

The Dulong-Petit law is a tag in thermodynamics that embodies the classic systems. It is clear from the Fig.4.1 that the notion “high temperatures=classical system” begin to act from  $0.15\omega_0$ , that is approximately 1400K, for carbon single-walled nanotubes. Thus, in real temperature intervals, single-walled nanotubes are non-classical objects.

The entropy behavior has similar characteristics at low temperatures and shows logarithmic growth at high temperatures both for zigzag and armchair nanotubes.

## V. Summary and discussion

A complex approach PQDM applied gives an opportunity to describe dynamics, kinetics and statistics of phonons in carbon nanotubes with zero-chirality. Fig.5.1 illustrates





the important role of averaging procedures in understanding of phonon, sound and heat propagation in low-dimensional atomic nets. The classical dynamical equations don't contain retardation in non-relativistic approach. This causes the infinite speed of vibrational excitation propagation along the net or nanotube (Fig.5.1, second column, upper row).

The first stage averaging is transition to presentation of dynamical equations in the finite differences (second column, middle row). Evaluations by data [9,10] ( $k=4.65 \cdot 10^{-12} \text{N/m}$ ) and our data [13] give for second row velocity  $V=18.3 \text{ km/s}$ . This value is close to sound velocity in diamond (1,1,0) direction.

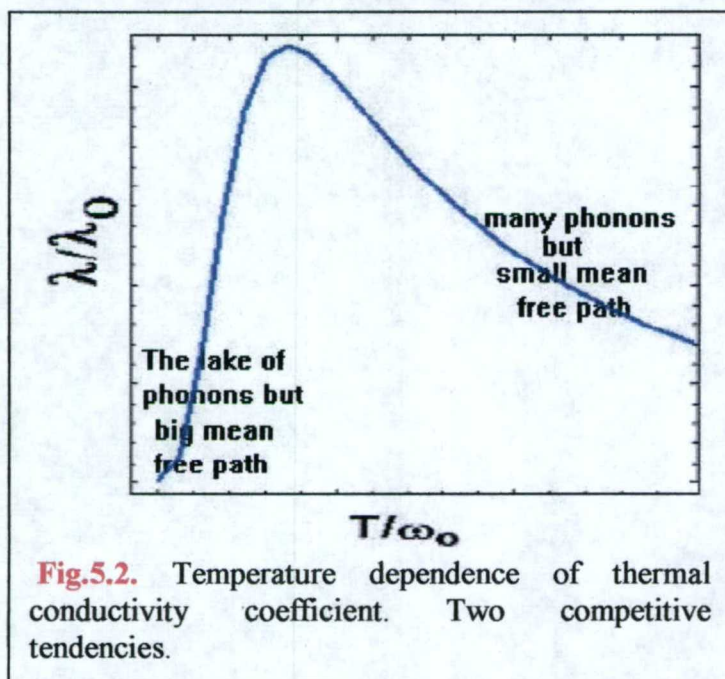


**Fig.5.2.** Temperature dependence of thermal conductivity coefficient. Two competitive tendencies.

More rough averaging at the phonon mean free path distances is used to describe heat spreading along carbon nets (Fig.5.1, second column, lowest row). Found from RBM frequency band width value of phase velocity  $V = a \cdot \Delta \rho / \pi$  is more than twenty times less ( $0.85 \text{ km/s}$ ) than for the pure sound.

Atom vibration dynamics was considered for carbon nanotubes of armchair geometry in comparison with the results obtained for graphene sheets. Vibrational eigenmodes, density of states and amplitude distribution for tube fragments of the length up to 40 hexagons were calculated in linear approximation for three types

of vibration: athimuthal or tangential  $\phi$ -mode, radial  $\rho$ -mode and longitudinal  $z$ -mode.

It's shown that phonon propagation in actual nanotubes is characterized by a kind of "compactification" of circular freedom's degree due to the big phonon mean free path. Nanotubes of actual diameters are ideal one-dimensional phonon and heat conductors.

Phonon band structure was investigated for armchair nanotubes on the base of hierarchical law and system symmetry.

Thermal fluxes and thermal conductivity were considered in PQDM. Temperature dependences were obtained. The mechanism of heat conductivity high temperature damping is reflected in Fig.5.2. Two competitive tendencies produce thermal conductivity maximum at intermediate temperatures (100-300)K.

The exact solution of generalized thermal conductivity equation was obtained for nanotubes. Temperature distribution along the tube was derived analytically.

Size dependences were considered for thermal conductivity. It was shown the linear increasing of heat conductivity with the growth of the phonon mean free path.

Statistical properties were investigated. Heat capacitance and the entropy of carbon linear tubes were calculated as the function of temperature.

Our theoretical approach (Fig.1.1) explains the nature of good thermal conductivity in carbon and carbon-like materials by existing of the soft vibration branch (low frequency RBM phonons with high DOS at thermal energies) accompanied by structure hardness (high frequency  $\phi$ - and  $z$ -branches) providing big mean free path for phonons (Fig.5.2).



Adding of new layers or new walls to single-walled NT makes breathing  $\rho$ -branch of vibrations harder. That causes the sharp decreasing of phonon density of states at the same phonon mean free path. Phonons leave the active thermal zone and heat conductivity decreases. Therefore, atomic monolayers and isolated single-walled nanotubes have to be champions in thermal conductivity. Uniting SWNT into the tight bundles quenches breathing mode too. PQDM approach predicts the sufficient worsening of thermal conductivity in SWNT tight bundles comparatively with free SWNT. The way of thermal conductivity enhancement in this case is "dissolving" of inter-tubes bonds and turning out tight bundles into the system of almost free tubes.

Pressure decreases thermal conductivity [14]. The effect is connected with total hardening of all bonds and phonon modes going away from active thermal zone.

Melting decreases thermal conductivity by another reason: the phonon's mean free path becomes small.

In conclusion we mark that the problem of creating "heat superconductors" may have a perspective on the way of hardness-softness uniting. It seems, the natural limit is given by isolated fragments of carbon-like structures: carbon sheets and single-walled nanotubes. The question is in the existing of possibility to create more complicate artificial heat superconductivity aimed systems.

## VI. References

- 13 M.Born, K.Xuang **Dynamical Theory of Crystal Lattice**. London: Oxford Univ.Press, 1954.
- 14 R.Berman, **Thermal conductivity in solids**, Clarendon Press, Oxford, 1976.
- 15 V.N.Popovl, L. Henrard **Evidence for existence of two breathing-like phonon modes**. Phys.Rev., **B63**(23), 233407 (2001).
- 16 P.Dubot, P. Cenedese **Modelling of molecular hydrogen on Li adsorption on single-wall NT**. Phys.Rev., **B63**(24), 241402 (2001).
- 17 A.G.S. Filho, A.Jorio, J.H. Hafner. **Electronic transition energy...** Phys.Rev., **B63**(24), 241404 (2001). Phys.Rev.Lett, **86**, 1118 (2001).
- 18 J.Chen, **Phonon heat conduction in nanostructures** Int.Journ.Therm.Sci., **39**(4), 471-480 (2000).
- 19 A.Balandin, A.Khitun, J.Chen, J.L. Liu; K.L. Wang, T. Borca-Tascuic. **Optimization of thermoelectric properties of low-dimensional structures via phonon engeneering**. Proceedings of 18<sup>th</sup> Int.Conf. on Termoelectricity, p189-192 (1999).
- 20 D.G.Cahill, W.K. Ford, K.E.Goodson; G.D.Mahan, A.Majuindar; H.J.Maris, R.Merlin, S.R.Philpott, **Nanoscale Thermal Transport**. J.Appl.Phys., **93**(2), 793-818 (2003).
- 21 J.Yu, R.K.Kalia, P.Vashishta. **Phonons in graphitic tubules: a tight binding molecular dynamics study**. J.Chem.Phys. **103**, 6697-6705 (1995).
- 22 Yu.Maniwa et.al **Thermal expansion of single-walled carbon nanotube bundles: X-ray diffraction study**. Phys.Rev. **B64**, 241402 (2002)



- 23 Shi, Li; Kim, Philip; McEuen, Paul L.; Majumdar, Arunava. **A microdevice for measuring thermophysical properties of nanowires and nanotubes.** Proceedings of the ASME Heat Transfer Division, Volume 1, 359-362 (2001).
- 24 M. Llaguno, J. Hone, T. Johnson, J. E. Fischer, **Thermal properties at single wall carbon nanotubes: diameter and annealing dependence.** management Preprint Archive, Condensed Matter (2001), arXiv:cond-mat/0108142
- 25 E. Ya. Glushko, V. A. Khrisanov, **Vibrational modes of the terminated atomic chain.** Low Temp. Phys., **23**(11), 910-916 (1997).
- 26 S. Anderson, L. Dzavadov, **Thermal conductivity and heat capacity of amorphous SiO<sub>2</sub>: pressure and volume dependence.** J. Phys.: Cond. Matter, **4**(29), 6209-6216 (2001).

## VIII. Attachment: Short investigation plan

### 2. Phonon(vibron) bands. Direct calculation in elastic approximation.

- a) Graphene molecules of various kinds, free and contacting with two leads. Influence of the number of bounding atoms on phonon structure.
- b) Phonon structure of 3-polar and 4-polar molecular bridges.
- c) Carbon tubes of various radii. Short fragments. Free and contacting with leads.
- d) BN- flat structures. Free and contacting.
- e) BN-tubes of various radii. Short fragments. Free and contacting with leads.
- f) More complicate geometry. Torus. Two wall C-tube as a heat conductor.

### 2 Heat transport investigation in PQDM.

- a. Linear carbon chains connecting electrodes (analytical approach)
- h) Graphene molecules of various kinds contacting with leads. Calculation.
- i) Carbon tubes of various radii. Short fragments. Free and contacting with leads.
- j) BN- flat structures. Free and contacting.
- k) BN-tubes of various radii. Short fragments. Free and contacting with leads

### 3 Macroscopic manifestations of phonon propagation in carbon nets.

- a. Generalized 2D and 3D equation of thermal conductivity in carbon nets.
- b. Boundary problem and temperature distribution in macroscopic carbon nets.
- c. Boundary problem for heat conductivity in carbon and BN tubulenes and temperature distribution along tubulene bridge..
- d. Carbon tubes of various radii. Short fragments. Free and contacting with leads.

### 4 Phonon-phonon effects in charge and heat transport.

- a. Spectrum modification due to phonon-phonon processes;
- b. Non-linear transport through flat carbon structures;
- c. Non-linear transport along carbon tubulenes;

### 5 Thermodynamics and statistics of closed and open carbon nets

- a) Statistical sum and entropy of carbon nets (graphene and tubulene).
- b) Heat capacitance of graphene and tubulene structures

### 6 Heat-transistor effects.

- a) Three pole systems
- b) Four pole systems

### 7 Electron-phonon effects in charge and heat transport.



- a) Transport through linear carbon chains connecting electrodes (analytical approach).  
Dragging in linear bridges.
- b) United transport in graphene molecules of various kinds, free and contacting with leads. Calculation.
- c) Electron-vibron interaction in carbon tubes of various radii. Short fragments. Free and contacting with leads.



### **1.3.2. Carbon heat radiators in polymer surroundings**

Here we consider the heat transfer problem for a solitary carbon nanotube (NT) inserted into a solid matrix with low thermal conductivity. Phonon eigenstates, density of states and vibration amplitude distribution along the molecule will be investigated for a NT laterally in contact with the continuous external medium. The temperature distribution inside a low-conducting medium containing a high-conducting channel will be calculated in the framework of boundary problems (point 3d). Concentration dependences of the effective conductivity of the composite will be evaluated. Also, the influence of the embracing polymer molecule on the phonon dynamics and the heat spreading along the nanotube will be calculated.

Heat conductivity properties of nanotubes are actively discussed in this literature. The following is a list of questions and problems under investigation:

- the general features of the temperature dependence of thermal conductivity - the mechanism of temperature damping at high temperatures and concrete law of increasing at low temperatures.
- the maximum thermal conductivity for a solitary carbon tube has not been measured reliably. Current values vary on a wide interval from 200 W/mK to 3000 W/mK from different authors.
- the temperature for maximum thermal conductivity for carbon tubes has not been reliably measured and also varies on a wide interval from 150 K to 300 K from different authors.
- the question is whether there exist differences in the thermal conductivity of solitary carbon tubes depending on the type (armchair or zigzag), chirality and diameter.
- are the differences between thermal conductivity of solitary carbon tubes, flat carbon structures like graphene and graphite (in plane) essential?

Different authors give different answers to these questions. Another complex problem arises in composites containing nanotubes as a mixture element. Experiments show that a medium like epoxy, having very low thermal conductivity, may change its thermal properties dramatically when a small amount of nanotubes is dissolved in it.

In [1], the single-walled carbon nanotubes (SWNTs) were used to augment the thermal transport properties of industrial epoxy. It was shown that the thermal and mechanical properties of SWNT-epoxy composites were improved significantly. Samples loaded with 1wt% unpurified SWNT material showed a 70% increase in thermal conductivity at 40 K, rising to 125% at room temperature.

The phenomenon of SWNT thermal conductivity was discussed in [2]. The comparison made in this article shows that the measured heat conductivity of single-walled nanotubes differs from that of both 2D graphene and 3D graphite, especially at low temperatures, where 1D quantization of the phonon band structure is observed. For aligned bundles of SWNTs a thermal conductivity of more than 200 W/mK was obtained at room temperature. A linear temperature dependence up to approximately 40 K was observed in [2] for SWNTs. Contradicting results, between quadratic and linear laws at low temperatures, were obtained



for the T-dependence of thermal conductivity of multi-wall NT (MWNT) [3]. The thermal conductivity of a MWNT bundle was measured in the interval  $T \in [8-350]$  K and a maximum of 1200 W/mK was reached at 300 K. In [4] it is shown that the heat processes of nanotubes are similar to that of two-dimensional graphene at high temperatures but is sensitive to the effects of rolling the graphene sheet into a small cylinder at low temperatures.

Measurements for tube bundles show that inter-tube coupling is relatively weak, and the thermal conductivity of nanobundles reflects the on-tube phonon structure [4]. The temperature dependence of electrical conductivity and thermopower were studied theoretically in [5] for single-wall carbon nanotubes using a Green's-function theory. It is shown that armchair and zigzag tubes exhibit quite different temperature dependencies of transport coefficients. The thermal conductivity and thermoelectrical power of a single carbon nanotube were measured in [6] using a micro-device. The observed thermal conductivity is more than 3000 W/Km at room temperature. The temperature dependence of the thermal conductivity exhibits a peak at 320 K. The molecular dynamics method was used in [7] to simulate heat conduction along a single walled carbon nanotube with the Tersoff-B Renner bond order potential [8]. SWNT models with different chiralities (5,5), (8,1), and (10,10) were investigated for the typical length about 125 Angstroms. Thermal conductivity values from 200-300 W/mK were obtained and the dependence on the length of the tube was relatively small. The thermal conductivity for (8,1) chiral tube was measured to be a little smaller than the armchair system. The phonon density of states were measured as the power spectra of velocity fluctuations and compared with the experimental Raman spectra.

Measurements of the thermal conductivity made in [9] show graphite-like behavior for MWNTs but a quite different behavior for SWNTs, specifically a linear temperature dependence at low temperatures, which is consistent with one-dimensional phonons. The room-temperature thermal conductivity of highly aligned SWNT samples is over 200 W/mK, and the thermal conductivity of individual nanotubes is likely to be higher still. Carbon nanotubes have very high thermal conductivity; comparable to diamond crystal and in-plane graphite sheet [10]. The nanotube bundles show very similar properties to graphite crystal in which dramatic differences exist in thermal conductivities along different crystal axis.

We will consider problems relevant to heat propagation in composites containing nanotubes weakly connected with the surrounding medium. Only zigzag and armchair single-walled nanotubes will be taken into account.

### **1.3.2a. Dynamics of carbon tubes laterally in contact with external medium**

The idea of the phonon quantum discrete model (PQDM) is to use a discrete microscopic model for phonon dynamics of relatively small molecular fragments that are approximately of phonon mean free path sizes. The dynamics of such a cluster may be described classically in the Born approach and all the important data may be obtained: eigenfrequencies, density of states and phonon amplitude distribution inside the molecular fragment during its lifetime. Connected fragments of a molecular net are in an uninterrupted process of phonon exchange. Due to the weak fragment-surrounding-medium interaction the process may be described by Fermi's "golden rule" that determines a value for the transfer rate. This quantum characteristic is a transport processes consideration and enables us to introduce a microscopic thermal conductivity coefficient that depends on the temperature difference between opposite sides of a fragment that is in contact with the baths.



The model developed here is based on fundamental data characterizing the structure with elastic modulus and elastic coefficients  $k$ , describing forces acting along the main axes of the bond potential ellipsoid. Thermal expansion coefficient, pressure coefficient, characteristic frequency (or phonon band width) temperature and pressure dependences may be included in the proposed model.

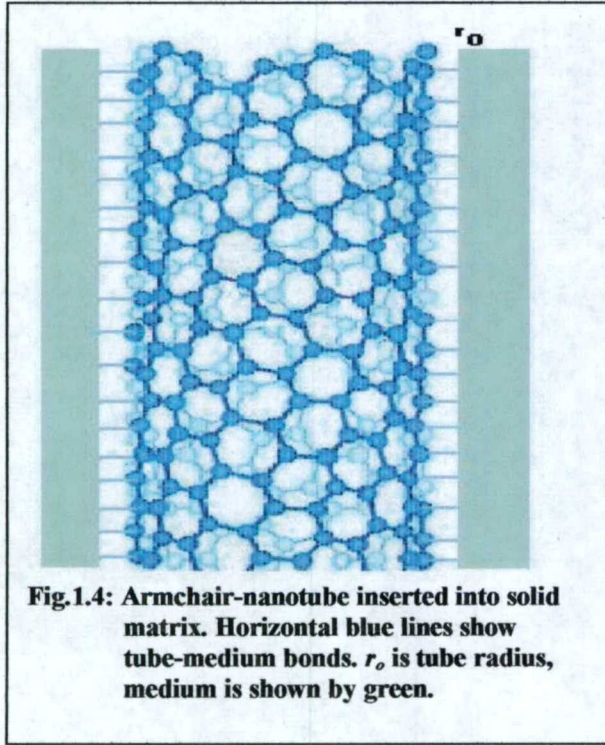


Fig.1.4: Armchair-nanotube inserted into solid matrix. Horizontal blue lines show tube-medium bonds.  $r_o$  is tube radius, medium is shown by green.

In this section, we consider a nanotube inserted into the solid matrix – a continuous medium of relatively small heat conductivity. Suppose here that the tube-matrix bonds are weak, that is, the bond is of a physical adsorption type. An armchair nanotube of radius  $r_o$  that is weakly connected with the walls of the channel by horizontal bonds is presented in Fig. 1.4.

The vibration dynamics of the armchair tube is represented by three equations for the main types of atomic motion. The adsorption bond will be described by elastic constant  $\kappa$  if the shift is directed along the bond and  $\kappa'$  if it is in the perpendicular direction. We assume that adsorption is weak and  $\kappa \approx k/5$ ,  $\kappa' \approx \kappa/10$ .

the tube surface is as following:

The equation for shifts,  $\rho_i$ , directed normal to

$$m \ddot{\rho}_i = -\kappa \rho_i - k'(3\rho_i - \rho_{i1} - \rho_{i2} - \rho_{i3}), \quad (1.4)$$

where  $i_1, i_2, i_3$  are indexes for the neighbors of atom  $i$ ,  $\kappa$  and  $k'$  are the elastic constants of external adsorption bond and intrinsic respectively. The united atomic number  $i$  is defined using its position in the row and column of the initial flat fragment creating the tube.

For tangential atomic shifts we will take into account the atomic space coordinates on the tube surface  $x = \varphi R$ , where  $R$  is the tube radius and  $\varphi$  is the azimuth angle. The armchair case with the absence of chirality is described by the system:

$$m \ddot{x}_i = -0.25k(2x_i - x_{i1} - x_{i2}) - k(x_i - x_{i3}) - \kappa' x_i \quad (1.5)$$

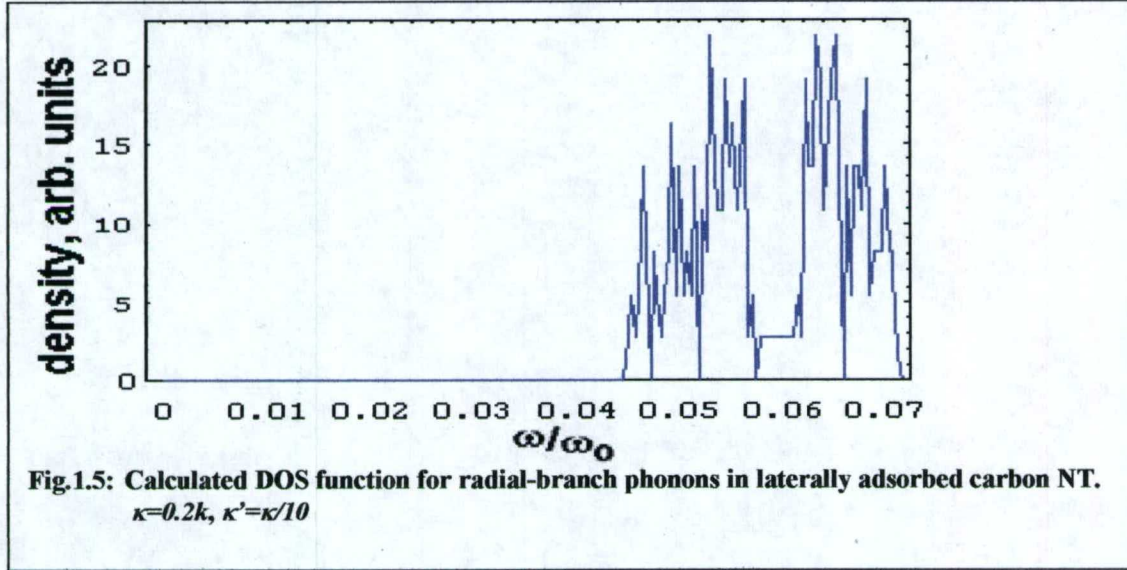
where coefficient 0.25 characterizes two weak bonds laying on the tube's surface for tangential atomic shift. Another bond directed along the atomic shift is most intensive. The bond of adsorption connection with the external medium is relatively weak for this motion.



For axial atomic shifts we have:

$$m \ddot{z}_i = -k(z_i - z_{i1}) - 0.75k(2z_i - z_{i2} - z_{i3}) - \kappa' z_i \quad (1.6)$$

where the coefficient 0.75 is connected with two strong bonds and  $\kappa'$  is the elastic constant describing motion perpendicular to the absorption bond  $\kappa$ .



Calculations show significant differences in phonon band characteristics for the radial branch of vibrations compared to that of a free armchair tube. In Fig.1.5, we see the DOS function for the  $\rho$ -branch of phonons found from (1.4) at  $\kappa=0.2k$  and  $\kappa'=\kappa/10$ . The bottom of this band rises at about  $0.04\omega_0$  though the top of the band remains almost at the same position. The effect has its explanation in an interesting quality of atomic radial motion. For radial shifts, even relatively weak adsorption bonds have elasticity coefficients bigger than inner bonds. This means that the radial band for a free nanotube transforms to a band of a system of almost non-connected atoms adsorbed onto the intrinsic medium surface.

The eigenstates are grouped in this case near the characteristic frequency of the adsorption bond. Radial vibrations occur as if each carbon atom is almost independent from the neighboring carbon atoms in the nanotube. Due to the band narrowing, the mean density of states becomes several times greater for a nanotube connected by adsorption bonds with a medium surrounding the nanotube surface. Comparison with the data for a free armchair tube shows that only the density of states of radial modes changes essentially with a shift and redistribution.



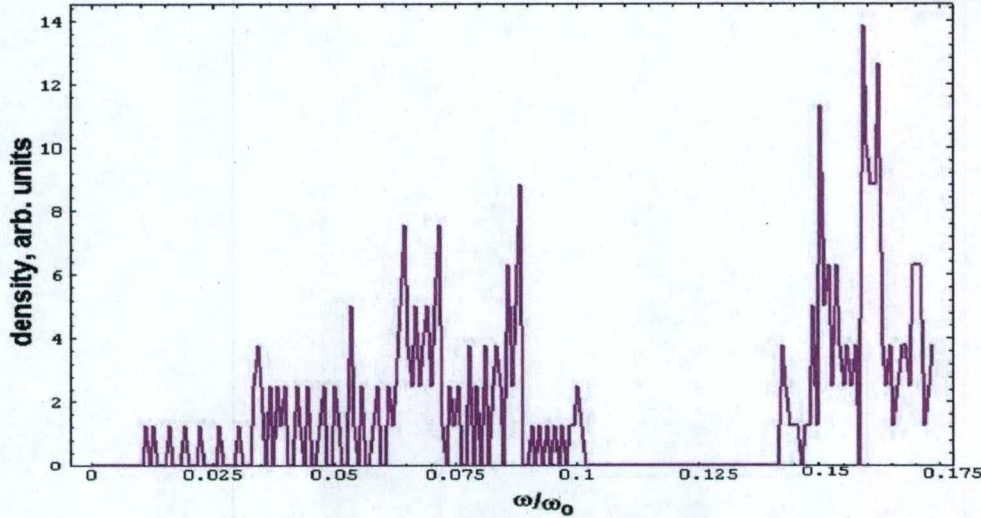


**Fig.1.6: Calculated DOS function for tangential branch of phonons in armchair nanotube having 8 hexagons in circumference and laterally adsorbed by external medium.  $\kappa=0.2k$ ,  $\kappa'=\kappa/10$ .**

The DOS function calculated for the  $\phi$ -branch of molecular vibrations found from (1.5) at  $\kappa=0.2k$  and  $\kappa'=\kappa/10$  is plotted in Fig.1.6. Minimal differences may be observed in the density of states distribution for the lowest phonon modes that are shifted up by approximately  $0.01\omega_b$ . The upper part of the band density remains unchanged.

Similar small deviations are observed for longitudinal z-branch vibrations in a laterally adsorbed armchair nanotube. The band bottom also shifts up by about  $0.01\omega_b$  at the immovable band top. The calculated DOS function for the z-branch of molecular vibrations, found from (1.6) at parameters given above, is plotted in Fig.1.7. Minimal differences in comparison with free armchair nanotube may be observed as well.

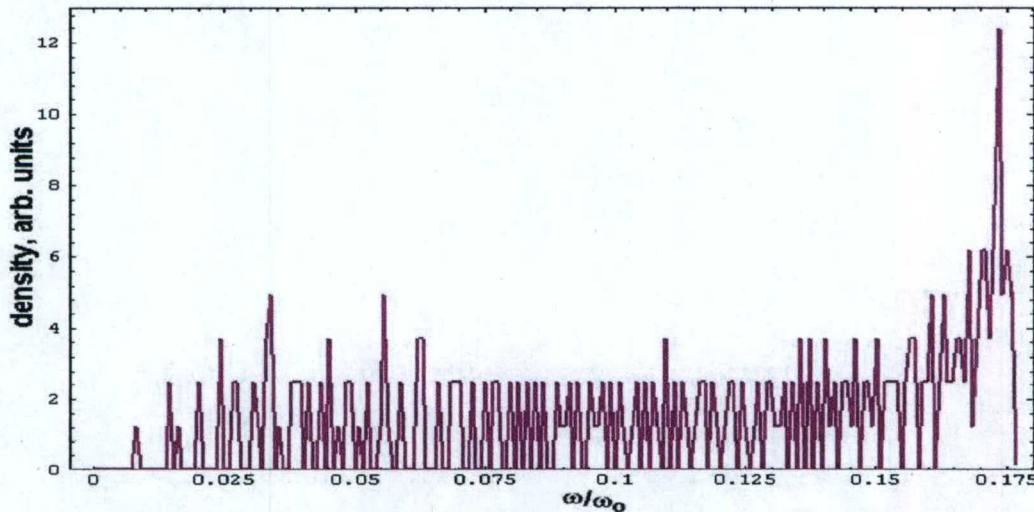


**Fig.1.7 Calculated DOS function for axial branch of phonons in armchair nanotube having 8 hexagons in circumference and laterally adsorbed by external medium.  $\kappa=0.2k$ ,  $\kappa'=\kappa/10$**

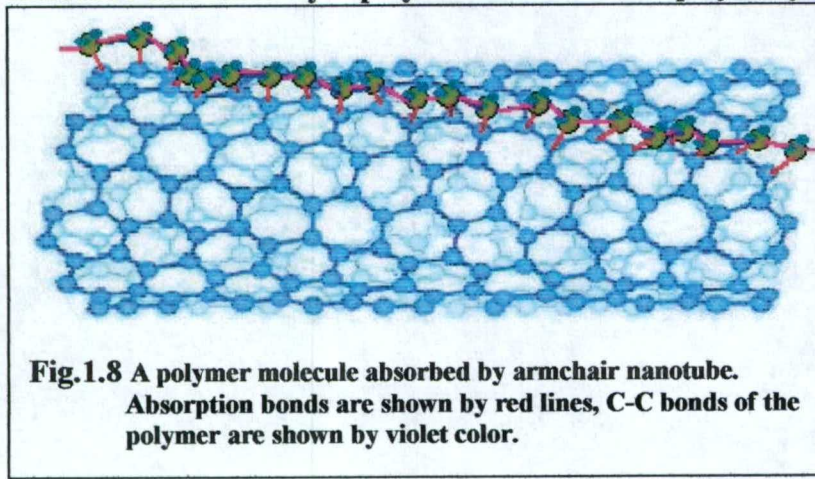


It should be marked that considerable changes arise only for radial the branch of vibration due to the direct influence of adsorption bonds on breathing modes. As radial vibrations play the key role in heat transport processes through nanotubes one should wait for a significant transformation of the thermal conductivity coefficient  $\lambda(T)$ .

The densities of phonon states for all three vibrational branches were found to have the same shape for different NT radii (parameter  $n$ ) and different lengths of fragment (parameter  $m$ ). The proportionality coefficient depends on the number of atoms in a fragment.

### 1.3.2b. Phonon dynamics of carbon tubes embraced by polymer molecule

We have also undertaken the investigation of a two-molecule system: a single-walled nanotube embraced by a polymer molecule like polyacetylene. The calculation of the system



was made in the PQDM framework for two molecules: an armchair NT  $\{n,m\}$  (created from a graphene sheet  $\{n,m\}$ ) and a polyacetylene chain  $(CH)_{2m+1}$ , adsorbed by the outer surface parallel to the tube axes. Here the index  $n$  describes the hexagon number along the tube circumference and index  $m$  is the same along the tube axes. In the armchair case the length of the tube equals  $2ma$ , where  $a$  is the

bond length. In zero-approximation, we consider carbon-hydrogen bonds in the polymer as absolutely rigid which leads to an effective mass of the polymer carbon equal to 13. The order of this problem's dynamical matrix becomes equal to  $2n(m+1)+2m+2$  and for the matrix shown in Fig.1.8 the  $(2m+2)$  subspace has to be added.

The most important for heat transport radial motion is described by equations for shifts  $\rho_i$  (nanotube atoms) and  $\rho_j$  (polyacetylene atoms) directed normally to the tube surface

$$\begin{aligned} m \ddot{\rho}_i &= -\kappa (\rho_i - \rho_j) - k' (3\rho_i - \rho_{i1} - \rho_{i2} - \rho_{i3}) \\ m' \ddot{\rho}_j &= -\kappa (\rho_j - \rho_i) - k' (2\rho_j - \rho_{j1} - \rho_{j2}) \end{aligned} \quad (1.7)$$

where  $m'=13m/12$ ,  $i_s$  and  $j_s$  are indexes for the neighbors of NT-atom  $i$  and polymer atom  $j$ ,  $\kappa$  and  $k'$  are elastic constants of external adsorption bond and intrinsic respectively. The united atomic number  $i$  is defined using its position in the row and column of the initial flat fragment creating the tube. For tangential atomic shifts we will take into account that atomic space coordinates on the tube surface  $x=\varphi R$ , where  $R$  is the tube radius and  $\varphi$  is the azimuth angle.



The armchair case with the absence of chirality is described by the system:

$$\begin{aligned} m \ddot{x}_i &= -0.25 k (2 x_i - x_{i1} - x_{i2}) - k (x_i - x_{i3}) - \kappa' (x_i - x_j) \\ m' \ddot{x}_j &= -k (2 x_j - x_{j1} - x_{j2}) - \kappa' (x_j - x_i) \end{aligned} \quad (1.8)$$

where coefficient 0.25 characterizes two strong bonds for tangential atomic shift. Another pair of bonds directed perpendicular to atomic shift is weak and includes a bond of absorption connection with external medium.

For axial atomic shifts we have:

$$\begin{aligned} m' \ddot{z}_j &= -k (2 z_j - z_{j1} - z_{j2}) - \kappa' (z_j - z_i) \\ m \ddot{z}_i &= -k' (z_i - z_{i1}) - 0.75 k (2 z_i - z_{i2} - z_{i3}) - \kappa' (z_i - z_j) \end{aligned} \quad (1.9)$$

where the coefficient 0.25 is connected with two weak bonds and  $\kappa'$  is elastic constant describing motion perpendicular to absorption bond  $\kappa$ .

In Fig.1.9, we present the general view of all branches of phonon spectra. In all cases, the spectrum is the superposition of nanotube and polyacetylene spectra deviated by additional bonds.

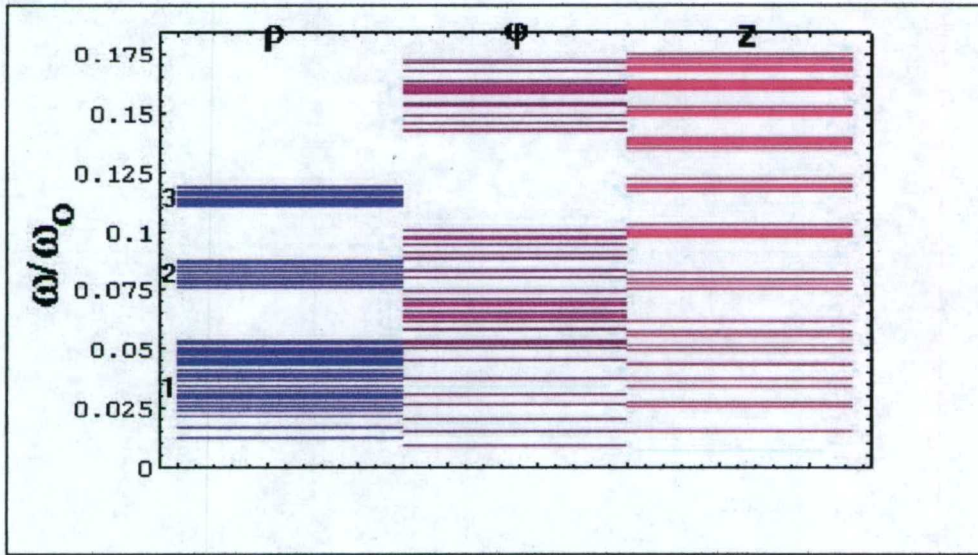


Fig.1.9: Calculated phonon spectra for radial ( $\rho$ ), tangential ( $\phi$ ), and axial ( $z$ ) branches of NT-polyacetylene system. 1 shows the nanotube modes, 2 and 3 are two halves of  $(CH)_n$  band. Here  $\kappa=k/5$ ,  $\kappa'=\kappa/10$ . There are eight hexagons in NT circumference.



### 1.3.3. Sound propagation in molecular nets

Molecular nets based on carbon and carbon-like systems provide the perfect natural target for 2D and 1D systems that allow us to consider the relation between pure non-thermodynamical sound, called hypersound (or nanosound), and atomic vibrations and the structure of phonon band. Wave phenomena in small flat and closed carbon fragments, films, fullerenes and nanotubes attract close attention now as they are an important part of thermal and transport processes in nanoelectronic devices [1]. Bulk mechanical properties expressed by elastic modules determine sound wave characteristics [2]. The most studied carbon materials, both experimentally and theoretically, are 3D crystals and thin layers [3]. The elastic properties of separated low-dimensional nanosize carbon fragments, single-walled nanotubes etc., give some theoretical troubles connecting the transformation of bulk notions to 2D and 1D ones and with the influence of small sizes [1-4]. Structural and phonon properties of carbon tubulenes were calculated in [5] with the tight binding approach and comparison with flat graphene sheets and bulk graphite was made. The vibrational density of states for 2D hierarchical quasicrystals has been calculated in [6] with the use of the Born approximation [2]. Experimental study of the elastic modulus in a multi-wall nanotube was performed in [7]. Thermal expansion of single-walled carbon nanotube bundles in X-ray diffraction experiments was studied in [8].

The classical theory of sound passing through the interface relies on macroscopic representations in regards to the nature of sound. The phenomenon characteristic sizes (wavelength and the size of averaging) are big compared to the lattice constant. Classical sound is the thermodynamic process uniting both time and space averaging and containing many phonons. The boundary conditions (BC) are introduced into the theory as an external term describing the contact type (strong or weak) between the media [9]. In that case, the BCs are not connected immediately with the microscopic structure of the boundary and have approximate characteristics. Really, for macroscopic rough boundary, the existing exact conditions of the vibration wave passing through the boundary have to be averaged at the distance of the sound wavelength. Now that nanoengineering technology is close to creating hierarchical molecular nets consisting of regularly alternating fragments, the problem of sound propagation in systems with sharp atomic contact boundaries has become the topic of interest.

Carbon nanotubes may be modified by periodic liquid surrounding, periodic intrinsic contain, periodic embracing by polymer, periodic other atoms adsorbed areas, periodic alternating of zigzag and armchair NT, alternating of carbon and BN-tubes, periodic isotope saturated areas and so on. A few pretenders where sound with extremely small wavelengths could exist are presented in Fig.1.10.



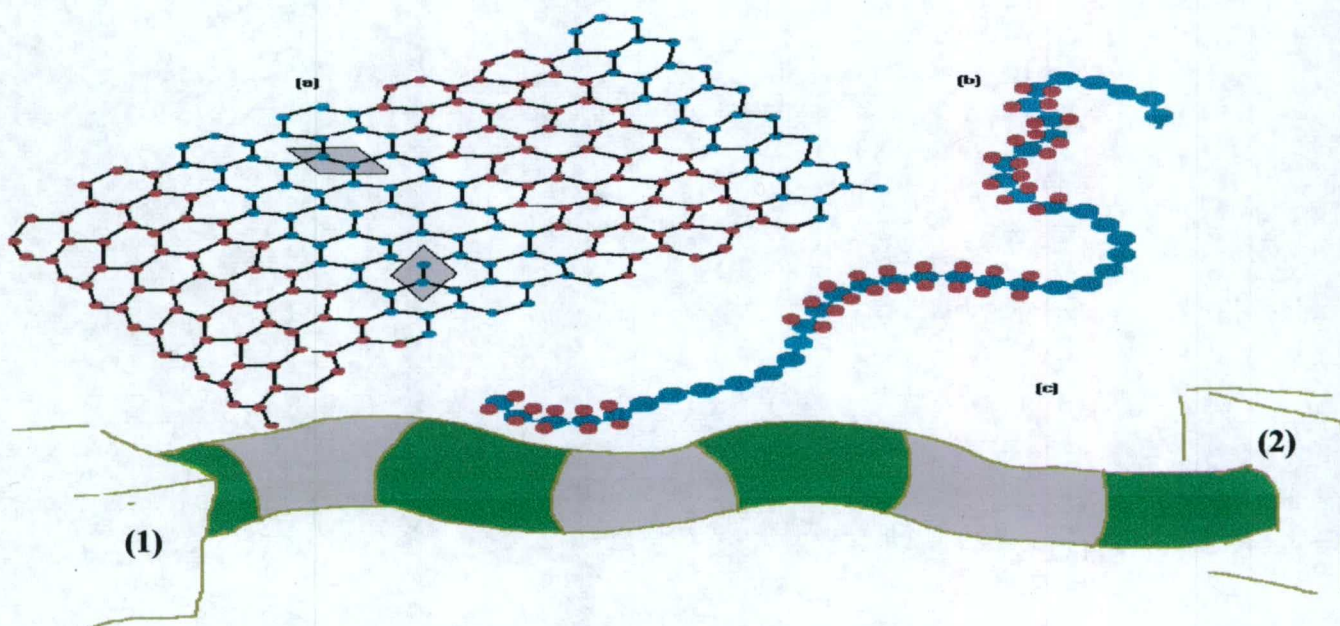


Fig. 1.10: Nanosize periodic structures – pretenders to detect nanosound interference.

(a) Cross-linked binary graphene sheet with zigzag type boundaries. Conventional elementary cells are shaded. (b) Carbine-polyethylene periodic linear chain. (c) Periodic fragments of a nanotube differed by elastic constants and (or) atomic mass. 1 and 2 are hypersound generator and receiver.

Such tailored structures may play the same role for the hypersound as photonic band gap materials perform for electromagnetic waves [10]. One can suppose the existence of the similarity between acoustic and electromagnetic wave phenomena is due to the band structure and energy transport through periodic systems [11].

It should be established that the connection between the nanostructure phonon dynamics and sound waves of small wavelengths is not investigated in detail for mesoscopic molecular nets, especially if it reaches the boundary condition problem in complex carbon nets. To obtain the exact BC for sound wave we propose here the integral procedure that starts from dynamical equations for atom vibrations in physically small areas near the boundary. The procedure includes averaging of discrete dynamical equations and transfer to a continuous description. The comparison of notions for native phenomena like phonons, sound and hypersound is used to emphasize the nanosound specifics in molecular nets. The hypersound band structure is calculated in linear approximation for periodically cross-linked nets of different nature. The structure and angular-frequency diagrams describing the sound band structure are obtained.

### 1.3.3a. Phonons and Hypersound in Low-dimensional Molecular Nets

The molecule vibrational eigenstates are called vibrons. In bulk crystals, the same are defined as “phonons”. Low-dimensional molecular nets occupy an intermediate position between small molecules and big macroscopic crystals. Nano-engineering allows the production of complex molecular net systems containing alternating fragments [12, 13]. The external geometry of such cross-linked systems is similar to well-known photonic crystals so sound propagation should possess the same properties including frequency bands and gaps [11]. Electron transport, light absorption and other impact processes in periodically cross-



linked molecular nets may be accompanied by sound pulses of comparatively short wavelength. Characteristic wavelengths of the sound must be about  $10^2$  nanometers with frequencies of the order of terahertz.

The difference between crystal vibrational eigenstates, phonons and sound is illustrated by the well-known solution for an isolated damped linear oscillator with external driving force

$$\ddot{x} + 2\gamma \dot{x} + \omega_0^2 x = F_0 e^{i\omega t}$$

$$x(t) = x_0 e^{-\gamma t} \cos(\omega_0' t + \varphi) + \frac{F_0 e^{i\omega t}}{\omega_0^2 - \omega^2 + 2i\gamma\omega} \quad (1.10)$$

where  $x_0$  is the vibration amplitude,  $\omega_0$  and  $\omega_0'$  are eigenfrequency and shifted eigenfrequency respectively,  $F_0$  and  $\omega$  are the external force amplitude and frequency respectively,  $\gamma$  is the damping constant,  $\varphi$  is the initial phase shift.

So, phonon modes have strongly determined frequencies and generally speaking they disappear with time but the sound that is connected with the external source of energy may be of any frequency. Principally, the same takes place for the net of linked oscillators. It is worthwhile to note that the solution for the system of linked oscillators also has a linear combination of partial solutions, like (1.10), and does not contain retardation or any sign of propagating waves.

Several remarkable features are present in periodic molecular nets that differ from bulk materials [9]. First, there exists a precise atomic scale of boundaries between the net fragments with the absence of intermediate layers. The second feature is that phonon branches participate in sound transportation independently in zero-approximation and obey separate boundary conditions. The third one is the strongly non-macroscopic characteristic of elastic waves in small molecular fragments containing a periodic net. This is the reason for the term "nanosound" to differentiate nanometer sound waves from macroscopic sound.

The averaging procedure plays an important role in understanding phonon, sound and heat propagation in low-dimensional atomic nets. Classical dynamical equations in the non-relativistic Born approximation do not contain retardation. This causes the infinite speed of initial vibrational excitation propagation along the net or nanotube.

The first stage of averaging is the presentation of dynamic equations in a finite differences view. More rough-averaging of the phonon mean free path distances is used to describe heat spreading along carbon nets.



	<b>Hypersound</b>	<b>Phonon standing waves</b>	<b>Macro-sound</b>
<b>Frequency spectrum type</b>	<b>Continuous</b>	<b>Discrete</b>	<b>Continuous</b>
<b>Wavelength diapason</b>	<b>0–10<sup>3</sup> nm</b>	<b>No wavelength</b>	<b>More than 1 mkm</b>
<b>Size of state</b>	<b>No</b>	<b>Mean free path(*)</b>	<b>No</b>
<b>Frequency diapason</b>	<b>(10<sup>10</sup> - 10<sup>13</sup>) c<sup>-1</sup></b>	<b>Phonon bandwidth</b>	<b>Less than 10<sup>10</sup> c<sup>-1</sup></b>
<b>Size of averaging range</b>	<b>1nm (elementary cell)</b>	<b>No averaging</b>	<b>1-10 mkm</b>
<b>Examples of activity processes</b>	<b>Impact effects, external sources</b>	<b>Raman effect</b>	<b>External sources</b>
<b>Transmitting energy</b>	<b>Energy of atomic vibrations</b>	<b>Heat</b>	<b>Energy of elastic deformation</b>
<b>Nature of phenomenon</b>	<b>Extending waves of atomic vibration</b>	<b>Standing waves of vibrations(eigenstates)</b>	<b>Extending deformation waves</b>

*Note: (\*) determined from the phonon lifetime relatively the interaction with other particles and external medium.*

Table 1: Sound, hypersound and phonons

Non-linearity may be presented directly in the dynamic equations as a consequence of averaging and transfer to the rough scale of the phenomena. It should be noted that non-linearity is not connected with the damping of whole phonon states. The energy dissipation and the width of states arise formally when first derivatives are added into the system of classical dynamical equations.

Hypersound waves occur as the result of averaging of classical equations of atomic dynamics. The transfer from equations in finite differences to continuous representation gives second derivatives in both space and temporal. As the averaging acts at very small areas having sizes of an elementary (conventional) cell, the result depends on the concrete symmetry of the elementary cell.

**a. Periodic linear chain:**

The simple case corresponds to waves in a linear chain with periodically alternating fragments. Let us consider a molecular chain with regular alternation of equal fragments of two types. There exists three vibrational branches that correspond to three degrees of freedom for each atom  $s=1,2,3$ . Immediately, from atomic dynamical equations, we have

$$\frac{\partial^2 \langle x \rangle_s}{\partial t^2} - V_s^2 \frac{\partial^2 \langle x \rangle_s}{\partial z_s^2} = 0, \quad V_s = a \sqrt{\frac{\chi_s}{m}} \quad (1.11)$$



where  $a$  is the interatomic distance,  $\langle x \rangle_s$  is the mean atomic shift in  $s$ -direction,  $z_s$  marks the extended coordinate of  $s$  degree of freedom. Evaluations by data [5,12] ( $\chi=330$  N/m) give for sound velocity along the carbon net  $V=18.3$  km/s. This value is close to the velocity of sound in diamond in the (1,1,0) direction.

**b. Square lattice:**

Waves in hypothetical simple quadratic 2D lattice are described by equation

$$\frac{\partial^2 \langle x \rangle_s}{\partial t^2} - V_s^2 \frac{\partial^2 \langle x \rangle_s}{\partial z^2} + (V'_s)^2 \frac{\partial^2 \langle x \rangle_s}{\partial y^2} = 0 \quad (1.12)$$

Here we are taking into account that the elastic constant for motion transverse to the bond direction differs from that for motion along the band. In 2D structure it is convenient to mark the degrees of freedom through the generalized coordinates. In quadratic lattice  $s=z, y, \rho$ , the latter describes vibrations perpendicular to the lattice plane. (1.12) is anisotropic for separate branches  $s=z, y$ . The medium in-plane isotropy manifests in correlation  $V_z = V'_y$  and  $V_y = V'_z$ .

**c. Honeycomb lattice zigzag nanostructure, Z-branch:**

The dynamics of longitudinal motion along the net or nanotube  $z$ -axes may be written for the whole elementary cell having two atoms. For any  $i$ -atom we have for  $s=1$  degree of freedom,

$$m\ddot{x}_i = -k(2x_i - x_i^l - x_i^r) - 0.25k(2x_i - x_i^u - x_i^d) \quad (1.13)$$

where the upper indexes mark coordinates of neighboring atoms in  $y$ - and  $z$ -directions. Two brackets in the right-hand part of (1.13) are transformed into the space coordinate second derivatives after averaging along  $z$ -direction and  $y$ -direction. In the zigzag case, the averaging distance between neighboring elementary cells equals to  $3a/2$  along  $z$ -axes and  $3^{1/2}a$  along  $y$ -axes. Inserting these distances into the finite differences derivatives gives the wave equation:

$$\frac{\partial^2 \langle x \rangle}{\partial t^2} - V_y^2 \frac{\partial^2 \langle x \rangle}{\partial y^2} - V_z^2 \frac{\partial^2 \langle x \rangle}{\partial z^2} = 0 \quad (1.14)$$

where, due to the system anisotropy for  $z$ -branch of vibrations as to  $z$ - and  $y$ -directions, we get different wave velocities along  $z$ - and  $y$ -directions:

$$V_z = \sqrt{3}V_y / 2 = 1.5a\sqrt{\tilde{k} / m} \quad (1.15)$$



**d. Honeycomb lattice, zigzag nanostructure,  $\phi$ -branch:**

This branch is connected with the  $s=2$  circumferential degree of freedom in a tube-like net and  $y$ -motion in plane structure. For all  $i$ -atoms, we have the system of connected equations,

$$m\ddot{x}_i = -\tilde{k}(2x_i - x_i^u - x_i^d) - k'(2x_i - x_i^l - x_i^r), \quad (1.16)$$

that transforms after the transfer to the finite difference view into the wave equation:

$$\frac{\partial^2 \langle x \rangle}{\partial t^2} - 3V_y^2 \frac{\partial^2 \langle x \rangle}{\partial y^2} - v_z^2 \frac{\partial^2 \langle x \rangle}{\partial z^2} = 0 \quad (1.17)$$

$$v_z = \frac{3a}{2} \sqrt{\frac{k'}{2m}} \quad (1.18)$$

where  $v_z$  is the  $\phi$ -wave velocity along  $z$ -direction.

### 1.3.3b. Sound Boundary Conditions

Boundary conditions arise in this approach as a consequence of integrating dynamical equations and averaging in the vicinity of the boundary. In contrast to electromagnetic waves, the vibrational dynamics has the exact meaning immediately for a non-homogeneous range including both sides of the boundary. To take into account the exact bonds between contacting nets of different nature, one has to perform integration or summing before the averaging procedure. In a sense, the sound BCs are a more pure phenomenon than BCs for electromagnetic waves that represent correlation between averaged fields in contacting materials.

#### a. Periodic linear chain:

The illustration to the BC standards is given by linear chains with periodically alternating fragments. Examples may be carbene fragments alternated by polyethylene or polyacethylene fragments.

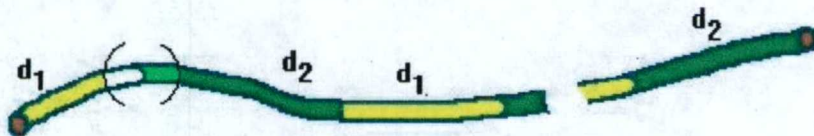


Fig.1.11: One-dimensional periodical chain. Tags  $d_1$  and  $d_2$  mark the length of alternating chain parts. Brackets show the physically small ranges of integration near the boundary.

Consider the range on both sides near the boundary of two molecular chains: from  $l_0$  to the end atom  $l$  of the left fragment  $d_1$  and from atom  $r$  to  $r_0$  on the right chain  $d_2$  (Fig.1.11).



$$\begin{cases}
m\ddot{x}_l = -q(x_l - x_r) - \chi(x_l - x_{l-1}) \\
m\ddot{x}_r = q(x_l - x_r) - \chi'(x_r - x_{r+1}) \\
m\ddot{x}_{l-1} = -\chi(2x_{l-1} - x_l - x_{l-2}) \\
m\ddot{x}_{r+1} = -\chi'(2x_{r+1} - x_r - x_{r+2}) \\
\text{-----} \\
m\ddot{x}_{l_0} = -\chi(2x_{l_0} - x_{l_0+1} - x_{l_0-1}) \\
m\ddot{x}_{r_0} = -\chi(2x_{r_0} - x_{r_0-1} - x_{r_0+1})
\end{cases} \quad (1.19)$$

Summation gives:

$$\sum_{i=l}^{l_0} m\ddot{x}_i + \sum_{i=r}^{r_0} m'\ddot{x}_i = -\chi(x_{l_0} - x_{l_0-1}) - \chi'(x_{r_0} - x_{r_0+1}) \quad (1.20)$$

The averaging of the finite difference expressions, on the right side of (1.20), leads to continuous space derivatives. Besides, taking into account the bulk wave equations, we change the time derivatives on the left side of (1.20) to the corresponding space derivatives.

$$\sum_{i=l_0}^l mV^2 \frac{\partial^2 \langle x \rangle}{\partial z^2} + \sum_{i=r}^{r_0} m'V'^2 \frac{\partial^2 \langle x \rangle}{\partial z^2} = -\chi \left( \frac{\partial \langle x \rangle}{\partial z} \right)_{l_0} + \chi' \left( \frac{\partial \langle x \rangle}{\partial z} \right)_{r_0} \quad (1.21)$$

On the left-hand side, we perform the transfer from summation to integration within the same limits and after the cancellation of end derivatives we get the exact BC,

$$\frac{mV^2}{a} \left( \frac{\partial \langle x \rangle}{\partial z} \right)_l = \frac{\bar{m}\bar{V}^2}{\bar{a}} \left( \frac{\partial \langle x \rangle}{\partial z} \right)_r \quad (1.22)$$

where  $a$  and  $\bar{a}$  are lattice constants on both sides of the boundary.

(1.23) gives the first of two BCs for near itinerant ranges on both sides of the boundary between chains of two types.

$$\begin{cases}
\chi^- a^- \frac{\partial \langle x \rangle^-}{\partial z} = \chi^+ a^+ \frac{\partial \langle x \rangle^+}{\partial z} \\
\langle x \rangle^- = \langle x \rangle^+
\end{cases} \quad (1.23)$$

Another condition arises from the continuity of displacement  $\langle x \rangle$  during the wave transition through the boundary. The first BC expression is a kind of material correlation like in the case of electromagnetic waves (EMW) in a medium.



An essential difference arises between sound waves and EMW when we begin considering the free edge of the molecular net. Sound waves are principally absent in the surrounding empty space. This leads to a special case of end boundary equations.

$$\left( \frac{\partial \langle x \rangle}{\partial z} \right)_{l,r} = 0 \quad (1.24)$$

Besides, in the EMW case, there is no need for a transfer from discrete equations to continuous ones due to the fact that the classical electromagnetic field is principally a continuous phenomenon.

#### b. Honeycomb lattice:

BCs in a honeycomb lattice may be obtained in an integral procedure similar to that considered above for a 1D periodical chain. The operation uses a substantially small summation range. The notion of an infinitely small range is a corner-stone of the electromagnetic theory in condensed matter. Its size (1-100nm) determines the size of a conventional point of continuous medium containing electromagnetic field. It is the same for the acoustics of hypersound extending in molecular nets where this has to be introduced on account of the reduced dimensionality and mechanical nature of sound waves. The left side of this interval may be active for hypersound, but in both cases the physically small element must contain many atoms. The summation of dynamical equations inside the small range on both sides near the boundary gives,

$$\begin{aligned} \sum_{j=d_0}^{u_0} \sum_{i=l_0}^l m \ddot{x}_{ij} + \sum_{j=d_0}^{u_0} \sum_{i=r}^{r_0} \bar{m} \ddot{x}_{ij} = & -\chi \sum_{j=d_0}^{u_0} (x_{l_0,j} - x_{l_0-1,j}) - \bar{\chi} \sum_{j=d_0}^{u_0} (x_{r_0,j} - x_{r_0+1,j}) \\ & -0.25\chi \sum_{i=l_0}^l (x_{i,u_0} - x_{i,u_0+1}) - 0.25\bar{\chi} \sum_{i=r}^{r_0} (x_{i,u_0} - x_{i,u_0+1}) - \\ & -0.25\chi \sum_{i=l_0}^l (x_{i,d_0} - x_{i,d_0-1}) - 0.25\bar{\chi} \sum_{i=r}^{r_0} (x_{i,d_0} - x_{i,d_0-1}) \end{aligned} \quad (1.25)$$

The parameters  $\chi$ -bar and  $m$ -bar belong to the right-hand material. The averaging and transfer to continuous forms of derivatives and sums give:



$$\begin{aligned}
& \frac{m}{S_0} \int_{d_0}^{u_0} dy \int_{l_0}^l dz \langle \ddot{x} \rangle + \frac{\bar{m}}{\bar{S}_0} \int_{d_0}^{u_0} dy \int_r^{r_0} dz \langle \ddot{x} \rangle = \\
& - \chi \frac{a_z}{a_y} \int_{d_0}^{u_0} dy \left( \frac{\partial \langle x \rangle}{\partial z} \right)_{l_0} + \bar{\chi} \frac{\bar{a}_z}{\bar{a}_y} \int_{d_0}^{u_0} dy \left( \frac{\partial \langle x \rangle}{\partial z} \right)_{r_0} + \\
& + 0.25 \chi \frac{a'_y}{a'_z} \int_{l_0}^l dz \left( \frac{\partial \langle x \rangle}{\partial y} \right)_{u_0} + 0.25 \bar{\chi} \frac{\bar{a}'_y}{\bar{a}'_z} \int_r^{r_0} dz \left( \frac{\partial \langle x \rangle}{\partial y} \right)_{u_0} - \\
& - 0.25 \chi \frac{a'_y}{a'_z} \int_{l_0}^l dz \left( \frac{\partial \langle x \rangle}{\partial y} \right)_{d_0} - 0.25 \bar{\chi} \frac{\bar{a}'_y}{\bar{a}'_z} \int_r^{r_0} dz \left( \frac{\partial \langle x \rangle}{\partial y} \right)_{d_0}
\end{aligned} \tag{1.26}$$

Here  $S_0$  marks the half-area of left material elementary cell. Taking into account the wave equation (1.14) connecting time and spatial second derivatives, we have for the left side of (1.26),

$$\begin{aligned}
& V_z^2 \frac{m}{S_0} \int_{d_0}^{u_0} dy \left( \left( \frac{\partial \langle x \rangle}{\partial z} \right)_l - \left( \frac{\partial \langle x \rangle}{\partial z} \right)_{l_0} \right) + V_y^2 \frac{m}{S_0} \int_l^{l_0} dz \left( \left( \frac{\partial \langle x \rangle}{\partial y} \right)_{u_0} - \left( \frac{\partial \langle x \rangle}{\partial y} \right)_{d_0} \right) \\
& \bar{V}_z^2 \frac{\bar{m}}{\bar{S}_0} \int_{d_0}^{u_0} dy \left( \left( \frac{\partial \langle x \rangle}{\partial z} \right)_{r_0} - \left( \frac{\partial \langle x \rangle}{\partial z} \right)_r \right) + \bar{V}_y^2 \frac{\bar{m}}{\bar{S}_0} \int_r^{r_0} dz \left( \left( \frac{\partial \langle x \rangle}{\partial y} \right)_{u_0} - \left( \frac{\partial \langle x \rangle}{\partial y} \right)_{d_0} \right)
\end{aligned} \tag{1.27}$$

Using explicit expressions for  $V_z$  and  $S_0$ , we may cancel edge  $z$ -derivatives in  $l_0$  and  $r_0$  points of (1.26) and (1.27) after substituting the left part of (1.26) by the expression in (1.27). Due to the fact that the boundary, in this case, is situated perpendicular to the  $z$ -axes and taking into account the limits  $l_0 \rightarrow l$ ,  $r_0 \rightarrow r$ ,  $d_0 \rightarrow u_0$ , we obtain the boundary condition of the type in (1.22):

$$\frac{m V_z^2}{S_0} \left( \frac{\partial \langle x \rangle}{\partial z} \right)_l = \frac{\bar{m} \bar{V}_z^2}{\bar{S}_0} \left( \frac{\partial \langle x \rangle}{\partial z} \right)_r \tag{1.28}$$

If the boundary is situated perpendicular to the  $y$ -axes (armchair-type boundary), then the expressions for  $V_y$  and  $S_0$  allow cancellation of the edge  $y$ -derivatives along the  $u_0$  and  $d_0$  lines in (1.26) and the boundary condition takes the form

$$\frac{m V_y^2}{S_0} \left( \frac{\partial \langle x \rangle}{\partial y} \right)_u = \frac{\bar{m} \bar{V}_y^2}{\bar{S}_0} \left( \frac{\partial \langle x \rangle}{\partial y} \right)_d \tag{1.29}$$

(1.29) represents material correlation between contacting media. The kinematic part of the BC is similar to the zigzag type of boundary for the continuity of the displacement  $\langle x \rangle$  when the wave transits through the boundary (see (1.23)). It should be noted that exact



cancellations during the derivation of the BC in the integral procedure performed above is a manifestation of the united nature of both itinerant 2D wave equation and boundary condition procedures. Contrary to electromagnetic waves where BCs are derived from the integral form of Maxwell equations, the analogous integral form of atomic dynamics equations are not very popular. Another significant difference with obtaining EMW boundary conditions consists of the direct presence of elementary cell parameters in material BCs ((1.22), (1.28) and (1.29)) and the atomic bonds elasticity.

### 1.3.3c. The Hypersound Frequency Bands in Periodic Molecular Nets

The hypersound wave of frequency  $\omega$  is described by two amplitudes inside each net band.

$$\langle x \rangle = A e^{i\omega t + ik_z z + ik_y y} + B e^{i\omega t - ik_z z + ik_y y} \quad (1.30)$$

There exist two z-projections of the wave vector  $k$  in a periodic binary molecular net or linear chain depending on the hypersound velocities in the separated materials.

The system of BC equations is described by the matrix presented in Table 2. The intrinsic problem for hypersound eigenstates when external sources are absent and the system is isolated from another sound conductor may be solved analytically as in the case of EMW in layered structures [11, 12].

$B_1$	$A'_1$	$B'_1$	$A_2$	$B_2$	$A'_2$	$B'_2$	$A_3$	$B_3$	$A'_{-1}$	$B'_{-1}$	$A_N$	$B_N$	$A'_N$
$Z_1$	-1	-1	0	0	0	0							
$Y_1$	$\eta_2$	$\eta_2^*$	0	0	0	0							
0	$\sigma_2$	$\sigma_2^*$	-1	-1	0	0							
0	$\delta_2$	$\delta_2^*$	$\eta_1$	$\eta_1^*$	0	0							
0	0	0	$\sigma_1$	$\sigma_1^*$	-1	-1							
0	0	0	$\delta_1$	$\delta_1^*$	$\eta_2$	$\eta_2^*$	0	0					
0	0	0	0	0	$\sigma_2$	$\sigma_2^*$	-1	-1					
					$\delta_2$	$\delta_2^*$	$\eta_1$	$\eta_1^*$					
					0	0	$\sigma_1$	$\sigma_1^*$					
					...	...							
							...	...					
									...	...			
											$\eta_2$	$\eta_2^*$	0
											$\sigma_2$	$\sigma_2^*$	-1
											$\delta_2$	$\delta_2^*$	$\eta_1$
											0	0	$\eta_1^*$
												$\sigma_1$	$\sigma_1^*$
												$\delta_1$	$\delta_1^*$
													$Z_r$
													$Y_r$

Note: Dotted lines show the minor  $\mu$  that is matrix element  $A_{ll}$ .

Table 2: The matrix of boundary condition equations



The generalized dispersion equation is represented in row-matrix-column production

$$(Z_l, -Y_l) \hat{\Lambda}^n \begin{pmatrix} Y_r \\ Z_r \end{pmatrix} = 0, \quad \hat{\Lambda} = \begin{pmatrix} \mu & \nu \\ \lambda & \bar{\mu} \end{pmatrix} \quad (1.31)$$

where  $n=N-1$ ; matrix elements  $\mu$ ,  $\bar{\mu}$ ,  $\nu$  and  $\lambda$  are minors of the dynamical matrix (Tab.2), index  $l$  corresponds to the left and index  $r$  corresponds to the right end of the net. The matrix  $A$  describing the lattice period in turn, is the product of each material matrix  $A=A_1 A_2$ . The matrix elements for the first instance are as follows:

$$\begin{aligned} \bar{\mu}_1 &= \mu_1 = -2i\chi k_z a_z \cos k_z d_1; & \nu_1 &= -2i(\chi k_z a_z)^2 \sin k_z d_1; & \lambda_1 &= 2i \sin k_z d_1 \\ Z_l &= \cos k_z d_1; & Z_r &= -\cos \bar{k}_z d_2; & Y_r &= -\bar{\chi} \bar{k}_z \bar{a}_z \sin \bar{k}_z d_2 \end{aligned} \quad (1.32)$$

The  $n$ -degree for transfer matrix  $A$  is found by canonical transformation,  $\hat{\Theta}$ , diagonalizing the matrix  $A$ .

$$\begin{aligned} \hat{\Theta} &= \frac{1}{D} \begin{pmatrix} x_{22} & -x_{21} \\ -x_{12} & x_{11} \end{pmatrix}; \quad \hat{\Theta}^{-1} = \begin{pmatrix} x_{11} & x_{21} \\ x_{12} & x_{22} \end{pmatrix}; \quad D = \det(\hat{\Theta})^{-1}; \\ \hat{\Lambda}^n &= \frac{1}{D} \begin{pmatrix} x_{11}x_{22}f_1^n - x_{12}x_{21}f_2^n & x_{11}x_{21}(f_2^n - f_1^n) \\ x_{22}x_{12}(f_1^n - f_2^n) & x_{11}x_{22}f_2^n - x_{12}x_{21}f_1^n \end{pmatrix}, \end{aligned} \quad (1.33)$$

where  $x_{ij}$  are elements of matrix  $A$  eigenvectors:  $\hat{X}_1^+ = (x_{11}, x_{12})$  and  $\hat{X}_2^+ = (x_{12}, x_{22})$   
 $x_{11} = x_{21} = \nu$ ;  $x_{12} = f_1 - \mu$ ,  $x_{22} = f_2 - \mu$

The eigenvalues  $f_1, f_2$  are,

$$f_{1,2} = (\mu + \bar{\mu})/2 \pm \sqrt{((\mu - \bar{\mu})/2)^2 + \lambda \nu} \quad (1.34)$$

Taking into account (1.32)-(1.34) and (1.31), we obtain a generalized dispersion equation for hypersound in periodic structures, describing sound wave frequencies and type of state: local or band.

$$f_1^n (Y_r x_{22} - Z_r x_{21})(Z_l x_{11} - Y_l x_{12}) - f_2^n (Y_r x_{12} - Z_r x_{11})(Z_l x_{21} - Y_l x_{22}) = 0 \quad (1.35)$$



Extended band states exist in the frequency range with a negative value of discriminant in  $f_1$  or  $f_2$ . In this case, there are two parts on the left side of (1.35) which are conjugated and the partial dispersion equation for band states takes the form

$$\nu^2 \sin(n\varphi + \varphi_l + \varphi_r) = 0 \quad (1.36)$$

where  $n\varphi$ ,  $\varphi_l$  and  $\varphi_r$  are complex phases of three multipliers in the first term of (1.35). A positive discriminant corresponds to frequency gaps. The result of band calculations using (1.35) is presented in Fig.4 for a 16-periodic carbene-polyethylene linear chain  $C-CH_2$ . The frequency is normalized.

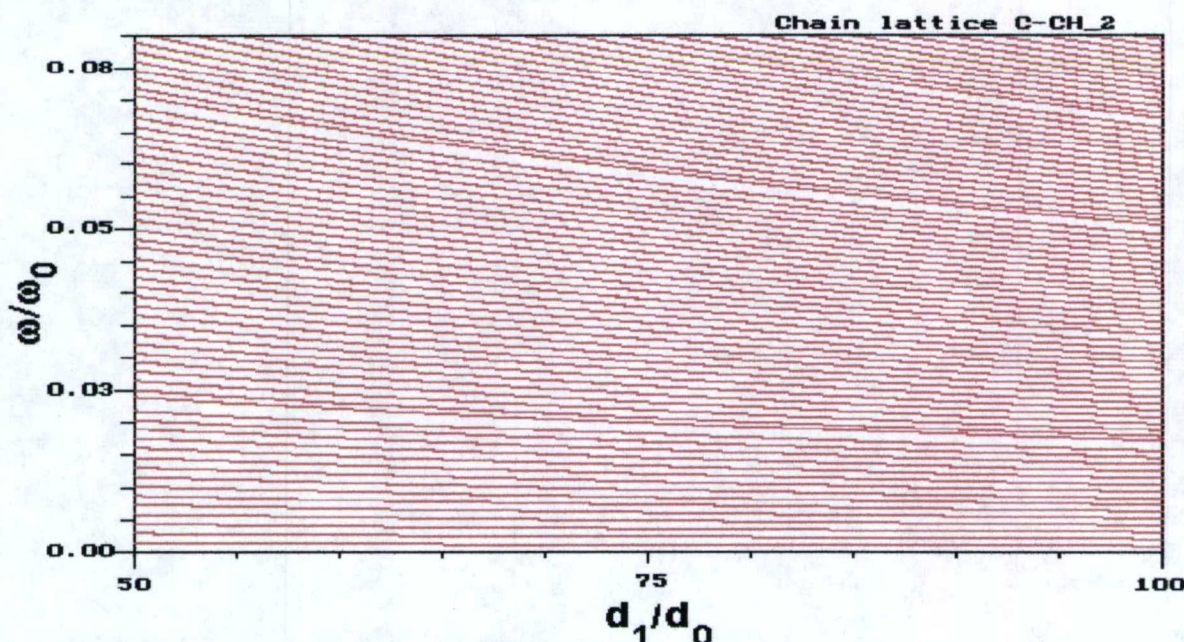


Fig.1.13: One-dimensional 16-periodic elastic chain carbon- $CH_2$ . Frequency-size diagram.  $d_1/d_0$  gives the dimensionless length of the "1-material" fragment,  $d_2=80d_0$ ,  $d_0=0.13\text{nm}$  is the accepted length unity (for normalizing) and  $\omega_0=20.48\text{ THz}$  is the accepted frequency unity.

A value of  $\omega_0 = 20.48\text{ THz}$  was obtained using the elasticity coefficient of the carbon-carbon bond  $\chi = 330\text{ N/m}$ :  $\omega_0 = (\chi/m)^{1/2}$ . The z-wave velocity of sound in pure 2D graphene sheet or tubulene is  $V_0=16730\text{m/s}$ . The velocity of sound in a hydrogenised graphene sheet is supposedly 7.5% less due to the bigger site mass. Characteristic frequencies are of the order of terahertz for chosen fragment sizes of the order a ten nanometers. If the fragments of chains that are in contact are taken to be near hundreds ( $10^2$ ) nanometers one may observe the same picture in frequency range but ten times lesser.

Calculations undertaken for different frequency and size scales gave very high similarity in the obtained band pictures at scale transformation  $\omega \rightarrow c\omega$ ,  $d_1, d_2 \rightarrow d_1/c, d_2/c$ . With increasing frequency, the bands and gaps became smaller and the slopes of the lines increase. Each frequency band contains the number of states (modes) that coincides with the number of periods in the structure. Only the lower band consists of one less state due to the absence of the trivial (zero-frequency) solution of (1.35). The width of the gap depends on the



difference between relations  $\chi/m$  for contacting chains and it becomes approximately equal to the band width at  $m_1 \approx 6m_2$ .

In two-dimensional systems consisting of alternating flat or tube fragments of different kinds, the hexagonal lattices have a new parameter – the incidence angle of the hypersound wave. Standing waves existing in the isolated periodical net depend on the direction of the wave vector. Due to the principal anisotropy of the propagation of z-waves in the hexagonal lattice, the constant velocities in the z- and y-directions are different. Therefore, the wave vector depends on the angle  $\theta$  of wave propagation.

$$k = \frac{\omega}{\sqrt{V_z^2 \cos^2 \theta + V_y^2 \sin^2 \theta}} \quad (1.37)$$

The same expression exists for the second material, for which the analogous notations are  $\bar{\theta}$ -bar and  $\bar{V}$ -bar. The Snellius-Descartes law  $k_y = \bar{k}_y$  gives for transition from medium-1 wave to medium-2 wave.

$$\sin \bar{\theta} = \frac{k_y \bar{V}_z}{\sqrt{\omega^2 + k_y^2 (\bar{V}_z^2 - \bar{V}_y^2)}} \quad (1.38)$$

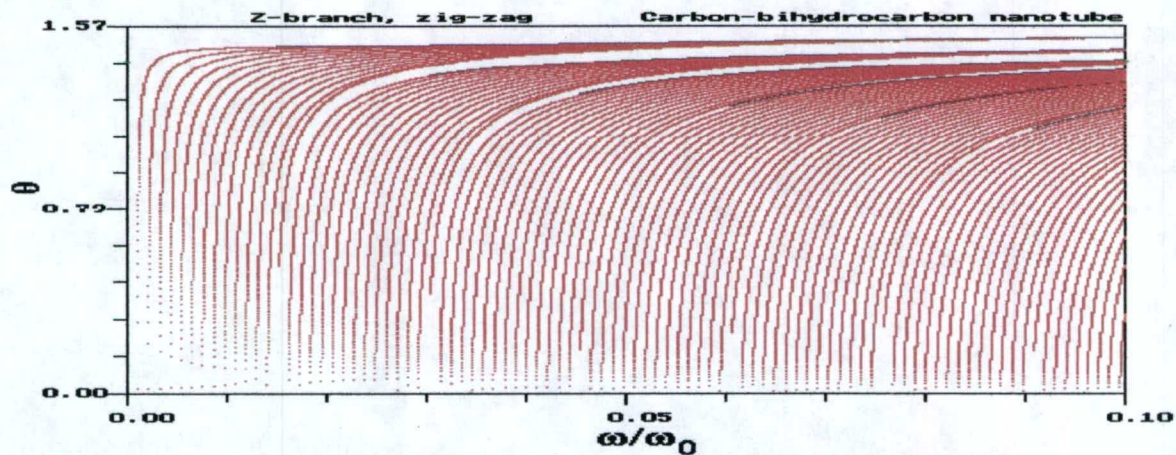


Fig.1.14: Two-dimensional flat 14-period elastic graphene-CH<sub>2</sub> net angular-frequency diagram. Calculated by Eqtns.1.35 and 1.36;  $d_1=100d_0$ ,  $d_2=200d_0$ ,  $\omega = (0,0.1)\omega_0$ .

The result of calculations by (1.36) for a 2D 14-periodic flat graphene-graphene or closed tube-tube system is presented in Fig.1.14. Accepted unities are  $\omega_0 = 20.48$  THz and  $\chi = 330$  N/m for both media. The z-wave velocity of sound in medium-2 was taken to be  $1.573V_0$  and  $V_z=1.388V_0$  in the acoustically less dense medium. Characteristic frequencies are of the order of teraherzs. The scale transformation  $\omega \rightarrow c\omega$ ,  $d_1, d_2 \rightarrow d_1/c, d_2/c$  does not change the system band structure in the 2D case either. The number of modes inside each frequency band coincides with the number of periods in the structure.



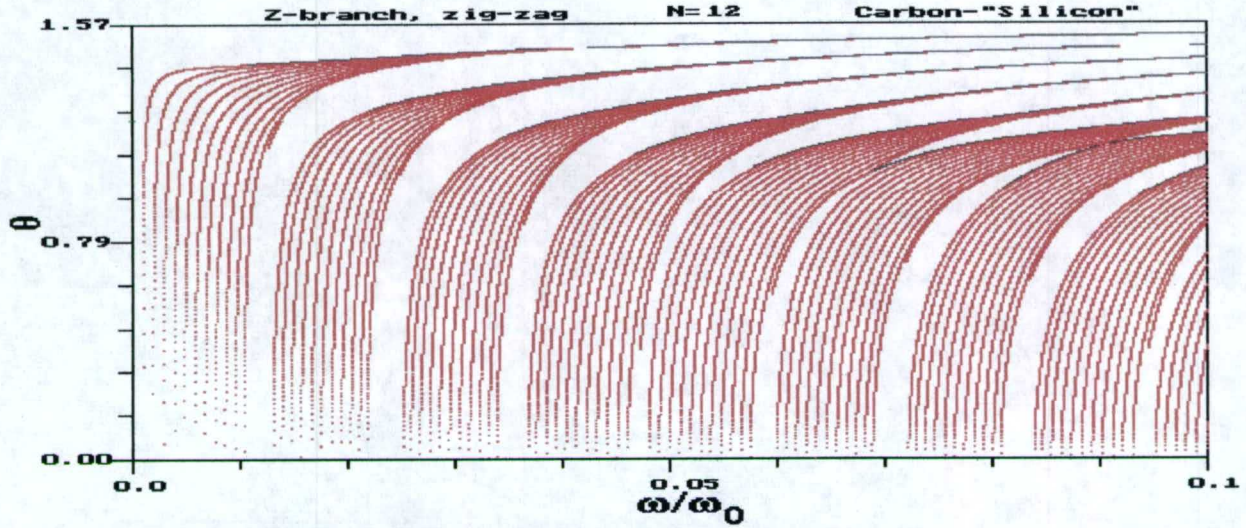


Fig.1.15: Two-dimensional flat 12-period elastic graphene-Si net. Calculated by (26), (27) angular-frequency diagram:  $d_1=100d_0$ ,  $d_2=200d_0$ ,  $\omega = (0,0.1)\omega_0$

The width of the gaps depend directly on the difference between  $\chi/m$  and  $\bar{\chi}/\bar{m}$ . This property and band structure may be illustrated by an imaginary system – acoustic crystal with sound velocities differed four times:  $\bar{V}_z = 1.53V_z$  (Fig.1.15). In Fig.1.14, we see that both bandwidth and gap width are almost regular at small incidence angles. Increasing the frequency leads to bands touching one another and splitting again. A similar phenomenon was observed in 1D photonic crystals [11, 14] for electromagnetic field structure.

The whole intrinsic reflection range occurs in periodic systems due to the difference in wave velocities of different materials. Equation 1.38 illustrates this when  $\omega^2 = k_y^2 \bar{V}_y^2$  and the formula gives unity. Then the angle of whole reflection in the acoustically less dense first medium is determined by the expression,

$$\sin \theta_{\max} = \frac{V_z}{\sqrt{V_z^2 + \bar{V}_y^2 - V_y^2}} \quad (1.39)$$

Waves from medium-1 that have the incidence angle bigger than  $\theta_{\max}$ , lose extending character and become damping after the transfer into the acoustically less dense medium-2. Wave vectors become complex  $\bar{k}_z \rightarrow i\bar{k}_z$  and trigonometric functions in (1.32) become hyperbolic. In the case under study,  $\theta_{\max}$  equals 1.22. The upper part of the frequency-angle diagram was calculated by (1.35) over a wide frequency range. The obtained results show that hypersound bands passing into the whole reflection range degenerate into narrow lines separated by relatively wide gaps.

It is worthwhile to note a difference between sound waves and EM waves in periodic structures that appears in the immediate vicinity of the BC - the boundary microscopic structure parameters in case of hypersound. The other circumstance is the principal presence of anisotropy in the sound wave equation for all vibration branches and all lattice types. In a certain sense, the wave mechanics of hypersound is the theory of spatially dispersed waves in anisotropic media [15]. Another peculiar property of sound waves in



separated structures is the absence of exit waves when all solutions have the characteristics of standing waves.

### 1.3.3d. Summary

The developed simple model of vibrational dynamics of “bulk” flat and closed carbon and boron-nitride (BN) nanostructures allows immediate transition to the boundary condition problem for sound of small wavelengths in tailored nets. As for the existence of flat carbon or BN systems, we predict that they are geometrically stable and may bridge the inter-electrode space in a strong external electric field. The reason is that negative charging accompanies the process of structure adsorption onto the cathode surface. The affinity electrons captured by the net may prevent its rolling up. The linear approximation used here gives a possibility to consider the vibrations of terahertz frequencies in low-dimensional molecular nets separate from other types of sound. All vibrational branches,  $z$ ,  $\phi$  and  $\rho$ , obey BC of the same view. The first two branches are mutually complementary for zigzag and armchair nanotubes [13, 16]. The third branch, called the radial mode  $\rho$ , is a slow elastic wave compared with other branches. A bandwidth value of phase velocity  $V_\rho = a \cdot \Delta \rho / \pi$ , found from radial frequency, is more than twenty times less (0.85km/s) than for the  $z$ -branch. The radial branch of vibrations plays a main role in heat transport but does not participate in sound energy transport.

Hypersound accompanies fast processes that occur in molecular nets during the passing of an electric current - the capture of an electron from the external medium, interaction with high energy particles and photons. On the other hand, sound irradiation in such processes may be used as the grounds for particle detecting. The periodical structures considered possess non-trivial frequency band structure for hypersound that allows us to raise the sensitivity of detection. Comparatively slow processes of adsorption also influence the hypersound band structure because adsorption bonds modify host atomic dynamics. The possible adsorption manifestation is the appearance of local states accompanied by a shape transformation of bands. If the adsorption occurs in a mixed gaseous media, each of the gas components matches the individual kind of local hypersound states. This may serve as a tag for sensor devices.

### 1.3.4. Conclusions

- The PQDM proposed is able to describe complex interdependent phenomena in open and closed molecular nets: phonon structure, phonon-phonon interaction, statistics, kinetics and irradiation.
- Our arguments based on PQDM put in the forefront the eigenstates of weakly bounded captured phonons participating in heat energy transport through the molecular bridges.
- Our theoretical approach explains the nature of extremely good thermal conductivity in carbon and carbon-like materials by the existence of the soft vibration branch (low frequency  $\rho$ -branch of phonons with high DOS at thermal energies) accompanied by structure hardness (high frequency  $\phi$ - and  $z$ -branches) providing large mean free path for phonons. We conclude that the radial mode contribution to heat transfer



is dominating in the temperature interval under consideration with the supposition that the phonon-phonon interaction constant  $G_0$  participating in the end atoms constants  $G_H$  does not depend on the phonon type ( $\rho$ ,  $\phi$  or  $z$ ). Then,  $\rho$ -vibrations essentially prevail due to the large density of states in narrow low-frequency  $\rho$ -band compared with the DOS for  $\phi$ - and  $z$ -vibrations. So, at actual temperatures  $\rho$ -branch of phonons determines heat propagation through the single-walled nanotube.

- Our results are in accordance with experiments for suspensions by David Cahill et.al (Letters, (Oct. 2003))

If we add new layers or new walls to single-walled NT, it makes the radial  $\rho$ -branch of vibrations harder (see Fig.1.5). This causes the sharp decrease in phonon density of states at the same phonon mean free path. The phonons leave the active thermal zone and heat conductivity decreases. Therefore, atomic monolayers and isolated single-walled nanotubes have to be the best thermal conductors. If we unite SWNT into the tight bundles, the radial mode quenches due to new inter-tube bonds arising. PQDM approach predicts the sufficient worsening of thermal conductivity in SWNT tight bundles compared with free SWNT. The method of thermal conductivity enhancement in this case is “dissolving” of inter-tubes bonds and turning out the tight bundles into the system of almost free tubes.

Intercalation may be a good way to do this “dissolving” of existing Van der Waals interaction inside bundles. From F.R.Gamble et.al. (Science, 168,568(1970)), the distance between atomic layers increases more than ten times after intercalation by organic molecules. For our case it is enough to increase inter-SWNT distances three or more times and we will obtain a really significant increase in thermal conductivity.

Our proposition is to modify the experimental technique of preparing NT bundles and accompany it by intercalation. Intercalation conserves the large density of states (DOS) of acoustic (radial) phonons in the actual temperature range of frequencies. Our results show that the dominating contribution is from radial (breathing and bending) vibrational degrees of freedoms. Maybe only bending modes are important it is not possible to tell with certainty because all the degrees are present in a common sum. This we will hopefully clarify soon.

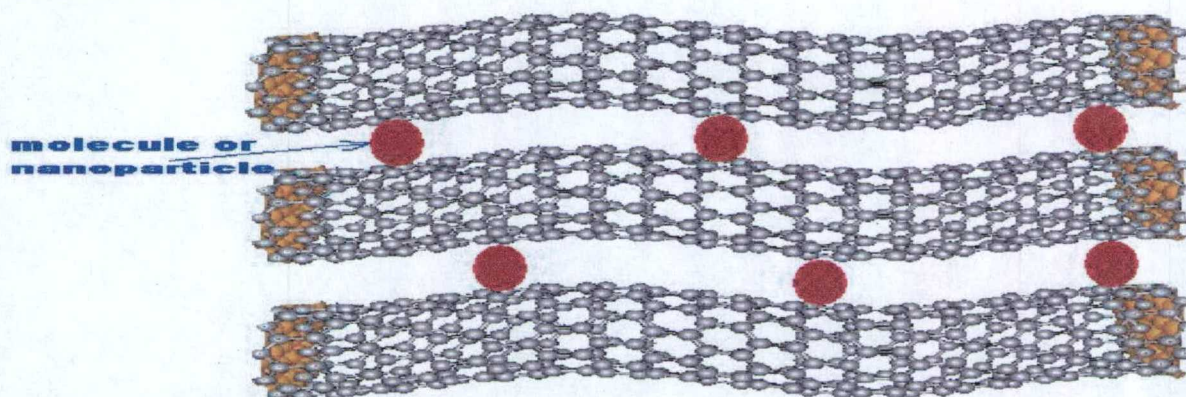


**Fig.1.16:** A nanotube bundle intercalated by organic molecules or nanoparticles. Intercalation conserves big acoustic (radial) phonon DOS in actual temperature range of frequencies. The distance in 10 or more Angstroms will be enough to switch on radial acoustic phonons for thermal conductivity



We also considered temperature dependencies for thermal coefficient in the entire temperature range and investigate size effects for graphene and tubulene bridges. We studied the transfer of vibration waves through the contact of differing carbon nets and nanometer sound wave interference in periodically alternating 1D or 2D molecular nets of two types. Boundary conditions for hypersound in tailored molecular nets are obtained ab initio by an averaging procedure. The intrinsic problem of vibron eigenstates is calculated for carbon net periodic structures. It is shown that hypersound standing wave frequencies are grouped into typical bands divided by frequency gaps. The whole intrinsic reflection effects are considered. In both cases the boundaries between cross-linked fragments lay in the plane perpendicular to z-axes.

### 1.3.5. References

- [1] D.G.Cahill, W.K. Ford, K.E.Goodson; G.D.Mahan, A.Majuindar; H.J.Maris, R.Merlin, S.R.Philpott. *J.Appl.Phys.*, 93(2), 793 (2003).
- [2] M.Born, K.Xuang Dynamical Theory of Crystal Lattice. London: Oxford Univ.Press, 1954; A.I.Anselm, Vvedenie v teoriju poluprovodnikov., M.: Nauka, 1978
- [3] C.E.Bottani. *NATO Science Series*, 24,149 (2001)
- [4] T. Ebessen, *Physics Today*, 6 , 26 (1996); A.Rubio, J.L.Corkill,, M.Cohen, *Phys.Rev.* B49, 5081 (1994)
- [5] J. Yu, R. K. Kalia, P. Vashishta, *Chem. Phys.* 103, 15, 6697 (1995)
- [6] Zh.Liu, Zh.Zhang,Q.Jang, D.Tian. *J.Phys.Condens.Matter*, 4, 6334 (1992)
- [7] N.G.Chopra, A.Zettl. *Sol.St.Comm.* 105, 297 (1998); J.Hone, M.Whitney, C.Piscoti, and A.Zettl. *Phys.Rev.* B59, R2514 (2001).
- [8] Yu.Maniwa et.al. *Phys.Rev.* B64, 241402 (2002)
- [9] L.M.Brekhovskikh, O.A.Godin. Acoustics of layered media. M: Nauka, 1989; J.Taker and V.Rampson. Hypersound in Condensed Matter Physics. M.:Nauka, 1975
- [10] UTAM Symposium on Mechanical and Electromagnetic Waves in Structured Media, Edited by R.C. McPhedran, L.C.Botten, and N.A Nicorovici. Kluwer Academic Publishers, Dordrecht, The Netherlands, 2001. Annual APS March Meeting 2003, March 3-7, 2003;Austin Convention Center; Austin, TX,USA.
- [11] E.Ya.Glushko, S.L.Legusha, A.A.Zakhidov, *Proc. of the SPIE*. 5065, 97-107 (2002).
- [12] E.Ya.Glushko, V.N.Khrisanov, *Low Temp.Phys.* 23, 910 (1997); E.Ya.Glushko, *Low Temp.Phys.* 26, 1130 (2000).
- [13] E.Ya.Glushko, V.N.Evteev, M.V.Moiseenko, N.L.Slusarenko, and A.A.Zakhidov. Annual APS March Meeting 2003, March 3-7, 2003;Austin Convention Center; Austin, TX,USA. Quantum model of phonon transport and heat conductivity in carbon nanoclusters and nanotubes, S26-016
- [14] E.Ya.Glushko, S.L.Legusha, *Proc. of the SPIE*. 5065, 47-53 (2002)
- [15] V.M.Agranovich and V.L.Ginzburg, The Crystal Optics of Media with Spatial Dispersion. M.:Nauka, 1979.



## Chapter 2: SYNTHESIS OF NANOSTRUCTURES

### 2.1 Synthesis of Zeolite Encapsulated Nanotubes

Considerable progress has been made in the synthesis of multi-walled and single-walled carbon nanotubes (SWCNT) by catalytic chemical vapor deposition (CVD) techniques. However, a typical preparation may result in a complex mixture of nanotube sizes and types. Between 1 and 3 nm in diameter there are 403 possible structures alone. To prepare one size and a single type of carbon nanotube remains a challenge. There are only 3 possible structures ((5,0), (4,2), (3,3)) for the  $0.40 \pm 0.01$  SWCNT, compared with the 403. To prepare such small diameter SWCNTs, one might employ a matrix to control the size during synthesis. It was reported that mono-sized (0.4nm) single-wall carbon nanotubes (SWCNTs) can be formed in the channels of large single crystal  $\text{AlPO}_4\text{-5}$  by pyrolysis of the organic template, tripropylamine (TPA), without any other external carbon source [Tang et al, Appl. Phys. Lett., 73 (1998), 2287].

We have now prepared single-wall carbon nanotubes in the channels of UTD-1, UTD-18 and UTD-12 (shown below) which are structurally related zeolites having one-dimensional channels that run in parallel. All of these zeolites are made using various cobalticinium ions. The thermal decomposition of these organometallic templates results in cobalt catalyst as well as a carbon source for making carbon nanotubes. The dimensions of the pores dictate the size of the resulting nanotubes such that we can systematically vary the CNT diameter by using the 10, 12 or 14 MR structures.

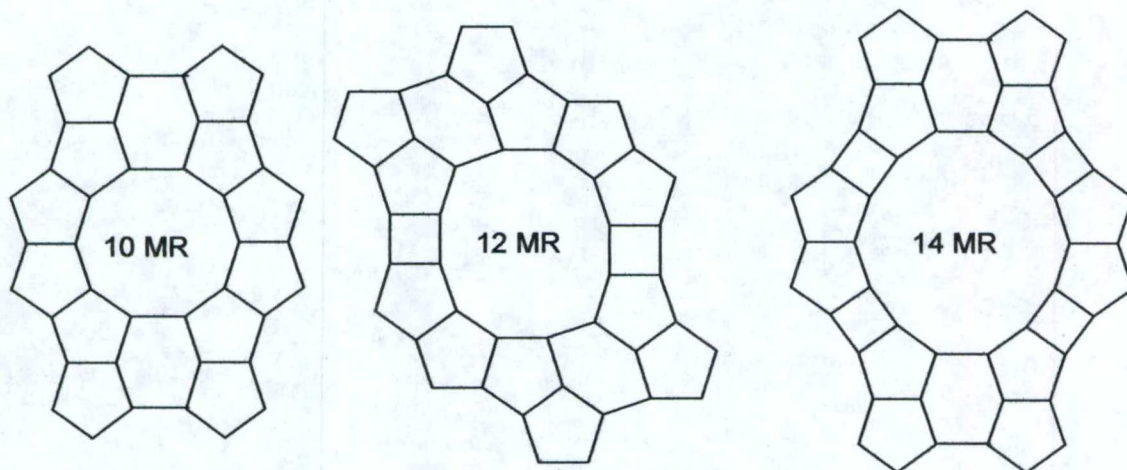


Fig. 2.1: 10, 12 or 14 MR structures

Fig. 2.2 shows the typical Raman spectra of the as synthesized UTD-1 (bottom - black) and the SWCNTs recovered after HF treatment of the UTD-1 crystals (top - purple). The Raman spectrum of the as synthesized UTD-1 shows characteristic Raman-active modes of  $\text{CH}_3$  symmetric stretching ( $2912\text{ cm}^{-1}$ ), the  $\text{CH}_3$  anti-symmetric deformation ( $1430\text{ cm}^{-1}$ ),  $\text{C}=\text{C}$  stretching ( $1650\text{ cm}^{-1}$ ) and the symmetric metal-ring stretching vibration ( $365\text{ cm}^{-1}$ ) of  $\text{Cp}^*_2\text{Co}^+$  molecules. When the sample is pyrolyzed at  $800^\circ\text{C}$  for 5 hrs and then HF treated, new Raman peaks appeared at  $1600\text{ cm}^{-1}$  and  $432\text{ cm}^{-1}$  (shown in Figure 2 top purple). The



strongest low-frequency Raman mode at  $432\text{ cm}^{-1}$  is expected to be the radial breathing  $A_{1g}$  mode. The radial breathing  $A_{1g}$  mode is not sensitive to nanotube structure but to the nanotube radius. The observed frequency of  $432\text{ cm}^{-1}$  indicates the radius of the carbon nanotube is  $0.54\text{ nm}$ .

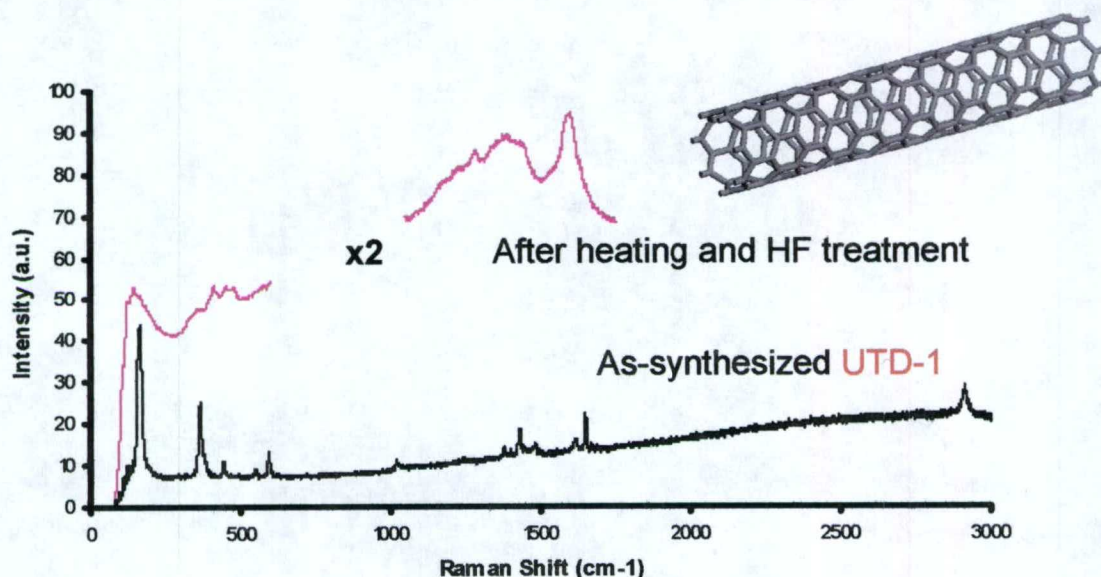


Fig.2.2: typical Raman spectra of as synthesized UTD-1 and SWCNTs recovered after HF treatment of the UTD-1 crystals

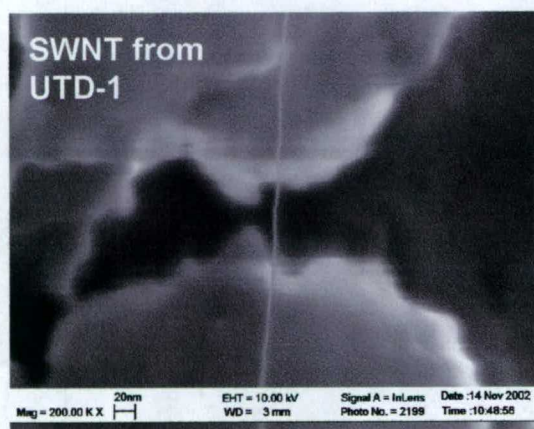


Fig.2.3: SEM image of a SWCNT obtained after HF treatment of calcined UTD-1

Fig. 2.3 shows the SEM image of a SWCNT obtained after HF treatment of calcined UTD-1. It shows the size of the carbon nanotube is less than  $1\text{ nm}$  and at least  $500\text{ nm}$  long, consistent with the Raman spectrum. The SEM results also indicate that the SWCNTs prepared in the UTD-1 channels are stable without the silica matrix. A high resolution TEM image of the SWCNTs recovered from UTD-1 is shown in Fig.2.5. From this image an estimate of the nanotube diameter is  $\sim 0.5\text{ nm}$ . The exact type of carbon nanotube prepared in



UTD-1 is uncertain but possible nanotubes might be the (4,4)-0.54nm, (7,0)-5.5nm and the (5,3)-0.55nm.

Zeolite UTD-18 is structurally related to SSZ-31 (polymorph C) which is comprised of elliptical 12 MR pores with dimensions of  $8.6 \times 5.7 \text{ \AA}$ . Fig. 2.4 shows the typical Raman spectra of the as synthesized UTD-18 (bottom - black) and the SWCNTs recovered after HF treatment of UTD-18 (top - purple). The Raman spectrum of the as synthesized UTD-18 shows characteristic Raman-active modes of C=C stretching ( $1650 \text{ cm}^{-1}$ ), the  $\text{CH}_3$  anti-symmetric deformation ( $1480 \text{ cm}^{-1}$ ),  $\text{CH}_2$  wag ( $1235 \text{ cm}^{-1}$ ) and twist ( $1211 \text{ cm}^{-1}$ ), C-H in phase bending ( $1052 \text{ cm}^{-1}$ ) and out-of-plane bending ( $849 \text{ cm}^{-1}$ ) and the symmetric metal-ring stretching vibration ( $332 \text{ cm}^{-1}$ ) of the  $(\text{EtCp})_2\text{Co}^+$  template molecules. When the zeolite is heated at  $800^\circ\text{C}$  for 5 hrs followed by HF treatment, new Raman peaks appear at  $1606 \text{ cm}^{-1}$  and  $445 \text{ cm}^{-1}$  (shown in Fig.2.7 top purple). The strongest low-frequency Raman mode at  $445 \text{ cm}^{-1}$  is expected to be the radial breathing  $\text{A}_{1g}$  mode. The observed frequency of  $445 \text{ cm}^{-1}$  indicates the radius of the carbon nanotube is  $\sim 0.52 \text{ nm}$ . The higher frequency radial breathing mode and smaller SWCNT diameter compared with UTD-1 is consistent with the smaller pore size of UTD-18. Fig.2.6 shows the SWNTs recovered from UTD-18.

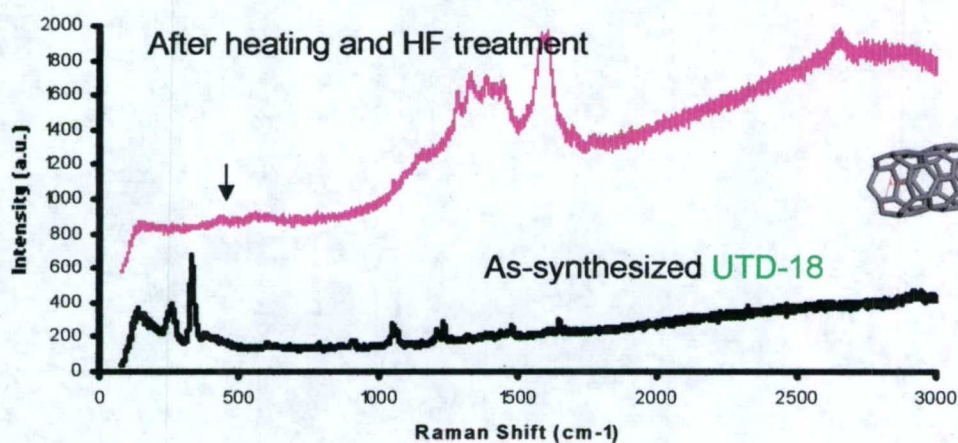


Fig.2.4: Typical Raman spectra of the as synthesized UTD-18 (black) and the SWCNTs recovered after HF treatment of UTD-18 (purple)





**Fig.2.5: SWNT recovered from UTD-1**



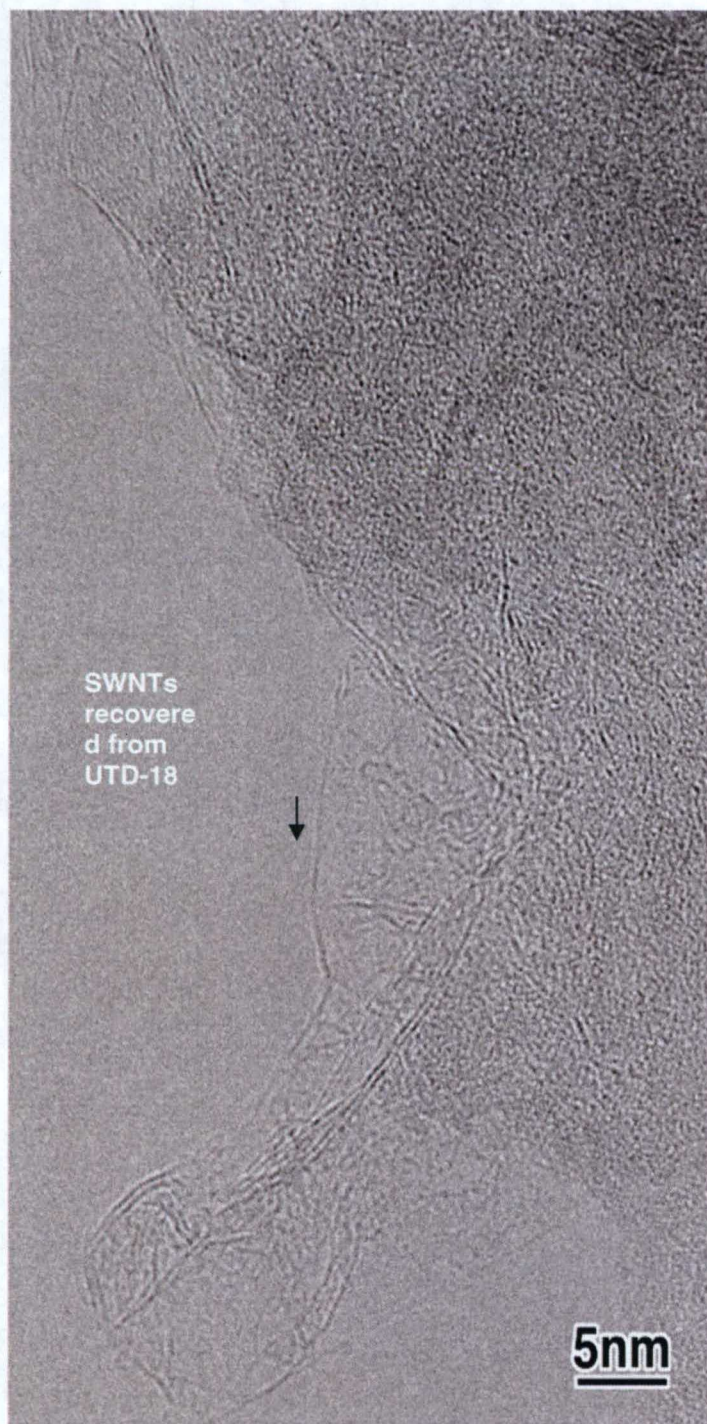
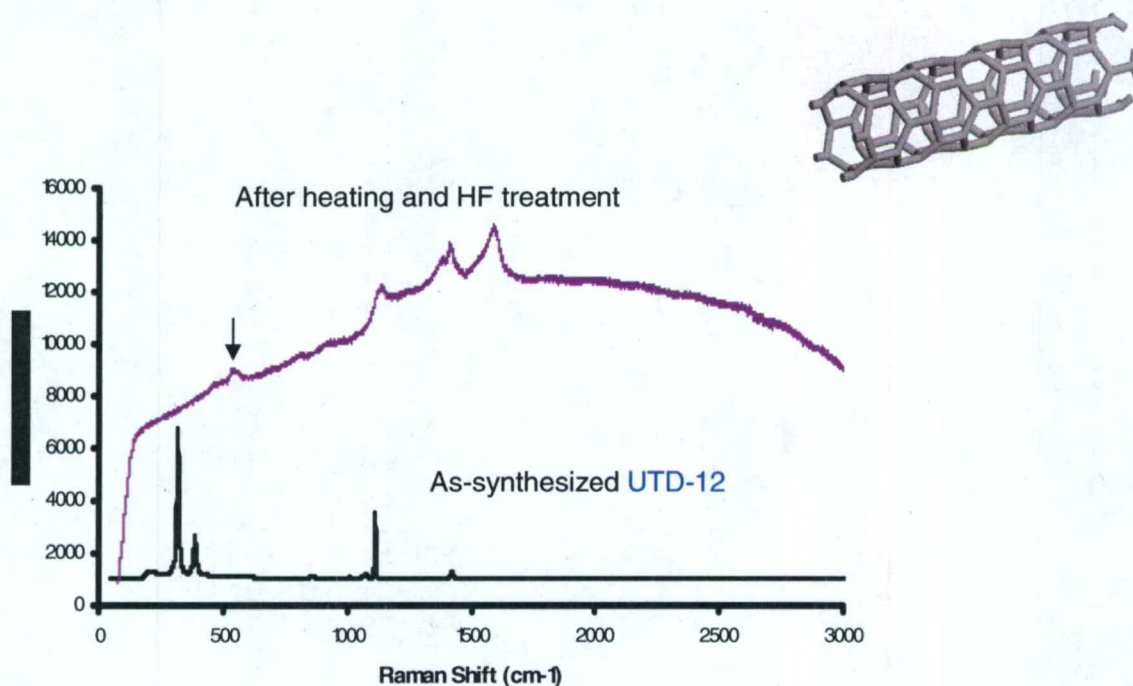


Fig.2.6: SWNTs recovered from UTD-18

Zeolite UTD-12, closely related to ZSM-48, possesses non-interpenetrating linear channels defined by 10 membered rings having dimensions of  $5.3 \times 5.6 \text{ \AA}$ . Fig. 2.7 shows the typical Raman spectra of as synthesized UTD-12 (bottom - black) and the SWCNTs recovered from UTD-12 after HF treatment (top - purple). The Raman spectrum of the as synthesized UTD-12 shows the characteristic Raman-active modes of C-C stretching ( $1421\text{cm}^{-1}$ ), the C-C ring breath ( $1113\text{cm}^{-1}$ ), C-H in-phase bending ( $1069\text{cm}^{-1}$ ) and C-H out-



of-plane bending ( $849\text{cm}^{-1}$ ), the symmetric metal-ring vibration ( $318\text{cm}^{-1}$ ) and the ring deformation ( $385\text{cm}^{-1}$ ) of the  $\text{Cp}_2\text{Co}^+$  template molecules [30]. When the sample is pyrolyzed at  $800^\circ\text{C}$  for 5 hrs followed by HF treatment, new Raman peaks appeared at  $1597\text{cm}^{-1}$  and  $559\text{cm}^{-1}$  (shown in Fig.2.7 top purple). The strongest low-frequency Raman mode at  $559\text{cm}^{-1}$  is expected to be the radial breathing  $A_{1g}$  mode. The observed frequency of  $559\text{cm}^{-1}$  indicates the radius of the carbon nanotube is 0.41 nm. This could very well be the smallest carbon nanotube ever made.



**Fig.2.7** typical Raman spectra of as synthesized UTD-12 (black) and the SWCNTs recovered from UTD-12 after HF treatment (purple)



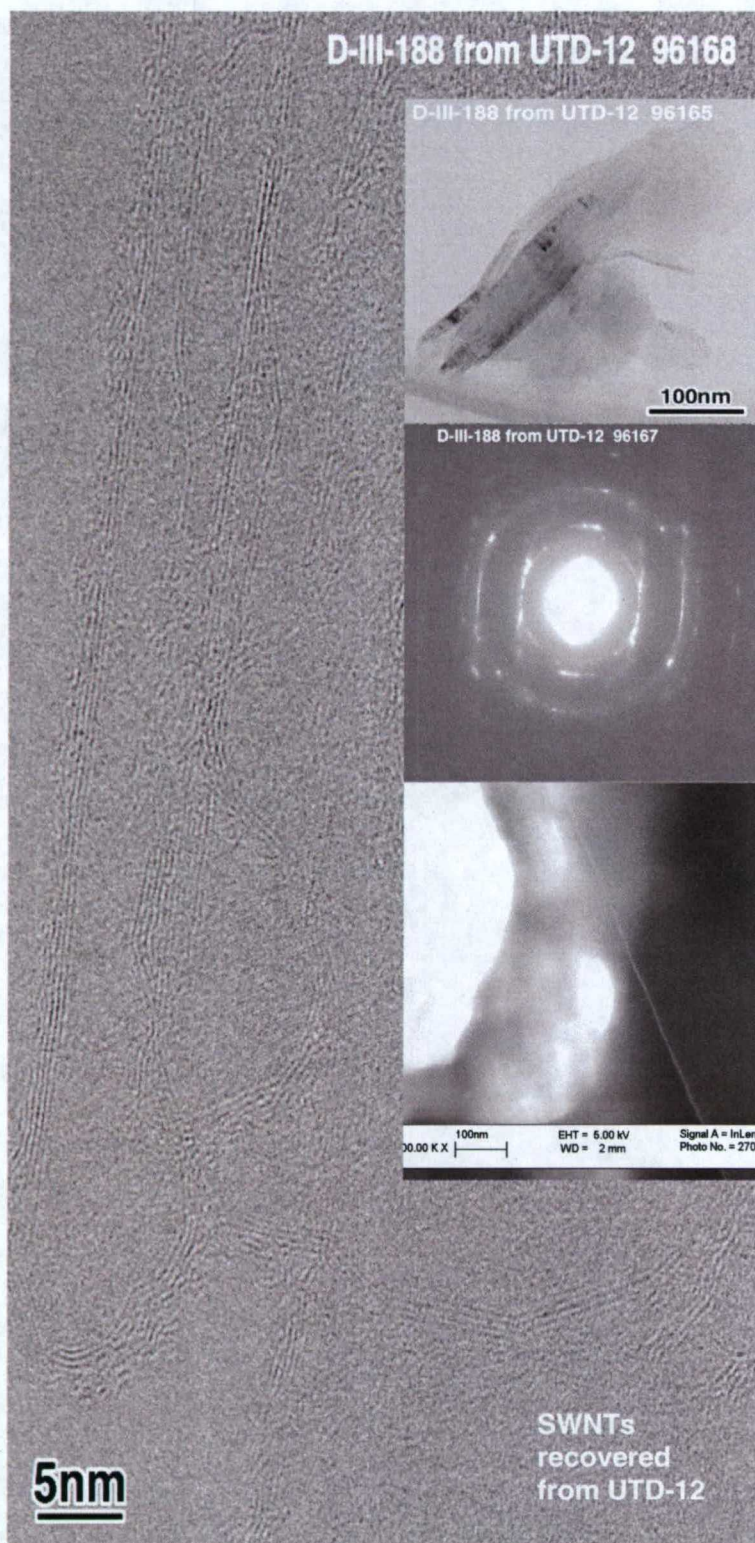


Fig.2.8: SWNTs recovered from UTD-12

CNTs this small may be metallic and superconducting. Preliminary magnetic susceptibility  $\chi T$ -dependence measurement of the UTD-12 (with SWCNTs) after HF treatment is shown below. Some of the unusual magnetic properties of the SWCNTs obtained



in the UTD-12 channels may be due to residual Co. However, there may be some evidence of superconductivity.

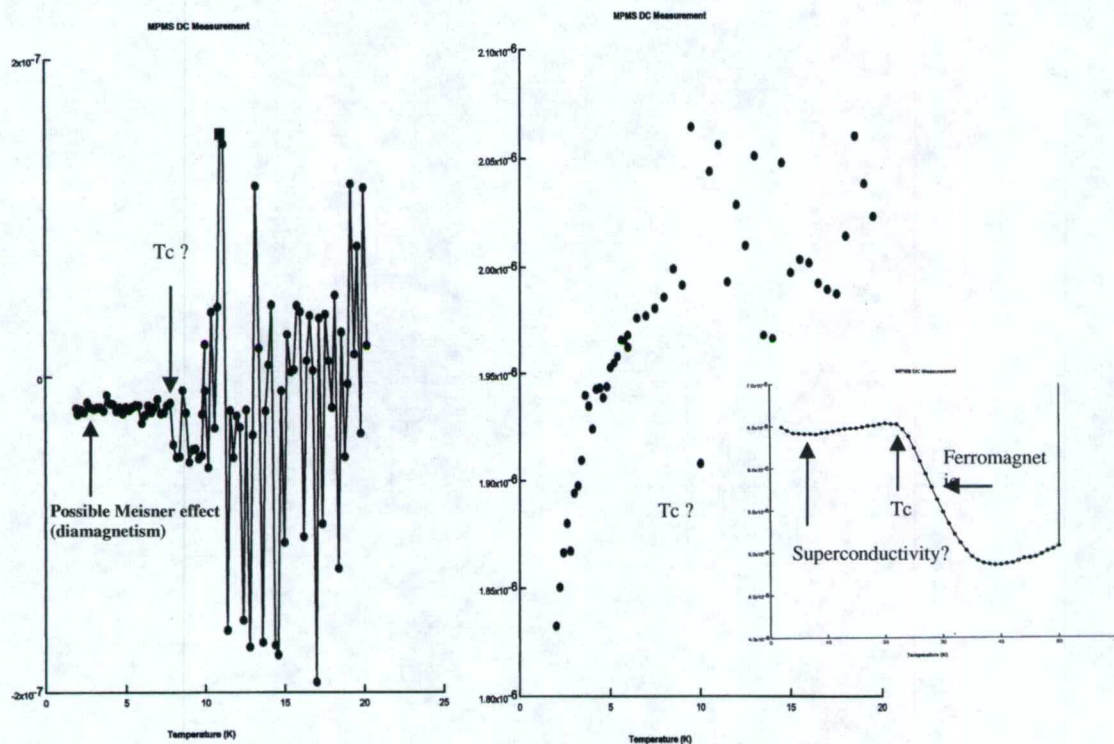


Fig.2.9

## Publications

Deng, S.; Dalton, A.; Terasaki, O.; Balkus, Jr., K.J., "Carbon Nanotubes Synthesized in Zeolites UTD-1, UTD-18 and UTD-12" *Proc. 14<sup>th</sup> Int. Zeolite Conf.* 2004, 903-910

Deng, S.; Dalton, A.; Terasaki, O.; Balkus, Jr., K.J., "Carbon Nanotubes Synthesized in Zeolites UTD-1, UTD-18 and UTD-12" *Stud. Surf. Sci. Catal.* 2004, 154.

An additional paper incorporating magnetic susceptibility data and synthesis variations is possible.

## Presentations

14<sup>th</sup> International . Zeolite Conference

2003 SPRING Conference



## 2.2 Synthesis of Conjugated Polymer-CNT Complexes

Poor heat dissipation in organic and polymeric electronic devices is a key problem that limits their performance at high current loading. It is known that addition of quite small amounts of nanotubes can improve the performance of organic devices, apparently due to improved heat dissipation via the nanotube component.

Various CNT-CNT interactions that can compromise the spectacular thermal conductivity properties of individual CNTs are shown in Fig. 2.10(a). The focus of this effort was to create new types of donor (acceptor) polymers, which could provide better unbundling of CNTs (Fig. 2.10(b)) to enhance dissipation of the heat generated in polymeric devices such as OLEDs or solar cells.

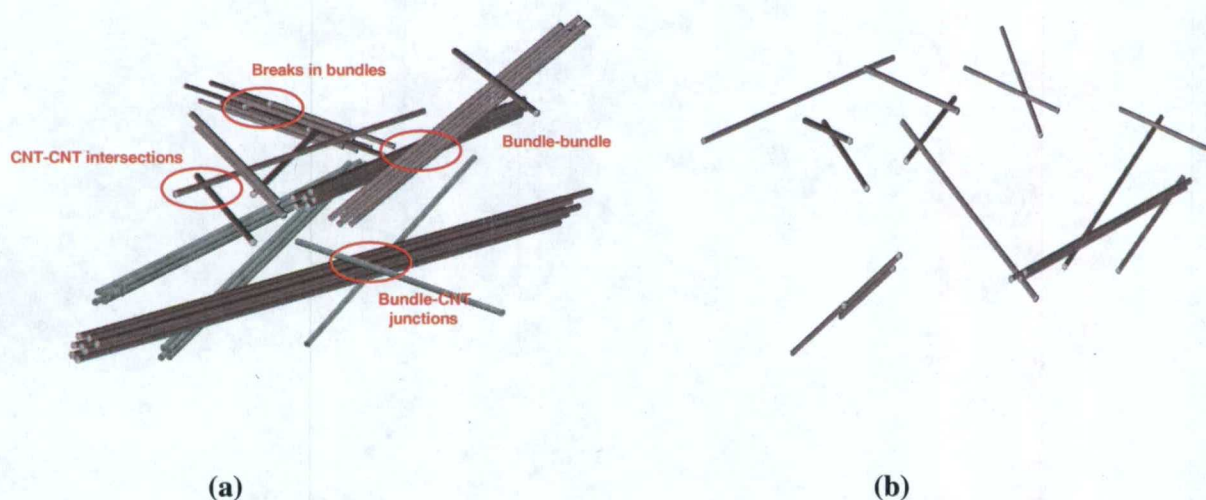


Fig. 2.10: Representative CNT-CNT interactions that compromise high thermal conductivity of CNTs (a), and reduction of these effects due to unbundling (b).

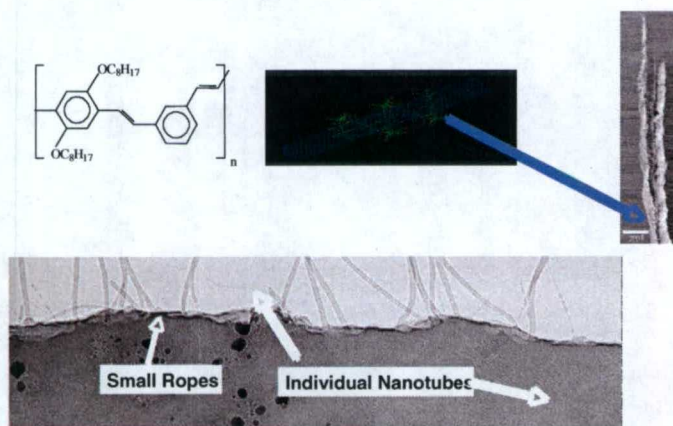
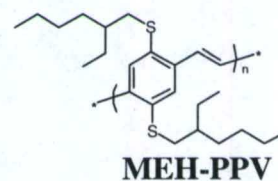
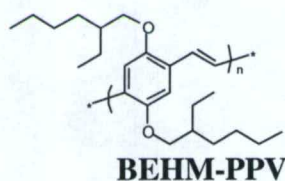
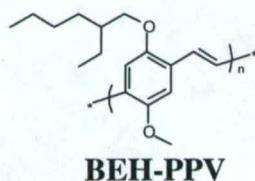


Fig.2.11: Bundle exfoliation using conjugated polymers

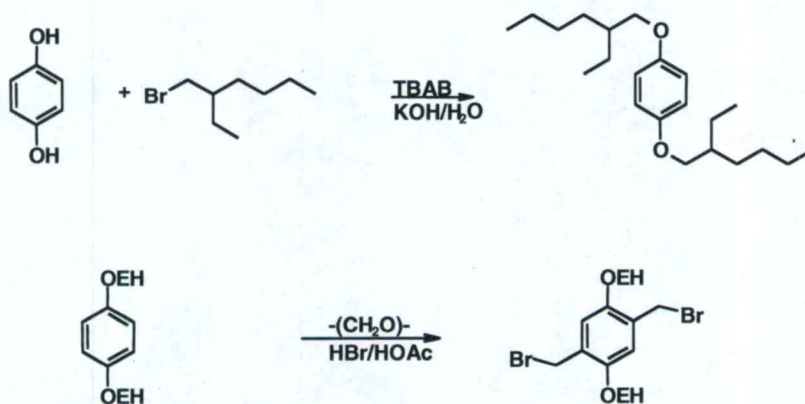


Several types of debundling polymer systems are known. Fig. 2.11 shows that CNTs can be effectively debundled using a phenylene-vinylene (PPV) conjugated polymer. Conjugated polymers (CP) afford the additional opportunity to introduce charge transfer to enhance CP-CNT interactions that can be “tuned” by polymer design.

Several PPV-derivatives were synthesized to determine their abilities to debundle CNTs with the goal toward enhancing thermal conductivities in CP-CNT composites. The well-studied MEH-PPV was prepared according to literature procedures and used as a reference material for the composites. The molecular weights of the samples used were 292,000 (Mn) with a polydispersity of 1.04 and 281,000 (Mn) with a polydispersity of <1.2.



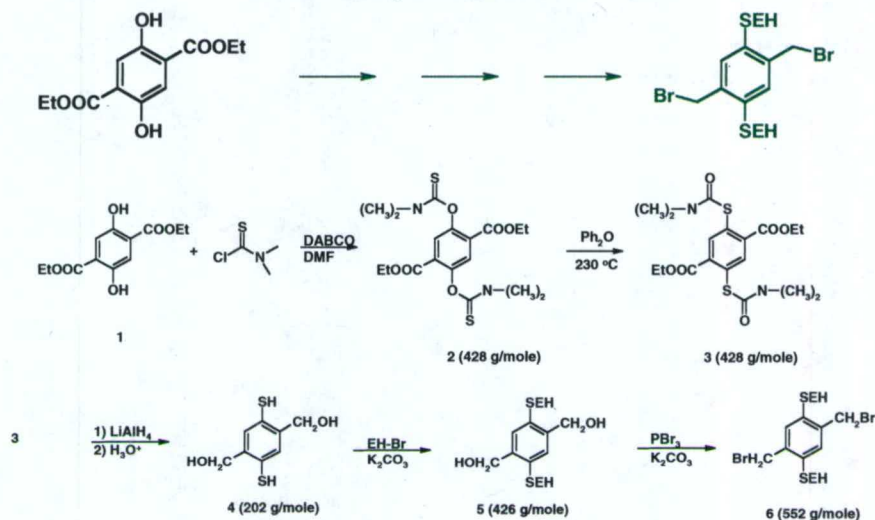
### Bis-ethylhexyloxy-PPV precursor Synthesis



BEH-PPV precursor monomer synthesis



## Bis-ethylhexylmercapto-PPV precursor Synthesis



### BEHM-PPV precursor monomer synthesis

Fig. 2.11

The composites were prepared using the following protocol. SWNTs were added to a solution of MEHPPV (or other CP) in THF or  $\text{CHCl}_3$ . The resulting suspension was stirred overnight and allowed to settle. The supernatant was then decanted and the composite film was obtained by rotary-evaporation of the solvent.



Fig. 2.12: The dramatic effect of adding SWNT to MEH-PPV (or BEH-PPV) can be seen from the accompanying figure. The pure polymer produces clear red films while the composite films exhibit a blue-green metallic sheen.



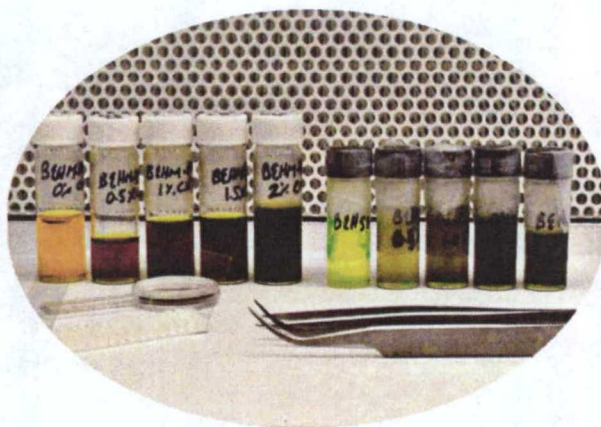


**Fig. 2.13:** Shows the solutions of BEHM-PPV mixed with SWNT in different concentrations. SEM images of several composite film compositions are shown below



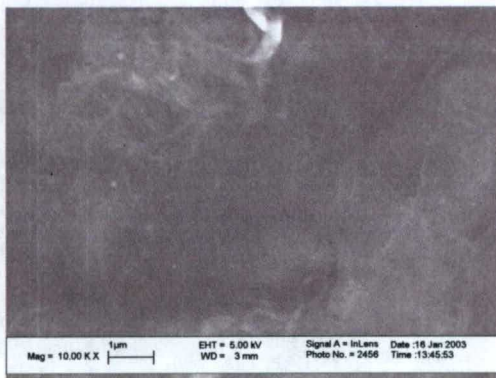
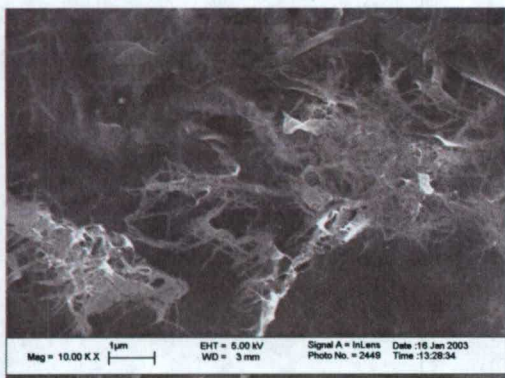


**Fig. 2.14: Dispersion of 1% SWNT in MEH-PPV. Note non-uniformity**

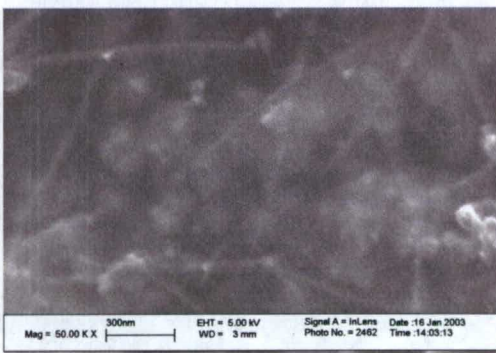
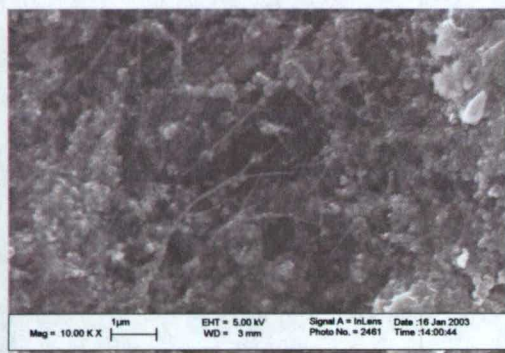
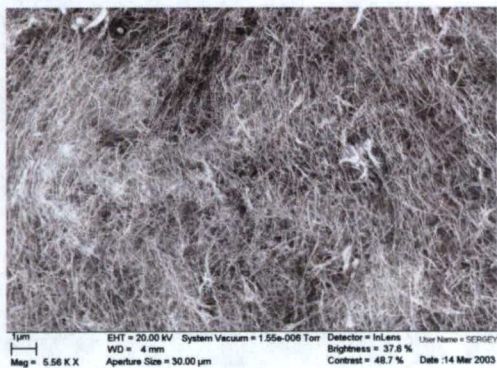
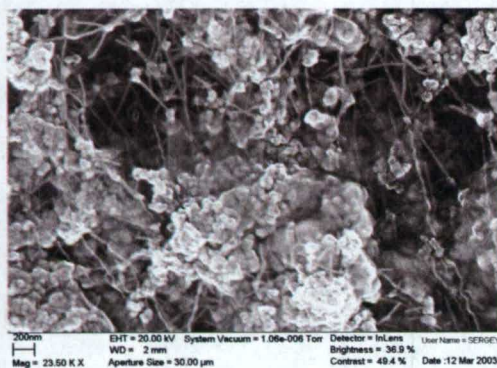


**Fig. 2.15: Dispersion of 5% SWNT in MEH-PPV. Note non-uniformity**



**MEH-PPV**

**BEHM-PPV**

**Fig.2.16: Enhanced dispersion of 2% SWNT in BEHM-PPV compared to 5% MEH-PPV**



## MEH-PPV Composites

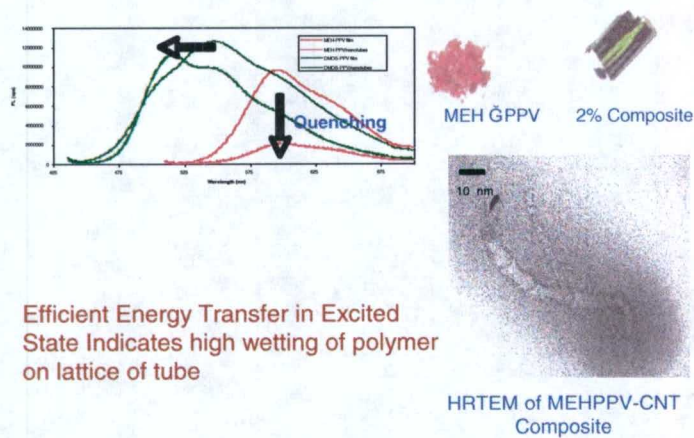


**Figure 2.17:** Even with modest dispersion of SWNT with MEH-PPV, the nanotubes are strongly wetted by the polymer composites as evidenced by the efficient energy transfer (quenching) in the excited state.

The hydrophobic SWNT mixed with MEH-PPV in chloroform solution gave rise to the agglomeration shown above in Fig. 2.16 (left). Better distribution of SWNT was obtained for BEHM-PPV polymer (Fig. 2.16, right). Strong anisotropy of  $\lambda(T)$  (Fig. 2.18) in MEH-PPV films mixed with SWNT indicates the in-plane distribution of nanotubes along the film.

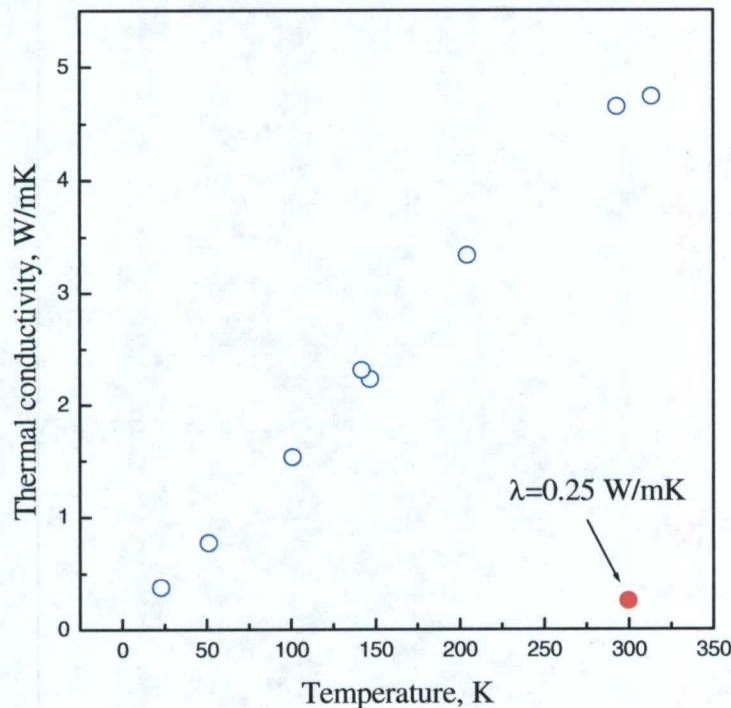


**Figure 2.18:** Temperature dependence of thermal conductivity of MEH-PPV conjugated polymer reinforced by 2% SWNT. Open circles show the heat flow along the film and solid circle corresponded to the thermal conductivity perpendicular to the film surface.



The concentration dependence of the thermal conductivity perpendicular to the MEH-PPV film surface is shown below (Figure 2.19). The considerable enhancement of the thermal conductivity is much below expectations, however, perhaps because of poor distribution of SWNT in MEH-PPV matrix.

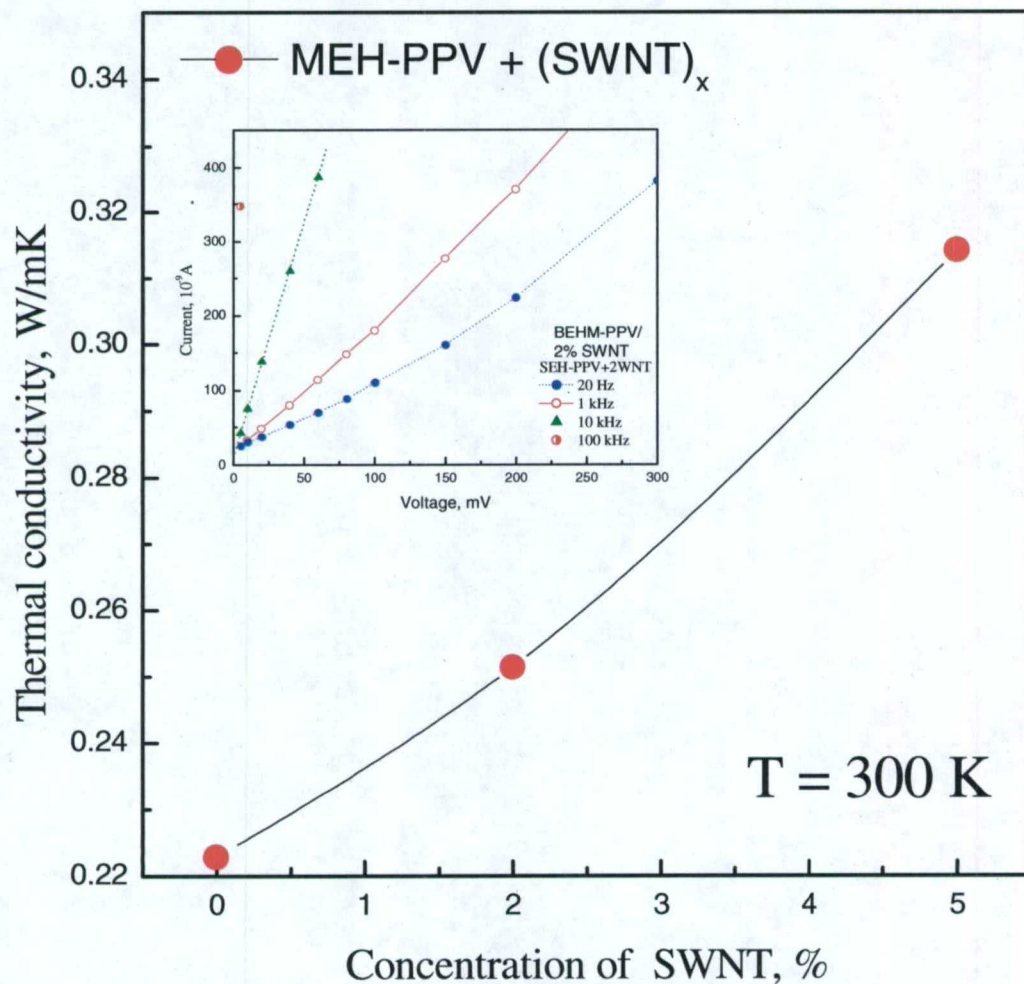


Fig. 2.19: Concentration dependence of thermal conductivity of MEH-PPV + SWNT composite. Insert shows the I-V curve for MEH-PPV + 2% SWNT composite.

The high frequency dependence of the electrical conductivity shown in the insert indicates the non-ohmic interconnection between carbon nanotubes. The agglomeration and non-ohmic contacts are the main reasons causing the low thermal conductivity of the studied composites.



### Chapter 3: CHARACTERIZATION AND OPTIMIZATION OF PHONON SPECTRA, THERMAL CONDUCTIVITY AND SUPERCONDUCTIVITY

#### 3.1. Thermal Conductivity Measurements on Nanocomposites with CNTs

##### 3.1.1. Comparative method in PPMS

To eliminate the heat losses through lead wires the comparative method was used for thermal conductivity measurements of thin CNT fibers and films. The PPMS (Quantum Design) Thermal Transport circuit was modified for the comparative method as shown in the schematic diagram below (Fig.3.1).

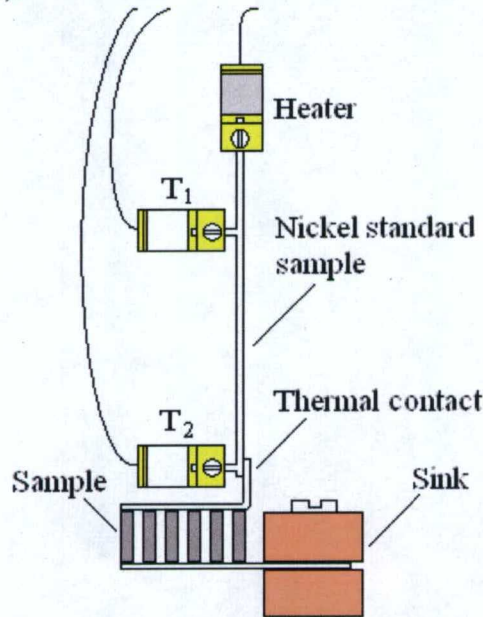


Fig.3.1: Schematic diagram of sample connection for comparative measurement of thermal conductivity using the nickel standard sample.

This method is a variation of the methodology commonly known as the cut-bar technique. In the cut-bar technique, a specimen of unknown thermal conductivity is sandwiched between two pieces of material with known thermal conductivity using a thermal grease and a pliable metal foil to eliminate interfacial thermal contact resistance between the materials. Thermocouples placed along the lengths of the three material pieces yield information on the rate of heat flow through the two reference-material sections of known conductivity. The heat-flow rate can then be used to determine thermal conductivity of the unknown specimen using the one-dimensional Fourier conduction equation:

$$Q = \lambda A \, dT/dx \quad (3.1)$$

where  $Q$  is the rate of heat flow,  $\lambda$  is the thermal conductivity,  $A$  is the cross-sectional area through which the heat flows, and  $dT/dx$  is the temperature gradient. Experimentally,  $dT$  is approximated by  $\Delta T$ , the finite temperature difference, and  $dx$  is approximated by  $\Delta x$ , the distance over which the temperature difference is measured.



In our measurement method, only one section of known material is used. Assuming that the heat flux through both samples and the Ni-standard is the same, the thermal conductivity of the unknown sample,  $\lambda_s$  can be calculated as:

$$Q_s = Q_R = \lambda_s A_s (\Delta T_s / L_s) = \lambda_R A_R (\Delta T_R / L_R). \quad (3.2)$$

$G = \lambda A / L$  is the sample conductance.

The thin SWNT fibers shown in Fig.3.2, in comparison with human hair, were arranged in parallel stack to enhance the sample conductance (see Fig.3.3). The fibers were glued to gold covered copper leads by silver filled epoxy H20E (EPO-TEK) [1]. The four probe assembly shown in Fig.3.3.

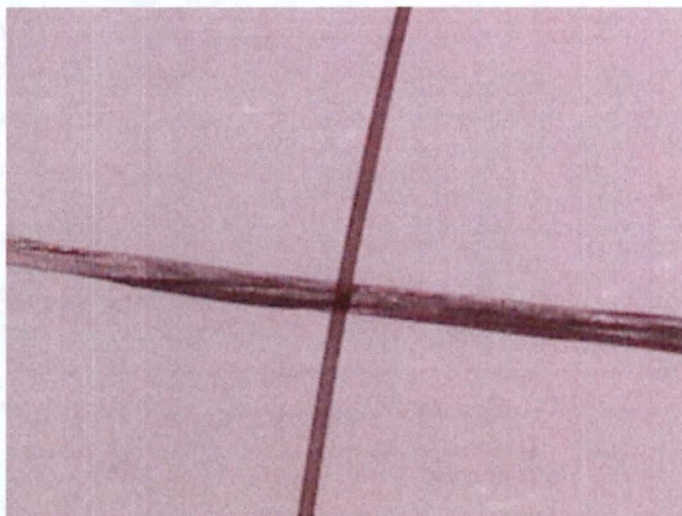


Fig.3.2: Bunch of 8 fibers prepared by coagulation method compared with human hair (vertical). The PVA polymer concentration in bunch is 35%

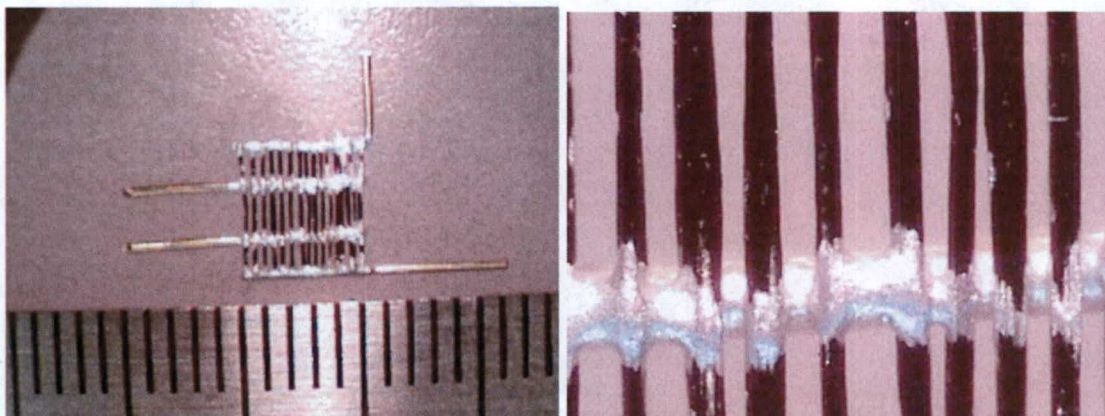


Fig.3.3: Four probe assembly of 16 fibers each comprising 8 fibers with 35% PVA.



## References

[1] M.J. Hodgin. Conductive Adhesives for Thermal Management; Case Study Issues in Hybrid Microelectronics and Plastic IC Packaging. Proc. Of 28<sup>th</sup> Annual new England IMAPS Conference, Boxborough, MA., May8, 2001.

### 3.1.2. Tunable thermal conductivity in carbon nanotube paper

Phonon transport in one-dimensional (1D) nanostructures such as carbon nanotubes has recently received a lot of attention. The very high thermal conductivity (10,000 W/m·K) predicted theoretically for single tubes [1,2] was not achieved experimentally. Due to the phonon-phonon interaction between carbon nanotubes, the measured thermal conductivity of a collection or a mat of carbon nanotubes was found to be much lower than predicted [3].

In disordered SWNT 'mat' samples, the room temperature thermal conductivity is only ~35 W/m·K [3]. However, in samples consisting of aligned SWNTs, the room-temperature thermal conductivity normalized to crystalline nanotube arrangement is above 200 W/m·K [4]. On the other hand, the thermal conductivity of a 14 nm diameter multiwall carbon nanotube (MWNT) measured by a microfabricated device [5] was about 3000 W/m·K at room temperature, which is in close agreement with the prediction value [1]. However the  $T^2$  temperature dependence suggests that MWNT behaves rather like a 2D system thermally. The very important result of this work, for our investigation, is a decrease in thermal conductivity with an increase in the number of nanotubes in the bundle: an 80 nm diameter MWNT bundle has the thermal conductivity of about ~1200 W/m·K, and a 200 nm diameter MWNT has about ~300 W/m·K respectively. The decrease mentioned above, compared to thermal conductivity in single nanotubes, is a consequence of a phonon-phonon interaction leading to the rise of umklapp processes between interconnected nanotubes in bundles or mats.

In this part of the project, we will show that charge injection in carbon nanotube bundles in bucky paper will decrease the phonon-phonon interaction between carbon nanotubes by increasing the nanotube separation as was predicted in theoretical part 1.

#### 3.1.2a Experiment

##### 1. *Techniques*

To measure the change in thermal conductivity, the laser flash method was chosen to measure the thermal diffusivity along a carbon nanotube paper. Thermal diffusivity  $D$  relate to the thermal conductivity  $\lambda$  by a simple equation,

$$\lambda = \rho \cdot C_v \cdot D, \quad (3.3)$$

where  $\rho$  is the density and  $C_v$  is the heat capacity.



The design of laser flash method is very appropriate for *in situ* measurements and  $D$  is the most sensitive parameter, in (3.3, to structural changes in medium with low heat capacity and density. A schematic view of the laser flash method used in this study is shown in Fig. 3.4.

A 135 mW IQ series laser module from Power Technology Inc., operated together with a build-in modulator or chopper (model SR540 with Chopper Controller), radiate a 2 mm diameter modulated beam with 830 nm wavelength. The laser beam is focused onto the sample with 50 mm focal length lens (or cylindrical lens for wide strip). The sample is mounted between two gold standoffs on a ceramic sink. The heated spot is adjustable so that it can be made occur at any position on the front surface of the prolonged specimen by using three-axis translation stages to move the sample holder (or the vacuum cryostat) together with the specimen. The periodic heating technique can provide two independent methods: frequency-variation method when the position of the heated spot is fixed just opposite to the sensing point and only the modulation frequency is changed and distance-variation method when the modulation frequency is fixed and the distance between the heated spot and the sensing point is changed. In the present study we are using distance-variation method.

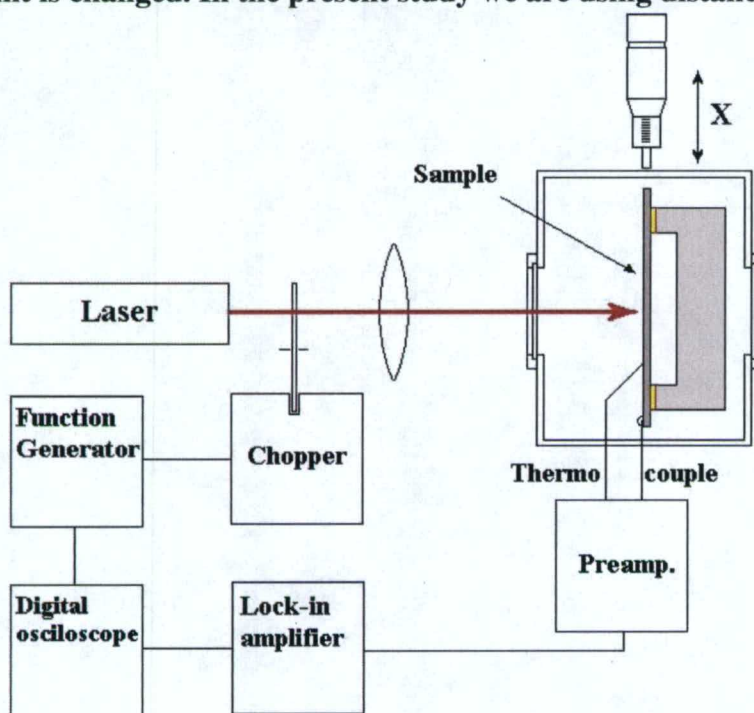


Fig.3.4: The instrumentation of laser flash technique used to measure the thermal diffusivity of SWNT bucky paper.

The measurements are made by changing the distance  $x$  between the fixed thermocouple tip and the laser spot in stationary conditions. This means that each measurement is done when the temperature distribution has reached its steady state and no dynamical problems arise. In our case, because of very thin and narrow bucky paper strip and very sharp thermocouple tip ( $d < 10 \mu\text{m}$ ), the relaxation time was less than 1s. To reduce the thermal inertia of thermocouple we used only one (constantan) wire with additional chemical treatment. The tip of  $75 \mu\text{m}$  constantan wire was etched by 50%  $\text{HNO}_3$  water



solution by dipping 1 mm end in solution for 1 min. The resulted tip diameter was less then 10 $\mu$ m. The other wire of thermocouple is the studied carbon nanotube strip.

The thermoelectrical signal from thermocouple constantan/carbon nanotube is amplified with Tektronix differential preamplifier ADA400A with tunable band. Then the resulted signal compared with reference signal from Agilent functional generator 33220A to obtain the phase delay between two periodic signals with the same frequency: heat source signal modulated with generator 33220A and signal of thermocouple tip outstanding on distance  $x$ . The phase delay is read from the display of lock-in amplifier SR540 and the magnitude of thermal signal from the two channel digital storage oscilloscope Tektronix TDS 2002.

If we have a periodic point heat source which liberates heat at the rate  $I_0 \exp(i\omega t)$ , the temperature on a line at distance  $x$  from the heated point is related to the temperature  $T(x=0)$  by

$$T(x) = T(0) \cdot \exp(-x/l_t) \quad (3.4)$$

where  $l_t$  is the thermal diffusion length. The ratio of the two moduli  $M$  of the thermal signals taken along the lines at  $x=0$  and  $x$  is

$$M(x)/M(0) = 2 \exp(-x/l_t), \text{ or } \ln \frac{M(x)}{M(0)} = \ln(2) - x\sqrt{\pi f / D} \quad (3.5)$$

and the phase  $\phi$  of the thermal signal on the distance  $x$  is  $\phi = -x(\pi f/D)^{1/2}$ , where  $f$  is the frequency of modulation of the laser beam intensity and  $D$  is the thermal diffusivity.

The calibration on the thin gold wire using phase shift measurement via distance shows very linear dependence and excellent agreement of thermal diffusivity,  $D=128.9 \text{ mm}^2/\text{s}$  with the data presented in the literature,  $D=130 \text{ mm}^2/\text{s}$ , [6]. However for CNT paper we have to take into account the high surface area and radiation losses.

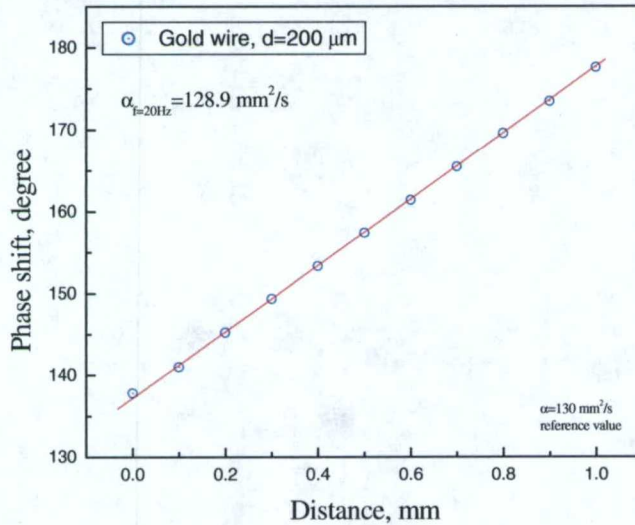


Fig.3.5: Phase shift of thermal signal chopped with the frequency 20 Hz as a function of offset between laser beam and thermocouple tip.

## 2. Charge Injection



Small diameter lithium or sodium ions seem to be ideal for ion insertion between nanotubes. 1M NaCl aqueous solution and platinum counter electrode was used to charge a thin bucky paper strip ( $20 \times 0.5 \times 0.035 \text{ mm}^3$ ) in chronoamperometry regime on CHI 660B Electrochemical Station. The positive ( $\text{Cl}^-$ ) or negative ( $\text{Na}^+$ ) charges with current 0.1 mA was applied to CWNT strip during 1h at 0.8V. Then the sample was washed in DI water and dried in vacuum during 4 h.

### 3. Results and discussion

#### a. HipCO:

First, we measured the thermal diffusivity of bucky paper consisting of HipCo SWNT. Fig.3.6 shows the phase shift of the thermal signal collected at different distances. To make sure that dipping in electrolyte solution and washing in DI water do not change the thermal properties of bucky paper, we first carried out the test measurement shown by green solid circles.

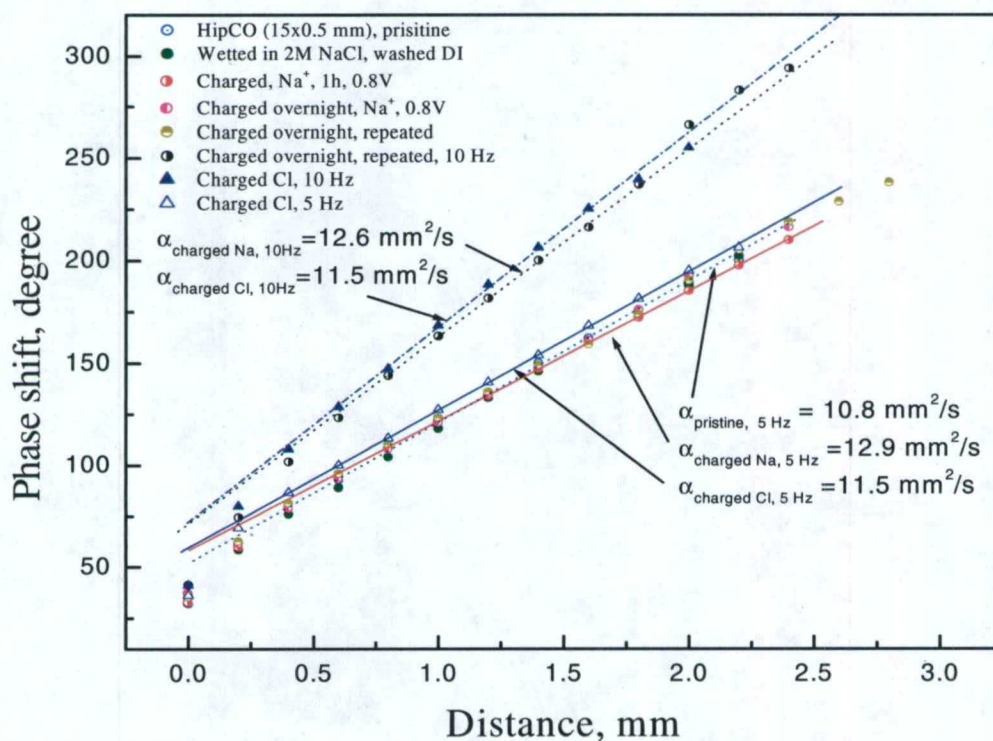


Fig.3.6: Thermal diffusivity of bucky-paper on the base of HiPCO SWNT.

#### b. Magnetically aligned bucky paper:

Magnetically aligned SWNT paper was obtained from National High Magnetic Field Laboratory in Florida, USA. SWNTs prepared by laser ablation technique at  $1100^\circ \text{C}$ , were purified and deposited by vacuum filtration from water suspension under high magnetic field, 17T.



To overcome the dominant role of contact resistance in SWNT bucky-paper, multiple attempts were made to align disordered bunches. It is supposed that increasing the paper density (and consequently contact surface area) and increasing the number of contacts in the alignment direction will increase the conductivity of the oriented paper significantly. Below, in Fig.3.7, the temperature dependence of resistivity for magnetically aligned “laser” SWNT bucky-paper is shown.

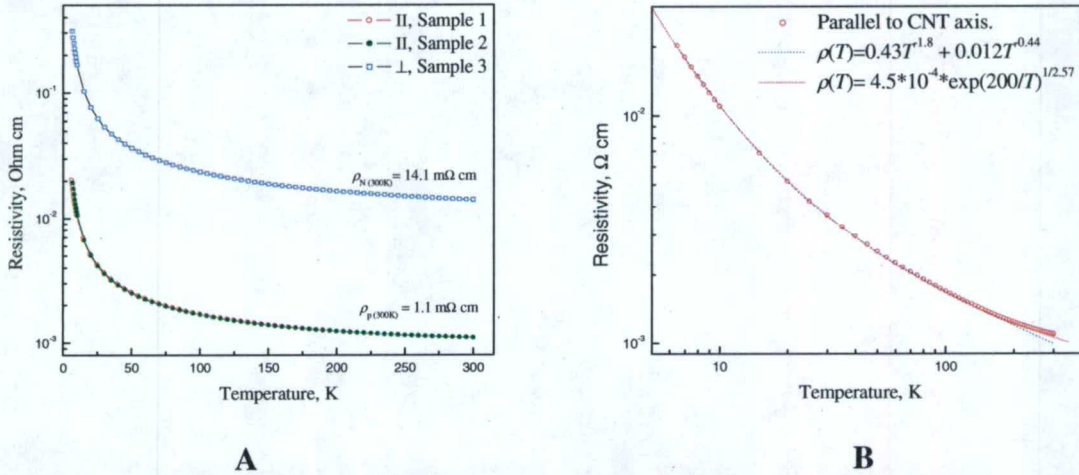


Fig.3.7: A. The temperature dependence of conductivity of magnetically aligned SWNT bucky-paper, measured along and across alignment direction by four-probe method. The dimensions for sample 1:  $15 \times 1 \times 0.012 \text{ mm}^3$ , the distance between potential electrodes is 10 mm; samples 2 and 3 have length 10 mm, distance between potential electrodes 8 mm. B. The temperature dependence of conductivity along the nanotube alignment direction. The fitting by Luttinger liquid and VRH models shown by dashed and dot lines, respectively.

Anisotropy of resistivity of  $R_{\text{perp}}/R_{\text{par}} \approx 14$  is temperature independent.  $R(T)$  curves for samples 1 and 2 with different distance between electrodes actually have coincided. Analysis of temperature dependence of resistivity ( $R_{\text{par}}(T)$ ) in the framework of VRH model leads to following expression (see Fig.3.7 B),

$$R(T) = 4.5 \cdot 10^{-4} \cdot \exp(200/T)^{1/2.57} \quad (3.6)$$

where the conductivity dimensionality has shifted toward a two-dimensional system. Such behavior of  $R(T)$  could be explained by the increase in contact area for the aligned CNT. However, it is important to mention that magnetically aligned samples were produced from “laser” SWNT. It is recognized that “laser” SWNT is less defective.

The lowering of  $T_0$  and new temperature dependences of hoping conductivity,  $\ln R \sim (T_0/T)^{2/5}$  was predicted in [23] for one-dimensional conductors with reduced concentrations of defects [26]. Decreasing the concentration of defects, keeps the hopping mechanism in rare short clusters, dissolved in long channels of one-dimensional conductors. However for the system of one-dimensional conductors, the weak excitations of the charge density now leads to the linear Coulomb gap with high shielding anisotropy of the Coulomb potential.

Fig.3.8 shows the thermal diffusivity measurement of magnetically aligned bucky-paper.



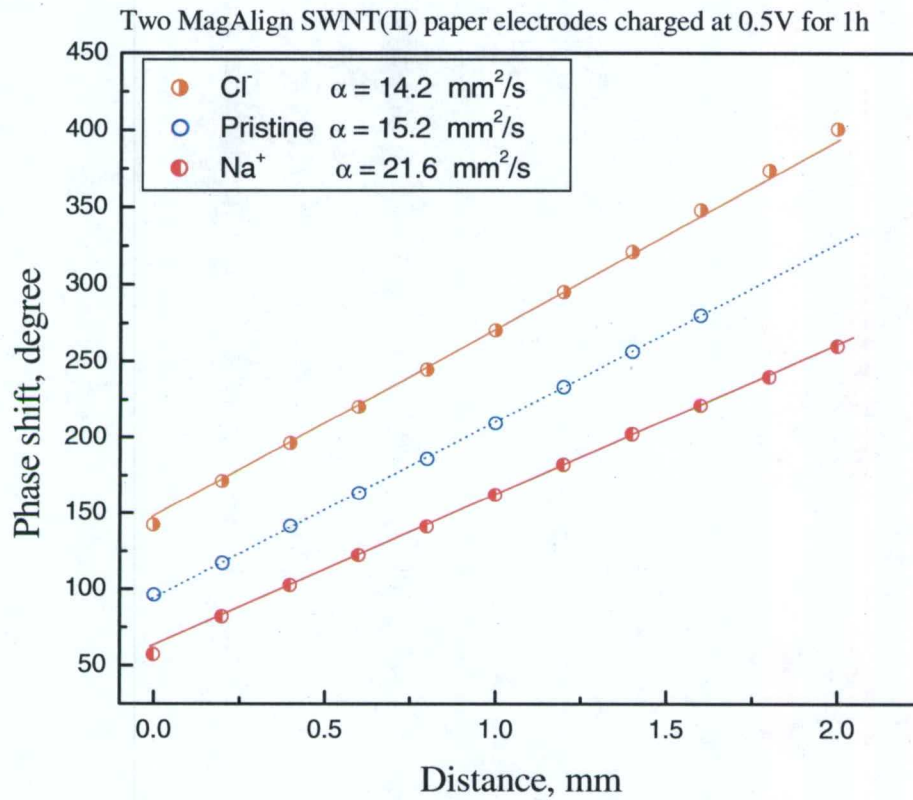


Fig.3.8: Thermal diffusivity of magnetically aligned bucky-paper.

### 3.1.3 References

- [1] S. Berber, Y.-K. Kwon, and D. Tomanek, Phys. Rev. Lett. 84 (2000) 4613.
- [2] M. A. Osman and D. Srivastava, Nanotechnology 12 (2001) 21.
- [3] J. Hone, M. Whitney, C. Piskoti, and A. Zettl, Phys. Rev. B 59 (1999) R2514.
- [4] J. Hone, M.C. Llaguno, M.J. Biercuk, A.T. Johnson, B. Batlogg, Z. Benes, J.E. Fischer. Appl. Phys. A 74 (2002) 339–343.
- [5] P. Kim, L. Shi, A. Majumdar, and P. L. McEuen, Phys. Rev. Lett. 87 (2001) 215502.
- [6] J.H. Barkyoumb, D.J. Land, Thermal diffusivity measurement of thin wires using photothermal deflection. J.Appl.Phys. 78, 2 (1995) 905-912.



### 3.2. Thermal Conductivity of Thin-wall Carbon Inverse Opal

In the last decade, a new material called photonic crystal (PC) has attracted much attention from both basic and applied science viewpoint. The behavior of photons in PCs is very much like that of electrons in semiconductors [1, 2]: the photonic band structure may show forbidden gaps in which photons cannot exist. Therefore, many of the devices and concepts based on the band gap phenomena may be extended to PCs.

This novel concept was developed for various new applications of PCs such as threshold-less lasers and optical transistors [3]. However, the obstacles to obtain this kind of PCs with a complete gap in the desired spectral region represent a big challenge. PCs can be defined as mesoporous materials with a periodic distribution of submicrometric pores. Mainly, there are two parameters that determine the existence of a photonic gap. First, the refractive index contrast, defined as the ratio between the refractive indices of the material and the surrounding substance; secondly, the filling fraction, defined as the percentage volume occupied by the voids, is a very important parameter. Also, the topology of the structure will be decisive in explaining the band structure.

Among the various preparation methods of three-dimensional periodic structures, a self-assembly method utilizing sedimentation of monodispersed nanoscale spheres is the simplest. Silica opal is a type of naturally occurring photonic crystal that consist of well-ordered three dimensional arrays of  $\text{SiO}_2$  spheres, which have diameters in the wavelength range of visible light [4]. As a consequence of periodicity they show opalescence colors that come from Bragg diffraction by the periodic distribution of particles. Bragg diffraction constitutes the fingerprint of photonic band gap (PBG) properties. However, theory predicts that inverse opals would show much better PBG properties than direct opals. Inverse opals that can be regarded as the negative replica of opals, have a well-ordered array of nanometric spherical cavities surrounded by a high refractive index material, in which both the cavities and the high refractive material is connected throughout the structure. To achieve a complete PBG, many laboratories are trying to fabricate high quality inverse opals with high contrast and filling factor [5-10].

At the same time, the unusual mesoscopic structure of the synthetic opal attracted a large effort to improve the efficiency of thermoelectric materials [11, 12]. A good thermoelectric material has low thermal conductivity  $\kappa$ , high electrical conductivity  $\sigma$ , and a high Seebeck coefficient, in order to maximize the thermoelectric figure of merit,

$$Z = \sigma S^2 / \kappa \quad (3.7)$$

where  $Z$  has units of inverse absolute temperature and is generally quoted as  $ZT$ .

For more than 40 years, the search for better thermoelectrics has not provided a material with  $ZT$  significantly larger than one.  $ZT$  of about four would make thermoelectric coolers able to compete with gas-compression technology. Assuming that the Seebeck coefficient in opal where silicon spheres replaced by thermoelectric materials will not be affected by the opal structure, if the thermal conductivity is reduced much more than the electrical conductivity, the opals could be useful thermoelectric materials. Unfortunately many experimental works [7,13,14] and theoretical calculations [15] show that the overall reduction for electrons and phonons in synthetic fcc opal structures will be the same.



On the other hand such porous and highly ordered materials as inverse opals open up new opportunities for further development of multifunctional nanodevices. Particularly, at the low filling factor usually achieving by infiltration of pores by sol-gel route or Chemical Vapor Deposition (CVD), inverse opals have two independent nets of pores divided by a very thin shell: one resulting from removing  $\text{SiO}_2$  spheres and the other consists of octahedral and tetrahedral pores reduced by thin wall covered on  $\text{SiO}_2$  spheres but still with interconnected windows. Both nets could be tuned independently: first net by changing the  $\text{SiO}_2$  sphere size, second net by filling factor. Moreover, at some condition they could be filled by functional materials divided by shell material.

In this part of the project we study the behavior of the heat flow through thin-wall carbon inverse opals produced by two different methods.

### 3.2.1. Experiment

Porous silica opals were used as templates for infiltration and carbon inverse opal synthesis as described in detail by Zakhidov *et al* [7,8,16]. Briefly, the carbon inverse opals were fabricated by infiltrating silica opal with a phenolic resin, thermally curing this resin at low temperature, dissolving the  $\text{SiO}_2$  from the infiltrated opal with aqueous HF, and pyrolyzing the resulting phenolic inverse opal at progressively increased temperatures up to  $1000^\circ\text{C}$ . The graphitic carbon inverse opal was fabricated by CVD method using 1:3 molar ratio of propylene and  $\text{N}_2$  as the feed gas followed by silica removal with aqueous HF.

Thermal and electrical conductivity measurements were performed using Quantum Design Physical Properties Measurement System (PPMS). For these measurements for both inverse opals two samples with different geometry ( $4.5 \times 1.8 \times 12 \text{ mm}^3$  and  $6.0 \times 2.0 \times 17 \text{ mm}^3$ ) and lead distance (6 and 10 mm) have been prepared. The gold covered copper leads were glued to sample by silver filled epoxy H20E (EPO-TEK) using four-probe design: heater - thermometer  $T_1$  - thermometer  $T_2$  - sink. To eliminate the thermal radiation "tail" in the thermal conductivity data, usually appearing at high temperatures, the thermal conductivity measurements above 200 K were confirmed by comparative method involving the series connection of Ni-standard and studied samples. The electrical resistivity for some of samples was measured by a conventional four-probe method using Agilent HP4284A milliohmmeter. Heat capacity measurements were performed using Perkin Elmer Pyris Diamond DSC,. The surface and fracture image of inversed opal were examined by a JSM-1500 (JEOL, Japan) Scanning Electron Microscope (SEM).

### 3.2.2. Results and discussion

#### 1. *Structure*

Fig.3.9 shows SEM images of cleft edges of (001) and (111) facet of the thin-walled inverse opal lattice (250 nm spheres). For both glassy carbon inverse opal fabricated by a phenolic route and graphitic carbon inverse opal fabricated by CVD route a highly periodic structure throughout the volume have been obtained. The void structure consists of an FCC arrangement of spherical carbon shells interconnected with 12 neighboring spherical shells via windows, which result from the sintering process.



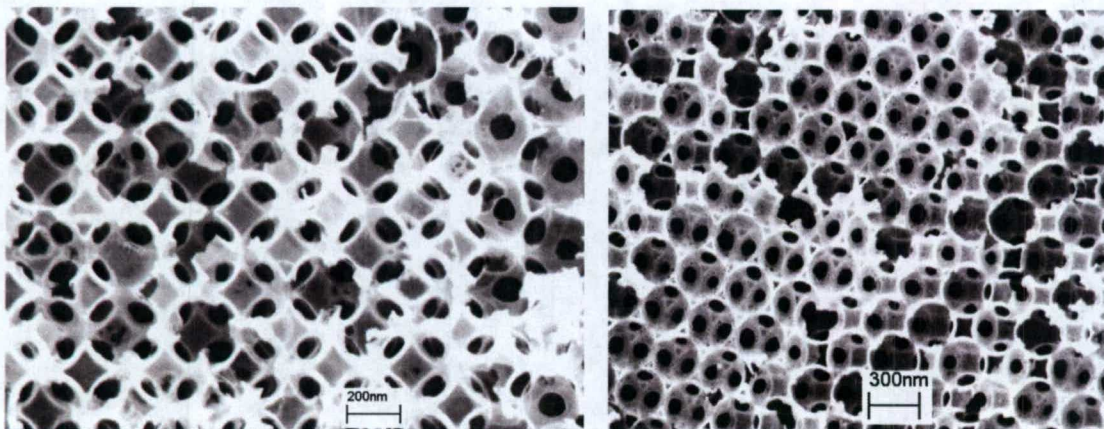


Fig.3.9: The (100) and (111) planes of surface-templated inverse opal. The rough appearance of a cleaved edge of carbon infiltrated inverse opal is due to the occurrence of fracture through hollow spheres (rather than between spheres in silica opal). The large windows interconnecting the spherical cavities are due to the sintering of the opal template.

## 2. Thermal conductivity

The temperature behaviors of thermal conductivity of both inverse carbon opals are almost similar: the linear increase at low temperatures shown in the insert of Fig.3.10 illustrates the changed slope at 20 K and the slight exponential growth above 75 K. The difference in absolute value of about 20% obtained for the whole measured range may be attributed to the difference in crystalline structure of the shells. The X-ray diffraction spectra show the higher crystallinity for CVD infiltrated samples. Moreover, SEM and TEM electron micrographs [7] indicate that the thin wall shells consist of graphite sheets that are preferentially oriented parallel to the void surface created by removal of the  $\text{SiO}_2$  spheres.

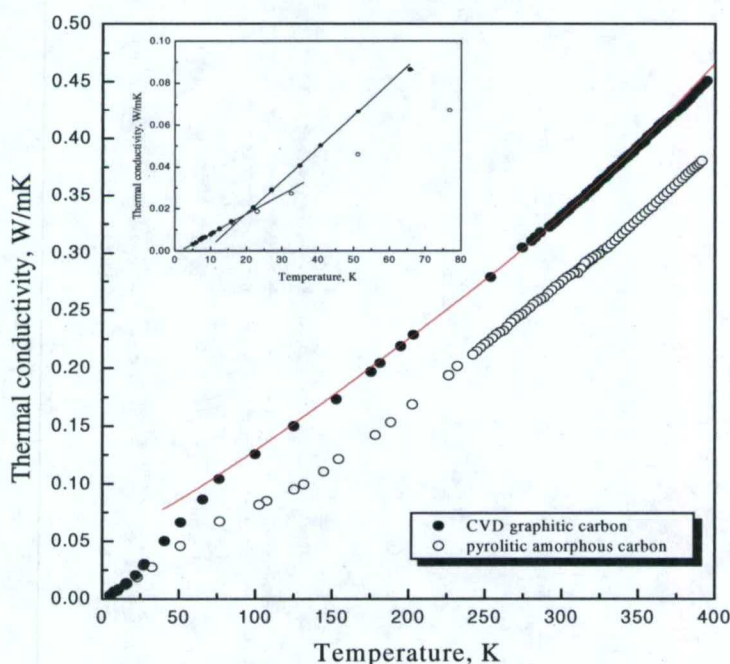




Fig.3.10: Temperature dependence of thermal conductivity of graphitic carbon (CVD) and glassy carbon (pyrolytic amorphous carbon) inverse opals.

**Effective thermal conductivity.** There are a lot of approaches to calculate the thermal conductivity of porous materials and composites using the known thermal conductivity of the parent material. Within a continuum description, the effective thermal conductivity of a composite with spherical voids ( $d=3$ ) or infinite cylindrical voids ( $d=2$ ) and the thermal conductivity of host material  $\kappa_o$  can be given by the following equation [17].

$$\kappa_{eff} = \frac{(1-p)\kappa_o}{1+p/(d-1)}, \quad (3.8)$$

where  $p$  is the fractional volume of the voids often called the “porosity”.

Another equation, taking into account the thermal conductivity of the material in pores,  $\kappa_{pores}$  [18] were used in [19,20] for the FCC opal,

$$\frac{\kappa_{eff}}{\kappa_o} = (1-p)\sqrt{1-p} + p^{\frac{1}{4}}v, \quad (3.9)$$

where  $v = \kappa_{pores}/\kappa_o$ .

The continuum approach to study the effective thermal conductivity of periodic composites was examined by Albrecht *et al* [21] for a number of two-dimensional and three-dimensional lattices.

### 3. Porosity

To calculate the effective thermal conductivity, we have to first estimate the porosity of the structure. The schematic representation of the face-centered cubic structure of inverse opal is given below.

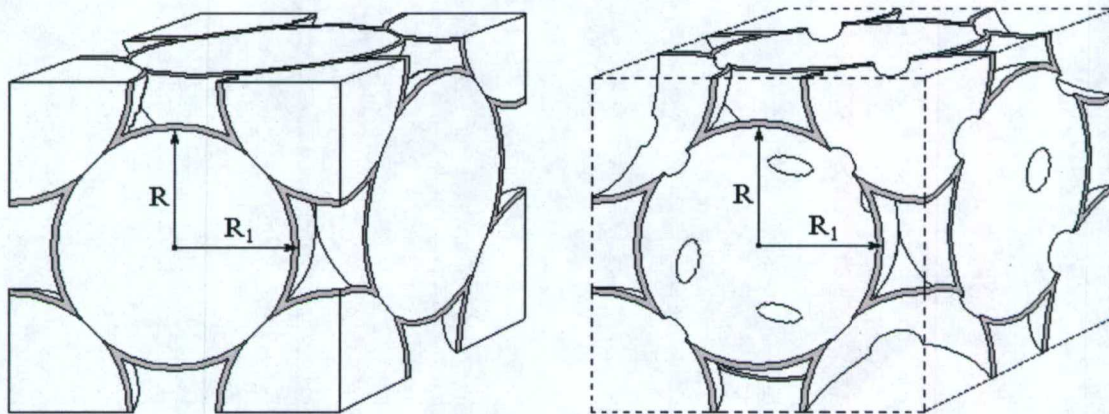


Fig.3.11: Schematic representation of surface-templated inverse opal.



The volume of the FCC structure unit is  $V_{\text{cub.}} = (2\sqrt{2}\cdot R)^3 = 16\sqrt{2}\cdot R^3$ , where  $R$  is  $\text{SiO}_2$  sphere radius. The unit comprises four spheres with volume  $V_{\text{sphere}} = 4 \cdot (4/3) \cdot \pi \cdot R^3 = (16/3) \cdot \pi \cdot R^3$ . For an opal structure we can find the commonly used filling factor  $F$  value,  $F = V_{\text{sphere}} / V_{\text{cub.}} = \pi/3\sqrt{2} = 0.74$ . For surface-templated inverse opal, the cubic volume filled only with thin shells of thickness  $h = R_1 - R$ , depends on filling conditions (Fig.3.11).

For the sample presented in Fig.3.9,  $D = 250$  nm, and the average layer thickness is  $h = 10$  nm. The volume of an empty sphere is,  $(4/3)\pi R_1^3 - (4/3)\pi R^3 = 0.26(4/3)\pi R^3$ , where  $R_1$  was shifted by  $1.08\cdot R$ ,  $R_1 = ((R+h)/R)R = 1.08R$ . The filling factor for surface-templated inverse opal is  $F = 0.74 \cdot 0.26 = 0.192$ , and the porosity is  $P = 1 - F = 0.808$ .

In this calculation, we neglected the structure shrinkage at the first sintering which provided the intersphere interconnection through which the  $\text{SiO}_2$  spheres were removed after infiltration, and we neglected the volume of these circular interfaces (12 holes per each sphere). Subtraction of the volume of 24 holes with average diameter 76 nm results in a reduction of the filling factor to 0.191. Consequently,  $P = 0.809$ .

Now we can calculate the thermal conductivity of the material of the shell (for graphitic carbon). At room temperature ( $T=300$  K),  $\kappa_{\text{effect}} = 0.33$  W/m·K (Fig.3.10). Considering that sphere voids and interstitials air filled, for (3.9) we can write,

$$\kappa_o = \frac{\kappa_{\text{effect}}}{(1-P)^{3/2}} = 3.95 \text{ W / mK} \quad (3.10)$$

By Albrecht approach for  $\kappa_{\text{pores}}/\kappa_o=0$  (air filling) giving  $\kappa_{\text{eff}}/\kappa_o=0.09$  for thermal conductivity of shell material, we found very close result,  $\kappa_o=3.67$  W/m·K.

The density of measured samples is  $0.22$  g/cm<sup>3</sup>. Taking into account the porosity of the studied inverse opal structure,  $P=19.1\%$ , we calculate the density of the host material to be  $\rho = 1.15$  g/cm<sup>3</sup> which is twice less than the density of crystalline graphite,  $\rho_c = 2.21$  g/cm<sup>3</sup>. Perhaps this difference is due to the porosity of the graphite layer and the extended diameter of interconnected windows appeared for the volume change at pyrolysis.

The schematic representation of graphitic shell structure in Fig.3.12 shows that for materials with high anisotropy of conductivity, both electric and thermal, the conducting path would be strongly dependent on the anisotropy factor:  $\gamma = \kappa_{\parallel} / \kappa_{\perp}$ . For pyrolytic graphite at room temperature  $\gamma = 342$  [22]. Heat flow from one sphere to another occurs only perpendicular to graphitic layers with thermal conductivity  $5.7$  W/m·K. As far as heat transferred to the surface layers of another sphere the high thermal conductivity along the graphitic layers,  $1950$  W/mK, shorts the heat flow near the sphere surface preventing further penetration of heat to deeper layers. In such structures, the thermal conductivity would be independent of the thickness of shell walls.



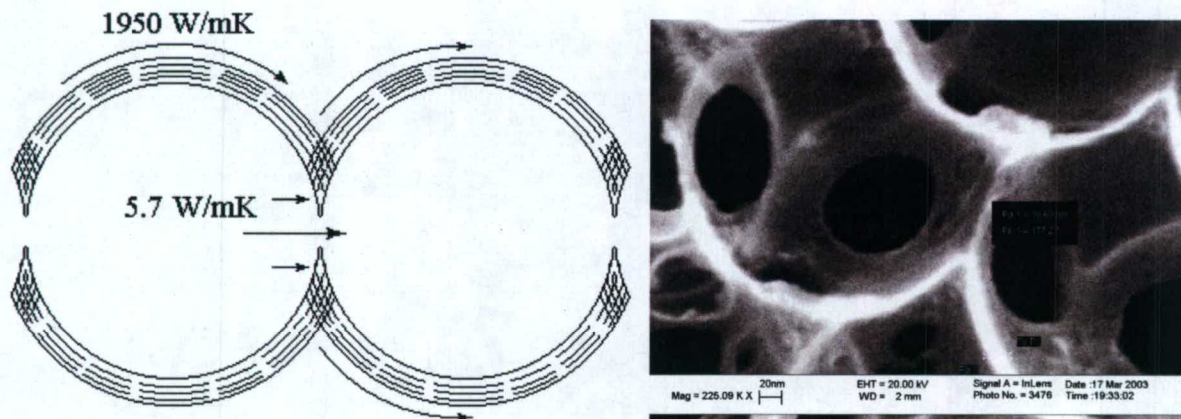


Fig.3.12: Schematic representation of heat flow through graphitic shell structure and real structure of interconnecting windows.

**Electrical conductivity.** Since graphite has a high electronic conductivity, let us estimate the electronic contribution to the thermal conductivity using the Wiedemann-Franz law:

$$\kappa/\sigma = LT \quad (3.11)$$

where  $L = 2.45 \cdot 10^{-8} \text{ W} \cdot \Omega / \text{K}^2$  is Lorenz number.

The temperature dependence of specific resistivity of the studied inverse opal, measured by two-probe and four-probe methods, is shown in Fig.3.13. The slope of the curve is in good agreement with the data for crystalline graphite for this temperature region [23] and for carbon inverse opals with high filling factor studied in [8,24] for various heat treatment temperatures. However, the absolute value of resistivity for our inverse opals heat treated at  $1000^\circ\text{C}$  is much lower than those obtained in [8,24]. The anisotropy factor for electrical conductivity in highly crystalline graphite is much higher than for thermal conductivity,  $\gamma_e = 0.5(\Omega \cdot \text{cm}) / 0.5 \cdot 10^{-3}(\Omega \cdot \text{cm}) = 10^3$  [23]. The obtained resistivity of graphitic inverse opal normalized to porosity is in good agreement with a resistivity of crystalline graphite across the graphite layers. This result shows excellent evidence that the transport properties of graphitic inverse opal are determined by the tiled structure of contacted area of the shells.

The electronic contribution to total thermal conductivity,  $\lambda_{e(300K)} = 3.7 \cdot 10^{-3} \text{ W/m} \cdot \text{K}$ , is two orders smaller than the measured value,  $\lambda_{(300K)} = 0.33 \text{ W/m} \cdot \text{K}$ . However at low temperature,  $T < 50\text{K}$ , the electronic contribution to the thermal conductivity could be predominant.



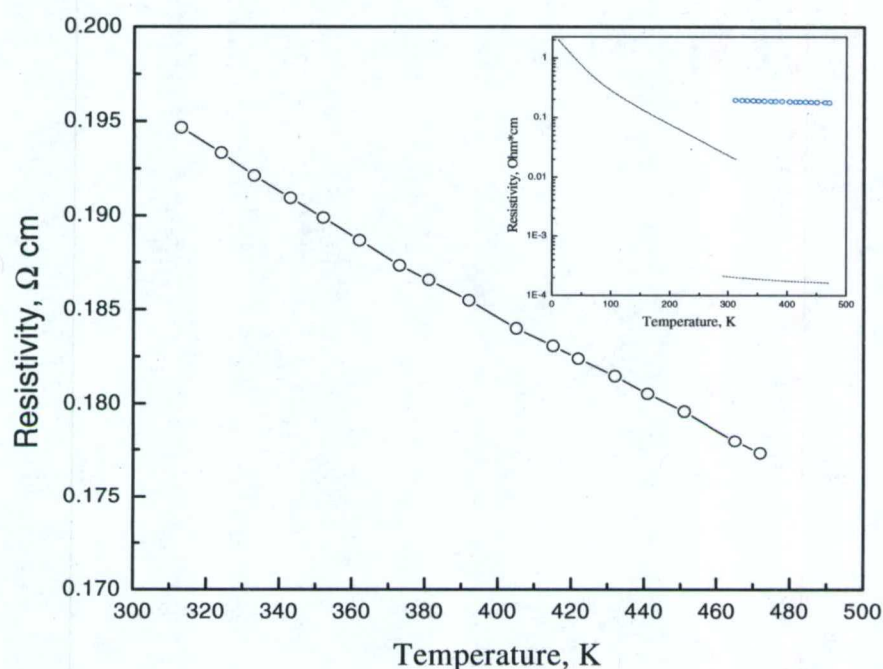


Fig.3.13: Temperature dependence of resistivity for the carbon inverse opal (carbon opal replica). The insert shows the comparative behaviour of resistivity for studied inverse opal (open circles), phenol replica with high filling factor, heat treated at 830°C [24] (dash-dot line), and POCO graphite[23].

**Heat capacity.** The temperature dependence of the specific heat capacity of graphitic inverse opal is shown in Fig.3.14. Within the measured temperature range the heat capacity exhibits the smooth rise closely resembling the 2-3D behavior of of bulk planar graphite (solid line) [23]. For comparison the specific heat capacity values of POCO graphite [23] was divided to the density ratio  $\rho_{POCO}/\rho_{invers\ opal} = 1.82\text{ g/cm}^3 / 0.22\text{ g/cm}^3$ .



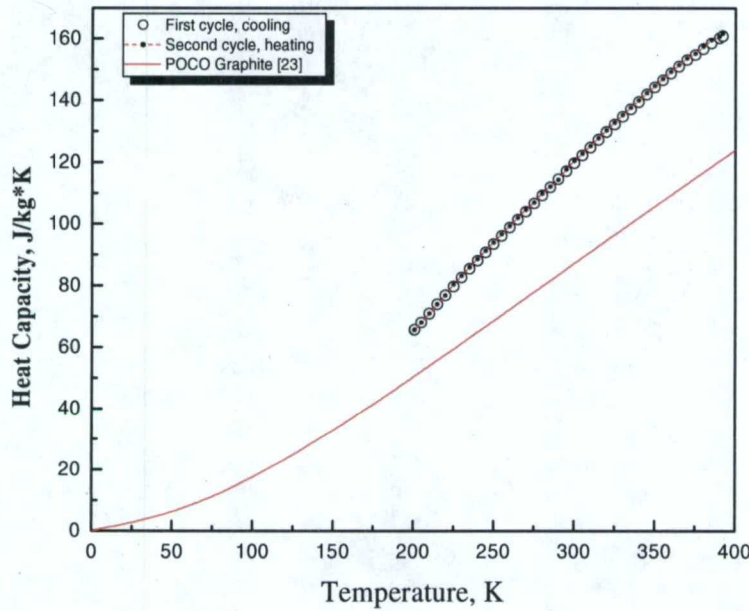


Fig.3.14: Temperature dependence of specific heat capacity,  $C_p$  of graphitic inverse opal prepared by CVD method.  $C_p$  vs  $T$  for pyrolytic POCO graphite was normalized to the density of studied inverse opal, ( $1.82 \text{ g/cm}^3 / 0.22 \text{ g/cm}^3$ ).

### 3.2.3. Conclusion

We measured the thermal conductivity of carbon inverse opals with different crystallinity of the infiltrated carbon. The obtained thermal conductivity in both samples is extremely low,  $0.33 \text{ W/m}\cdot\text{K}$ . The conducting path is strongly dependent on the anisotropy factor:  $\gamma = \kappa_{\parallel} / \kappa_{\perp}$ . For highly crystalline pyrolytic graphite ( $\gamma = 342$ ) the heat flow from one spherical shell to another occurs only perpendicular to graphitic layers with thermal conductivity  $5.7 \text{ W/m}\cdot\text{K}$ . These interconnecting interfaces determine the whole thermal conductance of the system. The heat transferred to the surface layers of another sphere is rapidly shorted by high thermal conductivity along the graphitic layers ( $1950 \text{ W/m}\cdot\text{K}$ ) thus, preventing the further penetration of heat to deeper layers. In such structures, the thermal conductivity would be independent of the thickness of shell walls.

The electronic contribution to the thermal conductivity,  $\kappa_{e(300\text{K})} = 3.7 \cdot 10^{-3} \text{ W/m}\cdot\text{K}$ , is negligible compared to the measured value,  $\kappa_{(300\text{K})} = 0.33 \text{ W/m}\cdot\text{K}$ .

The low thermal conductivity with an appreciably high electronic conductivity suggests the possible application for these materials in thermoelectric cells.



### 3.2.4 References

1. E. Yablonovitch, Phys. Rev. Lett. 58 (1987) 2059.
2. S. John, Phys. Rev. Lett. 58 (1987) 2486.
3. S. John, T. Quang, Phys. Rev. Lett. 78 (1997) 1888.
4. J.V. Sanders. Nature 204 (1964) 1151.
5. Yu.A. Vlasov, V.N. Astratov, O.Z. Karimov, A.A. Kaplyanskii, V.N. Bogomolov, and A.V Prokofiev. Phys. Rev. B, 55 (1997) R13357.
6. C. Lopez, et al., Superlattices Microstructure. 22 (1997) 399.
7. A.A. Zakhidov, R.H. Baughman, Z. Igbal, C. Cui, I.Khayrullin, S.O.Dantas, J.Marti, and V.G. Ralchenko, Science 282, (1998) 897.
8. K. Yoshino, H. Kajii, Y. Kawagishi, M. Ozaki, A.A. Zakhidov, and R.H. Baughman. Jpn. J. Appl. Phys. 38 (1999) 4926-4929.
9. Y.A. Vlasov, N. Yao, D.J. Norris. Advanced Mater. 11 (1999) 165-169.
10. A. Stein, R.C. Schrodin. Current Opinion in Solid State and Materials Science. 5 (2001) 553-564.
11. T.M. Tritt, Science 283 (1999) 804.
12. F.J. DiSalvo, Science 285 (1999) 703.
13. R.H. Baughman, A.A. Zakhidov, I.Khayrullin, Z. Igbal, P. Eklund, and G.D. Mahan, in Opals and Replicas, Proc. of the XVII Int. Conf. on Thermoelectrics, Nagoya, Japan, edited by K. Kaumoto (IEEE, New York, 1998).
14. V. N. Bogomolov, L. S. Parfen'eva, A. V. Prokof'ev, I. A. Smirnov, S. M. Samolovich, A. Jezýowski, J. Mucha, and H. Miserek, Fiz. Tverd. Tela, (St.Petersburg) 37 (1995) 3411, [Phys. Solid State 37 (1995) 1874].
15. J.O. Sofo, G.D. Mahan, Phys. Rev. B, 62, 4 (2000) 2780.
16. A.A. Zakhidov, I.Khayrullin, R.H. Baughman, Z. Igbal, K. Yoshino, Y. Kawagishi, S. Tatsuhara. NanoStructured Materials 12 (1999) 1089-1095.
17. J.C. Maxwell, A Treaties on Electricity and Magnetism (Dover, New York, 1954), pp. 435-441.
18. E.Ya. Litovsky. Izv. AN SSSR. Inorganic Materials, 16, 3 (1980) pp.559.
19. V.N. Bogomolov, D.A. Kurdyukov, L.S. Parfen'eva, A.V Prokof'ev, S.M. Smoilovich, and I.A. Smirnov, Fiz. Tverd. Tela (St.Peterburg) 39, 392 (1997) [Phys. Solid State 39, 341 (1997)].
20. A.E. Aliev and N.Kh. Akhmedjanova. Uzbek Fiz. Jurnal. 1 (1999) 373-379.
21. J.D. Albrecht, P.A. Knipp and T.L. Reinecke. Phys.Rev. B, 63, 134303 (2001).
22. CRC Handbook of Chemistry and Physics, edited by B.R Lide, 82<sup>nd</sup> edition, 2001-2002, pp.12-221.



23. R.E. Taylor, H. Groot. Thermophysical Properties of POCO Graphite. High Temperature – High Pressures, 12, 2 (1980) 147-60.

24. K. Yoshino, H. Kajii, Y. Kawagishi, M. Ozaki, A.A. Zakhidov, R.H. Baughman. Jpn. J. Appl. Phys. 38, 1 (1999) 4926-4929.

## Chapter 4: SUMMARY AND CONCLUSIONS

### 4.1 Summary on Carbon Nanotubes

“Modest” applications of nanotubes for thermal management (like 100-200% increase for composites with low conductivity matrices) look quite feasible.

However, in order to evaluate prospects of more aggressive goals fully exploiting the claimed potential, much more research work is needed to provide a firm understanding of issues involved. Among the problems could be:

- Details of the physics of individual tube behavior, especially the low-T regime
- Microscopic picture of intertube/interlayer interactions and scattering
- Microscopic study of contacts with various media (leads)
- Possibility of (self-) assembly of contacts and environments that would be beneficial to the therm. conductivity
- Optimization issues given the understanding achieved

### 4.2 Conclusions on Thermal Conductivity Enhancement

1. Ph-Polaritons are found to contribute to  $K(T)$  of thin films, with T-peak.  
Position of T-peak depends on  $W$  op, the line width of OP and the TO-LO splitting.
2.  $K(T)$  can be 10-20 times stronger than the conventional radiative contribution to  $K$  by free photons.
3. T-peak shifts to lowest  $T$  in microcavities ( $L \sim 1-10$  mm), which can be used in cryogenic heat transfer.
4. To create a material with high enough polaritonic  $K(T)$  at RT, compared to the usual, phonon  $K_{ph}$  one should create an organic material with OP at 1500-2000  $\text{cm}^{-1}$ , which has large oscillator strength. In organic materials  $K_{ph}$  is usually low ( $< 0.1-1$  W/mK), the  $K_{pol}$  can become a main contribution.
5. One candidate for polaritonic heat pipe, can be a doped fullerene film  $MxC_{60}$  in which giant oscillator strength  $S$  enhancement is found, which is quadratic in doping level  $x$ :  $S \sim x^2$ .



- 6. The strong dependence of  $K_{\text{pol}}(T)$  on  $S(x)$  leads to tunability of  $K(T)$  by charge transfer and thus may be used in “polariton-transistors”, in which  $K$  can be amplified by charging gate  $G$ .**
- 7. Phonon-Polaritons can be used for “Polariton-lasers”, which will emit monochromatic and coherent IR radiation, due to Bose-Einstein condensation in microcavity.**



## APPENDICES



## **5.1 Theory of Thermal Conductivity by Polaritons**



# Phonon-polariton in heat conduction

V. R. Coluci<sup>1,3</sup>, A. A. Zakhidov<sup>1</sup>, and V. M. Agranovich<sup>1,2\*</sup>

<sup>1</sup>NanoTech Institute and Department of Chemistry, University of Texas, Richardson, Texas 830688

<sup>2</sup>Institute of Spectroscopy, Russian Academy of Sciences, 142190 Troitsk, Moscow Region, Russia and

<sup>3</sup>Instituto de Física "Gleb Wataghin", Universidade Estadual de Campinas, C.P. 6165, 13083-970 Campinas SP, Brazil

(Dated: May 29, 2003)

abstract

PACS numbers:

## I. INTRODUCTION

It is well-known that the contribution of radiative transport to thermoconductivity of majority of solids is important only at rather high temperatures of the order of a few thousands K. At much lower temperatures the radiative transport is usually small because is small the density of photon states which have an energy of the order of  $k_B T$ . The energy of the transverse photons, responsible for the radiative transport (we assume that the medium is isotropic), is  $E(k) = \hbar c k / \sqrt{\epsilon}$ , where  $c$  is the velocity of photon in vacuum,  $k$  is its wave vector and  $\epsilon$  is the dielectric constant of medium. The density of states is proportional to  $k^2 (dk/d\omega)$  or (for transverse photons) to  $\omega^2$  what is a smooth function of  $\omega$  and small for small  $\omega$ .

The situation changes if to take into account the dependence of dielectric constant on  $\omega$  which may be strong in the region of dipole allowed resonances. In this region of spectrum the interaction of dipole active quasi-particles (transverse optical phonons) with transverse photons (retardation effect) is responsible for the appearance of a new quasi-particles, so called phonon-polaritons [1,2]. For these quasi-particles most important is vicinity of transverse optical phonon frequency where dielectric constant has a resonance. The polariton dispersion in the region of isolated resonance (a dependence of its frequency on wave vector) can be found from the relation

$$\frac{k^2 c^2}{\omega^2} = \epsilon(\omega), \quad (1)$$

$$\epsilon(\omega) = \epsilon_b \frac{\omega^2 - \omega_{\parallel}^2}{\omega^2 - \omega_{\perp}^2}, \quad (2)$$

where  $\omega_{\parallel}$  and  $\omega_{\perp}$  are frequencies of longitudinal and transverse optical phonons. For some crystals the transverse-longitudinal splitting  $\Delta = \omega_{\parallel} - \omega_{\perp}$ , which is proportional to the oscillator strength at the resonance frequency  $\omega_{\perp}$ , can be rather large. For example, for SiC crystal<sup>4,5</sup>  $\omega_{\perp} = 793 \text{ cm}^{-1}$ ,  $\omega_{\parallel} = 969 \text{ cm}^{-1}$  and, thus,  $\Delta = 176 \text{ cm}^{-1}$ ; for crystal MgO<sup>6</sup>, where  $\omega_{\perp} = 396 \text{ cm}^{-1}$ ,  $\omega_{\parallel} = 719 \text{ cm}^{-1}$  this splitting is even larger:  $\Delta = 323 \text{ cm}^{-1}$ .

If we take into account the dissipation or scattering of polaritons we can use for dielectric constant a more

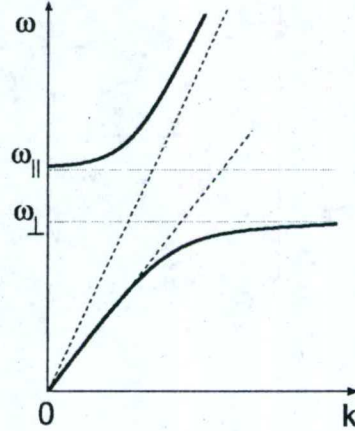


FIG. 1:

general expression

$$\epsilon(\omega) = \epsilon_b \frac{\omega^2 - \omega_{\parallel}^2}{\omega^2 - \omega_{\perp}^2 - 2i\gamma\omega}, \quad (3)$$

The approach to calculate the polariton heat conductivity is dependent on the relation between size of sample and the length of polariton mean-free-path. If this length is larger than the sample size it is necessary to consider polaritons in ballistical regime. If, however, the size of sample is large in comparison with the length of polariton mean-free-path we can use the same statistical random walks approach which usually is in use in calculation of phonon heat conductivity in solids. In this note below we consider crystals MgO and SiC at temperature

$T \approx 1000 \text{ K}$ . At this temperature the states of polaritons with energy  $E \approx 0.1 \text{ eV}$  are mainly populated and statistical approach in calculation of polaritons heat conductivity can be justified because for these phonon-polaritons in mentioned crystals a mean-free-path is rather small. For example, as it follows from the measurements of absorption in MgO crystal[3], the absorption coefficient at temperature  $T \approx 1000 \text{ K}$  changes in wide interval values up to  $10^5 \text{ cm}^{-1}$  but in all cases it is larger than  $10^2 \text{ cm}^{-1}$  at least in the interval of wave numbers  $150 - 1500 \text{ cm}^{-1}$  (unfortunately, we have no other measurements). It means that a polariton mean-free-path  $\Lambda$  for these wave numbers is less than value of order of  $\approx \frac{1}{150} \approx 0.07 \text{ cm}$  and similar situation we meet for



many another crystals as it follows from experimental data on light absorption. It means that for calculation of polariton thermoconductivity of the sample with thickness of order of 1cm we can use statistical theory taking into account the contribution to thermoconductivity the phonon-polaritons with the mean-free-path smaller than the sample size. We will show that this restriction is important for the temperature interval where the statistical theory can be used. The total thermoconductivity is the sum, roughly speaking, of two parts arising from ballistical and diffusive propagation of polaritons. Thus, in comparison with experimental data it is necessary to take into account that the part of total thermoconductivity arising from statistical approach can determine only the lower limit of its total value.

## II. THERMAL CONDUCTIVITY

The thermal conductivity  $\kappa(T)$  can be calculated by the using of following well-known expression

$$\kappa(T) = \frac{1}{3} \sum_p \int C(\omega) v(\omega) \Lambda(\omega) d\omega, \quad (4)$$

where  $\omega$  is the polariton frequency,  $C(\omega)$  is its thermal capacity,  $v(\omega)$  is its the group velocity, and  $\Lambda(\omega)$  is its mean-free-path. The sum is carried out over two transverse polariton polarizations  $p$ .

In order to determine  $\kappa(T)$  we firstly have obtained  $C$ ,  $v$ , and  $\Lambda$ . The polaritons energy at thermal equilibrium can be written as

$$E(\omega, T) = \hbar\omega \frac{D(\omega)}{\exp(\hbar\omega/k_B T) - 1}, \quad (5)$$

where the density of states  $D(\omega)$  is given by

$$\frac{D(\omega)}{V} = \frac{4\pi k^2}{(2\pi)^3} \frac{dk}{d\omega}. \quad (6)$$

Therefore, the thermal capacity can be written as

$$\begin{aligned} C(\omega) &= \frac{1}{V} \frac{dE}{dT} = \\ &= \frac{D(\omega)}{V} \frac{(\hbar\omega)^2 e^{\hbar\omega/k_B T}}{k_B T^2 (e^{\hbar\omega/k_B T} - 1)^2}. \end{aligned} \quad (7)$$

As the absorption is rather weak we can express the group velocity as

$$v(\omega) = \frac{d\omega}{dk}. \quad (8)$$

The last quantity to determine is the mean free path. Since the intensity  $I$  is proportional to the squared electrical field we have

$$I \sim |E|^2 \sim e^{i2kz} = e^{i2(n' + in'')\omega z/c} \sim e^{-2n''\omega z/c} = e^{-z/\Lambda(\omega)} \quad (9)$$

thus,

$$\Lambda(\omega) = \frac{c}{2\omega n''(\omega)}. \quad (10)$$

Using the relation

$$\frac{k^2(\omega)c^2}{\omega^2} = (n' + in'')^2 = \varepsilon(\omega) = \varepsilon' + i\varepsilon'', \quad (11)$$

and assuming weak absorption ( $(n'')^2 \simeq 0$ ) one can obtain

$$\varepsilon'(\omega) = \varepsilon_\infty \left( 1 + \frac{(\omega_\parallel^2 - \omega_\perp^2)(\omega_\perp^2 - \omega^2)}{(\omega_\perp^2 - \omega^2)^2 + 4\Gamma^2\omega^2} \right), \quad (12)$$

$$\varepsilon''(\omega) = \varepsilon_\infty \left( \frac{2\Gamma\omega(\omega_\parallel^2 - \omega_\perp^2)}{(\omega_\perp^2 - \omega^2)^2 + 4\Gamma^2\omega^2} \right), \quad (13)$$

$$n'(\omega) = \sqrt{\varepsilon'(\omega)}, \quad n''(\omega) = \frac{\varepsilon''(\omega)}{2n'(\omega)}. \quad (14)$$

In order to check the approximation considered here for the calculation of  $\Lambda(\omega)$  we plot in Fig. 1 the absorbance obtained from (11) and experimental values for the MgO crystal. We can notice a reasonable agreement between them.

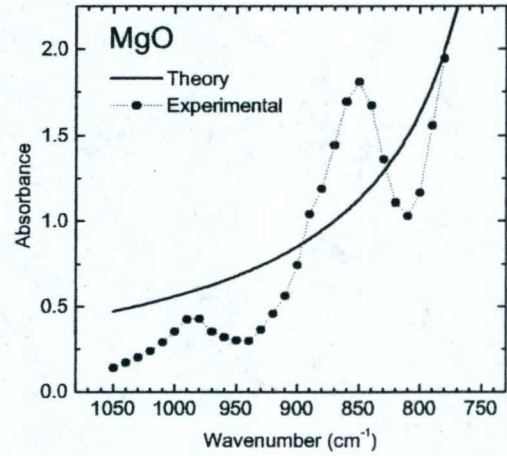


FIG. 2: Absorption spectra of MgO. Experimental points correspond to the MgO crystal at  $T=305$  K with 0.16 mm thick<sup>7</sup>. The dotted line just connects the points.

Grouping (8), (9), (11), and (13)-(15) and summing over two photon polarizations, the thermal conductivity, considering polaritonic resonance, becomes

$$\kappa(T) = \frac{k_B^3 T^2}{3\pi^2 \hbar^2 c} \left[ \int_0^{x_\perp} h(x) dx + \int_{x_\parallel}^\infty h(x) dx \right] \quad (15)$$

where

$$x(T) \equiv \frac{\hbar\omega}{k_B T}, \quad x_\perp(T) \equiv \frac{\hbar\omega_\perp}{k_B T}, \quad x_\parallel(T) \equiv \frac{\hbar\omega_\parallel}{k_B T}, \quad (16)$$



and

$$h(x) \equiv \frac{x^3 e^x}{(e^x - 1)^2} \frac{\sqrt[3]{\varepsilon'(x)}}{\varepsilon''(x)} \quad (17)$$

### III. RESULTS AND DISCUSSIONS

We have used data for SiC and MgO in order to establish a comparison with the thermal conductivity values obtained here. The experimental data considered were:  $\varepsilon_b = 6.7$ ,  $\omega_\perp = 793 \text{ cm}^{-1}$ ,  $\omega_\parallel = 969 \text{ cm}^{-1}$ , and  $\Gamma = 4.76 \text{ cm}^{-1}$  for SiC<sup>4,5</sup>, and  $\varepsilon_b = 2.96$ ,  $\omega_\perp = 396 \text{ cm}^{-1}$ ,  $\omega_\parallel = 719 \text{ cm}^{-1}$ , and  $\Gamma = 7.60 \text{ cm}^{-1}$  for MgO<sup>6</sup>. Experimental values of thermal conductivity were extracted from<sup>8</sup> for SiC (p. 279) and for MgO (p. 283).

Figure 2 presents the thermal conductivity as function of temperature considering one polaritonic resonance. Experimental data are also shown. For  $T > 300 \text{ K}$ ,  $\kappa(T)$  behaves as  $\kappa(T) \sim T^5$ .

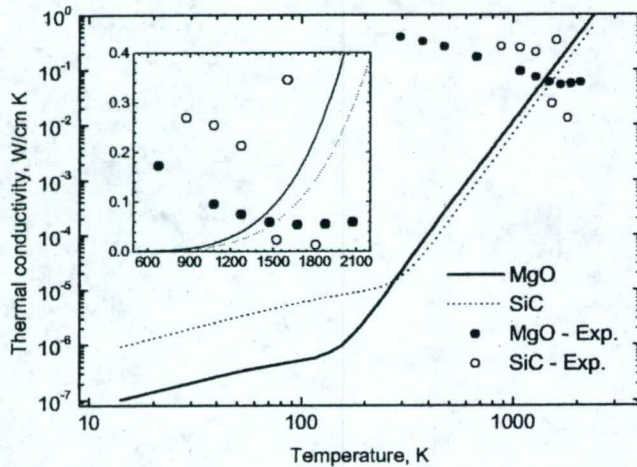


FIG. 3: Thermal conductivity as function of temperature. The lines were obtained using the expression (16). The inset graph is the zoom for the region  $600 \text{ K} < T < 2200 \text{ K}$ .

### IV. CONCLUSIONS

#### Acknowledgments

The authors acknowledge financial support from the Robert A. Welch Foundation. VRC acknowledges the Brazilian agencies CAPES and FAPESP for the financial support.

\* Author to whom correspondence should be addressed. FAX: Electronic address: vladimir.agranovich@utdallas.edu

<sup>1</sup> ref 1 agranovich, Phys. Rev. B 55 (1997) 10105.

<sup>2</sup> ref 2 agranovich, Phys. Rev. B 55 (1997) 10105.

<sup>3</sup> ref 2 agranovich, Phys. Rev. B 55 (1997) 10105.

<sup>4</sup> J. Le Gall, M. Oliver, and J.-J. Greffet, Phys. Rev. B 55 (1997) 10105.

<sup>5</sup> W. G. Spitzer, D. Kleinman, and D. Walsh, Phys. Rev. 113

(1959) 127.

<sup>6</sup> Handbook of Optical Constants of Solids II, ed. Edward D. Palik, Academic Press, New York (1991) p. 937.

<sup>7</sup> J.T. Gourley and W.A. Runciman, J. Phys. C: Solid State Phys. 6 (1973) 583.

<sup>8</sup> Materials Science and Engineering Handbook, ed. J.F. Shackelford, W. Alexander, and J.S. Park, CRC Press, 2nd Edition 2001.



## **5.2 “Vibrations of single-wall carbon nanotube: lattice models and low-frequency dispersion**





## Vibrations of single-wall carbon nanotubes: lattice models and low-frequency dispersion

Yu.N. Gartstein

*Department of Physics, The University of Texas at Dallas, P.O. Box 830688, FO23, Richardson, TX 75083, USA*

Received 14 April 2004; accepted 2 May 2004

Available online 18 May 2004

Communicated by V.M. Agranovich

### Abstract

We address a somewhat controversial question of the low-frequency dispersion of transverse acoustic (TA) modes of single-wall carbon nanotubes by studying an empirical lattice model with a set of elastic interactions no less comprehensive than the frequently used force constant model. Differently from the latter, however, our approach utilizes only geometrically invariant quantities such as variations of lengths and various angles, which makes the issue of force constant adjustment irrelevant. All the salient qualitative features of vibrational spectra of arbitrary nanotubes naturally follow from the vibrational Hamiltonian of graphene upon its isometric mapping onto a cylindrical surface and are calculated on the same footing with graphene. We find that the low-frequency dispersion of the TA modes is manifestly parabolic in agreement with the continuum analysis and with the earlier lattice study by Popov et al. but contrary to the conclusions of a linear dispersion reached in many other lattice calculations.

© 2004 Elsevier B.V. All rights reserved.

Vibrational spectra of individual single-wall carbon nanotubes are of considerable interest and have been studied within different frameworks such as an empirical force constant model [1–4], *ab initio* studies [5,6], tight-binding molecular dynamics [7], a valence force field model [8,9] and continuum mechanics [10, 11]. It is known that the higher-frequency part of the nanotube spectra is relatively well represented already by the zone folding of the graphene spectrum. The lower-frequency part, however, has generic features owing to the one-dimensional character of nanotubes. Particularly, the spectra exhibit four types of acoustic

modes with vanishing frequencies: one longitudinal (LA), two transverse (TA) and one twisting (TW). The existence of these modes has to do with general considerations—displacements of the tube as a whole along and perpendicular to its axis, and the rotation of the tube about the axis do not cost energy—rather than with specific nanotube interactions. Analogous vibrations were also discussed in the context of quantum wires as dilatational, flexural and torsional modes [12]. These modes are important contributors to the low-temperature quantized thermal conductance of such phonon waveguides [13,14].

A more subtle question is the low-frequency dispersion of those acoustic modes. While LA and TW modes clearly have a usual linear dispersion, the de-

*E-mail address:* [yuri.gartstein@utdallas.edu](mailto:yuri.gartstein@utdallas.edu) (Yu.N. Gartstein).



generate TA modes have been calculated as having either linear [1–5,7] or parabolic [9–11] dispersion. Although the exact dispersion law is apparently irrelevant for the quantized ballistic thermal conductance [13,14], the parabolic dispersion would lead to a one-dimensional singularity of the vibrational density of states near zero frequency and particularly results in a very different behavior of the low-temperature specific heat [15,16]. We believe the parabolic character of the low-frequency TA mode dispersion should be quite generic in one-dimensional systems similarly to the well-known bending waves of rods [17] with wavelengths much longer than the transverse rod size. For nanotubes specifically, the parabolic dependence has been analytically illustrated in continuum models [10, 11] similar to used in the analysis of vibrations of elastic cylindrical shells [18,19]. A parabolic dispersion was also found for the lowest flexural modes of quantum wires [12,13], other interesting recent applications of elastic cylinder models include vibrations of cytoskeletal filaments and microtubules [20].

The issue however still remains controversial for more detailed nanotube lattice dynamics models as is clear from the recent analysis [4] of a modified force constant model [1] yielding a linear dispersion of the TA mode. A linear dispersion was also apparent in *ab initio* studies [5]. The main goal of this Letter (for more details see [21]) is to demonstrate a manifestly parabolic dispersion of the low-frequency TA modes for arbitrary carbon nanotubes by using a model with a set of elastic interactions no less comprehensive than the force constant model but in a formulation that naturally exploits all the invariance requirements. Our conclusion is therefore in agreement with the earlier study of a lattice valence force field model by Popov et al. [9] that found the parabolic dispersion. We note that Mahan and Jeon [22] have also recently argued in favor of that type of dispersion in a nanotube lattice model with fewer lattice couplings.

The frequently used force constant model [1] was first developed for planar graphene based on the experimental data for graphite and then adapted for nanotube geometries. Direct application of the graphene force constant values for nanotubes is known to lead to some spurious results and therefore various corrections [1] and adjustments [4] have been used in nanotube calculations. In this Letter we use another empirical model, where the harmonic vibrational Hamil-

tonian of graphene is built using only rotationally invariant quantities such as variations of bond lengths, interbond and dihedral angles. Such a description is akin in spirit to used in conformational analysis and stereochemistry (e.g., [23]) and in bond models for vibrations in covalent semiconductors ([24] and references therein). Further mapping of the graphene Hamiltonian onto a cylindrical surface of the nanotubes then allows to derive all features of arbitrary nanotube spectra “naturally”, without any ad hoc modifications. In this regard, our approach is quite similar to the one used in Refs. [8,9].

To have a comparatively comprehensive set of elastic couplings, we follow [1] in considering carbon–carbon interactions up to the fourth nearest neighbor. The harmonic potential energy  $U = U_i + U_o$  is however expressed as a function of variations of bond lengths and various angles. The first term  $U_i$  would correspond here to in-plane deformations of graphene and in general requires ten elastic parameters  $K_i^m$ :

$$U_i = \sum_{\langle ijk \rangle} [K_1(\delta l_{ij}^2 + \delta l_{jk}^2) + K_2\delta\varphi_{ijk}^2 + K_3\delta l_{ij}\delta l_{jk} + K_4\delta\varphi_{ijk}(\delta l_{ij} + \delta l_{jk})] \quad (1a)$$

$$+ \sum_{m=3}^4 \sum_{\{il\}=m} [K_5^m \delta l_{ij} \delta l_{kl} + K_6^m \delta\varphi_{ijk} \delta\varphi_{jkl} + K_7^m (\delta\varphi_{ijk} \delta l_{kl} + \delta\varphi_{jkl} \delta l_{ij})], \quad (1b)$$

while term  $U_o$  would describe out-of-plane graphene distortions and needs three elastic parameters:

$$U_o = \sum_{m=2}^4 \sum_{\langle i j k l \rangle} K_8^m \delta\chi_{ijkl}^2. \quad (2)$$

The structure of Eqs. (1), (2) has a very clear geometric interpretation and can be conveniently thought of in terms of triangular plaquettes  $\langle ijk \rangle$  formed by bonds  $\langle ij \rangle$  and  $\langle jk \rangle$  connecting nearest carbons  $i$  and  $j$ , and  $j$  and  $k$ , respectively. Variation of bond  $\langle ij \rangle$  length is denoted  $\delta l_{ij}$ , and variation of the inter-bond angle at the common carbon  $j$  denoted  $\delta\varphi_{ijk}$ . Correspondingly, Eq. (1a) completely describes the deformation energy of individual plaquettes. Eqs. (1b), (2), on the other hand, completely describe the interactions of deformations on neighboring plaquettes; specifically,  $\langle i j k l \rangle$  stands for plaquettes  $\langle ijk \rangle$  and  $\langle jkl \rangle$  that



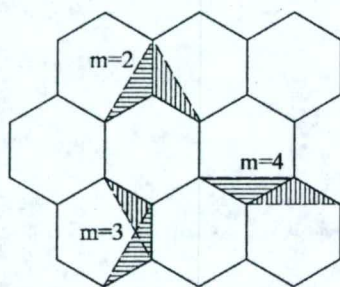


Fig. 1. Nomenclature of possible triangular plaquette pairs adjacent along a nearest-neighbor carbon-carbon bond. To guide the eye, individual adjacent plaquettes are filled with lines at different angles.

are adjacent along bond  $\langle jk \rangle$ . There are three different ways to form adjacent plaquette pairs and notation  $\{il\} = m$  distinguishes them by indicating that carbons  $i$  and  $l$  are the  $m$ th nearest neighbors ( $m = 2, 3, 4$ ), as illustrated in Fig. 1. (In case  $m = 2$ , it is actually plaquettes  $\langle ijk \rangle$  and  $\langle ljk \rangle$  that are adjacent along  $\langle jk \rangle$ . This case is not explicitly included in Eq. (1b) because of the constraint that a sum of inter-bond angles for three plaquettes surrounding a carbon atom is fixed.) The “out-of-plane” interaction, Eq. (2), involves the variations  $\delta\chi_{ijkl}$  of the dihedral angles between corresponding plaquettes. (Eq. (2) can also be rewritten without a  $m = 2$  term.)

It is worth stressing that for the *planar* graphene, Eqs. (1), (2) give the most general description of harmonic interactions involving up to the fourth nearest neighbors. As such, it, of course, can reproduce a force constants description. The latter would be derived by expanding Eqs. (1), (2) in the atomic pair differences. Evidently, then there would be certain relationships between a larger number of force constants as dictated by the invariance of the potential energy with respect to overall rotations [25]. Specifically, ten elastic parameters of Eqs. (1) yield twelve force constants, comprising eight in-plane constants of the type explicitly considered in [1] and four constants mixing radial and tangential displacements that were implicitly set to zero in that reference. Three elastic parameters of Eq. (2) yield four out-of-plane force constants [1].

The advantage of using invariant quantities in Eqs. (1), (2) is that the same functional form of the potential energy can be directly used when carbon atom positions are (isometrically) mapped from the graphene plane onto the cylindrical surface of a

nanotube. Variations of the bond lengths and various angles then just need to be calculated from the carbon atom displacements using actual positions of carbons on the nanotube surface. Of course, a new set of force constants appropriate for the now curved geometry could be again derived through the pair expansions. Force constants so obtained would automatically obey the correct relationships to satisfy the invariance with respect to rotations.

Despite the fact that atoms of carbon nanotubes are arranged in a 3d fashion, the excitations of nanotubes can be described on the same footing as excitations of the planar graphene out of which a nanotube is rolled. (The way we treat this somewhat more involved problem is similar to a simpler but analytically instructive example of the relationship between vibrations of a linear chain of atoms and vibrations of a ring of atoms that can be found in [21].) The indexing of carbons on nanotubes can follow that of the parent graphene plane, where carbon index  $\mathbf{n}\alpha$  consists of a 2d vector  $\mathbf{n}$  specifying the graphene unit cell and  $\alpha = 1, 2$  specifying one of the 2 carbons in the graphene unit cell. The 2d invariance of the effective nanotube vibrational Hamiltonian with respect to translations by graphene primitive vectors  $\mathbf{a}_1$  and  $\mathbf{a}_2$  is easily restored if displacements of carbons are expressed not in terms of common for all carbons  $(xyz)$  coordinates but in terms of local orthogonal coordinates  $(uvw)$ :  $u$ —along the nanotube axis,  $v$ —perpendicular to the tube axis and parallel to the tube surface, and  $w$ —perpendicular to the tube surface. That is, depending on carbon  $\mathbf{n}\alpha$  actual geometric position on the cylindrical surface of the tube, one describes its displacement by using a local base  $(u_{\mathbf{n}\alpha}, v_{\mathbf{n}\alpha}, w_{\mathbf{n}\alpha})$ . This way, obviously, the structure of elastic interactions is seen the same for any hexagon of the nanotube lattice. Correspondingly, 2d wave vectors  $\mathbf{k}$  will “know” only differences between neighboring hexagon indices  $\mathbf{n}$ . The problem is thereby reduced to calculation of the usual, “graphene-like”,  $6 \times 6$  dynamical matrix, but which naturally contains the correct mixing of the “in-plane” and “out-of-plane” displacements in nanotubes. Using proper quantization rules for the allowed phonon wavevectors  $\mathbf{k}$ , one can then readily derive the vibrational spectra of nanotubes of arbitrary chirality. It is worth mentioning that reduction of the dynamical matrix to  $6 \times 6$  in our derivation does not require using the helical symmetry upfront [8,9] but rather only local displacement bases.



The chirality of nanotubes affects results through the positioning of carbons and the quantization rules.

To parameterize the elastic constants  $K_i$  in Eqs. (1), (2) in this Letter, we use the published values of the force constants [1] and some experimental data for graphene. We stress however that numerical calculations here serve mostly illustrative and qualitative purposes. Although we could exactly reproduce results of the force constant model [1] for the graphene spectrum, Fig. 2(a) has been calculated with a parameterization of elastic constants  $K_i$  such as to achieve only a close similarity to the published spectrum [1]. In our parameterization, we chose to slightly and somewhat arbitrarily modify the graphene tangential force constants  $\phi_i^{(n)}$  from the published [1] values so as to satisfy  $\phi_i^{(1)} + 6\phi_i^{(2)} + 4\phi_i^{(3)} + 14\phi_i^{(4)} = 0$ . The latter equality is required by the rotational invariance for both in- and out-of-plane tangential constants—elastic energy should be zero for the overall rotation of the graphene plane. Original constants [1] do not obey it. A recently published new set of force constants [26] also does not satisfy this requirement. The overall scaling of elastic constants was chosen here so as to reproduce graphene experimental optical frequencies of 1580 and 868  $\text{cm}^{-1}$ . Once the values of elastic constants  $K_i$  have been defined for graphene, the same values are used to calculate spectra of nanotubes, examples of which are shown in Fig. 2(b)–(d).

In displaying the nanotube spectra in Fig. 2, we use an unconventional definition of the Brillouin zones (BZs) that is related to the helical symmetry of nanotubes [27,28]. Such a BZ construction is aimed at having BZs as wide as possible and the number of branches in the zone as small as possible. The transverse quantization of the 2d wave vector  $\mathbf{k}$  of the parent graphene band excitations in nanotubes requires

$$\mathbf{k} \mathbf{C}_h = 2\pi l, \quad (3)$$

where  $\mathbf{C}_h = N\mathbf{a}_1 + M\mathbf{a}_2$  is the chiral vector [1] determining the geometry of a specific nanotube. The quantization results in the appearance of one-dimensional sub-bands characterized by the integer quantum number  $l$ . The construction employed here recognizes that there would be only  $d_c$  “unique” quantization levels, where  $d_c$  is the greatest common divisor of integers  $N$  and  $M$ . That is, there are only  $d_c$

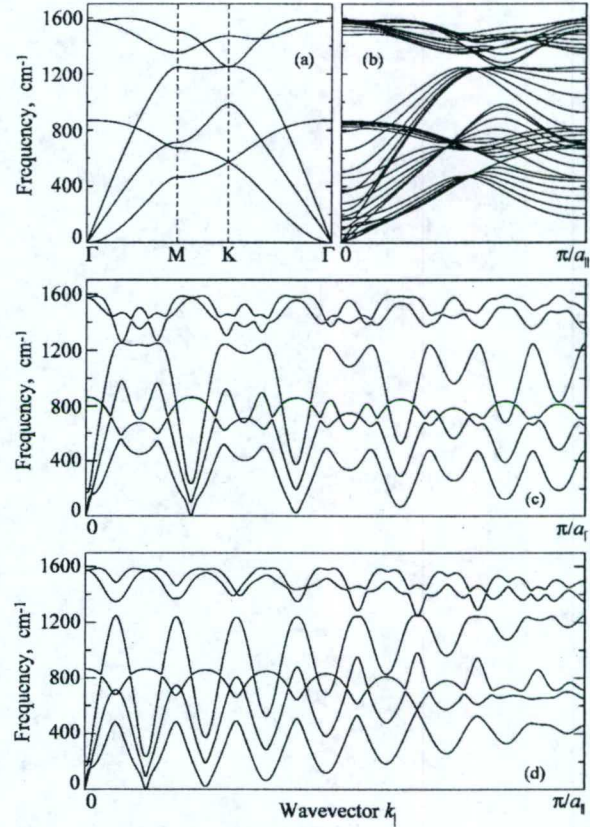


Fig. 2. Model vibrational spectra: (a) graphene; (b) (10, 10) tube; (c) (10, 9) tube; (d) (16, 1) tube. See text for definition of  $a_{||}$ .

independent integers  $l$ : all other allowed  $\mathbf{k}$ -vectors can be obtained with translations by graphene reciprocal vectors. Indeed, if  $\mathbf{G} = n_1\mathbf{b}_1 + n_2\mathbf{b}_2$  (where  $\mathbf{b}_1$  and  $\mathbf{b}_2$  are primitive graphene reciprocal vectors defined with respect to  $\mathbf{a}_1$  and  $\mathbf{a}_2$  and  $n_1$  and  $n_2$  are integers) is the vector of the reciprocal lattice of graphene, then  $\mathbf{k}_1 = \mathbf{k} + \mathbf{G}$  is physically equivalent to  $\mathbf{k}$ . In general,  $\mathbf{k}$  and  $\mathbf{k}_1$  may correspond to different quantum numbers in Eq. (3), say  $l$  and  $l_1$ . One derives the integer difference of these quantum numbers as

$$\delta l = l - l_1 = n_1 N + n_2 M = d_c(n_1 N_1 + n_2 M_1).$$

The last, “irreducible”, factor above can take any integer values:  $n_1 N_1 + n_2 M_1 = 0, \pm 1, \pm 2, \dots$ , with appropriate choices for integer  $n_1$  and  $n_2$ . It is then clear that the number of unique sub-bands in the extended BZ scheme equals precisely  $d_c$ —one can, e.g., choose quantum numbers  $l = -d_c/2 + 1, \dots, 0, \dots, d_c/2$  for



“independent” sub-band indexing, all other values of  $l$  would be reducible to independent values with the appropriate adjustment for the one-dimensional continuous quasi-momentum  $k_{\parallel}$  along the quantization lines. Many branches of the conventional [1] narrower BZ would not exhibit gaps at that BZ boundary; they would correspondingly become single continuous bands when properly “unfolded” in the construction we use. The quantization lines within “wide” BZs can span several hexagons of the graphene reciprocal lattice [21,28]. With that definition, the BZ contains  $2d_c$  continuous branches per each degree of freedom of a carbon atom (factor 2 because of the two atoms in the hexagon), that is,  $6d_c$  for vibrational excitations.

In real space this picture corresponds to the helical symmetry of carbon nanotubes [27,28] (we follow our exposition in [21]): in the parent graphene plane, the nanotube unit cell containing *only two carbons* can be built with two primitive vectors  $\mathbf{C}_h/d_c$  and  $\mathbf{T}$  (since hexagon positions are defined with accuracy to  $\mathbf{C}_h$ , it is only vector  $\mathbf{T}$  that is needed to visit all hexagons of nanotubes with  $d_c = 1$ ). Different from the conventional [1] translational vector parallel to the tube axis, primitive vector  $\mathbf{T} = P\mathbf{a}_1 + Q\mathbf{a}_2$  is in general *not parallel* to the axis and characterized by integers  $P$  and  $Q$  such as to satisfy condition  $MP - NQ = d_c$ . It is the projection of vector  $\mathbf{T}$  onto the axis that determines the “true” longitudinal period

$$a_{\parallel} = \sqrt{3}d_c a^2 / 2C_h$$

and the width  $2\pi/a_{\parallel}$  of the BZ as used in Fig. 2. Here  $a$  is the length of the graphene primitive vectors. For the reciprocal lattice vectors, defined through  $\mathbf{K}_1 \cdot \mathbf{C}_h = 2\pi$ ,  $\mathbf{K}_2 \cdot \mathbf{T} = 2\pi$ ,  $\mathbf{K}_1 \cdot \mathbf{T} = 0$ , and  $\mathbf{K}_2 \cdot \mathbf{C}_h = 0$ , one readily obtains  $\mathbf{K}_1 = -Q\mathbf{b}_1 + P\mathbf{b}_2$ ,  $\mathbf{K}_2 = (M\mathbf{b}_1 - N\mathbf{b}_2)/d_c$ . One easily finds that  $|\mathbf{K}_2|$  indeed coincides with  $2\pi/a_{\parallel}$ .

For armchair tubes,  $a_{\parallel} = a/2$  and the BZ in Fig. 2(b) is twice as wide as the conventional BZ, that picture would be restored by simple folding. Fig. 2(b) exhibits  $d_c = 10$  “independent” transverse quantization levels. On the other hand, Fig. 2(c) and (d) with  $d_c = 1$  correspond to only one transverse quantization level, that is, to six branches. Each polarization band/branch exhibits a continuous evolution of the polarization vectors with in general a strong  $k_{\parallel}$  dependence. It is only in the vicinity of certain points where a simple classification of modes can be done.

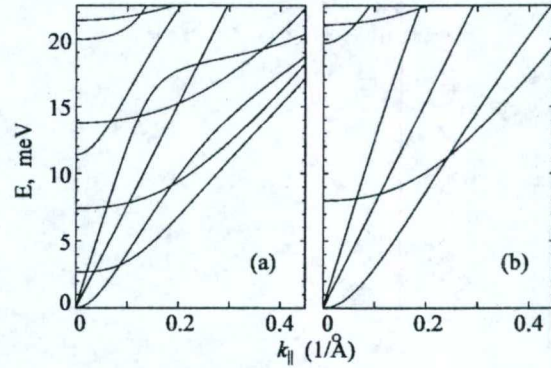


Fig. 3. The low-frequency part of calculated nanotube vibrational spectra: (a) (10, 10) tube; (b) (10, 0) tube. Note that here wave vectors  $k_{\parallel}$  are “reduced”, that is, measured with respect to closest  $\Gamma$  points of hexagons of the reciprocal graphene lattice. The TA mode branches are the ones with the lowest frequencies when reduced  $k_{\parallel}$  approaches zero.

In the limit of the infinitely long wavelength, the degenerate (because of the circular symmetry of the cross-section of the tubular structure) TA modes correspond to the displacements of the tube as a whole perpendicular to the tube axis. For finite long wavelengths, the TA modes correspond to the bending waves of the tube as a whole. In the extended BZ scheme of Fig. 2, the dispersion curves of these modes can touch the zero-frequency line either at  $k_{\parallel} = 0$  as in panel (b) or at finite  $k_{\parallel}$  as in panels (c) and (d). The latter finite  $k_{\parallel}$  points of course lie in a hexagon of the graphene reciprocal lattice other than the one where  $k_{\parallel} = 0$  is. To study the low-frequency region more closely, wave vectors  $k_{\parallel}$  can conveniently be reduced by measuring them along the quantization lines with respect to the closest  $\Gamma$  points. Fig. 3 shows examples of the low-frequency part of the vibrational spectra of the “popular” (10, 10) and (10, 0) tubes reduced to a single hexagon of the reciprocal lattice. Panel (a) can be directly compared to the published results [2] derived from the force constant model. Apart from the small differences, such as values of acoustic velocities, caused by our modification of the force constants, there is one obvious qualitative difference. The lowest-frequency dispersion of the TA modes in Fig. 3 is clearly seen (and confirmed numerically) to be parabolic in agreement with [9] but in contrast to a linear dispersion found in Refs. [1–5,7]. The same pattern



is observed for nanotubes of arbitrary chiralities. By comparing Fig. 3(a) and (b), the parabolic dispersion is seen to have a smaller curvature when going to tubes of smaller radii  $R$ . This in fact is precisely what is expected from the continuum analysis of TA vibrations [10,21], which yields the TA frequency  $\omega(k) \propto k^2 R$  for the long wavelengths  $kR \ll 1$ . With reduced  $k_{\parallel}$  further deviating from zero, the dispersion of the TA modes, of course, ceases to be parabolic.

In summary, we have described a simple empirical model, in which vibrations of graphene and individual single-wall carbon nanotubes are treated and calculated on the same footing, and which has no less comprehensive structure of elastic couplings as the force constant model [1]. Our results illustrate that, when a calculation procedure consistently satisfies all the invariance requirements, the lowest-frequency dispersion of the nanotube TA modes turns out to be parabolic, no matter how many elastic interactions are present in the description [9,22]. This behavior is related to the rotational invariance perpendicular to the axis of one-dimensional systems and should be observed when the wavelength of the TA modes is much larger than the transverse size of the system. These long-wavelength TA modes correspond to bending oscillations and are generically similar to bending vibrations of rods, whose low-frequency spectrum is well known to be parabolic [17]. Details of this part of the spectrum can depend on details of a particular spatial configuration under consideration, for instance the TA modes can become non-degenerate for other shapes of the cross-section [17], but the functional dependence on the wavevector should remain parabolic. The parabolic dispersion is, e.g., evident in calculations of the lowest flexural modes of quantum wires of various shapes [12,13].

So far as the representative completeness of empirical models is concerned, we note that the model presented in this Letter has its qualitative limitations in describing the vibrational spectra of nanotubes. For instance, it would not automatically yield the curvature-induced softening of the phonon modes observed in *ab initio* studies such as that of the twisting mode [5] or more complex dependencies for the breathing mode [5,6,29]. These effects are not deducible from the graphene properties and therefore do not follow from the isometric mapping procedure. To describe them, an empirical model would need to include both the re-

laxation of nanotube geometries as well as an explicit dependence of the elastic energy on nanotube radius and with the axial anisotropy. We discussed such a generalization in the context of uniform deformations [30] which, e.g., leads to the chirality-dependent stiffness of nanotubes [31]. A more complete model for the tubes may have elastic interaction terms beyond those described in graphene-based Eqs. (1), (2). Such empirical models can be developed and then parameterized by comparison with *ab initio* calculations. A more accurate parameterization is, needless to say, required even for the present model. Such quantitative aspects have not been pursued in this Letter.

### Acknowledgements

This work was started in the context of DARPA program on "Phonon Engineering" funded under the contract No. MDA 972-02-C-0044. I am grateful to V. Agranovich, R. Baughman, A. Efros, M. Kertesz and A. Zakhidov for discussions and various inputs related to the subject.

### References

- [1] R. Saito, G. Dresselhaus, M.S. Dresselhaus, *Physical Properties of Carbon Nanotubes*, Imperial College Press, London, 1998.
- [2] M.S. Dresselhaus, P. Eklund, *Adv. Phys.* 49 (2000) 705.
- [3] J.X. Cao, X.H. Yan, Y. Xiao, Y. Tang, J.W. Ding, *Phys. Rev. B* 67 (2003) 045413.
- [4] E. Dobardžić, I. Milošević, B. Nikolić, T. Vuković, M. Damnjanović, *Phys. Rev. B* 68 (2003) 045408.
- [5] D. Sánchez-Portal, E. Artacho, J.M. Soler, A. Rubio, P. Ordejón, *Phys. Rev. B* 59 (1999) 12678.
- [6] O. Dubay, G. Kresse, *Phys. Rev. B* 67 (2003) 035401.
- [7] J. Yu, R.K. Kalia, P. Vashishta, *J. Chem. Phys.* 103 (1995) 6697.
- [8] V.N. Popov, V.E. Van Doren, M. Balkanski, *Phys. Rev. B* 59 (1999) 8355.
- [9] V.N. Popov, V.E. Van Doren, M. Balkanski, *Phys. Rev. B* 61 (2000) 3078.
- [10] G.D. Mahan, *Phys. Rev. B* 65 (2002) 235402.
- [11] H. Suzuura, T. Ando, *Phys. Rev. B* 65 (2002) 235412.
- [12] N. Nishiguchi, Y. Ando, M.N. Wybourne, *J. Phys.: Condens. Matter* 9 (1997) 5751.
- [13] L.G.C. Rego, G. Kirczenow, *Phys. Rev. Lett.* 81 (1998) 232.
- [14] K. Schwab, E.A. Henriksen, J.M. Worlock, M.L. Roukes, *Nature* 404 (2000) 974.
- [15] I.M. Lifshitz, *Zh. Eksp. Teor. Fiz.* 22 (1952) 475.



- [16] V.N. Popov, *Phys. Rev. B* 66 (2002) 153408.
- [17] L.D. Landau, E.M. Lifshitz, *Elasticity Theory*, Pergamon, Oxford, 1986.
- [18] Š. Markuš, *The Mechanics of Vibrations of Cylindrical Shells*, Elsevier, Amsterdam, 1988.
- [19] A.E.H. Love, *Treatise on the Mathematical Theory of Elasticity*, Dover, New York, 1944.
- [20] M.A. Strosio, M. Dutta, *Phonons in Nanostructures*, Cambridge Univ. Press, Cambridge, 2001.
- [21] Y.N. Gartstein, cond-mat/0402286, note that in this preprint many results have been re-derived without knowledge of the earlier studies.
- [22] G.D. Mahan, G.S. Jeon, 2004, preprint.
- [23] E.L. Eliel, S.H. Wilen, M.P. Doyle, *Basic Organic Stereochemistry*, Wiley, New York, 2001.
- [24] P.Y. Yu, M. Cardona, *Fundamentals of Semiconductors*, Springer, Berlin, 1999.
- [25] O. Madelung, *Introduction to Solid-State Theory*, Springer, Berlin, 1978.
- [26] G.G. Samsonidze, R. Saito, A. Jorio, A.G. Souza Filho, A. Grüneis, M.A. Pimenta, G. Dresselhaus, M.S. Dresselhaus, *Phys. Rev. Lett.* 90 (2003) 027403.
- [27] C.T. White, D.H. Robertson, J.W. Mintmire, *Phys. Rev. B* 47 (1993) 5485.
- [28] J.W. Mintmire, C.T. White, in: T.W. Ebbesen (Ed.), *Carbon Nanotubes: Preparation and Properties*, CRC Press, 1997, p. 191.
- [29] J. Kürti, V. Zólyomi, M. Kertesz, G. Sun, *New J. Phys.* 5 (2003) 125.
- [30] Y.N. Gartstein, A.A. Zakhidov, R.H. Baughman, *Phys. Rev. B* 68 (2003) 115415.
- [31] D.H. Robertson, D.W. Brenner, J.W. Mintmire, *Phys. Rev. B* 45 (1992) 12592.



### **5.3 “Simple empirical model for vibrational spectra of single-wall carbon nanotubes”**



# Simple empirical model for vibrational spectra of single-wall carbon nanotubes

Yu.N. Gartstein

Department of Physics, The University of Texas at Dallas,  
P. O. Box 830688, FO23, Richardson, Texas 75083

A simple empirical model and approach are introduced for calculation of the vibrational spectra of arbitrary single wall carbon nanotubes. Differently from the frequently used force constants description, the model employs only invariant quantities such as variations of lengths and angles. All the salient qualitative features of vibrational spectra of nanotubes naturally follow from the vibrational Hamiltonian of graphene upon its isometric mapping onto a cylindrical surface and without any *ad hoc* corrections. A qualitative difference with previous results is found in a parabolic, rather than a linear, long wavelength dispersion of the transverse acoustic modes of the nanotubes. The parabolic dispersion is confirmed and elucidated in the provided continuum analysis of the vibrations. We also discuss and use an alternative definition of the nanotube unit cell with only two carbons per cell that illustrates a "true" longitudinal periodicity of the nanotubes, and of the corresponding Brillouin zone.

PACS numbers: 61.46.+w, 62.25.+g, 62.30.+d, 46.40.-f

## I. INTRODUCTION

Vibrational spectra of individual single wall carbon nanotubes are of considerable interest and have been calculated previously within different frameworks such as an empirical force constant model,<sup>1-3</sup> *ab initio* studies<sup>4</sup> and tight-binding molecular dynamics.<sup>5</sup> It is known that the higher-frequency part of the nanotube spectra is relatively well represented already by the zone folding of the graphene spectrum. The lower-frequency part, however, has generic features owing to the one-dimensional character of nanotubes. Particularly, the spectra exhibit four types of acoustic modes with vanishing frequencies: one longitudinal, two transverse and one twisting. The existence of these modes has to do with general considerations – displacements of the tube as a whole along and perpendicular to its axis, and the rotation of the tube about the axis do not cost energy – rather than with specific nanotube interactions. Analogous vibrations were also discussed in the context of quantum wires as dilatational, flexural and torsional modes.<sup>6</sup> These modes are important contributors to the low-temperature quantized thermal conductance of such phonon waveguides.<sup>7,8</sup>

The frequently used force constant model of Ref. 1 was first developed for planar graphene based on the experimental data for graphite and then adapted for nanotube geometries. Direct application of the graphene force constant values was not found to lead to zero frequencies for all four modes mentioned above. To overcome this difficulty, special curvature corrections were introduced to the force constants.<sup>1</sup> In this paper we develop another empirical model, where the harmonic vibrational Hamiltonian of graphene is built using only "invariant" quantities such as variations of bond lengths, interbond and dihedral angles. Such a description is similar in spirit to used in conformational analysis and stereochemistry (see, e.g., Ref. 9) and in bond models for vibrations in covalent semiconductors (Ref. 10 and references therein). Further mapping of the graphene Hamiltonian onto a cylindrical

surface of the nanotubes then allows to derive all features of arbitrary nanotube spectra "naturally", without any curvature corrections. This way the idea of Ref. 1 of using the same type of vibrational Hamiltonian for both graphene and nanotubes turns out to be realized with no need for *ad hoc* modifications.

We find a qualitative difference with the previously published results in a parabolic, rather than a linear, dispersion of the transverse acoustic modes of nanotubes. This parabolic dispersion is further illustrated in the corresponding continuum model of vibrations and is in agreement with the analysis of vibrations of elastic cylindrical shells.<sup>11</sup> The continuum model also shows the origin of another salient long wavelength feature of the nanotube spectra: a coupling of the longitudinal acoustic with the breathing mode. We believe the parabolic character of the low-frequency part of the transverse mode dispersion is quite generic similarly to the well-known bending waves of rods<sup>12</sup> with wavelengths much longer than the rod size. Such a parabolic dispersion was, e.g., calculated for the lowest flexural modes of quantum wires;<sup>6,7</sup> recent applications of elastic cylinder models also include vibrations of cytoskeletal filaments and microtubules.<sup>13-15</sup> To our knowledge, the parabolic dispersion was not calculated previously for carbon nanotubes.

With our approach we can easily calculate vibrational spectra of arbitrary  $(N, M)$  nanotubes. In doing this, we also employ an alternative definition of the nanotube unit cell with only two carbons per cell as opposed to possibly many carbon atoms of the conventional definition.<sup>1</sup> This way a "true" longitudinal periodicity of the nanotubes is elucidated. The period is a projection of one of the primitive vectors onto the nanotube axis, the primitive vector itself being in general not parallel to the axis. The Brillouin zones can correspondingly be wider than usually used and the total number of the vibrational branches turns out to be just  $6d_c$ , where  $d_c$  is the greatest common divisor of  $N$  and  $M$ .



For numerical computations, we will be using some parameterization of the model, specifically based on a set of data from Ref. 1 as well as on some experimental data. However, the numerical computations here serve mostly illustrative and qualitative purposes.

## II. VIBRATIONAL HAMILTONIAN

Despite the fact that atoms of carbon nanotubes are arranged in a 3-d fashion, the excitations of nanotubes can be described in the way very similar to excitations of the planar graphene. To clearly see this connection for vibrational excitations, one can use local (position-dependent) coordinate systems for atomic displacements and the elastic potential energy written in an "invariant" form. This way the qualitative transformation from vibrational spectra of an infinite plane to spectra of curved cylindrical structures appear naturally without *ad hoc* corrections.

Following Ref. 1, we also consider carbon-carbon elastic interactions up to the fourth nearest neighbor. The harmonic potential energy  $U = U_i + U_o$  is however expressed as a function of only invariant quantities such as variations of bond lengths and various angles. The first term  $U_i$  would correspond here to in-plane deformations of graphene and in general requires ten elastic parameters  $K_i^m$ :

$$U_i = \sum_{\langle ijk \rangle} [K_1(\delta l_{ij}^2 + \delta l_{jk}^2) + K_2\delta\varphi_{ijk}^2 + K_3\delta l_{ij}\delta l_{jk} + K_4\delta\varphi_{ijk}(\delta l_{ij} + \delta l_{jk})] \quad (1a)$$

$$+ \sum_{m=3}^4 \sum_{\langle ijl \rangle} [K_5^m \delta l_{ij} \delta l_{kl} + K_6^m \delta\varphi_{ijk} \delta\varphi_{jkl} + K_7^m (\delta\varphi_{ijk} \delta l_{kl} + \delta\varphi_{jkl} \delta l_{ij})], \quad (1b)$$

while term  $U_o$  would describe out-of-plane graphene distortions and needs three elastic parameters:

$$U_o = \sum_{m=2}^4 \sum_{\langle ijl \rangle} K_8^m \delta\chi_{ijkl}^2. \quad (2)$$

The structure of Eqs. (1,2) can be conveniently thought of in terms of triangular plaquettes  $\langle ijk \rangle$  formed by bonds  $\langle ij \rangle$  and  $\langle jk \rangle$  connecting nearest carbons  $i$  and  $j$ , and  $j$  and  $k$ , respectively. Variation of bond  $\langle ij \rangle$  length is denoted  $\delta l_{ij}$ , and variation of the inter-bond angle at the common carbon  $j$  denoted  $\delta\varphi_{ijk}$ . Correspondingly, Eq. (1a) completely describes the deformation energy of individual plaquettes. Equations (1b,2), on the other hand, completely describe the interactions of deformations on neighboring plaquettes; specifically,  $\langle ijl \rangle$  stands for plaquettes  $\langle ijk \rangle$  and  $\langle jkl \rangle$  that are adjacent along bond  $\langle jk \rangle$ . There are three different ways to form adjacent plaquette pairs and notation  $\{il\} = m$  distinguishes them by indicating that carbons  $i$  and  $l$  are the

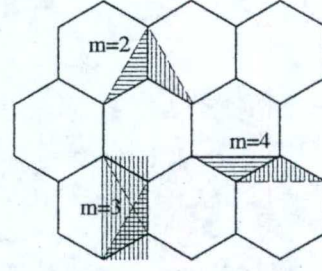


FIG. 1: Nomenclature of possible triangular plaquette pairs adjacent along a nearest-neighbor carbon-carbon bond. To guide the eye, individual adjacent plaquettes are filled with lines at different angles.

$m$ th nearest neighbors ( $m = 2, 3, 4$ ), as illustrated in Fig. 1. (In case  $m = 2$ , it is actually plaquettes  $\langle ijk \rangle$  and  $\langle ljk \rangle$  that are adjacent along  $\langle jk \rangle$ . This case is not explicitly included in Eq. (1b) because of the constraint that a sum of inter-bond angles for three plaquettes surrounding a carbon atom is fixed.) The "out-of-plane" interaction, Eq. (2), involves the variations  $\delta\chi_{ijkl}$  of the dihedral angles between corresponding plaquettes.

It is worth stressing that for the *planar* graphene, Eqs. (1,2) give the most general description of harmonic interactions involving up to the fourth nearest neighbors. As such, it, of course, can reproduce a force constants description. The latter would be derived by expanding Eqs. (1,2) in the atomic pair differences. Evidently, then there would be certain relationships between a larger number of force constants as dictated by the invariance of the potential energy with respect to overall rotations.<sup>16</sup> Specifically, ten elastic parameters of Eq. (1) yield twelve force constants, comprising eight in-plane constants of the type explicitly considered in Ref. 1 and four constants mixing radial and tangential displacements that were implicitly set to zero in that reference. Three elastic parameters of Eq. (2) yield four out-of-plane force constants.<sup>1</sup>

The advantage of using invariant quantities in Eqs. (1,2) is that the same functional form of the potential energy can be directly used when carbon atom positions are (isometrically) mapped from the graphene plane onto the cylindrical surface of a nanotube. When on the nanotube surface, variations of the bond lengths and various angles just need to be calculated from the carbon atom displacements using the actual curved geometry. Of course, a new set of force constants appropriate for the now curved geometry can be again derived through the pair expansions. Force constants so obtained would automatically obey the correct relationships to satisfy the invariance with respect to rotations.

The standard translational invariance of the vibrational Hamiltonian is preserved if displacements of carbons are expressed not in terms of common ( $xyz$ ) coordinates but in terms of local orthogonal coordinates ( $uvw$ ):  $u$  - along the nanotube axis,  $v$  - perpendicular



to the tube axis and parallel to the tube surface, and  $w$  - perpendicular to the tube surface. These simple ideas are illustrated in more detail in Appendix A for an easier to follow example of the relationship between vibrations of a linear chain of atoms and vibrations of a ring of atoms. For the problem at hand, we use the local displacements ( $u_{n\alpha}, v_{n\alpha}, w_{n\alpha}$ ) depending on carbon  $n\alpha$  actual geometric position on the cylindrical surface of the tube. (Here carbon index  $n\alpha$  consists of a 2- $d$  vector  $\mathbf{n}$  specifying the unit cell of the parent graphene plane and  $\alpha = 1, 2$  specifying one of the 2 carbons in the graphene unit cell.) With local displacement bases in place, the invariance of the vibrational Hamiltonian with respect to translations by graphene primitive vectors is held on equal footing in graphene and nanotubes: wave vectors  $\mathbf{k}$  will “know” only differences between neighboring carbon indices  $n\alpha$ . The problem is thereby reduced to calculation of the usual, “graphene-like”,  $6 \times 6$  dynamical matrix, but which naturally contains the correct mixing of the “in-plane” and “out-of-plane” displacements in nanotubes. Using proper quantization rules for the allowed phonon wavevectors, one can then readily derive the vibrational spectra of nanotubes of arbitrary chirality.

### III. PRIMITIVE CELLS AND BRILLOUIN ZONES

The geometry of a single wall carbon nanotube is determined by the chiral vector<sup>1</sup>

$$\mathbf{C}_h = N\mathbf{a}_1 + M\mathbf{a}_2, \quad (3)$$

where  $\mathbf{a}_1$  and  $\mathbf{a}_2$  ( $|\mathbf{a}_1| = |\mathbf{a}_2| = a$ ) are two primitive vectors of the 2- $d$  graphene (hexagonal) crystal structure. Vector  $\mathbf{C}_h$  is perpendicular to the nanotube axis. Conventionally,<sup>1</sup> the translational vector *parallel* to the tube axis is defined, which we denote here as  $\mathbf{T}_D$ :  $\mathbf{T}_D = t_1\mathbf{a}_1 + t_2\mathbf{a}_2$ , where  $t_1 = (2M + N)/d_R$ ,  $t_2 = -(2N + M)/d_R$  and  $d_R$  is the greatest common divisor of  $(2N + M)$  and  $(2M + N)$ . The resulting unit cell of the nanotube built of  $\mathbf{C}_h$  and  $\mathbf{T}_D$  can contain many carbons  $N_a = 4(N^2 + M^2 + NM)/d_R$ , and the longitudinal period  $|\mathbf{T}_D|$  of chiral tubes be much larger than  $a$ . The corresponding Brillouin zones (BZs) would then be narrow and contain many excitation spectrum (whether vibrational or electronic) branches.

In this paper we use an alternative picture of the unit cell and BZ construction that is aimed at having as small number of branches in the zone as possible. As described in more detail in Appendix B, this number of branches is determined by the greatest common divisor of  $N$  and  $M$ , denoted by  $d_c$ . The total number of continuous branches in BZ is equal to  $2d_c$  per each degree of freedom of a carbon atom, that is,  $6d_c$  for vibrational excitations. This corresponds to the nanotube unit cell containing *only two carbons* and which can, e.g., be built with primitive vectors  $\mathbf{C}_h/d_c$  and  $\mathbf{T}$ . Different from vector  $\mathbf{T}_D$ , the translational vector  $\mathbf{T} = P\mathbf{a}_1 + Q\mathbf{a}_2$  is in general *not paral-*

*lel* to the nanotube axis. As discussed in Appendix B (see Eq. (B7)), integers  $P$  and  $Q$  here satisfy condition  $MP - NQ = d_c$ . It is the projection of vector  $\mathbf{T}$  onto the axis that determines the longitudinal period

$$a_{\parallel} = \sqrt{3}d_c a^2 / 2C_h \quad (4)$$

and the width  $2\pi/a_{\parallel}$  of the BZ.

The number of branches in the BZ is related to the transverse quantization of the 2- $d$  wave vector  $\mathbf{k}$  of the parent graphene band excitations:

$$\mathbf{k}C_h = 2\pi l, \quad (5)$$

resulting in the appearance of one-dimensional sub-bands characterized by the integer quantum number  $l$ . The construction of the unit cell and BZ employed in this paper recognizes that there would be only  $d_c$  “unique” quantization levels (that is, only  $d_c$  independent integers  $l$ ): all other allowed  $\mathbf{k}$ -vectors can be obtained with translations by graphene reciprocal vectors. Many branches of the conventional<sup>1</sup> BZ would not exhibit gaps at that BZ boundary; they would correspondingly become single continuous bands when properly “unfolded” in our construction. The quantization lines within our BZs can span several hexagons of the graphene reciprocal lattice (see example of Fig. 9).

### IV. VIBRATIONAL SPECTRA

As was mentioned above, potential energy in Eqs. (1,2) is capable of reproducing results of the force constant model<sup>1</sup> for the graphene spectrum. Figure 2 (a), however, has been calculated with a parameterization of elastic constants  $K_i$  in Eqs. (1,2) such as to achieve only a close similarity to the published spectrum.<sup>1</sup> In our calculations, we chose to slightly and somewhat arbitrarily modify the tangential force constants  $\phi_t^{(n)}$  from the published<sup>1</sup> values so as to satisfy  $\phi_t^{(1)} + 6\phi_t^{(2)} + 4\phi_t^{(3)} + 14\phi_t^{(4)} = 0$ . The latter equality is required by the rotational invariance - elastic energy should be zero for the overall rotation of the graphene plane. Original constants<sup>1</sup> do not obey it. A recently published new set of force constants<sup>17</sup> also does not satisfy this requirement. The overall scaling of elastic constants was chosen here so as to reproduce graphene experimental optical frequencies of 1580 and 868  $\text{cm}^{-1}$ . Once the values of elastic constants  $K_i$  have been defined for graphene, the same values are used to calculate spectra of nanotubes, examples of which are shown in Figures 2 (b)-(d). As discussed in Sec. II, we do not need the knowledge of force constants of Ref. 1 for curved geometries because the Hamiltonian used automatically preserves all invariance requirements.

In displaying the nanotube spectra, we use the definition of BZ as discussed in Sec. III and Appendix B. With that definition, the BZ contains only  $6d_c$  vibrational branches. For armchair tubes,  $a_{\parallel} = a/2$  and the



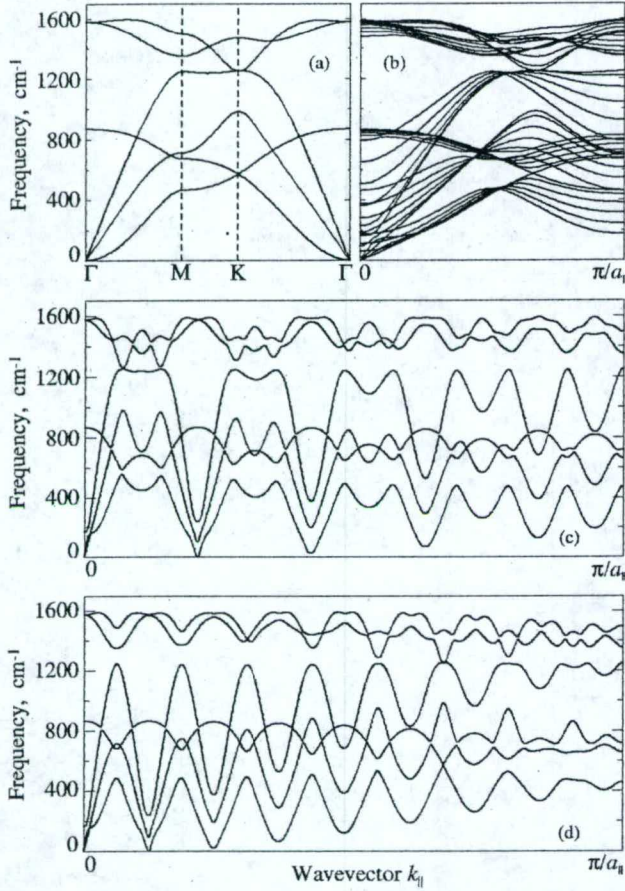


FIG. 2: Model vibrational spectra: (a) Graphene; (b) (10,10) tube; (c) (10,9) tube; (d) (16,1) tube. See text for definition of  $a_{||}$ .

BZ in Figure 2 (b) is twice as wide as the conventional BZ, that picture would be restored by simple folding. Figure 2 (b) exhibits  $d_c = 10$  “independent” transverse quantization levels. On the other hand, Figures 2 (c) and (d) with  $d_c = 1$  correspond to only one transverse quantization level, that is, to six branches. Each polarization band/branch exhibits a continuous evolution of the polarization vectors with in general a strong  $k_{||}$  dependence. It is worth noting that transverse acoustic modes in this picture have their frequency vanishing at finite  $k_{||}$  (which, of course, lie in a hexagon of the graphene reciprocal lattice other than the one where  $k_{||} = 0$  is).

Figure 3 shows low-frequency parts of the vibrational spectra of the (10,10) and (10,0) tubes reduced to a single hexagon of the reciprocal lattice. Panel (a) can be directly compared to the published results<sup>2</sup> derived from the model of Ref. 1. Apart from the small differences, such as values of acoustic velocities, likely caused by our modification of the force constants, there is one qualitative disparity. The dispersion of the transverse acoustic modes in Figure 3 is clearly seen to be parabolic in con-

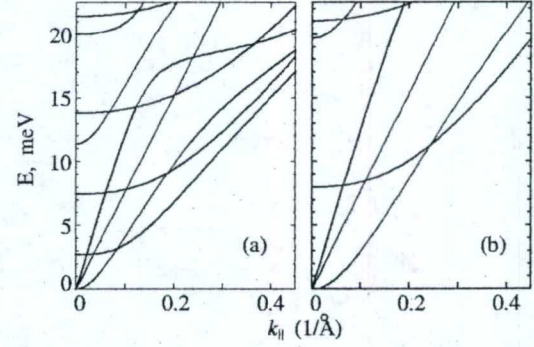


FIG. 3: The low-frequency part of calculated nanotube vibrational spectra: (a) (10,10) tube, (b) (10,0) tube. Note that here wave vectors  $k_{||}$  are measured with respect to closest  $\Gamma$  points of hexagons of the reciprocal graphene lattice.

trast to a linear dispersion discussed in Refs. 1,2,5. The parabolic dispersion is seen over a wider range of  $k_{||}$  on going to tubes of smaller radii, compare Figures 3 (a) and (b). In Sec. V we give an analytic confirmation of this observation within a framework of a continuum mechanics.

## V. CONTINUUM ANALYSIS

Analysis of deformations and vibrations of thin-walled elastic cylinders goes back as far as to Rayleigh and Love; see, e.g., Refs. 18–21, references therein, and Refs. 11,22 for a dedicated analysis of vibrations.

In the case of a planar, graphene, structure, the continuum potential elastic energy can be written as

$$U_i = \frac{\rho}{2} \int dx dy [C_1(u_x + v_y)^2 + C_2((u_y + v_x)^2 - 4u_x v_y)], \quad (6)$$

$$U_o = \frac{\rho}{2} \int dx dy [D_1(w_{xx} + w_{yy})^2 + D_2(w_{xy}^2 - w_{xx} w_{yy})]. \quad (7)$$

Here  $x$  is a coordinate that would later become along the cylinder axis and  $y$  coordinate along the cylinder circumference,  $\rho$  is the mass density. Displacements fields  $u$ ,  $v$  and  $w$  would become, respectively, parallel to the cylinder axis, parallel to its circumference, and perpendicular to the cylindrical surface;  $x$  and  $y$  subindices denote the differentiation over corresponding coordinates. This type of deformation energy is well known in the continuum mechanics of plates<sup>12,20</sup> and can be readily derived from the discrete form (1,2). In the former picture, elastic constants  $C_1$ ,  $C_2$ ,  $D_1$  and  $D_2$  in Eqs. (6,7) are expressed in terms of stretching and bending rigidities and Poisson’s ratio. In the latter derivation, they would be expressed through constants  $K$ ’s in Eqs. (1,2). Note, however, that



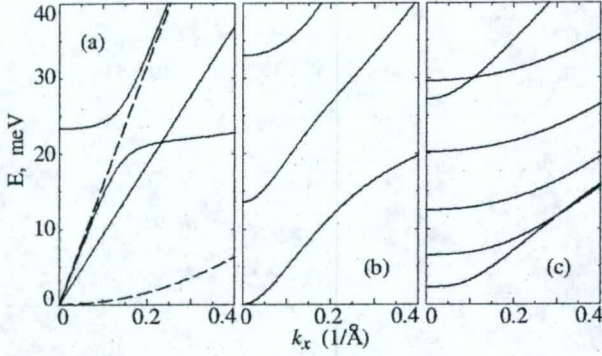


FIG. 4: Branches of the vibrational spectra obtained in the continuum model described in the text at (a)  $k_y = 0$ , (b)  $k_y = 1/R$ , (c)  $k_y = n/R$  with  $n \geq 2$ . Calculations were performed for  $R = 6.78 \text{ \AA}$  that one would have for the (10,10) tube. Elastic parameters used in calculations for this Figure would correspond to graphene velocities  $c_{ta} = 24 \text{ km/s}$ ,  $c_{tb} = 14 \text{ km/s}$ . Dispersion of the out-of-plane graphene vibrations  $\omega = \delta k^2$  was taken with  $\delta = 6 \times 10^{-7} \text{ m}^2/\text{s}$  (see Ref. 4), and  $D_2/D_1 = 4C_2/C_1$ . Graphene results are shown by the dashed lines for comparison. Dispersion of the graphene transverse acoustic mode practically coincides with that of the nanotube twisting mode.

Eqs. (1,2) should then be transformed only in the context of purely acoustic deformations, in which two carbons in a hexagon move “in-phase”. That is why we will be dealing here with the  $3 \times 3$  matrix in Eq. (9) rather than with a  $6 \times 6$  dynamical matrix. One can develop a continuum model that would include optical “out-of-phase” deformations as well. The deformation energy of type of Eqs. (6,7) was already proved to be useful in studies of large deformations of carbon nanotubes.<sup>23</sup>

The modification of Eqs. (6,7) upon formation of a cylindrical body in continuum mechanics is, e.g., discussed in Refs. 11,20,21. As is also shown in Appendix A for a discrete model, this corresponds to a simple substitution in (6,7):  $v_y \rightarrow v_y + w/R$  and  $w_y \rightarrow w_y - v/R$ ,  $R$  being the cylinder radius. Using this substitution, one can easily study the problem of small vibrations of a continuum cylinder. The vibrational frequencies  $\omega$  for the plane waves with a two-dimensional wave vector  $(k_x, k_y)$  are determined from the eigenvalue equation

$$\omega^2 \mathbf{d} = \mathbf{M} \mathbf{d}, \quad (8)$$

where displacement vector  $\mathbf{d} = (u, v, w)$  and matrix  $\mathbf{M}(k_x, k_y)$  is

$$\mathbf{M} = \begin{bmatrix} C_1 k_x^2 + C_2 k_y^2 & (C_1 - C_2) k_x k_y & i A k_x / R \\ (C_1 - C_2) k_x k_y & \tilde{C}_1 k_y^2 + \tilde{C}_2 k_x^2 & -i B k_y / R \\ -i A k_x / R & i B k_y / R & \omega_b^2 + D_1 (k_x^2 + k_y^2)^2 \end{bmatrix}. \quad (9)$$

Here  $\tilde{C}_1 = C_1 + D_1/R^2$ ,  $\tilde{C}_2 = C_2 + D_2/R^2$ ,  $A = 2C_2 - C_1$ ,  $B = C_1 + (D_1 + D_2/2)k_x^2 + D_1 k_y^2$  and  $\omega_b^2 = C_1/R^2$ .

In the case of the planar structure,  $R \rightarrow \infty$ , Eqs. (8,9) lead to two acoustic waves of in-plane vibrations (with

longitudinal  $c_{ta} = C_1^{1/2}$  and transverse  $c_{tb} = C_2^{1/2}$  velocities) and an acoustic wave of the out-of-plane vibrations with a parabolic spectrum  $\omega = D_1^{1/2}(k_x^2 + k_y^2)$ , see Figure 4 (a).

For a cylinder/tube of a finite radius  $R$ , the transverse quantization imposes a restriction on values of  $k_y = n/R$ , where  $n$  is an integer. Of special interest to us here are values of  $k_y$  equal to 0 and to  $\pm 1/R$ . The case of  $k_y = 0$  (Fig. 4 (a)) yields two of the four acoustic modes of the tube with vanishing frequencies: (i) the longitudinal mode with a low-frequency dispersion coinciding with the longitudinal acoustic wave of the graphene and (ii) the twisting mode whose dispersion is somewhat modified from the transverse acoustic mode of graphene by virtue of the elastic constant  $D_2$ :  $c_{ta} = \tilde{C}_2^{1/2}$ . The longitudinal mode in the case of the cylinder couples with the breathing mode, whose frequency at  $k_x = 0$  is  $\omega_b$  and whose dispersion is determined by constant  $D_1$ . As a result of this coupling, an anti-crossing behavior of the branches arises as is clearly seen in the Figure. (iii) The two other, degenerate, acoustic modes of the tube spectrum, usually referred to as transverse acoustic modes for carbon nanotubes<sup>1</sup> or as flexural modes in other applications,<sup>6,13,14,22</sup> correspond to  $k_y = \pm 1/R$  (Fig. 4 (b)). It is apparent from the Figure that these modes have a parabolic spectrum. In fact, one can easily show this analytically by the perturbation analysis of (8,9) in  $k_x$ : contributions to the linear coefficient in dispersion  $\omega(k_x)$  exactly cancel. The low-frequency parabolic dispersion of these modes, although modified by the curvature rigidity, Eq. (7), is mainly determined by the in-plane stretching rigidity, Eq. (6). Neglecting Eq. (7), one would obtain the long wavelength, for  $k_x R \ll 1$ , dispersion of this mode as  $\omega(k_x) = (2(C_1 - C_2)C_2/C_1)^{1/2} k_x^2 R$ . Evidently, the parabolic character of the dispersion becomes even more apparent for smaller-radius tubes. These modes correspond to bending vibrations of the tube as a whole and, in this sense, are similar to the bending vibrations of rods, whose generic long-wavelength parabolic dispersion is well known.<sup>12</sup> Similarities between Figures 4 and 3 (a) are obvious. Note, however, some quantitative differences caused by different values of effective parameters.

## VI. SUMMARY AND DISCUSSION

We have described a simple empirical model, in which vibrations of the graphene and individual single wall carbon nanotubes are treated and calculated on the same footing. Differently from the force constant model, our model uses only “invariant” quantities: variations of bond lengths, interbond and dihedral angles. As a result, the isometric mapping from the planar graphene onto a cylindrical surface of nanotubes automatically preserves all the right relationships between equivalent force constants. Importantly, all calculated vibrational spectra of



nanotubes correctly exhibit four types of acoustic excitations with vanishing frequencies (one longitudinal, two transverse and one twisting), which are derived naturally and follow from the symmetries of the underlying system. Although the results obtained are largely similar to the earlier published, we have also found an important qualitative difference. The long-wavelength dispersion of the transverse acoustic modes is shown to be parabolic rather than linear. One consequence of this is that the vibrational density of states should exhibit a one-dimensional singularity near zero frequency. We cannot exclude that there can be other physical implications of our finding, although this apparently is not the case for the quantized ballistic thermal conductance,<sup>7,8</sup> for which the exact dispersion law is irrelevant. These long-wavelength (wavelength much larger than the tube radius) transverse modes correspond to bending oscillations of a nanotube as a whole and, therefore, are similar to bending vibrations of rods, whose low-frequency spectrum is known to be parabolic.<sup>12</sup> The parabolic dispersion is, e.g., evident in calculations of the lowest flexural modes of quantum wires.<sup>6,7</sup> The origin of the parabolic dependence for nanotubes has been analytically illustrated using a continuum elastic model similar to used in the analysis of vibrations of cylindrical shells.<sup>11</sup> The continuum model also clarified the coupling between longitudinal acoustic and breathing modes resulting in the anti-crossing behavior clearly seen in the calculated spectra of nanotubes.

The simplicity of our model allows us to easily calculate vibrational spectra of nanotubes of arbitrary chiralities. To better handle such spectra, we employed an alternative definition of the nanotube unit cell with only two carbons per cell. This definition reveals a “true” longitudinal periodicity of carbon nanotubes that can be substantially shorter than used in the conventional definition.<sup>1</sup>

Being a result of the straightforward isometric mapping, the model presented in this paper, has its qualitative limitations. For instance, it does not automatically yield the curvature-induced softening of the phonon modes observed in *ab initio* studies such as that of the twisting mode,<sup>4</sup> or more complex dependencies for the breathing mode.<sup>4,24</sup> Of course, these effects are not deducible from the graphene properties. To describe them, the model would need to include both the relaxation of nanotube geometries (mapping would not be exactly isometric) as well as an explicit dependence of the elastic energy on nanotube radius and with the axial anisotropy.<sup>27</sup> We discussed such a generalization in the context of uniform deformations,<sup>25</sup> which, e.g., leads to the chirality-dependent stiffness of nanotubes.<sup>26</sup> We believe the present model can also be further developed in this regard and correspondingly parameterized by comparison with *ab initio* calculations. A more accurate parameterization is, needless to say, required even for the present model. Such quantitative aspects have not been pursued in this paper.

## Acknowledgments

This work was started in the context of DARPA program on “Phonon Engineering” funded under the contract No. MDA 972-02-C-0044. I am grateful to V. Agranovich, R. Baughman, A. Efros, M. Kertesz and A. Zakhidov for discussions and various inputs related to the subject.

## APPENDIX A: A RING EXAMPLE

Here we study in more detail a simpler illustrative example of the relationship of vibrations of an infinite linear atomic chain and a ring of atoms. For clarity, displacements of atoms are restricted to the plane in which a ring and chain belong. Atom-atom interactions correspond to formation of bonds and result both in stretching and bending rigidity of a linear chain. Figure 5 is a picture of the ring consisting of  $N = 10$  atoms, which is assumed to preserve the nature of interactions in the chain. The figure shows a common system of coordinates  $(y, z)$  as well as local systems  $(v, w)$  related to the tangential and normal displacements of the corresponding atom. Obviously, the kinetic energy

$$T = \frac{M}{2} \sum_n (\dot{y}_n^2 + \dot{z}_n^2) = \frac{M}{2} \sum_n (\dot{v}_n^2 + \dot{w}_n^2), \quad (\text{A1})$$

where  $n$  is the 1-d positional index of the atom along the ring circumference. We first write the potential energy of a linear chain in an invariant form as

$$U = \frac{K}{2} \sum_n \delta l_n^2 + \frac{K_b l^2}{2} \sum_n \delta \chi_n^2, \quad (\text{A2})$$

where the first term describes the stretching and second the bending rigidity. Then we assume that the same functional form holds for the ring. From the geometry of

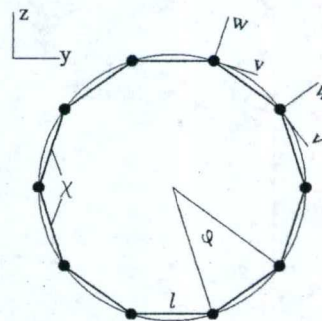


FIG. 5: A ring of  $N = 10$  atoms connected by interatomic “bonds” (thicker lines). The stretching rigidity corresponds to variations of the bond lengths  $l$ , the bending rigidity to variations of the inter-bond angles  $\chi$ . Number of atoms  $N$  (or the radius of the ring) determines the angle  $\varphi = 2\pi/N$ .



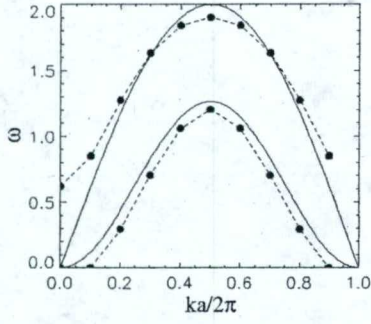


FIG. 6: The vibrational spectra of the linear chain (solid lines) and of the ring (filled circles) of atoms. The parameters used for the plot are  $K/M = 1$  and  $K_b/M = 0.1$ .

Figure 5, the variation of the bond lengths, as a function of the local displacements, is

$$\delta l_n = (v_{n+1} - v_n) \cos(\varphi/2) + (w_{n+1} + w_n) \sin(\varphi/2), \quad (\text{A3})$$

while the variation of the inter-bond angles

$$l \cdot \delta \chi_n = (2w_n - w_{n+1} - w_{n-1}) \cos(\varphi/2) + (v_{n+1} - v_{n-1}) \sin(\varphi/2). \quad (\text{A4})$$

For the linear chain ( $\varphi = 0$  and  $v_n = y_n$ ,  $w_n = z_n$ ), Eq. (A3) describes a conventional longitudinal stretching while Eq. (A4) would yield a conventional local curvature. Tangential and normal vibrations in a linear chain are fully decoupled. The corresponding two branches of the vibrational spectrum are simply

$$\begin{aligned} \omega_s^2(k) &= (4K/M) \sin^2(ka/2), \\ \omega_b^2(k) &= (16K_b/M) \sin^4(ka/2), \end{aligned} \quad (\text{A5})$$

where  $a = l$  is the distance between the atoms along the chain. This spectrum is shown in Figure 6 with solid lines.

In the curved system (our ring with  $\varphi \neq 0$ ), on the other hand, tangential and normal displacements are coupled, as is well known in the elasticity theory for curved surfaces<sup>12,20</sup> and clearly seen in Eqs. (A3,A4). If we were to use the common system of coordinates for displacements ( $y_n, z_n$ ), the atom contributions to the potential energy, Eq. (A2), would be position dependent and the translational invariance with respect to  $n \rightarrow n+1$  would be lost. With the local coordinates ( $v_n, w_n$ ), this invariance is preserved and one can directly use the conventional transition to  $k$ -states, which would now be quantized as

$$k = (2\pi/Na)i, \quad i = 0, \dots, N-1. \quad (\text{A6})$$

The unit cell length  $a > l$  here is now the distance between the atoms of the ring along its circumference. The derivation of the spectrum from the equations of motion follows straightforwardly from Eqs. (A1-A4),

and the results are shown in Figure 6 with filled circles. In accordance with Eq. (A6), it is now a set of discrete frequencies. The coupling between normal and tangential displacements resulted in important qualitative modifications of the spectrum, which have been obtained exactly and naturally. Particularly, one notices 3 zero-frequency modes. Two of them (with  $i = 1$  and  $i = N-1$ , or  $i = -1$ , in Eq. (A6) – precisely one wavelength on the ring circumference) correspond to the displacements of the ring as a whole in two orthogonal directions. The other (with  $i = 0$ ) is a pure tangential mode describing the rotation of the ring as a whole. The  $k = 0$  finite-frequency mode, on the other hand, is a pure normal, breathing, mode that “borrowed” its strength from the parent stretching oscillations of the linear chain.

Equations (A3,A4) can be used to study the continuum limit, when, keeping the same radius  $R$ , we increase the number of atoms  $N \rightarrow \infty$  and bond length  $l \rightarrow 0$ . Then, evidently,

$$\begin{aligned} \delta l/l &\rightarrow [\partial v / \partial y + w/R], \\ \delta \chi/l &\rightarrow -\partial [\partial w / \partial y - v/R] / \partial y. \end{aligned} \quad (\text{A7})$$

The expressions in brackets in Eq. (A7) provide a recipe for a transition from the continuum model of a chain to the continuum model of a ring. The subsequent analysis of vibrations is straightforward with the wavevector  $k$  quantized as  $kR = n$  ( $n$  being an integer) yielding three zero-frequency modes and the breathing mode as in the discrete case above.

It should be noted here that in reality the very values of the unit cell length  $a$  and elastic constants  $K$ ,  $K_b$  can in fact somewhat differ for the ring and the linear chain, and the difference would be  $N$ -dependent as determined by the equilibrium bond length in the ring. In this sense, what is compared in Figure 6 is the structure of the spectra for the same values of the essential parameters upon isometric mapping of the linear system onto a circular ring. In addition, the elastic energy of the ring could in general contain terms absent in the energy of the chain, such as  $\delta \chi_n \delta l_n$ . They are not deducible from the functional form of the linear system and would have to be explored on their own. We also note that Eq. (A2) can be generalized to include longer range interactions.

## APPENDIX B: TRANSVERSE QUANTIZATION AND UNIT CELLS

Two carbons connected by  $C_h$  (Eq. (3)) on the graphene plane correspond to the same carbon on the nanotube after wrapping. The effective 2-d cyclic condition can therefore be written as

$$\mathbf{R}_{nm} + \mathbf{C}_h = \mathbf{R}_{nm}, \quad \mathbf{R}_{nm} = n\mathbf{a}_1 + m\mathbf{a}_2, \quad (\text{B1})$$

$\mathbf{R}_{nm}$  being the position of one of the carbons (there are two of them) of an arbitrary unit cell of graphene. If  $k$



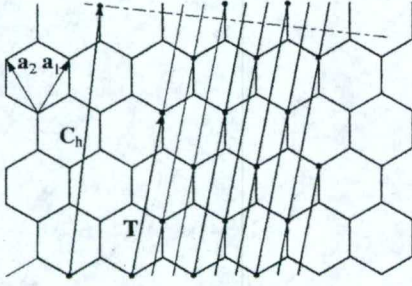


FIG. 7: Unwrapped (3,2) tube with carbons rearranged to form a horizontal strip here. The tube axis is shown by the dash-dotted line. Here  $d_c = 1$  and the  $\mathbf{T}$  vector, Eq. (B2), is defined by the  $(P, Q)$  pair (2,1). Small circles connected by thinner lines indicate a sequence of carbons reached by the  $\mathbf{T}$ -translation. It is transparent that all hexagons of the strip would be visited this way, forming an effectively 1-d enumeration of Eq. (B5). The conventional vector  $\mathbf{T}_D = 7\mathbf{a}_1 - 8\mathbf{a}_2$  and such a unit cell would have 38 hexagons.

is the 2-d wave vector of the band excitations, then in the infinite graphene plane it would have two independent continuous components. In nanotubes, the cyclic condition leads to the transverse quantization of Eq. (5). In other words, wave vectors  $\mathbf{k} = \mathbf{k}_\perp + \mathbf{k}_\parallel$  allowed by Eq. (5) lie only on certain quantization lines in the reciprocal plane of graphene,  $\mathbf{k}_\perp$  being quantized according to Eq. (5) and  $\mathbf{k}_\parallel$  being actually a 1-d continuous wave vector parallel to the tube axis.

Let us define vector

$$\mathbf{T} = P\mathbf{a}_1 + Q\mathbf{a}_2 \quad (\text{B2})$$

with integer  $P$  and  $Q$ . From Eqs. (3) and (B2), one finds

$$\mathbf{a}_1 = (-QC_h + MT)/\Delta, \quad \mathbf{a}_2 = (PC_h - NT)/\Delta, \quad (\text{B3})$$

where

$$\Delta = MP - NQ. \quad (\text{B4})$$

Evidently, if one can find such  $P$  and  $Q$  (of course, we are interested in the "smallest"  $P$  and  $Q$ ) for a given tube  $(N, M)$  that  $\Delta = \pm 1$  in Eq. (B4), then original primitive vectors  $\mathbf{a}_1$  and  $\mathbf{a}_2$  in Eq. (B3) will be represented through integer amounts of  $\mathbf{C}_h$  and  $\mathbf{T}$ . Correspondingly, an arbitrary vector  $\mathbf{R}_{nm}$ , Eq. (B1), will be expressed through integer quantities of  $\mathbf{C}_h$  and  $\mathbf{T}$  as well. Since the cyclic condition defines  $\mathbf{R}_{nm}$  in Eq. (B1) with accuracy to  $\mathbf{C}_h$ , this would actually mean that the position of any hexagon in the unwrapped tube is determined through a single vector  $\mathbf{T}$ :

$$\mathbf{R}_{nm} \rightarrow \mathbf{R}_i = i\mathbf{T}, \quad (\text{B5})$$

where, e.g.,  $i = nM - mN$  for  $\Delta = 1$ . One can think of the corresponding unit cell built of  $\mathbf{C}_h$  and  $\mathbf{T}$  that would contain only 2 carbons in the cell. Of course, vector  $\mathbf{T}$  does not have to be parallel to the tube axis. The

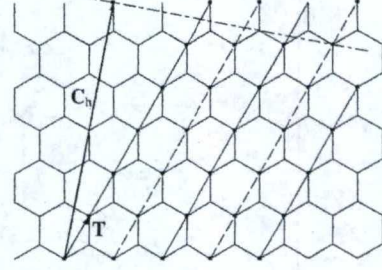


FIG. 8: Unwrapped (4,2) tube with carbons rearranged to form a horizontal strip here. The tube axis is shown by the dash-dotted line. Here  $d_c = 2$  and the  $\mathbf{T}$  vector, Eq. (B2), is defined by the "reduced"  $(P, Q)$  pair (1,0). Two sequences of carbons resulting from  $\mathbf{T}$ -translations are shown by thinner lines: small circles of one sequence are connected by the solid line, and circles of the other by the dashed line. Translation from one sequence to the other is achieved with vector  $\mathbf{C}_h/2$ . All hexagons of the strip would be visited this way, forming effective enumeration of Eq. (B8). The conventional vector  $\mathbf{T}_D = 4\mathbf{a}_1 - 5\mathbf{a}_2$  and such a unit cell would have 28 hexagons.

projection of  $\mathbf{T}$  on the nanotube axis  $T_\parallel = \sqrt{3}a^2\Delta/2C_h$  – it would be directed in opposite ways for  $\Delta = 1$  vs  $\Delta = -1$  – and its modulus determines the corresponding longitudinal period

$$a_\parallel = \sqrt{3}a^2/2C_h, \quad (\text{B6})$$

where  $C_h = |\mathbf{C}_h|$ . Note that vector  $\mathbf{T}$  is different from the symmetry vector defined in Ref. 1.

It is easy to see that the picture described in the previous paragraph is indeed realized whenever  $d_c = 1$  – we will call it the irreducible case – where  $d_c$  is the greatest common divisor of  $N$  and  $M$ . (Considering only positive  $N$  and  $M$  does not restrict the generality.) Then, in fact, any integer value of  $\Delta$  in Eq. (B4) can be established with an appropriate choice of  $P$  and  $Q$ . Examples of positive  $(P, Q)$  pairs satisfying  $\Delta = 1$  are listed here as  $(N, M) \rightarrow (P, Q)$ :  $(3, 1) \rightarrow (1, 0)$ ,  $(3, 2) \rightarrow (2, 1)$ ,  $(5, 2) \rightarrow (3, 1)$ , and  $(10, 9) \rightarrow (9, 8)$ . An illustration for the (3,2) tube is shown in Figure 7. A visual picture of the irreducible case is that of a 1-d chain (of period  $|\mathbf{T}|$ ) that is wrapped around the nanotube cylinder with an appropriate helix angle, as is clearly seen from Figure 7.

"Reducible" cases – with  $d_c > 1$  – can be described in a similar but somewhat more involved fashion. One would extract the irreducible structure factors  $N_1$  and  $M_1$ :

$$N = d_c N_1, \quad M = d_c M_1,$$

so that the greatest common divisor of  $N_1$  and  $M_1$  equals 1. Then the procedure described above for the irreducible case can be applied for the geometry  $(N_1, M_1)$  resulting in the first translational vector  $\mathbf{T}$ . In other words, integers  $P$  and  $Q$  of Eq. (B2) should satisfy condition

$$MP - NQ = d_c. \quad (\text{B7})$$

One however could not visit all hexagons by using only so defined  $\mathbf{T}$ . The needed second translational vector



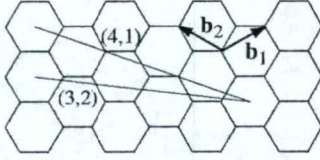


FIG. 9: An illustration of the range of variation of  $k_{\parallel}$  for (3,2) and (4,1) tubes. In the former case  $\mathbf{K}_2 = 2\mathbf{b}_1 - 3\mathbf{b}_2$ , in the latter case  $\mathbf{K}_2 = \mathbf{b}_1 - 4\mathbf{b}_2$ . The corresponding ranges are shown as thick lines between the centers of hexagons of the reciprocal lattice of graphene. Each line crosses several hexagons. If all inside-a-hexagon segments are displaced to one hexagon with a graphene reciprocal vector, they would form a traditional picture of quantization lines in the first BZ of graphene.

can be found as  $C_h/d_c$ . The resulting enumeration of all hexagons will then read as

$$\mathbf{R}_{nm} \rightarrow \mathbf{R}_{ij} = i\mathbf{T} + j\mathbf{C}_h/d_c, \quad j = 0, 1, \dots, d_c - 1. \quad (\text{B8})$$

Index  $i$  here is, as in Eq. (B5), an arbitrary integer that would define unique carbons while  $j$  results only in  $d_c$  unique translations due to the cyclic condition in Eq. (B1). An illustration for the (4,2) tube is shown in Figure 8. A visual picture of the irreducible case is then of  $d_c$  1-d chains (of period  $|\mathbf{T}|$ ) that are wrapped around the nanotube cylinder with an appropriate helix angle. The elementary unit cell contains two carbons and built of vectors  $\mathbf{T}$  and  $\mathbf{C}_h/d_c$ . Longitudinal periodicity will again be determined by the projection of vector  $\mathbf{T}$  on the nanotube axis which is Eq. (4) becoming Eq. (B6) at  $d_c = 1$ .

For the reciprocal lattice vectors, defined through  $\mathbf{K}_1 \cdot \mathbf{C}_h = 2\pi$ ,  $\mathbf{K}_2 \cdot \mathbf{T} = 2\pi$ ,  $\mathbf{K}_1 \cdot \mathbf{T} = 0$ , and  $\mathbf{K}_2 \cdot \mathbf{C}_h = 0$ , one readily obtains

$$\mathbf{K}_1 = -Q\mathbf{b}_1 + P\mathbf{b}_2, \quad \mathbf{K}_2 = M_1\mathbf{b}_1 - N_1\mathbf{b}_2,$$

where  $\mathbf{b}_1$  and  $\mathbf{b}_2$  are primitive graphene reciprocal vectors defined with respect to  $\mathbf{a}_1$  and  $\mathbf{a}_2$ . One easily finds that  $|\mathbf{K}_2|$  indeed coincides with  $2\pi/a_{\parallel}$ . An illustration for cases of (3,2) and (4,1) tubes is given in Figure 9.

This way one arrives at the band excitation picture with  $2d_c$  (for each component of the wave function or polarization) continuous bands corresponding to 2 atoms in the unit cell and  $d_c$  transverse quantization levels, e.g. with quantum numbers

$$l = -d_c/2 + 1, \dots, 0, \dots, d_c/2. \quad (\text{B9})$$

The latter define the quantized component of the parent 2-d quasi-momentum  $\mathbf{k}$  perpendicular to the tube axis:

$$k_{\perp} = (2\pi/C_h)l. \quad (\text{B10})$$

The continuous component  $k_{\parallel}$  parallel to the tube axis, on the other hand, would be defined within a BZ whose width is

$$2\pi/a_{\parallel} = 4\pi C_h/\sqrt{3}d_c a^2. \quad (\text{B11})$$

One can easily calculate that the resulted number of continuous bands and the width of the BZ lead to the correct total number of states in the system, which corresponds to  $2C_h/\sqrt{3}a^2$  hexagons per unit length of the nanotube.

The conclusion that there are only  $d_c$  “truly unique” quantization levels can be confirmed another way as well. If  $\mathbf{G} = n_1\mathbf{b}_1 + n_2\mathbf{b}_2$  is the vector of the reciprocal lattice of graphene, then  $\mathbf{k}_1 = \mathbf{k} + \mathbf{G}$  is physically equivalent to  $\mathbf{k}$ . In general,  $\mathbf{k}$  and  $\mathbf{k}_1$  may correspond to different quantum numbers in Eq. (5), say  $l$  and  $l_1$ . One derives the integer difference of these quantum numbers as

$$\delta l = l - l_1 = n_1 N + n_2 M = d_c(n_1 N_1 + n_2 M_1). \quad (\text{B12})$$

Once again, the last, “irreducible”, factor in Eq. (B12) can take any integer values:

$$n_1 N_1 + n_2 M_1 = 0, \pm 1, \pm 2, \dots,$$

with appropriate choices for integer  $n_1$  and  $n_2$ . It is then clear that the number of unique sub-bands in the extended scheme equals precisely  $d_c$  – one can, e.g., choose quantum numbers of Eq. (B9) for “independent” sub-band indexing, all other values of  $l$  would be reducible to independent values with the appropriate adjustment for the one-dimensional continuous quasi-momentum  $k_{\parallel}$ .

It is worth mentioning that in the  $(N, M)$  family of nanotubes with  $N > M$ , it is the armchair and zigzag nanotubes that have maximal number of transverse quantization levels  $d_c = N$ . The tubes immediately next to them,  $(N, N-1)$  and  $(N, 1)$ , on the other hand, would have only one quantization level. The armchair tubes have then the longitudinal period of  $a/2$ , twice as small as is with the conventional definition.<sup>1</sup> One can easily see it with  $\mathbf{T}$  vector defined by the  $(P, Q)$  pair (1,0).

<sup>1</sup> R. Saito, G. Dresselhaus, and M. S. Dresselhaus, *Physical Properties of Carbon Nanotubes* (Imperial College Press, London, 1998).

<sup>2</sup> M. S. Dresselhaus and P. Eklund, *Adv. Phys.* **49**, 705 (2000).

<sup>3</sup> J. X. Cao, X. H. Yan, Y. Xiao, Y. Tang, and J. W. Ding, *Phys. Rev. B* **67**, 045413 (2003).

<sup>4</sup> D. Sánchez-Portal, E. Artacho, J. M. Soler, A. Rubio, and P. Ordejón, *Phys. Rev. B* **59**, 12678 (1999).

<sup>5</sup> J. Yu, R. K. Kalia, and P. Vashishta, *J. Chem. Phys.* **103**,



- 6697 (1995).
- <sup>6</sup> N. Nishiguchi, Y. Ando, and M. N. Wybourne, *J. Phys.: Condens. Matter* **9**, 5751 (1997).
  - <sup>7</sup> L. G. C. Rego and G. Kirczenow, *Phys. Rev. Lett.* **81**, 232 (1998).
  - <sup>8</sup> K. Schwab, E. A. Henriksen, J. M. Worlock, and M. L. Roukes, *Nature* **404**, 974 (2000).
  - <sup>9</sup> E. L. Eliel, S. H. Wilen, and M. P. Doyle, *Basic Organic Stereochemistry* (Wiley, New York, 2001).
  - <sup>10</sup> P. Y. Yu and M. Cardona, *Fundamentals of Semiconductors* (Springer, Berlin, 1999).
  - <sup>11</sup> Š. Markuš, *The Mechanics of Vibrations of Cylindrical Shells* (Elsevier, Amsterdam, 1988).
  - <sup>12</sup> L. D. Landau and E. M. Lifshitz, *Elasticity Theory* (Pergamon, Oxford, 1986).
  - <sup>13</sup> Y. M. Sirenko, M. A. Strosio, and K. W. Kim, *Phys. Rev. E* **53**, 1003 (1996).
  - <sup>14</sup> Y. M. Sirenko, M. A. Strosio, and K. W. Kim, *Phys. Rev. E* **54**, 1816 (1996).
  - <sup>15</sup> M. A. Strosio and M. Dutta, *Phonons in Nanostructures* (Cambridge University Press, Cambridge, 2001).
  - <sup>16</sup> O. Madelung, *Introduction to Solid-State Theory* (Springer, Berlin, 1978).
  - <sup>17</sup> G. G. Samsonidze, R. Saito, A. Jorio, A. G. Souza Filho, A. Grüneis, M. A. Pimenta, G. Dresselhaus, and M. S. Dresselhaus, *Phys. Rev. Lett.* **90**, 027403 (2003).
  - <sup>18</sup> A. E. H. Love, *Treatise on the Mathematical Theory of Elasticity* (Dover, New York, 1944).
  - <sup>19</sup> J. W. S. Rayleigh, *The theory of sound* (Dover, New York, 1976).
  - <sup>20</sup> S. P. Timoshenko and S. Woinowsky-Krieger, *Theory of Plates and Shells* (McGraw-Hill, New York, 1959).
  - <sup>21</sup> S. P. Timoshenko and J. M. Gere, *Theory of Elastic Stability* (McGraw-Hill, New York, 1961).
  - <sup>22</sup> R. N. Arnold and G. B. Warburton, *Proc. Roy. Soc. A* **197**, 238 (1949).
  - <sup>23</sup> B. I. Yakobson, C. J. Brabec, and J. Bernholc, *Phys. Rev. Lett.* **76**, 2511 (1996).
  - <sup>24</sup> J. Kürti, V. Zólyomi, M. Kertesz, and G. Sun, *New Journal of Physics* **5**, 125.1 (2003).
  - <sup>25</sup> Y. N. Gartstein, A. A. Zakhidov, and R. H. Baughman, *Phys. Rev. B* **68**, 115415 (2003).
  - <sup>26</sup> D. H. Robertson, D. W. Brenner, and J. W. Mintmire, *Phys. Rev. B* **45**, 12592 (1992).
  - <sup>27</sup> See Appendix A for a discussion of some of these issues for a simpler example.



#### **5.4 “Phonon-Polariton Physics: Thermal Conductivity, Phonon-Polariton Lasers and Phonon Transistors in Nanostructures”**





*"DSRC Nanoscopic Phonon Engineering Workshop"*

*Booz Allen Hamilton, Arlington, May 9, 2005*



**Phonon-Polariton Physics:**  
**Thermal Conductivity, Phonon-Polariton Lasers**  
**and**  
**Phonon Transistors in Nanostructures**

**Anvar Zakhidov on behalf of UTD PEOM Team**

*NanoTech Institute*  
*University of Texas at Dallas*

Anvar A. Zakhidov, University of Texas at Dallas



**Outline :**

**Motivation for Tuning Phonon K(T) in Our 2 Main Systems.**

**System 1.**

**Phonon-Polaritons: New Mechanism of Thermal Conductivity**  
**Phonon-Polariton Lasers**

**Overview of Phonon-Polaritonics**

**System 2.**

**Carbon Nanotube Yarns and Sheets for Enhanced Thermal Conductivity**  
**Phonon Transistor with Charge Injection Gate**

Anvar A. Zakhidov, University of Texas at Dallas





## Our Main Systems and Materials:



### 1. New Mechanism of Phonon-Polariton Thermal Conductivity

### 2. Carbon Nanotubes with Enhanced $K(T)$ CNT in CNT Yarns and Oriented CNT bucky-aerogels

Anvar A. Zakhidov, University of Texas at Dallas

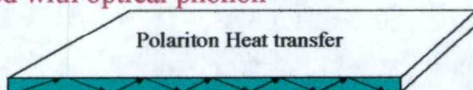


## Our Main Concepts: "Solid State Heat Pipes" And "Phonon Transistor or Valve"



Two types of heat pipes:

1. We predict an analog of optical fiber for heat transfer by light mixed with optical phonon



Polariton Heat transfer

Wave-guide in which Phonon-Polariton can propagate like light and contribute to  $K(T)$  of low- $K$  organic matter

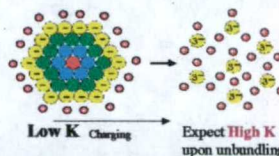
2. CNT are nanoscale analog of optical fibers in which phonons flow is ballistic and 1-d. Can it be a Heat-pipe

How to preserve this ballistic transport and high  $K$  in fibers of CNTs and CNT dispersed in polymers?

Giant  $K(T) = 3000 - 6000$  W/mK, Predicted in SWCNT and measured in MWCNTs



a) Conjugated Polymers-CNT for distributed heat removal in Organic Electronics



Low  $K$  Charging

Expect High  $K$  upon unbundling

Anvar A. Zakhidov, University of Texas at Dallas





## Physical Ideas

### for Engineering Phonons at Nanoscale for Enhanced thermal conductivity $K(T)$



1. Optical Phonons dispersion is flat, group velocity small: no contribution to  $K(T)$
2. It can be really engineered: changed to **Phonon-Polariton** with large  $V_g$  and we found sizable contribute to thermal conductivity  $K(T)$ .
3. In Organic matter a **Phonon-Laser** is proposed, which can be pumped by heat and produce monochromatic and coherent IR
4. In single Carbon nanotubes phonons are ballistic and  $L_m \sim 1 \mu m$ , providing high  $K(T)$  for one CNT.

Our Approach is to achieve and control high  $K(T)$  in real systems:

- unbundle tubes: decrease **Phonon-Phonon** scattering both inter-tube and UP
- coat tubes with polymers and mix into a matrix of low-K conjugated polymer at concentration lower or close to percolation for nano-scale distributed heat removal.

5. **Phonon-Transistor** concept appeared as a result of tunable  $K(T)$

Anvar A. Zakhidov, University of Texas at Dallas

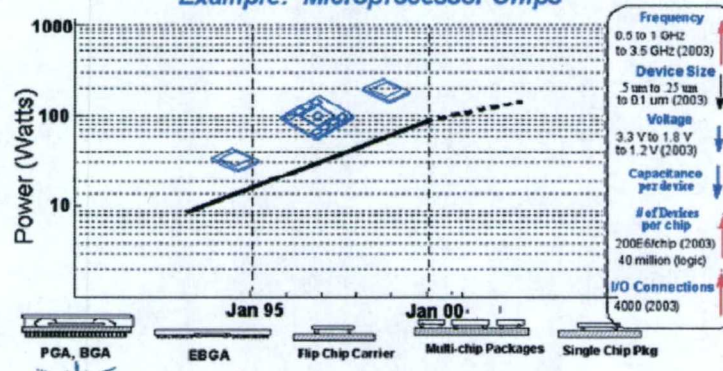


## DoD Needs Better Cooling Systems for Electronic Warfare Chips



### High-performance Chip Dissipation

Example: Microprocessor Chips



Anvar A. Zakhidov, University of Texas at Dallas

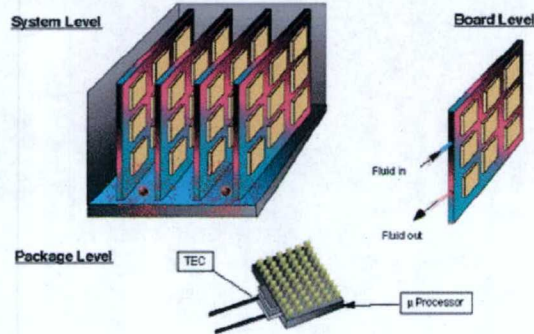




DARPA has a strong interest in Thermal Management: Previous HERETIC Program and Phonon Engineering Program are examples



### Conventional Thermal Management Hierarchy



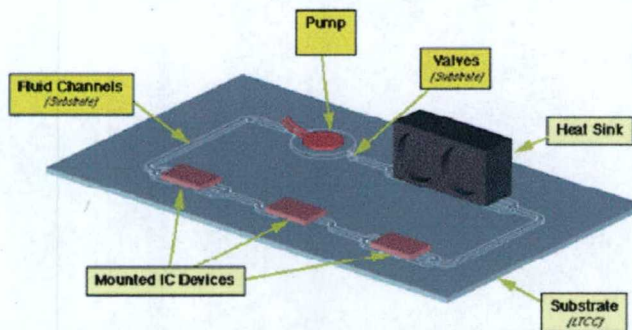
Anvar A. Zakhidov, University of Texas at Dallas



State-of-Art Heat Removal Circuitry Targets Fluids: Solid State Systems for cooling would be much more attractive for DoD Applications



### Fluidic Based Cooling Using Channels



Anvar A. Zakhidov, University of Texas at Dallas





## Impact 1: for Heat Management Circuitry for DoD Applications



### Goal:

Develop micro- and nano-scale solid state heat removal circuitry with control devices (valves, couplers, switches, etc.) which can be Ultimately integrated with electronic and photonic circuitry. This technology will be unique, since it will enable controllable, adaptable, distributed and programmable thermal management

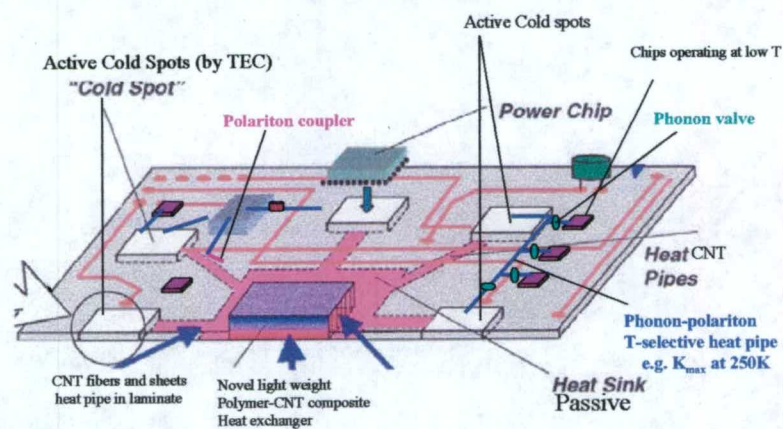
### Impact:

Efficient, compact and controllable (with active feedback) heat removal circuitry will enable design of low power, small form-factor DoD systems, such as radars, high performance computers, and other electronic and photonic warfare subsystems

Anvar A. Zakhidov, University of Texas at Dallas



## Our Concept: Solid State Cooling Circuitry Integrated on Chip, Heat Pipes (CNTs or "Polaritonic Fibers")



Anvar A. Zakhidov, University of Texas at Dallas



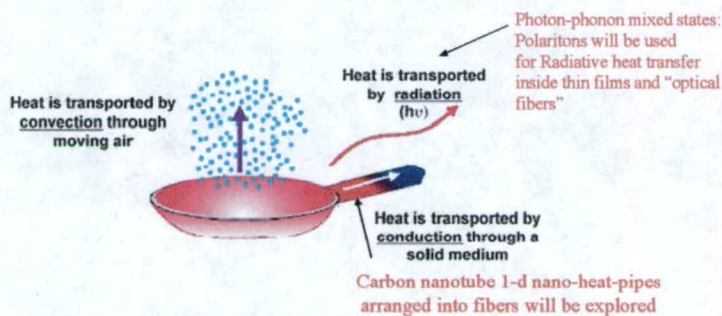


## Physical Concepts for Solid State Heat Pipes:

1. Heat Transfer by Polaritons in Organic Thin Films
2. Achieve high  $K(T)$  of Carbon Nanotubes with engineered Phonon-phonon interaction



### Modes of Heat Transport



Anvar A. Zakhidov, University of Texas at Dallas



## Phonon-Polaritons Contribution to Thermal Conductivity

### Prospects for Organic Phonon-Polariton Heat Pipes And Phonon-Polariton Laser

### Overview of Polaritonics (MIT, France,)



Anvar A. Zakhidov, University of Texas at Dallas





## Thermal conductivity in solis:



- Known: by phonons, photons, electrons
  - **New: by Phonon-Polaritons**
- Bulk and Thin Films (Microcavity)
  - Ballistic regime:  $\Lambda(\omega) > d$
  - Statistical, diffusive regime  $\Lambda(\omega) \ll d$
- Phonon-Polariton Microcavity Laser

Anvar A. Zakhidov, University of Texas at Dallas



## Motivation



- Contribution of phonon-polaritons to thermal conductivity **has never been estimated**  
(Klemens P.G. et al. Term. Conduct. (1988), 19, 453 )
- Phonon-polaritons can have **very long** mean free paths  $\Lambda(\omega)$  of mm and even cm – **ballistic propagation**
- **Enhancement** of  $K(T)$  may be expected in nanostructures with sizes,  $d$  smaller than  $\Lambda(\omega)$

In thick samples  $K(T)$  still can have contribution from polaritons

Anvar A. Zakhidov, University of Texas at Dallas

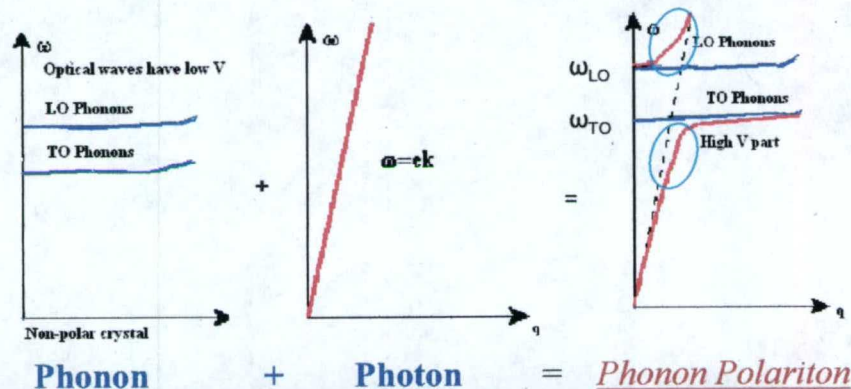




## What is phonon-polariton?



Polariton is a mixed excitation, has phonon and electromagnetic components, and can propagate with high velocity



Anvar A. Zakhidov, University of Texas at Dallas

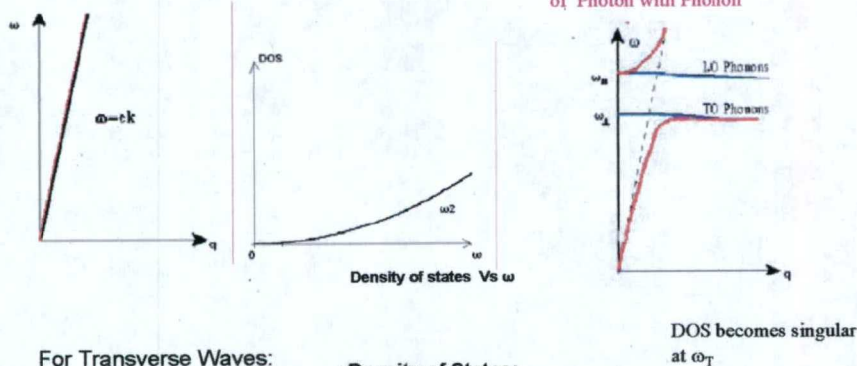


## POLARITONS vs PHOTONS



Photons in the Bulk,  $\epsilon = \epsilon_\infty$  - constant

Polaritons: Coherent mixture of Photon with Phonon



For Transverse Waves:

$$q^2 \epsilon^2 / \omega^2 = \epsilon_\infty$$

$$\omega = q \epsilon / \sqrt{\epsilon_\infty}$$

Density of States:

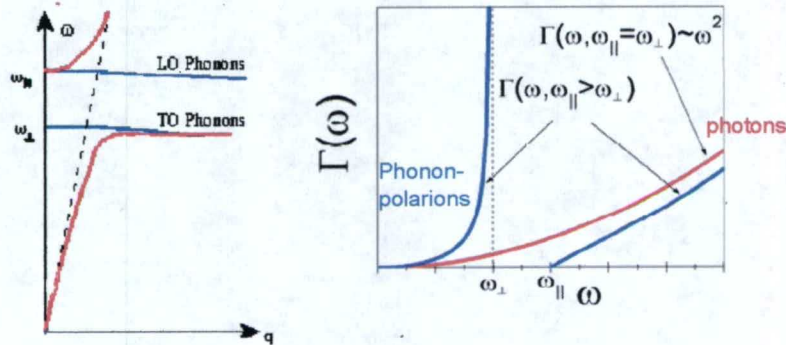
$$\text{DOS} \sim q^2 dq / (2\pi)^3 \sim \omega^2 d\omega$$

Anvar A. Zakhidov, University of Texas at Dallas





## Phonon-Polaritons in Bulk: Dispersion and DOS



Anvar A. Zakhidov, University of Texas at Dallas

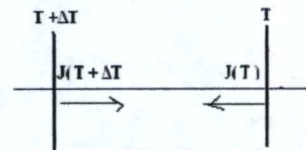


## PHOTONS: Radiative Contribution to Thermal Conductivity in ballistic regime (Landauer)

$$J_z = 2 \int \left( \frac{k^2}{(2\pi)^3} \right) \left( \frac{1}{e^{\hbar\omega(k)/k_B T} - 1} \right) (\hbar\omega(k)) \left( \frac{d\omega}{dk} \right) dk \sin\theta \cos\theta d\phi$$

$$\text{Total current } J = J_z(T + \Delta T) - J_z(T)$$

$$\frac{J(T)}{\Delta T} \cong 26 \frac{k_B c}{(2\pi)^2 \sqrt{\epsilon_\infty}} \left( \frac{k_B T \sqrt{\epsilon_\infty}}{\hbar c} \right)^3$$



Anvar A. Zakhidov, University of Texas at Dallas





## Ballistic Propagation



$$\varepsilon = \varepsilon_\infty$$

$$J(T) = 2 \int_0^\infty \frac{q^2 dq \sin \theta}{(2\pi)^3} \cos \theta \hbar \omega \frac{d\omega}{dq} [\eta_{hot} - \eta_{cold}]$$

$$\frac{J(T)}{\Delta T} = \frac{k_B c}{(2\pi)^2 \sqrt{\varepsilon_\infty}} \left( \frac{k_B T \sqrt{\varepsilon_\infty}}{\hbar c} \right)^3 \int_0^\infty \frac{x^4 e^x}{(e^x - 1)^2} dx$$

But we have,  $\int_0^\infty \frac{x^4 e^x}{(e^x - 1)^2} dx \cong 26$

$$\frac{J(T)}{\Delta T} \cong 26 \frac{k_B c}{(2\pi)^2 \sqrt{\varepsilon_\infty}} \left( \frac{k_B T \sqrt{\varepsilon_\infty}}{\hbar c} \right)^3$$

Anvar A. Zakhidov, University of Texas at Dallas



## Phonon-Polaritons:

Contribution to Thermal Conductivity:  
Resonance with Optical Phonon at  $\omega = \omega_\perp$



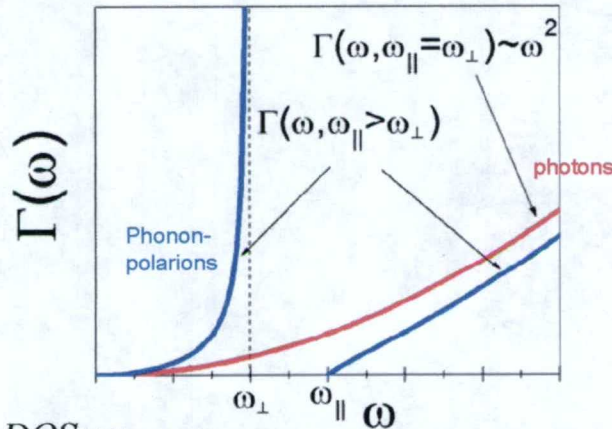
$$k^2 = \frac{\varepsilon_\infty \omega^2}{c^2} \left( \frac{\omega_\parallel^2 - \omega^2}{\omega_\perp^2 - \omega^2} \right), \quad \varepsilon(\omega) = \varepsilon_\infty \left( \frac{\omega_\parallel^2 - \omega^2}{\omega_\perp^2 - \omega^2} \right)$$

$$\begin{aligned} \frac{J^{BULK}(T)}{\Delta T} = & \frac{k_B c}{(2\pi)^2 \sqrt{\varepsilon_\infty}} \left( \frac{k_B T \sqrt{\varepsilon_\infty}}{\hbar c} \right)^3 \left\{ \int_0^{x_\perp} \left( \frac{(x_\parallel^2 - x^2)(x_\perp^2 - x^2)}{(x_\perp^2 - x^2)^2 + 4x^2 x_\perp^2 \delta^2} \right) \frac{x^4 e^x}{(e^x - 1)^2} dx + \right. \\ & \left. + \int_{x_\parallel}^\infty \left( \frac{(x_\parallel^2 - x^2)(x_\perp^2 - x^2)}{(x_\perp^2 - x^2)^2 + 4x^2 x_\perp^2 \delta^2} \right) \frac{x^4 e^x}{(e^x - 1)^2} dx \right\} \end{aligned}$$

$$x_\perp = \frac{\hbar \omega_\perp}{k_B T}, \quad x_\parallel = \frac{\hbar \omega_\parallel}{k_B T}$$

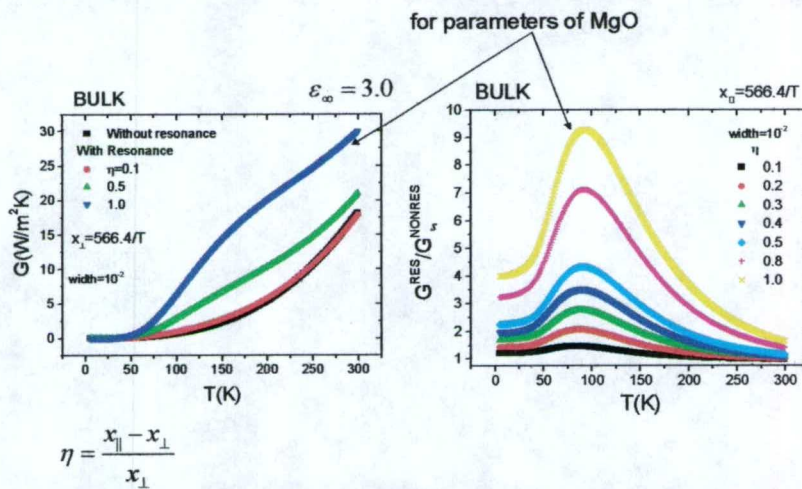
Anvar A. Zakhidov, University of Texas at Dallas





$$\Gamma(\omega) \propto DOS \times v_{GROUP}$$

Anvar A. Zakhidov, University of Texas at Dallas



Anvar A. Zakhidov, University of Texas at Dallas

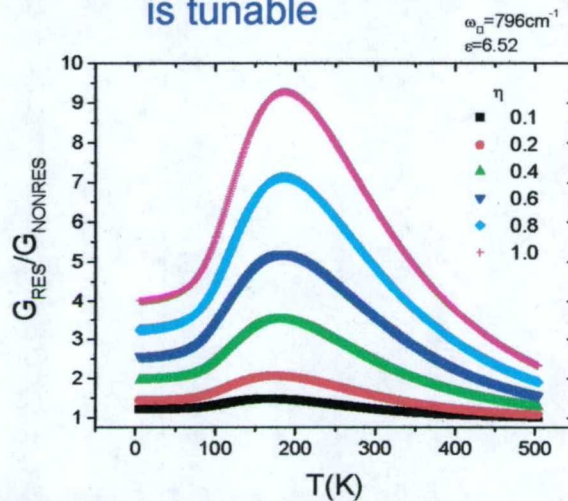




## Position of the enhancement peak is tunable



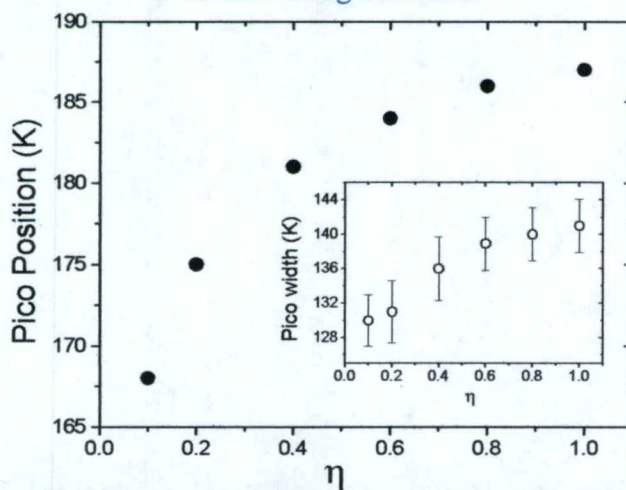
For parameters  
of phonon in SiC



Anvar A. Zakhidov, University of Texas at Dallas



## The Dependence of T-Peak Position on the Tuning Parameter

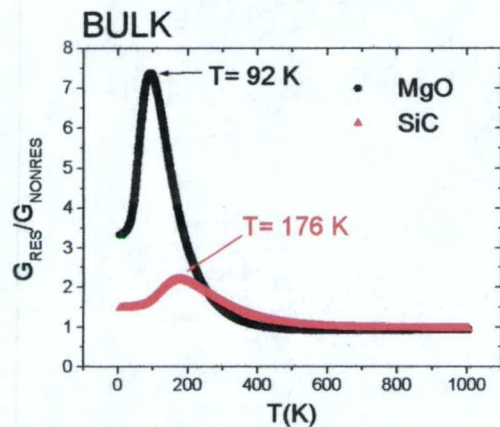


Anvar A. Zakhidov, University of Texas at Dallas





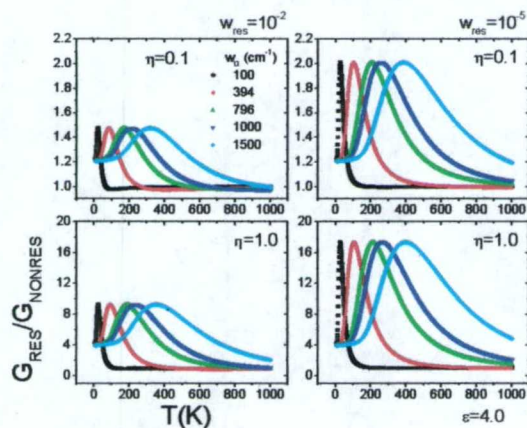
## Comparison of Polaritonic $K(T)$ in SiC and MgO



Anvar A. Zakhidov, University of Texas at Dallas



## Position and intensity of the enhancement peak is tunable



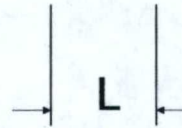
- Depends on:
- Frequency  $\omega_{TO}$
  - Line width  $\delta\omega$
  - Polaritonic gap  $\Delta$

To get a peak at RT, we need optical phonons with  $\omega_{TO} = 1500\text{ cm}^{-1}$

Anvar A. Zakhidov, University of Texas at Dallas



$$q^2 = \frac{\omega^2 \varepsilon_\infty}{c^2} - \left(\frac{\pi}{L} s\right)^2$$



Film thickness

$$L = \lambda_{\text{TO}}/2$$

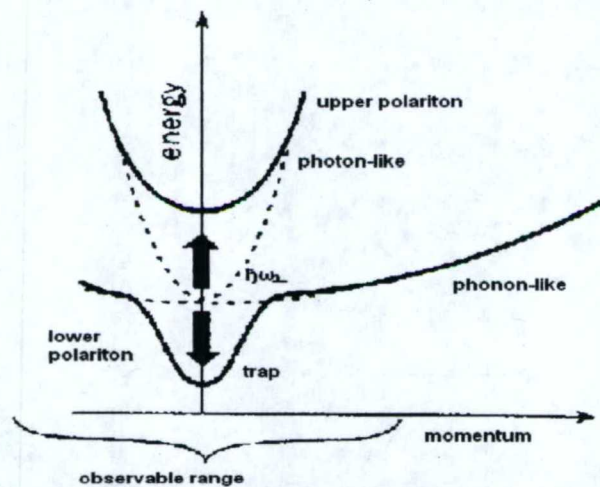
$$G^{\text{eff}}(L, T) = \frac{1}{L} \frac{J^{\text{MC}}}{\Delta T} = \frac{2}{L} \frac{k_B \varepsilon_\infty}{c(2\pi)^2} \left(\frac{k_B T}{\hbar}\right)^2 \sum_{s=1}^{\infty} F(x_s)$$

$$F(x_s) \equiv \int_{x_s}^{\infty} x^2 \sqrt{x^2 - x_s^2} \frac{e^x}{(e^x - 1)^2} dx$$

$$\omega(q=0) = \frac{\pi c}{L \sqrt{\varepsilon_\infty}}$$

$$x_s \equiv \frac{\hbar \omega(q=0)}{k_B T} s, \quad s = 1, 2, \dots$$

Anvar A. Zakhidov, University of Texas at Dallas

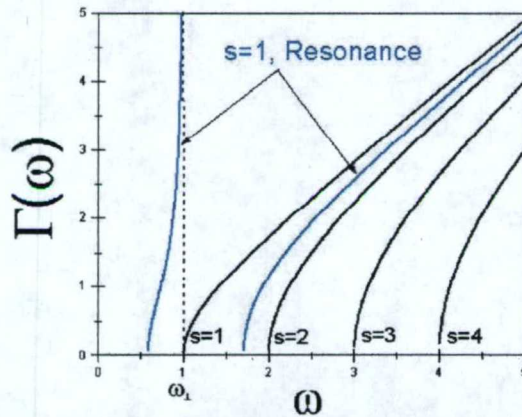


Anvar A. Zakhidov, University of Texas at Dallas





$$\Gamma(\omega) \propto DOS_{MC} \times v_{GROUP}$$



Anvar A. Zakhidov, University of Texas at Dallas



### Thin Films: Phonon-polariton contribution to thermal conductivity

$$q^2 = \frac{\varepsilon_\infty}{c^2} \left( \omega^2 - \omega_c^2 + \omega^2 \left( \frac{\omega_\perp^2 - \omega_\parallel^2}{\omega^2 - \omega_\perp^2} \right) \right)^2$$

$$\frac{J^{MC}}{\Delta T} = \frac{k_B \varepsilon_\infty}{c(2\pi)^2} \left( \frac{k_B T}{\hbar} \right)^2 \left\{ \int_{x_1}^{x_\perp} f(x, x_c, x_\parallel, x_\perp) dx + \int_{x_2}^{\infty} f(x, x_c, x_\parallel, x_\perp) dx \right\}$$

$$f(x, x_c, x_\parallel, x_\perp) \equiv \frac{x^2 e^x}{(e^x - 1)^2} \sqrt{x^2 - x_c^2 + x^2 \left( \frac{x_\perp^2 - x_\parallel^2}{x^2 - x_\perp^2} \right)}$$

Thin films = Planar waveguides = Planar microcavities

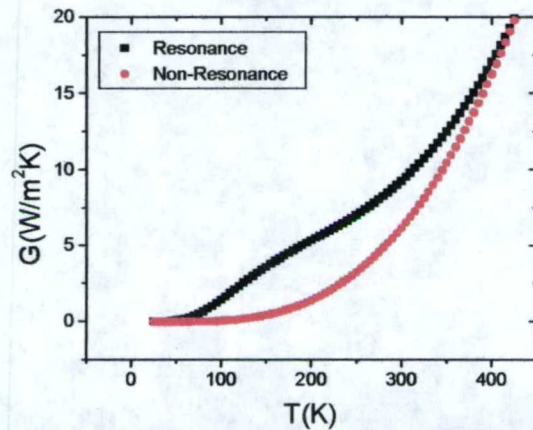
Anvar A. Zakhidov, University of Texas at Dallas





## Thin films: resulting enhancement of thermal conductivity

(Again from difference in DOS)

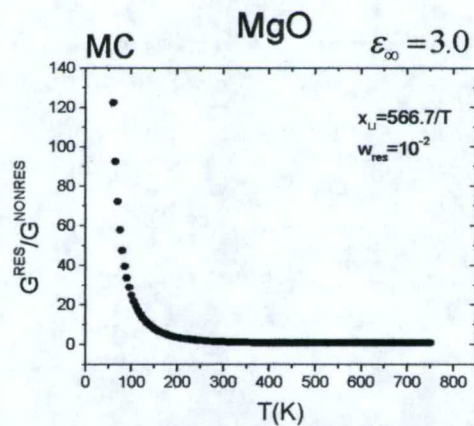


MgO

Anvar A. Zakhidov, University of Texas at Dallas



## Relative Enhancement of Heat Conductance by Polaritonic Effect in MICROCAVITY: The ratio of $G_{res}$ to $G_{nonres}$



Anvar A. Zakhidov, University of Texas at Dallas





## Thick samples: $\Lambda(\omega) < d$ Diffusive heat transfer



The thermal conductivity  $\kappa(T)$  can be calculated by the using of following well-known expression

$$\kappa(T) = \frac{1}{3} \sum_p \int C(\omega) v(\omega) \Lambda(\omega) d\omega, \quad (4)$$

where  $\omega$  is the polariton frequency,  $C(\omega)$  is its thermal capacity,  $v(\omega)$  is its the group velocity, and  $\Lambda(\omega)$  is its mean-free-path. The sum is carried out over two transverse polariton polarizations  $p$ .

### Phonon-polariton in heat conduction

V. R. Coluci<sup>1,3</sup>, A. A. Zakhidov<sup>1</sup>, and V. M. Agranovich<sup>1,2\*</sup>

<sup>1</sup>NanoTech Institute and Department of Chemistry, University of Texas, Richardson, Texas 75080  
<sup>2</sup>Institute of Spectroscopy, Russian Academy of Sciences, 142190 Troitzk, Moscow Region, Russia and

Anvar A. Zakhidov, University of Texas at Dallas



## Specific Heat $C(\omega)$



$$\begin{aligned} C(\omega) &= \frac{1}{V} \frac{dE}{dT} = \\ &= \frac{D(\omega)}{V} \frac{(\hbar\omega)^2 e^{\hbar\omega/k_B T}}{k_B T^2 (e^{\hbar\omega/k_B T} - 1)^2} \end{aligned}$$

$$E(\omega, T) = \hbar\omega \frac{D(\omega)}{\exp(\hbar\omega/k_B T) - 1},$$

where the density of states  $D(\omega)$  is given by

$$\frac{D(\omega)}{V} = \frac{4\pi k^2}{(2\pi)^3} \frac{dk}{d\omega}.$$

Anvar A. Zakhidov, University of Texas at Dallas





## Mean free path $\Lambda(\omega)$ of Phonon-Polaritons:



Since the intensity  $I$  is proportional to the squared electrical field we have

$$I \sim |E|^2 \sim e^{2kz} = e^{2(n' + in'')\omega z/c} \sim e^{-2n''\omega z/c} = e^{-z/\Lambda(\omega)}$$

$$\Lambda(\omega) = \frac{c}{2\omega n''(\omega)}.$$

Using the relation

$$\frac{k^2(\omega)c^2}{\omega^2} = (n' + in'')^2 = \epsilon(\omega) = \epsilon' + i\epsilon'', \quad (11)$$

and assuming weak absorption ( $(n'')^2 \simeq 0$ ) one can obtain

$$\epsilon'(\omega) = \epsilon_\infty \left( 1 + \frac{(\omega_0^2 - \omega_1^2)(\omega_1^2 - \omega^2)}{(\omega_1^2 - \omega^2)^2 + 4\Gamma^2\omega^2} \right), \quad (12)$$

$$\epsilon''(\omega) = \epsilon_\infty \left( \frac{2\Gamma\omega(\omega_0^2 - \omega_1^2)}{(\omega_1^2 - \omega^2)^2 + 4\Gamma^2\omega^2} \right), \quad (13)$$

$$n'(\omega) = \sqrt{\epsilon'(\omega)}, \quad n''(\omega) = \frac{\epsilon''(\omega)}{2n'(\omega)}. \quad (14)$$

Anvar A. Zakhidov, University of Texas at Dallas



## Check of Approximation for $\Lambda(\omega)$ in MgO

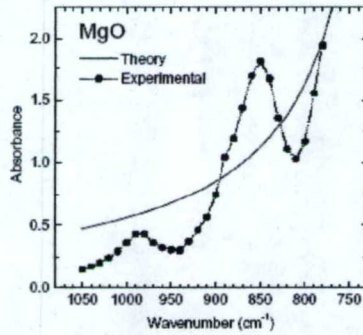


FIG. 2: Absorption spectra of MgO. Experimental points correspond to the MgO crystal at  $T=305$  K with 0.16 mm thick<sup>7</sup>. The dotted line just connects the points.

Anvar A. Zakhidov, University of Texas at Dallas





## Polaritonic K(T) in kinetic limit



$$\kappa(T) = \frac{k_B^3 T^2}{3\pi^2 \hbar^2 c} \left[ \int_0^{x_\perp} h(x) dx + \int_{x_\parallel}^{\infty} h(x) dx \right]$$

where

$$x(T) \equiv \frac{\hbar\omega}{k_B T}, \quad x_\perp(T) \equiv \frac{\hbar\omega_\perp}{k_B T}, \quad x_\parallel(T) \equiv \frac{\hbar\omega_\parallel}{k_B T},$$

$$h(x) \equiv \frac{x^2 e^x}{(e^x - 1)^2} \frac{\sqrt[3]{\varepsilon'(x)}}{\varepsilon''(x)}$$

Anvar A. Zakhidov, University of Texas at Dallas



## Comparison of Polaritonic contribution with experimental K(T)

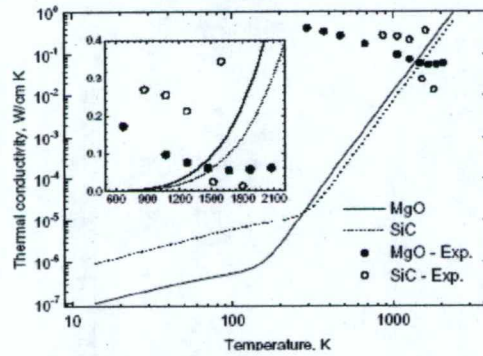


FIG. 3: Thermal conductivity as function of temperature. The lines were obtained using the expression (16). The inset graph is the zoom for the region  $600 \text{ K} < T < 2200 \text{ K}$ .

Anvar A. Zakhidov, University of Texas at Dallas





Giant vibrational resonances in  $A_6C_{60}$  compounds

Ke-Jian Fu,\* William L. Karney, Orville L. Chapman, Shiou-Mei Huang, Richard B. Kaner, Francois Diederich, Károly Holczér,<sup>†</sup> and Robert L. Whetten

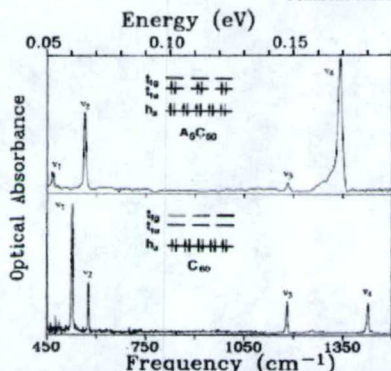


FIG. 1. Optical absorption spectrum in the midinfrared region of films of  $C_{60}$  (lower panel) and  $A_6C_{60}$  (upper panel), recorded

Anvar A. Zakhidov, University of Texas at Dallas

$F_{4u}$  optical IR mode is a great candidate for OP-Polariton with tunable K(T).

The intensity of optical absorption increase 88 times (!) upon doping  $x=6$  electrons in  $C_{60}$

Oscillator strength  $S \sim x^2$ , increases dramatically,  
Polariton Gap ( TO-LO splitting):  $\Delta \sim S^{1/2}$  ,  
So that the parameter  $\eta \sim x$

Polaritonic Thermal conductivity  $K(T) \sim \eta \sim x$ ,

K becomes tunable by doping level x.

K can be increased x times ( 6 in measured case)



Map of materials to choose  $\omega$  and  $\eta$

Material	$\omega_{\perp}$ (cm <sup>-1</sup> )	$\omega_{\parallel}$ (cm <sup>-1</sup> )	$\epsilon_{\infty}$	$\eta$
TlBr	48	114	5.41	1.375
TlCl	64	161	5.1	1.516
RbI	75	103	2.62	0.373
AgBr	81	136	4.62	0.679
AgCl	103	171	4.04	0.660
K-I	103	144	2.59	0.398
KBr	116	168	2.34	0.448
NaI	117	181	3.03	0.547
RbCl	119	178	2.14	0.496
NaBr	135	210	2.63	0.556
KCl	144	216	2.16	0.500
RbF	160	293	1.93	0.831
NaCl	164	262	2.31	0.598
LiBr	173	354	3.16	1.046
KF	192	330	1.85	0.719
LiCl	204	425	2.75	1.083
NaF	246	424	1.72	0.724
LiF	304	660	1.9	1.171

Anvar A. Zakhidov, University of Texas at Dallas



$$\eta = \frac{\omega_{\parallel} - \omega_{\perp}}{\omega_{\perp}}$$





Map of  
materials  
to choose  
 $\omega$  and  $\eta$

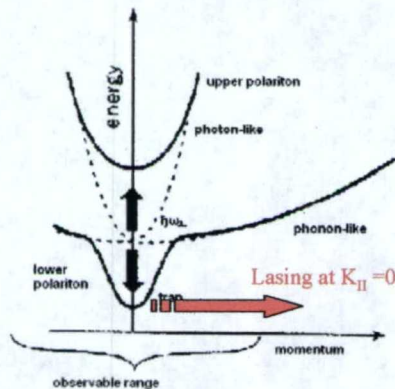
Material	$\omega_{\perp}$ (cm <sup>-1</sup> )	$\omega_{\parallel}$ (cm <sup>-1</sup> )	$\epsilon_{\infty}$	$\eta$
CdTe	140	171	7.2	0.221
CdSi	171	214	—	0.251
ZnTe	177	208	7.3	0.175
InSb	179	200	15.7	0.117
BaF <sub>2</sub>	184	336	2.16	0.826
ZnSe	203	252	5.9	0.241
CdTe	202	380	2.4	0.881
CuCl	172	210	3.71	0.221
InAs	210	243	12.3	0.157
SrF <sub>2</sub>	217	387	2.07	0.783
GaSb	225	233	14.4	0.036
CaF <sub>2</sub>	257	464	2.05	0.805
CdS	234	305	—	0.303
ZnS	274	349	5.2	0.274
GaP	366	402	9.1	0.098
MgO	394	719	2.956	0.825
SiC	796	970	6.52	0.219



Anvar A. Zakhidov, University of Texas at Dallas



## Idea of IR Phonon-Lasers: Condensation of phonon-polaritons in planar microcavities at Room-T



•Exciton-polariton condensation  
has been recently demonstrated  
in semiconductor MC.

•If condensation of lowest  
energy cavity phonon-polaritons  
is achievable, IR lasing would  
become possible with  
**zero pumping threshold.**

•The life-time of phonon-  
polaritons is a crucial parameter:

$$t_{\text{lifetime}} > t_{\text{relaxation}}$$

is needed

Anvar A. Zakhidov, University of Texas at Dallas

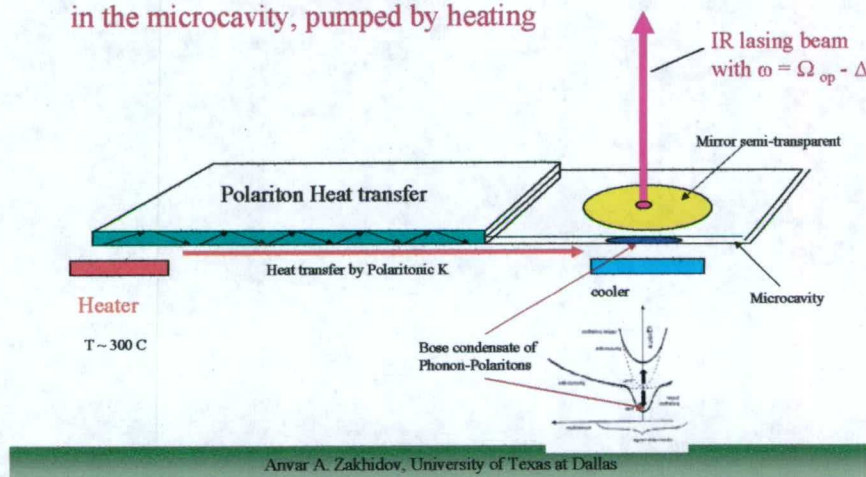




## New Concepts: "Phonon-Polariton Laser"



1. We propose: Phonon-Polariton laser in the microcavity, pumped by heating



## Phonon-Polariton Laser



- **Polariton Laser** - The polariton laser is a relatively new lasing mechanism postulated by several research groups and recently observed in GaAs at cryogenic temperatures by a Japanese researcher visiting in the US. The laser operates on the principle of Bose-Einstein condensation of excitonic polaritons within microcavities to align phase, with radiation from the condensate. Theoretical calculations by Professor Kavokin's group indicate that the same opto-electronic effects will be possible in wide-bandgap semiconductors at room temperature. Their calculations show that the kinetic blocking of polariton relaxation preventing formation of the B-E condensation of polariton phase at low temperatures should disappear at higher temperatures. These lasers have very low threshold currents, are very efficient, produce very little heat, and should have applications in very low power optical communications and optical computing.

Anvar A. Zakhidov, University of Texas at Dallas





## European Activities



- **New Laser Principle for Low Power and Fast Optoelectronic Devices:** Dr. Harvey, of ARL-ERO, visited Blaise Pascal University, FR, to discuss new room temperature lasing mechanism based on Bose-Einstein condensation in wide-bandgap semiconductor microcavities. This opens the door to very low power laser communications, THz optical signal processing, quantum computing, spintronic devices, THz modulation in photonic bandgap structures, and THz electronic signal processing. Such devices will enable the communication and processing of the massive amounts of data necessary to support FCS concepts. The Physics Dept at, Blaise Pascal University, has a very strong theoretical program and a good experimental program which is focusing on electron-light interactions in semiconductors, in particular excitonic polariton effects in semiconductor microcavities. Professor Kavokin leads a European collaboration funded by the European Community and focused on phenomena in semiconductor microcavities under the EC Framework program on "High Technology for Communications and Information Processing".

Anvar A. Zakhidov, University of Texas at Dallas



## Polariton Transistor



- **THz Excitonic Polariton Transistor and THz Optoelectronic Devices** - The Blaise Pascal group has shown theoretically and experimentally that the excitonic polaritons can be accelerated in the plane of microcavities, with the gradient of the microcavity thickness acting as the forcing function. Observed velocities are one to two orders of magnitude faster than the electronic ballistic transport in bulk semiconductors, with the potential for using the polaritons as carriers in a very fast transistor type device and for ultrafast optical processing.
- 

Anvar A. Zakhidov, University of Texas at Dallas





## Polaritonics: bridging the gap between electronics and photonics



- Between electronics and photonics there exists a frequency gap of approximately 2 octaves, i.e. the frequency range between 100~GHz and 10~THz. Here we demonstrate that **phonon-polaritons in ferroelectric crystals** like LiNbO<sub>3</sub> or LiTaO<sub>3</sub> may be able to bridge this gap. The ability to fabricate structures within the crystal by femtosecond laser machining facilitates all integrated signal guiding and processing. Spatiotemporal imaging is employed for direct visualization of the electromagnetic field within the crystal. Polaritonic resonators, waveguides, photonic crystals and focusing, dispersive, and diffractive elements will be demonstrated.
- Authors:** David Ward, Thomas Feurer, Eric Stats, Joushua Vaughan, Keith Nelson, Massachusetts Institute of Technology)

Anvar A. Zakhidov, University of Texas at Dallas



## Conclusions on K(T) by Phonon-Polaritons



- Ph-Polaritons are found to contribute to K(T) of thin films, with T-peak. Position of T-peak depends on  $\Omega$  op, the line width of OP and the TO-LO splitting.
- K(T) can be 10-20 times stronger than the conventional radiative contribution to K by free photons.
- T-peak shifts to lowest T in microcavities ( $L \sim 1-10 \mu\text{m}$ ), which can be used in cryogenic heat transfer.
- To create a material with high enough polaritonic K(T) at RT, compared to the usual, phonon K<sub>ph</sub> one should create an organic material with OP at 1500-2000  $\text{cm}^{-1}$ , which has large oscillator strength. In organic materials K<sub>ph</sub> is usually low ( $< 0.1-1 \text{ W/mK}$ ), the K<sub>pol</sub> can become a main contribution.
- One candidate for polaritonic heat pipe, can be a doped fullerene film  $\text{M}_x\text{C}_{60}$  in which a giant oscillator strength S enhancement is found, which is quadratic in doping level x:  $S \sim x^2$ .
- The strong dependence of K<sub>pol</sub>(T) on S(x) leads to tunability of K(T) by charge transfer and thus may be used in "polariton-transistors", in which K can be amplified by charging gate G.
- Phonon-Polaritons can be used for "Polariton-lasers", which will emit monochromatic and coherent IR radiation, due to Bose-Einstein condensation in microcavity.

Anvar A. Zakhidov, University of Texas at Dallas





## Our Main Systems and Materials:



1. New Mechanism of Phonon-Polariton Thermal Conductivity

2. Carbon Nanotube Systems with Enhanced  $K(T)$  CNT:

- CNT Fibers and Yarns and
- Oriented CNT-ribbon aerogels

Anvar A. Zakhidov, University of Texas at Dallas



## PHONON TRANSISTOR in NANOTUBE FIBERS with Electrochemical Gate

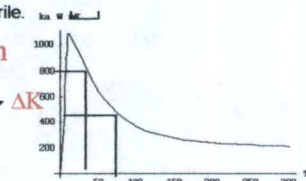


Capacitance of 134 F/gm, versus usual 15-30 F/gm.

**Electrolyte:** 1.0 M tetrathylammonium hexafluorophosphate in acetonitrile.

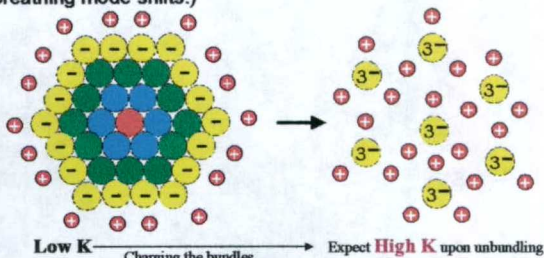
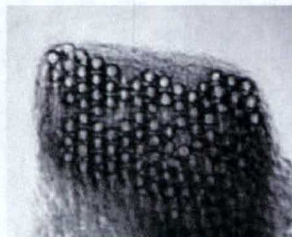
Debundling should decrease tube-tube phonon scattering, and increase  $K(T)$  dramatically:

**Phonon Transistor**



Increased capacitance results from debundling.

(Raman measurements of radial breathing mode shifts.)



Anvar A. Zakhidov, University of Texas at Dallas



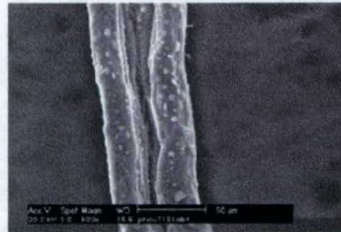


Prove of Unbundling: Twice Increased Diameter of Fibers



## SEM images of Purified Unannealed Oleum -spun HiPCo fibers

Phonon Transistor in 'OFF' state



Before cycling in EMIm  
Fiber diameter  $\approx 50 \mu\text{m}$

Transistor in 'ON' state



After cycling in EMIm  
Fiber diameter  $\approx 100 \mu\text{m}$

Anvar A. Zakhidov, University of Texas at Dallas

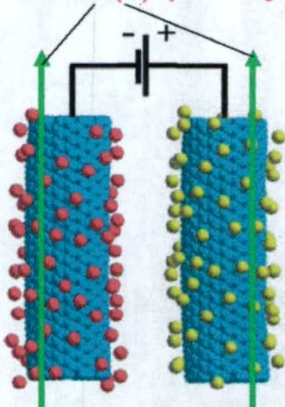
51



## Phonon Transistor with Electrochemical Charge Injection Gate



Increased  $K(T)$  upon G voltage



Gate function:

$C = \text{charge/voltage}$   
 $C = \text{Area} \times \text{dielectric constant} / d$   
 Area/weight is above  $300 \text{ m}^2/\text{gm}$ ;  
 $d$  is in nanometers

### Modulation of Thermal Conductivity $K(T)$

Charge injection will cause change  
 in tube-tube interaction, which changes  
 $\Omega$  of intertube phonon and modulate  
 The Tube-Tube scattering.

Anvar A. Zakhidov, University of Texas at Dallas





## Charging Setup:

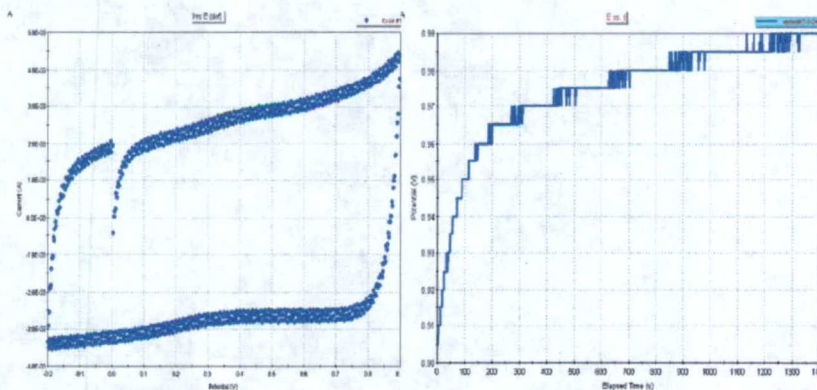


- SWNT paper was used to charge and study the effect of charge injection in field emission characteristics. SWNT paper was used as both the positive and negative electrode.
- Chronopotentiometry was used for performing the double layer charging. Princeton model 273A instrument contains both a potentiostat and a galvanostat, and hence can perform both controlled potential (potentiostatic) and controlled current (galvanostatic) experiments.
- Cyclic Voltammetry was also performed before the charging by cycling from  $-0.2$  to  $0.9$  V. The direction of the potential is reversed at the end of the first scan. This has the advantage that the product of the electron transfer reaction that occurred in the forward scan can be probed again in the reverse scan. It is a powerful tool for the determination of formal redox potentials, detection of chemical reactions that precede or follow the electrochemical reaction and evaluation of electron transfer kinetics.

Anvar A. Zakhidov, University of Texas at Dallas



## Charging I-t Curves



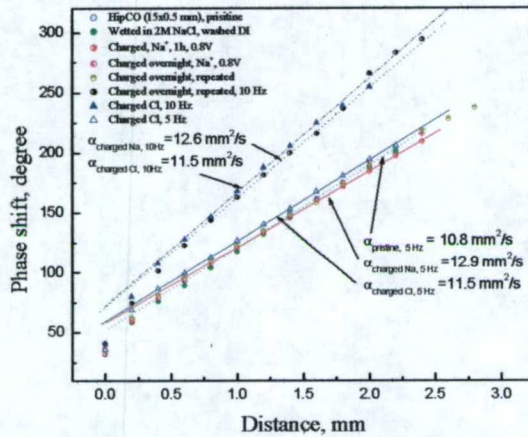
Capacitance of SWCNT paper is very large:  $C \sim 20-30$  F/g

Anvar A. Zakhidov, University of Texas at Dallas





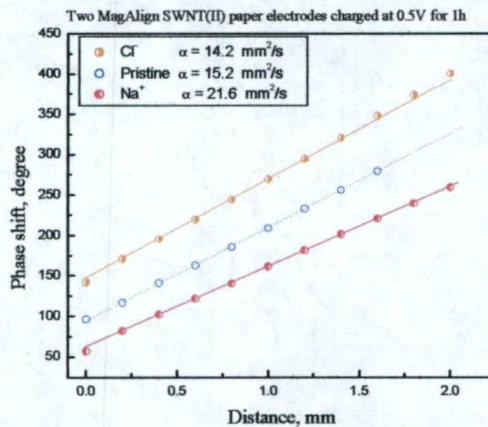
## Tuning K by Charge Injection



Anvar A. Zakhidov, University of Texas at Dallas



## Tuning K by Charge Injection: A Step towards Phonon Transistor



Thermal diffusivity and thus thermal Conductivity of CNT is proved to be tuned by Charge injection into

Oriented CNT paper at  $V = 0.5 \text{ V}$

Effect is 25 %:

From  $D = 15.2 \text{ mm}^2/\text{s}$  to  $21.6 \text{ mm}^2/\text{s}$

Anvar A. Zakhidov, University of Texas at Dallas



## Draw and Twist of yarns from MWNT forests

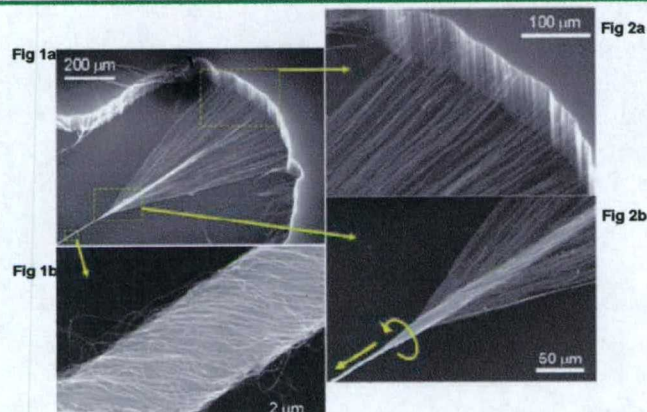
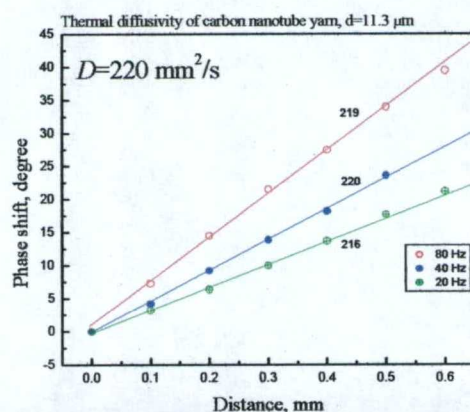


Fig. S2. SEM micrographs showing the structures formed during the draw-twist process. The relationships between the SEM micrographs of Fig. 1 and Fig. 2A are shown, as well as a higher magnification image of the partially bundled MWNTs being pulled from the forest wall. The draw twist process was interrupted, and the sample was transferred to a SEM for recording these images.

## High Thermal Diffusivity of Single CNT Yarn: Better than Cu



Anvar A. Zakhidov, University of Texas at Dallas





## Thermal conductivity of Single CNT Yarn: Better than Cu



- The thermal conductivity  $\lambda$  of single-strand MWNT yarn was obtained at room temperature from the relationship  $\lambda = \rho C_p D$ , by measuring the thermal diffusivity  $D$ , density  $\rho$ , and specific heat capacity  $C_p$ . The measurements of  $D$  were carried out using the laser flash technique.
- One end of a specimen of length  $L$  is uniformly irradiated by a laser beam  $Q = Q_0 \sin \omega t$ .
- 
- $\lambda = \rho C_p D = 0.8 \text{ g/cm}^3 \cdot 0.715 \text{ J/gK} \cdot 2.20 \text{ cm}^2/\text{s} =$
- $1.25 \text{ W/cm} \cdot \text{K} = 125 \text{ W/m} \cdot \text{K}$ ,
- where the specific heat capacity of graphite with density  $2.26 \text{ g/cm}^3$ :  $C_p(300\text{K}) = 8.58 \text{ J/(mol K)} = 0.715 \text{ J/gK}$  [1], (For comparison the specific heat capacity value for  $10 \mu\text{m}$  Amoco P-55 carbon fibers, with density of  $2 \text{ g/cm}^3$  at  $25^\circ\text{C}$  is  $0.717 \text{ J/gK}$  [2]),  $\rho = 0.8 \text{ g/cm}^3$  is the density of fiber, and  $D = 2.20 \text{ cm}^2/\text{s}$  is the thermal diffusivity of the fiber.
- For comparison, the thermal diffusivity of thin wire ( $100 \mu\text{m}$ ) of copper and gold are much lower:  $D_{\text{copper}} = 117 \text{ mm}^2/\text{s}$ ,  $D_{\text{gold}} = 130 \text{ mm}^2/\text{s}$ .

Anvar A. Zakhidov, University of Texas at Dallas



## 'Draw-Twist' process to convert MWNT in a forest to 'Twisted Yarns'



### Multifunctional Carbon Nanotube Yarns by Downsizing an Ancient Technology

M. Zhang, Ken Atkinson, Ray Baughman, *Science* 306 (2004) 1358

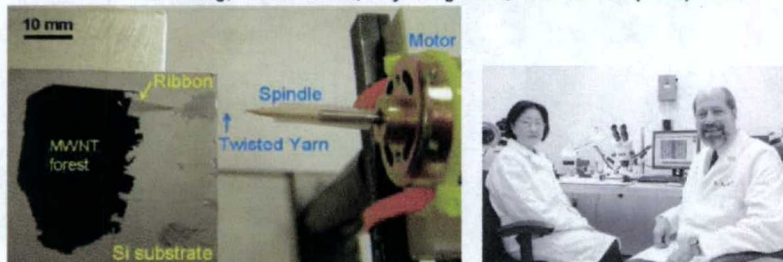
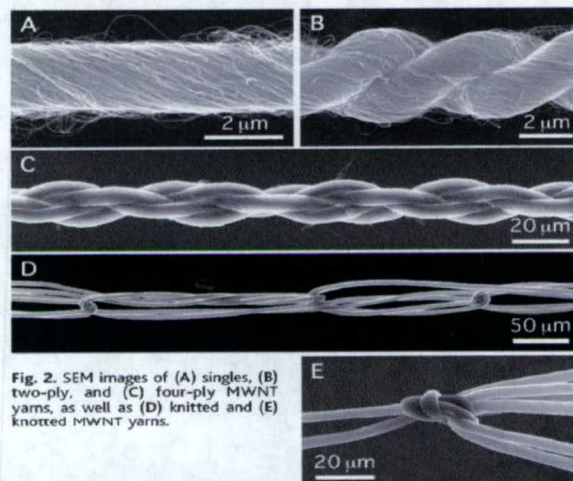


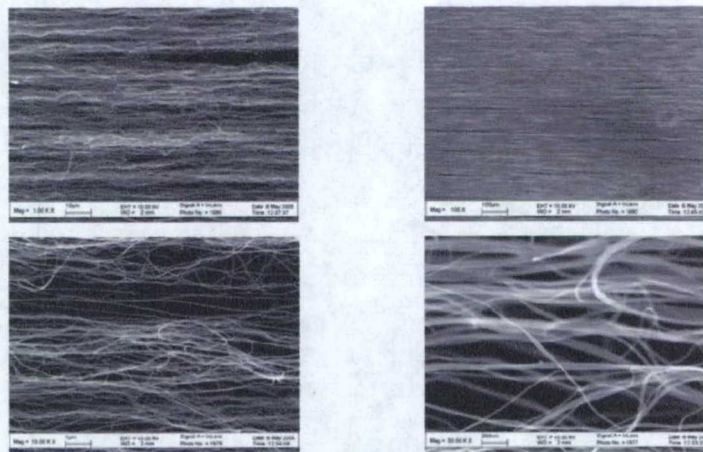
Fig. S1. Photograph taken during interruption of the draw-twist process used to convert MWNTs in a forest to a twisted MWNT yarn. The overlapping images of both the nanotube wedge and yarn are a result of reflection in the silicon substrate.

Anvar A. Zakhidov, University of Texas at Dallas



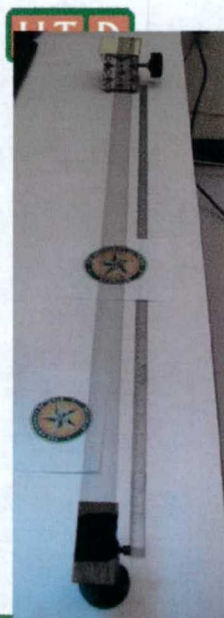


Anvar A. Zakhidov, University of Texas at Dallas



Anvar A. Zakhidov, University of Texas at Dallas





## NanoTech Institute MWNT Sheet Fabrication Process



Sheets (presently 5 cm X 1 m) are fabricated At 3 m/minute. These width and length are not fundamentally limited and the rate is limited by our present draw apparatus.

We have promising initial results for diverse applications:

- \* transparent elastomeric electrodes;
- \* light-emitting diodes;
- \* incandescent sources of polarized light;
- \* two-dimensionally reinforced composites; & microwave absorbing appliquéés

Anvar A. Zakhidov, University of Texas at Dallas



## Spun nanotube sheets as an incandescent light source.



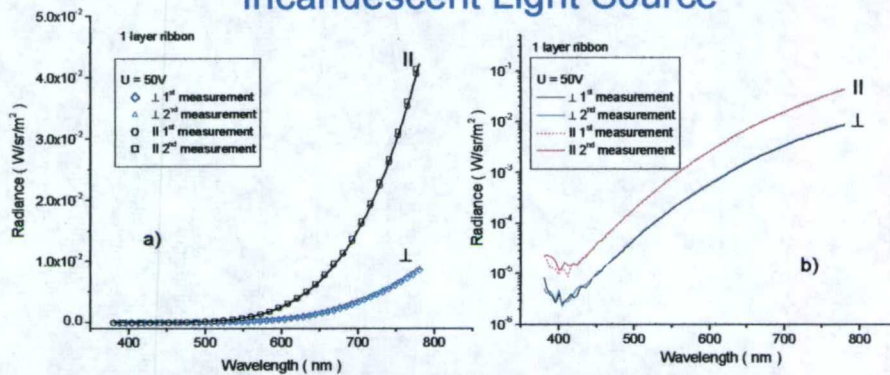
The light output is polarized, with a degree of polarization that increases with wave length from 0.6 at 500 nm to 0.66 at 780 nm.

Anvar A. Zakhidov, University of Texas at Dallas





## Polarized Emission of Nanotube Sheet Incandescent Light Source

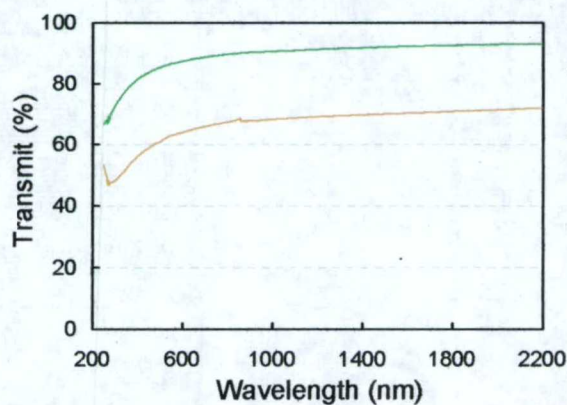


Spectral radiance of incandescent light from single sheet of parallel carbon nanotubes: a) linear scale, b) semi logarithmic scale. The solid line in a) is a fit by black body radiation with  $T=1350$  K.

Anvar A. Zakhidov, University of Texas at Dallas



## Optical Transparency of MWNT Sheet



Polarizer Alignment:

*Perpendicular*

*Parallel*

Resistance: ~600  $\Omega/\square$  (in aligned direction)  
~15 K $\Omega/\square$  (in cross direction)

Anvar A. Zakhidov, University of Texas at Dallas



## **5.5 “Phonon and Thermal Transport in Carbon Nanotube Systems”**



# Phonons and Thermal Transport in Carbon Nanotube Systems

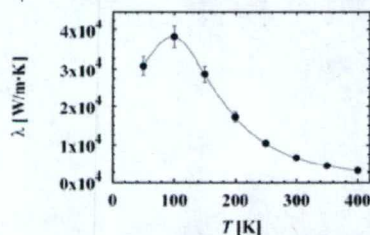
*An informal review*

Yuri Gartstein  
Department of Physics  
The University of Texas at Dallas

DARPA DSRC Nanoscopic Phonon  
Engineering Workshop  
May 9, 2005

## "What's the buzz?" – Great Promise:

"Due to the combination of a high speed of sound, hard optical vibration modes and a large phonon mean free path, carbon nanotubes prove to be the most efficient thermal conductors." (*D. Tomanek, 2005*)



In MD simulations of *Tomanek's* group (2000), the peak therm. cond. of (10,10) **SWNT** found to be 37000  $\text{W/m}\cdot\text{K}$ , on par with the highest value ever observed in a solid (diamond). RT value of 6600  $\text{W/m}\cdot\text{K}$  is also very high...

"The stiff  $\text{sp}^3$  bonds, resulting in a high speed of sound, make monocrystalline diamond one of the best thermal conductors. An unusually high thermal conductance should also be expected in carbon nanotubes, which are held together by even stronger  $\text{sp}^2$  bonds..."

The rigidity of nanotubes, combined with a virtual absence of atomic defects or coupling to soft phonon modes of the embedding medium, should make these systems very good candidates for efficient thermal conductors".



## But can we measure and utilize it?

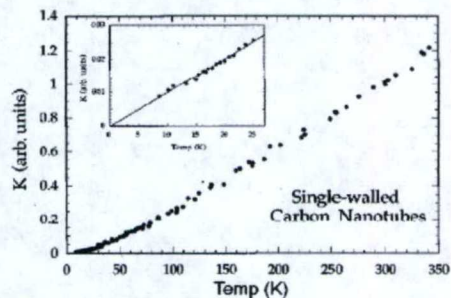
- "The expected high thermal conductivity value in nanotubes makes its direct experimental observation very difficult. Since thermal transport is likely to be dominated by phonon scattering in the contact region, the most important and currently unsolved challenge is to reproducibly create and characterize thermal contacts to a nanotube. Even if thermal scattering in the contact region could be minimized, the net thermal transport would still be limited by that of the leads". (*D. Tomanek, 2005*)

- "Interlayer interactions quench the thermal conductivity ... by nearly 1 order of magnitude. We should expect a similar reduction of the thermal conductivity when ... nanotubes form a bundle or rope, become nested in multiwall nanotubes, or interact with other nanotubes in the "nanotube mat" of "bucky paper". (*Berber, Kwon and Tomanek, 2000*)

## In fact, even experimental data are relatively scarce

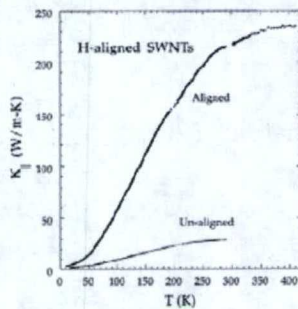
Some "standard" references

Thermal conductivity of mats of crystalline ropes of SWNTs. RT value of  $\kappa$  deduced  $\sim 35$  W/m-K. (*Hone et al, 1999*). Analysis suggests that phonons dominate thermal transport.

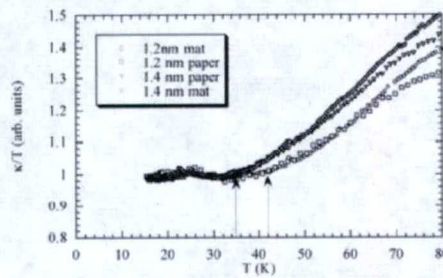




### Experimental Data continued: Morphology and Ordering Matter

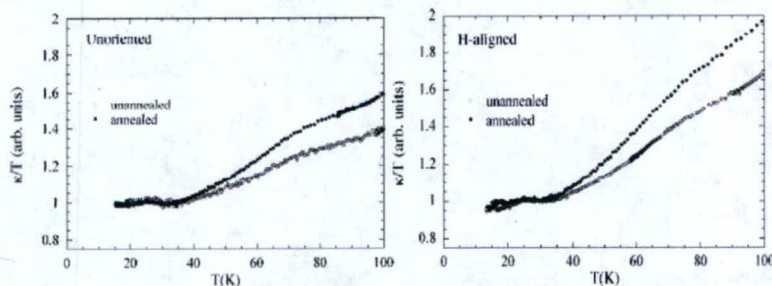


Thermal conductivity of the "thick" annealed sample of aligned SWNT, measured in the parallel direction. At 300 K,  $\kappa$  is much higher than in unaligned material, and is within an order of magnitude of graphite or diamond. (Hone *et al*, 2000)



Crossover suggests 1-d quantization is indeed up to higher T for smaller diameters (Llaguno *et al*, 2002)

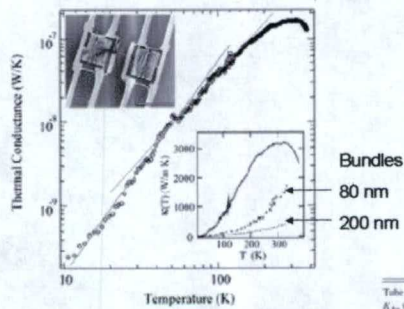
### Morphology Effects (Defects) can be Improved also by additional processing



Annealing helps by eliminating impurities and healing defects (Llaguno *et al*, 2002)

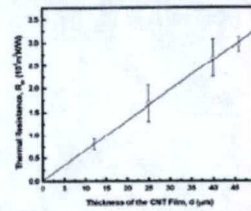


# Experimental Data: Multiwall Nanotubes



Individual suspended MWNT ( $d=14$  nm) per Kim, Shi, Majumdar, and McEuen (2001). Maximum  $\kappa=3000$  W/m·K much larger than 20 W/m·K reported for mats (Yi et al, 1999). Bundling deteriorates  $\kappa$ .

MWNT films (Yang et al, 2002) – noncontact measurements



Tube length ( $\mu\text{m}$ )	12	25	40	46
$R_{\text{CNT}}$ (W/m·K)	268–288	182–243	267–293	230–310
$R_{\text{SiO}_2}$ (W/m·K)	13–17	12–16.5	11–17	14–17
Thermal diffusivity $\alpha_{\text{SiO}_2}$ ( $10^{-6}$ m <sup>2</sup> ·s <sup>-1</sup> )	1–2.6	1–10	5–8	6.7–1

$\kappa \sim 20$  W/m·K deduced independent of tube length. "Taking the volume-filling fraction of CNT's into account, the effective thermal conductivity for the MWNT's is about 200 W/m·K".

Overall sentiment on experimental situation seems to be that room-temperature values of  $\kappa$  vary from units and tens of W/m·K to a couple of hundred of W/m·K for various arrays, the results ordinarily improving with the decrease of the bundle size. A record result of 3000 W/m·K relates to individual MWNT.

Can this record result have to do with a higher density of layers of the "material" of the sample accompanied by the absence of the need of entangled 3-d heat transfer?

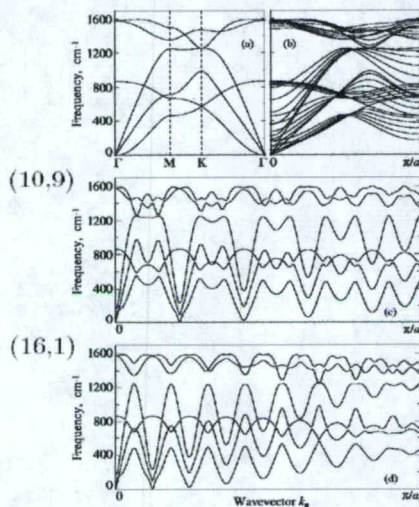
Also,  $\kappa$  seems to be an increasing function of temperature up to about room temperatures.

- Now, what about our understanding of phonons in NTs and the thermal transport?



## Model vibrational spectra shown using spiral symmetry

Graphene (10,10)

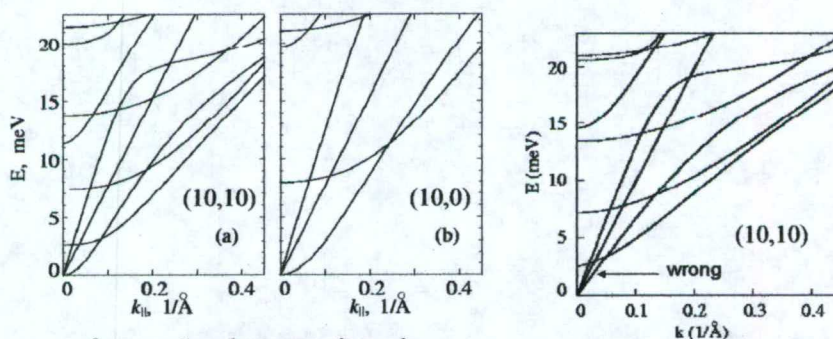


Vibrational spectra of individual SWNTs are basically well understood:

High-frequency part of the spectrum is well represented by zone-folding of the graphene spectrum.

Low-frequency part reflects generic 1-d features common with vibrations of elastic cylinders.

## Low-frequency part of the spectrum



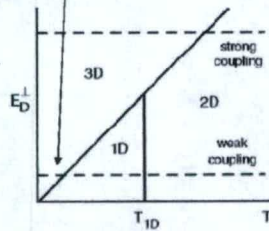
features 4 gapless acoustic modes:  
longitudinal and twisting with linear dispersion  $\omega \sim k$  and degenerate bending with parabolic dispersion  $\omega \sim k^2$  as well as higher energy modes with quantized gaps.

In the "older" picture (however being sometimes used even now) bending (transverse) modes were believed to have  $\omega \sim k$ .

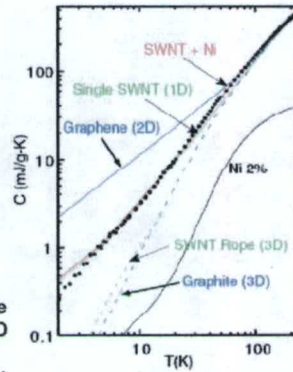


## Intertube Phonon Coupling and Dimensional Crossovers

Experimental data of Hone et al (2000) on specific heat in SWNT ropes suggests that intertube phonon coupling is weak.

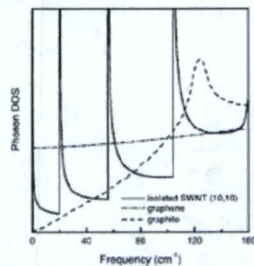


- Isolated tube phonons cross over from a 1D regime where only acoustic subbands are occupied to a 2D regime as higher (optic) subbands are populated.
- In a bundle of weakly coupled tubes, phonons are 3D at very low temperature, then crossing over to a 1D regime.
- If the coupling were strong, the 1D regime would be bypassed and a quantized 1-d phonon spectrum would not be observed.

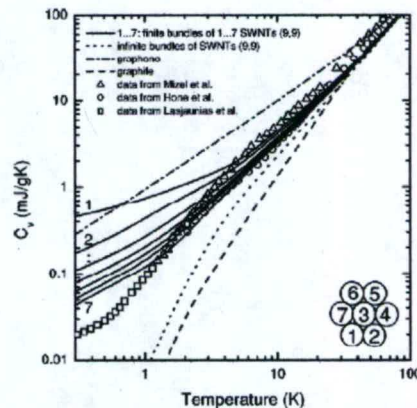


More accurate analysis of specific heat by Popov (2002) does not seem to contradict the conclusion of weak intertube phonon coupling

System	Acoustic branch	Phonon dispersion	Phonon DOS	Specific heat
Graphite	LA, TA	$\omega \propto q$	$D(\omega) \propto \omega^2$	$C_v \propto T^3$
Graphene	LA, TA	$\omega \propto q$	$D(\omega) \propto \omega$	$C_v \propto T^2$
	ZA	$\omega \propto q^2$	$D(\omega) = \text{const}$	$C_v \propto T$
SWNT	LA, TW	$\omega \propto q$	$D(\omega) = \text{const}$	$C_v \propto T$
	TA	$\omega \propto q^2$	$D(\omega) \propto 1/\sqrt{\omega}$	$C_v \propto \sqrt{T}$



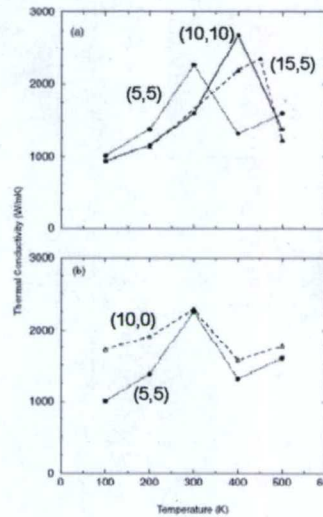
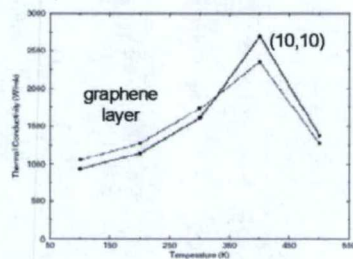
Phonon DOS with correct bending modes



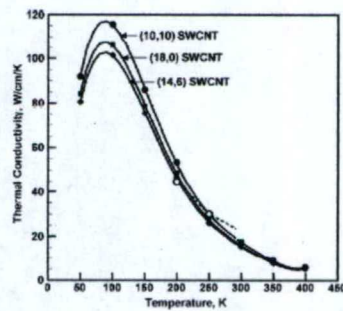
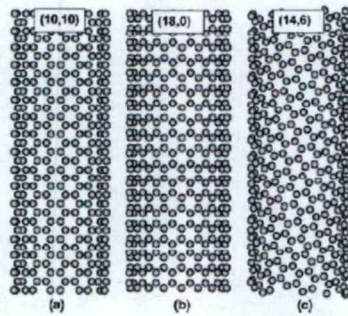


## More simulations of thermal conductivity of SWNTs

MD simulations of *Osman and Srivastava (2001)* also (comp. to Tomanek's) reveal a maximum of  $\kappa$  but of different magnitude and at higher T, and indicate a dependence on tube radius



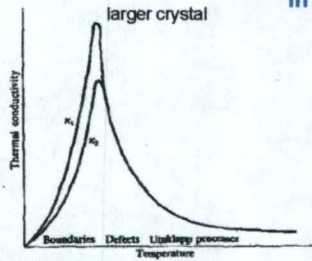
MD simulations of *Grujicic, Cao and Roy (2005)*



Results are closer to Tomanek's



Despite the variations, MD results show a similar pattern well known in the theory of solids



"Between the Umklapp region and the boundary scattering region... the conductivity maximum, whose appearance is perhaps one of the most striking predictions of the quantum theory of solids".  
(J. Ziman, 1960)

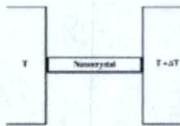
Qualitatively,  $\kappa \sim C \cdot v \cdot l$

At high  $T$ , it is phonon-phonon interactions (umklapp scattering) that reduce mean-free path  $l$ .

At low  $T$ , umklapp processes are not efficient and mean-free path is overtaken by the sample size  $L$ .  $T$ -dependence is largely that of heat capacity  $C$ .

But what is it that plays the role of  $L$  in MD simulations, where sample sizes are at best hundreds of angstroms with or without periodic boundaries? Estimates for mean-free paths are normally given as fractions or comparable to a micron. Moreover, one can make simple but fundamental estimates...

### Conductance and Conductivity



Conductance  $G$  of a "sample": Heat current  $J = -G \cdot \Delta T$

Conductivity  $\kappa$  of a "material": Heat current density  $j = -\kappa \frac{dT}{dx}$

$$\kappa = G \frac{L}{S}; \text{ Length } L, \text{ cross-section } S$$

• Additional scatter in reported results is due to various choices of  $S$

### Low-T Ballistic Conductance Quantization

(Rego and Kirczenow, 1998)

In the absence of phonon interactions (*ballistic*) and for ideal contacts, each acoustic mode in the limit of low  $T$  brings quantized contribution to the conductance

$$G_1 = \frac{\pi^2 k_B^2}{3h} T = 9.456 \cdot 10^{-13} \text{ (W/K}^2\text{)} \cdot T; \quad G = N_{\text{channels}} G_1$$

In general, ballistic conductance

$$G = \frac{k_B^2 T}{h} \sum_{\alpha \text{ all monotonic segments}} \int_{Z_{\alpha \text{ lower}}}^{Z_{\alpha \text{ upper}}} dx \frac{x^2 e^x}{(e^x - 1)^2}; \quad Z = \frac{\hbar \omega}{k_B T}$$



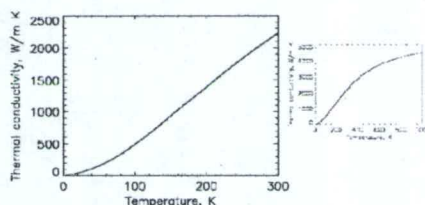
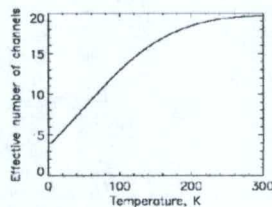
## Ballistic conductivity results: A likely upper limit

Trying to rationalize MD results, consistency check...

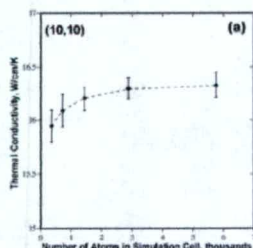
Knowing vibrational spectrum, it is very easy to calculate ballistic conductance, no other scattering but the boundary one. Here ball. cond. is shown translated into  $\kappa$  for a (10,10) tube, give or take for the accuracy of the spectrum.

Length used is  $L=1$  micron and cross-section  $S=250$  angstrom<sup>2</sup>.

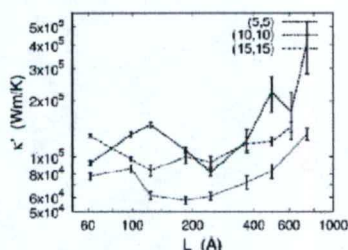
To get, e.g., Tomanek's result at  $T=100$  K, the length would need to be increased by a factor of  $\sim 80$ . So what is the meaning of the effective lengths appearing in those MD calculations?



## Interesting comments on the convergence of MD results upon the increase of the simulation sample size



"... despite the fact that the phonon mean free path is considerably larger than the sizes of the computational cells used, an apparent convergence in the thermal conductivity can be obtained". (Grujicic et al, 2005)

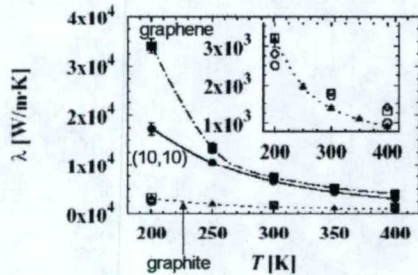


"We find that the low-frequency vibrational modes of the lattice are limited by the size of simulation domain, and the thermal conductance of an infinite long CNT may be infinite". (Yao et al, 2005)



## Intertube Phonon Coupling and Thermal Conductivity

Not that much has been done...



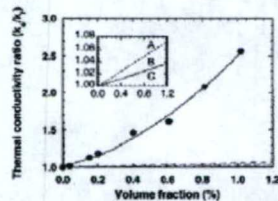
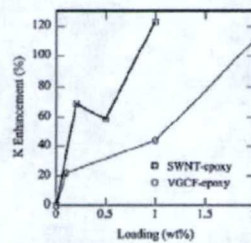
Berber et al (2000) base their conjecture on the analysis of the interlayer effect for graphite:

"Very interesting is the fact that once graphene layers are stacked in graphite, the interlayer interactions quench the thermal conductivity of this system by nearly 1 order of magnitude... We should expect a similar reduction of the thermal conductivity when a nanotube is brought into contact with other systems".

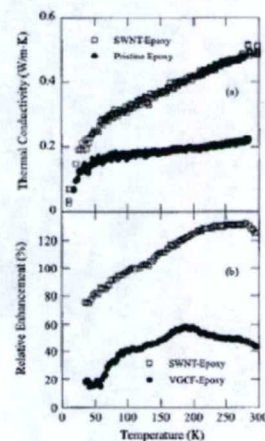
Che, Cagin and Goddard (2000): "We also carried out the thermal conductivity calculation for (10, 10) nanotube bundles in close packing condition. The simulations show that the nanotube bundle has very high thermal conductivity along the tube axis, 9.5 W/cm/K [ $T=300$  K], which is comparable to simulated graphite in-plane thermal conductivity, 10 W/cm/K."

## Thermal Conductivity Enhancement in Composites

SWNTs in Epoxy  
(Biercuk et al 2002)



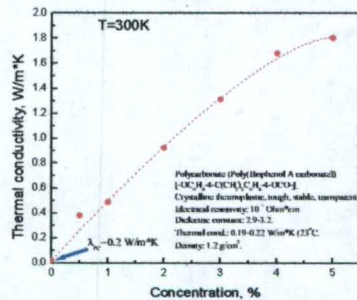
MWNTs in Synthetic Oil  
(Choi et al 2001)



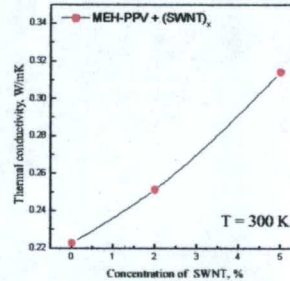


## "In-House" (UTD Nano-Tech) Measurements

(courtesy of Dr. A. Aliev)



Substantial enhancement in nearly uniform mixtures of SWNTs in polycarbonate



Much more modest effect for mixtures in conjugated polymer MEH-PPV (attributed to agglomeration of SWNTs).

## Effective Medium Analysis for Composites

(Nan et al, 2003, 2004)

low volume fraction  $f$  result

$$\frac{\kappa_c}{\kappa_m} = 1 + \frac{f \cdot p}{3} \frac{\kappa_c / \kappa_m}{p + \frac{2a_K \kappa_c}{d \kappa_m}}$$

$\kappa_c$  - composite

$\kappa_m$  - matrix

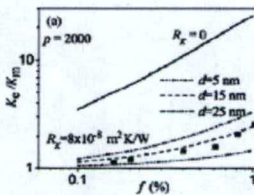
$\kappa_c$  - nanotube

$p$  - aspect ratio

$d$  - nanotube diameter

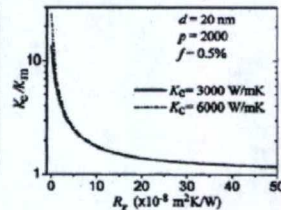
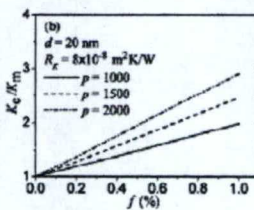
Kapitza radius  $a_K = R_K \kappa_m$

due to interfacial thermal resistance  $R_K$



Some exp. data can be rationalized (here  $\kappa_c=3000$  and  $\kappa_m=0.4$  W/m·K)

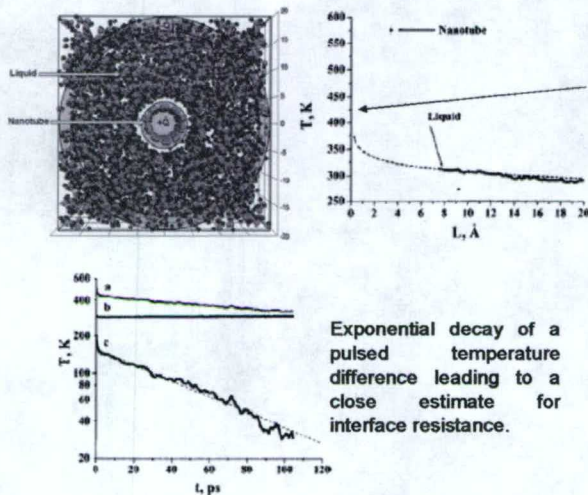
Extremely important role of interface resistance





## Thermal Interface Resistance between SWNT and octane liquid

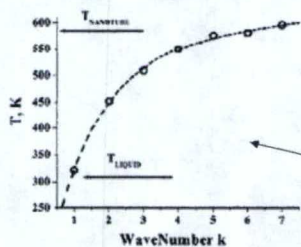
(Cahill and Koblinski's groups, 2003, 2004)



Steady state flow between NT and a sink – local  $T$  vs distance from NT.

Dramatic temperature gradient at the interface - the largest thermal resistance is with the nanotube-liquid interface estimated to be  $\sim 3 \cdot 10^{-8} \text{ m}^2\text{K/W}$  for NT  $\sim 4 \text{ nm}$  long and  $d=0.7 \text{ nm}$ . With liquid  $\kappa \sim 0.1 \text{ W/m-K}$ , the interface resistance is equivalent to having NT surrounded by  $\sim 5 \text{ nm}$  thick extra layer of octane!

## Vibrational Mode Analysis of Interface Resistance



Spectral temperature of nanotube bending modes as a function of mode number. The lowest frequency mode has nearly the same temperature as the surrounding fluid while the high frequency modes have temperatures close to the average temperature of the nanotube.

Decrease of the interface resistance with the NT length led to conjecture that it is coupling of low-frequency bending modes of NT to low-frequency octane vibr. modes that provides heat flow – all interactions being driven by dispersion forces (octane-octane and octane-NT).

Spectral temperature analysis confirms.

### Shenogin's et al (2004) scenario:

1. The heat energy first flows from the high frequency modes to the low frequency transverse vibration modes (controlled by the intrinsic phonon-phonon scattering in the tube)
2. It then transfers to the layer of octane liquid adjacent to the nanotube (controlled by the coupling between soft modes in the tube and in the liquid)



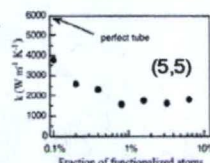
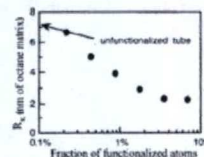
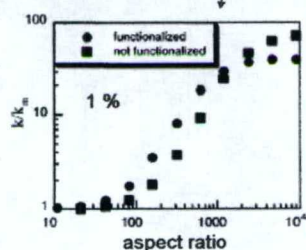
### Can Interface Resistance be Decreased by Increasing Coupling to the Matrix? – Yes but only by so much (Shenogin et al 2004)

Chemical functionalization – introducing chemical bonds between molecules of matrix (octane) and carbon atoms of nanotube:

1. Interface resistance IS decreased ... but

2. Defects formed on NT decrease its own  $\kappa$

**Net result:** A limited improvement by a factor of 2 for a range of aspect ratios



### Concluding Remarks

"Modest" applications of nanotubes for thermal management (like 100-200% increase for composites with low conductivity matrices) look quite feasible.

However, in order to evaluate prospects of more aggressive goals fully exploiting the claimed potential, much more research work is needed to provide a firm understanding of issues involved. Among the problems could be:

- Details of the physics of individual tube behavior, especially the low-T regime
- Microscopic picture of intertube/interlayer interactions and scattering
- Microscopic study of contacts with various media (leads)
- Possibility of (self-) assembly of contacts and environments that would be beneficial to the therm. conductivity
- Optimization issues given the understanding achieved